BESSY
Berliner Elektronenspeicherring-Gesellschaft
für Synchrotronstrahlung m.b.H.

Anna Zimina

Novel Nanomaterials Studied by the Method of Soft X-ray Fluorescence Spectrocopy

Novel Nanomaterials Studied by the Method of Soft X-ray Fluorescence Spectroscopy

vorgelegt von
Diplom-Physikerin
Anna Zimina
aus Sankt-Petersburg

von der Fakultät II - Mathematik und Naturwissenschaften
der Technischen Universität Berlin
zur Erlangung des akademischen Grades
Doktor der Naturwissenschaften
Dr.rer.nat.

genehmigte Dissertation

Promotionsausschuss:

Vorsitzender:	Prof. Dr. C. Thomsen
Berichter:	Prof. Dr. W. Eberhardt
Berichter:	Prof. Dr. P. Zimmerman

Tag der wissenschaftlichen Aussprache 27. Oktober 2006

Berlin 2006
D 83

Dedicated to my family

Contents

Chapter 1

Introduction.

> Nanotechnik bedeutet nicht kleiner, billiger, schneller.
> Nanotechnik heisst: intelligenter, intelligenter, intelligenter.
>
> Heinrich Rohrer, the 1986 Nobel Prize for Physics.

Materials with characteristic structure sizes of a few nanometers are a forefront area of modern materials science due to the possibility to tailor many properties by changing size, shape and dimensionality. Such materials are fabricated by a variety of different approaches in order to achieve a specific mechanical, chemical, optical or electronic performance. Often, such nanomaterials have to be embedded in a matrix in order to be suitable for technological applications, for example in order to achieve stability under ambient conditions or in order to interface to other components of an integrated device.

Nanostructured materials are different from both molecules and bulk solid state material. A large number of publications is devoted to the synthesis of nanostructured materials and to the examination of their properties by different experimental and theoretical methods. It becomes obvious that it is an important aspect to refine methods of theoretical consideration of the electronic structure due to size-specific effects. To realize the refinement a high level control over the synthesis is required. It was achieved for some materials, for other structures the challenge is still there.

In the present work the results of investigation of several nanostructured materials using of synchrotron radiation are presented, among them are Si nanoclusters, Mo - S - I based nanotubes/nanowires and $Sc_3N@C_{80}$, an endohedral fullerene.

Silicon is the standard material in current microelectronics technology. Attempts have been made to realize optoelectronic functions by silicon based structures. After the discovery of the strong, size dependent photoluminescence (PL) of porous silicon in the visible spectral range [1], further research focused on such Si nanoparticles which are more stable under ambient conditions. Si nanoparticles can be produced in a silicon dioxide matrix by ion implantation [2], sputtering of Si rich oxides [3], reactive evaporation of Si rich oxides [4], and high temperature annealing of SiO/SiO_2 superlattices [5]. The last method has the advantage to provide good control of the size and space distribution of the Si clusters. While the optical properties of such structures are directly accessible by optical spectroscopy in the visible or infrared spectral range, the underlying electronic structure is difficult to probe directly. The electrically isolating glass matrix hampers

efforts to perform transport measurements and tunneling spectroscopy. The chemical sensitivity and the atomic selectivity of the method of soft X-ray absorption and emission are explored here for the study of the electronic structure of such Si clusters embedded into the class matrix (Chapter 4).

Since the discovery of a new type of carbon structure, namely carbon nanotubes (NTs), in 1991 by Iijima and coworkers [6], they have been investigated by many researchers all over the world. Their large length (up to several microns) and small diameter (a few nanometers) result in a large aspect ratio. It was Prof. Richard Smalley, 1996 Nobel Prize for Chemistry for the development of the fullerenes together with Prof. Robert E. Curt and Prof. Harold W. Kroto, who said: "These nanotubes are so beautiful that they must be useful for something". Physical properties of carbon nanotubes are determined to a large extent by their nearly two dimensional structure. The most important properties of CNTs and their molecular background are stated below.

Chemical reactivity. [7] The enhanced chemical reactivity of a carbon NT is, compared with a graphene sheet, is directly related to the π-orbital mismatch caused by an increased curvature. For the same reason, a smaller nanotube diameter results in increased reactivity. Though, direct investigation of chemical modifications on nanotube behavior is difficult as the crude nanotube samples are still not pure enough.

Electrical conductivity. [8] Depending on their chiral vector (rolling-up direction) and diameter, carbon nanotubes are either semiconducting or metallic. The differences in conduction properties are caused by the molecular structure that results in a different band structure and thus a different band gap. The differences in conductivity can easily be derived from the graphene sheet properties [9].

Mechanical strength. Carbon nanotubes have a very large Young modulus in their axial direction. Therefore, these compounds are potentially suitable for applications in composite materials that need anisotropic properties.

The discovery of carbon fullerenes and nanotubes, jointly with the basic understanding of the origin of their remarkable properties and the potential applications in nanoelectronics, initiated many investigations in this field of material science in the last decade [10]. It was found that other, carbon-free materials, which posses layered structures in their normal modification, can be synthesized in fullerene- and nanotubes-like forms [11, 12]. MoS_2 is such a material which can exist in a 3D cage structure, single- and multi-wall nanotubes, and ropes. Theoretical work [13] on individual MoS_2 tubes with an outside diameter ranging from 8 $\mathring{A}$ to 26 $\mathring{A}$ predicted that the electronic structure of the MoS_2 NT differs from the bulk material: it depends on the chirality and the band gap increases monotonously toward the bulk value with increasing tube diameter. Zigzag MoS_2 NTs are predicted to have a narrow direct gap and thus might be used for future optoelectronic devices [14]. However, a MoS_2 NT with a diameter smaller than 20 $\mathring{A}$ appeared to be unstable in theory [13] due to the strong distortions when the trilayer is curved to a tube.

For nanotubes to be useful for electronics monodisperse materials are required. Alternatively, a weak dependence of the band gap on diameter is preferable, so that a small distribution in the diameter still can be used. Carbon NTs do not fulfill either of these requirements [15]. From the application point of view the situation is more favorable for MoS_2 NTs, where perfect size control is not absolutely necessary, since a distribution in the diameter does not cause a large change of the band gap character (i.e. direct vs. indirect).

Prospects for application of NTs in electronics were improved with the reported synthesis of the self-assembling subnanometer-diameter $Mo_xS_yI_z$ nanostructures [16, 17, 18]. The material grows in the form of bundles of identically structured molecules, with an outer diameter of less than 1 nm. Bundles can be up to several hundreds of micrometers long and consist of up to 10^6 individual nanotube-like objects. By applying the method of soft X-ray absorption and emission spectroscopy to study the Mo-S-I nanowires the information about the electronic structure of those materials can be obtained. This will help to confirm the geometrical structure of the nanowires and to explain their outstanding electronic properties (Chapter 5).

The discovery in 1985 of a third allotrope of pure carbon, the fullerenes, has enriched solid state science with a new class of materials exhibiting fascinating and potentially useful properties [19]. A great number of publication is devoted to the experimental and theoretical investigation of the chemical and physical properties of fullerenes (see for example [20]). Since the discovery, scientists have discussed possible uses for these unusual molecules. Just some of these possibilities are described here.

Chemical sponges. Medical researchers believe that fullerenes could be put to work as tiny chemical sponges, mopping up dangerous chemicals from injured brain tissue. Excess production of free radicals (eg, peroxide) in the brain following a head injury or a stroke destroys nerve cells. Fullerenes, made soluble in water, appear able to catch and hold free radicals, thereby reducing the damage to tissue [21].

Fullerenes in miniature circuits. A supercomputer with the size of a paperback is the ambition of researchers who have managed to attach a single fullerene to a sheet of copper [22]. The scientists compressed the fullerenes by 15 %, improving electrical conductivity by more than 100 times compared to the undisturbed molecule. A tiny electronic component like this could make miniature circuits feasible.

Lubricants, catalysts and superconductors. Other exciting potential uses of fullerenes include fullerens behaving as "molecular ball bearings" allowing surfaces to glide over one another [23]. Fullerenes with metal atoms attached to them might function as catalysts, increasing the rate of important chemical reactions [24]. It is teoretically predicted that some fullerenes can act as superconductors even at room temperatures [25].

Molecular sieves. Because of the way they stack, fullerenes could act as molecular sieves, trapping particles of particular sizes while leaving others unaffected. Scientists talk of designing sieve-like membranes from fullerens that allow biological materials to pass through, but not larger particles such as viruses [26]. This would be useful for handling transplant organs, for example.

Buckycopiers. The idea to improve the charge-generation efficiency of organic-photoreceptor materials used in xerography and for laser printers by mixing the material with buckminsterfullerene was developed. The improvement is based on an electron transfer from the C_{60} excited excitonic state of the photoreceptor molecule to the C_{60} thus reducing the recombination probability [27]. In the United States, Xerox owns patents (United States Patent Nr. 5232810) for using fullerenes to improve resolution of photocopies.

More then 9000 fullerenes and their derivatives are synthesised now. After the discovery of the fact than fullerenes with only certain number of carbon atoms are observed the

theoretical calculation were devoted to explain this fact. Some of the fullerenes obey the isolated pentagon rule (IPR): this rule states that the most stable molecules are those in which every pentagon is surrounded by five hexagons. However, it is not possible to satisfy this rule in a molecule with fewer than 60 carbon atoms. So-called non-IPR fullerenes often have unusual properties, but it also makes them structurally unstable and difficult to synthesize. The carbon fullerenes with other number of atoms were predicted to be stable only as ions. The possibility to stabilize the unstable C_{80}^{6-} by introduction of a molecule was proposed based on the estimation of the static stability and electronic properties [28]. Indeed, the C_{80} fullerene was successfully synthesized by introducing small amount of Sc and N into the oven. The charge transfer from the molecule to the cage is assumed to be a reason for the cage stabilization. This prediction was examined by several experimental methods and by theoretical calculations. The charge transfer is found to drastically change the current-voltage characteristics: the current through a $Sc_3N@C_{80}$ based device is double of that through a bare C_{80} device as predicted by the *ab initio* calculation [29]. To study the electronic structure of endohedral fullerenes different experimental methods [30, 31] and theoretical calculations [28, 32] were applied. To obtain an information about the state of the enculapsed in the carbon cage molecule soft X-ray absorption and emission spectroscopy has been applied as it is a bulk sensitive and atom selective method (Chapter 6).

Chapter 2

Theory of Soft X-ray Spectroscopy.

2.1 Methods for the study of the electronic structure of solids.

In modern physics the methods of X-ray spectroscopy and electron spectroscopy play important roles in the investigation of the electronic properties of solids. There is a wide spectrum of experimental techniques to investigate the electronic structure of solids which differ from each other mostly by the excitation method and electronic states which are probed.

In the atom electrons form a system where they occupy some space around the nucleus. The closer the electron is to the nucleus the more energy one needs to remove it from the atom. When atoms approach to build a molecule, outer electrons ('valence electrons') change their position and energy to form a bond. The inner electrons in general preserve their states. Atoms agglomerate to form solids consisting of the order of 10^{23} atoms per cm^3. The geometric structure of the solid is the result of the self-organization of atoms optimising the energy of the structure. The geometrical structure is reflected in the shape of the macroscopic crystal. Individual atomic valence states with discrete eigenenergies transform into delocalized states ("bands") which are common in the whole solid due to the translation symmetry. The electronic structure defines almost all properties of the solid. Delocalizied common states are organized into the "valence band" (VB) of occupied states and the "conduction band" (CB) of unoccupied states. In the case of insulators and semiconductors these bands are separated from each other by an energy gap which is called the "band gap". In metals there is no gap, the bottom of the CB follows directly after the VB . Thus, inner electrons reflect the individual character of the atom in the solid whereas outer electrons experiece the presence of many nuclear potentials and particirate in the formation of chemical bonds [33].

To examine physical and chemical properties of the solid the energy distribution of core and valence electrons needs to be measured. The binding energy of the electrons can be measured after the electron is excited from its ground state by radiation or particles. The created vacancy can decay in different ways (radiative or non-radiative). Processes of the electron excitation and the following relaxation of the system define different experimental methods shown in Table 2.1.

Method	Incident particle	Observed particle	Probed states
Soft X-ray absorption (SXA)	photon	photon/electron	conduction band
Soft X-ray fluorescence (SXF)	photon/electron	photon	valence band / core levels
X-ray photoelectron emission spectroscopy (XPS, PES)	photon	electron	core levels / valence band
Inverse photoemission (IPE)	electron	photon	conduction band
Auger electron spectroscopy (AES)	electron / photon	electron	core levels / valence band

Table 2.1: Some wide used methods to study of the electronic properties of solids.

In this work soft X-ray absorption (SXA) and soft X-ray fluorescence (SXF) spectroscopies were applied to examine the electronic structure of materials. The photon energy of interest typically lies between several tens of eV and one keV. Photons with energies in this region are absorbed in the air and referred to as "soft X-rays". A schematic picture of the absorption and emission as a two-steps processe in one-electron approximation (see section 2.2) is shown in Fig. 2.1. First, the absorption of the incident photon with the energy close to the binding energy of the core electron causes the transition of the core electron into the CB. The probability of the electron transition depends on the energy of the primary photon and on the number of empty states in the CB. Additionally, the electron transitions in this energy range obey the dipole selection rules. These rules couple the transition probability with the symmetry of the core level involved. The measured absorption intensity reflects the local partial density of states (LPDOS) in the CB of the solid in this simple picture. The absorption behavior can be monitored by measuring the intensity of the primary beam in the transmission mode or by measuring a secondary process which is proportional to the absorption. The most widely used secondary processes are the non-radiative decay cascade of the core vacancy ("electron yield") and the radiative decay ("fluorescence yield").

The dipole selection rules are also valid for the process involved in the SXF experiment. The observed process is the emission of soft X-ray photons after the filling of the core hole by electrons from the VB. The intensity and the energy distribution of the outgoing photons reflect the distribution of electrons in the VB in one-electron picture. SXF is an atomic selective method due to the involvement of well localized core state in transitions and a chemically sensitive method due to the probing states participating in a bond formation. In the "photon-in photon-out" mode bulk features of a sample are probed. In the case of the electron induced emission, a much higher surface sensitivity is caused by the limited penetration depth of incident electrons and depends on the primary electron energy and the geometry.

The one-electron approximation and the two-step description of the scatteing process is valid for many materials. There are, in turn, many materials where one-electron picture breaks down. First, a dependence of the fluorescence on the excitation energy was

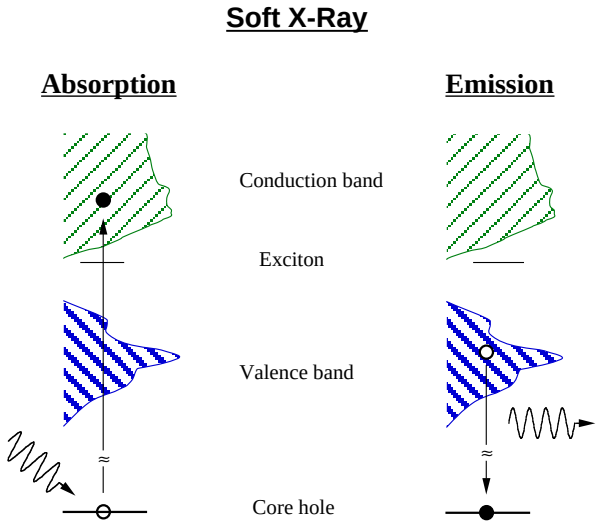

Figure 2.1: Schematically presented energy transitions occurred in the soft X-ray absorption and emission processes for a semiconductor in one-electron approximation in a two-step picture.

observed in molecules [34] and it indicates strong electron correlation effects as molecule orbitals are well localized in contrast to the wide energy band in solids.

Later a strong primary energy dependence of fluorescence spectra was observed in many solids like silicon [35], diamond [36], graphite [37]. For broad band materials the first explanation of this observation was given by Ma et. al. in 1992 [38]. The basic idea that the scattering of the photons must be treated as one-step process and that the moment conservation leads to crystal moment selection rules for the final states in the recombination act. This results in transitions from specific points of the band and the shape of the fluorescence band differ from the VB density of states.This let to the development of the Resonant Inelastic Soft X-ray spectroscopy (RIXS) [35, 39] (see section 2.3).

The one electron approximation is valid for broad band solids, where the created core hole is well screened by the common valence electrons from the excited electron. Nevertheless, this is not a general case. The strong interaction between the core hole and the electron system can occure in ionic compounds, for instance. The interpretation of the SXS spectra has to go beyond the single electon approximation in these cases (see section 2.4). The natural objects for the observations of electron correlation effects are isolated systems like free atoms. If the excitation energy does not exceed the ionization threshold, the transfered energy remains localized in the atom. Strong correlations effects can be expected due to the limited number of electrons for the screening of the excited holes.

Quasi-isolated systems exist also in solids. In strong ionic systems the ions behave in many respects like free atoms. The valence electrons are localized at the anions and form a nearly dispersionless VB. The core hole at the cation site is thus only weakly screened by the valence electrons. The CB is mainly built by the orbitals of the cation. An excited

cation electron remains localized and weakly screened at the cation site. The Coulomb interaction between the excited electron and the cation core hole is strong and give rise to the core exciton binding energies on the order of eV in strong ionic compounds [40].

The strong localization of the empty states can be observed in the absorption. The observed SXA spectra have atomiclike shape, representing the coupling of the electron in the CB with the core hole. The SXF spectra demonstrate strong primary energy dependence as well due to the fact that the fluorescence is excited resonantly into the narrow energy intermediate state. The emission reflects the decay of an excitonic core-hole state. The SXF spectra can be identified as consisting of several excited electronic states with specific interaction energies. Such correlation effects can be observed in both core-to-core and VB fluorescence spectra.

Other methods of the investigation of the electronic structure of solid mentioned in the Table 2.1 are brifely disscused.

The well known method of photoelectron spectroscopy utilizes photoionization and energy dispersive analysis of the emitted photoelectrons to study the composition and electronic states of the surface region of a sample. The method provides the binding energy of the core electrons (XPS) or of the weak bonded electrons in the valence band (PES). For each and every element, there will be a characteristic binding energy associated with each core atomic orbital i.e. each element will give rise to a characteristic set of peaks in the photoelectron spectrum at kinetic energies determined by the photon energy and the respective binding energies. XPS also provides an information about the electron distribution in the VB of the material.

Inverse photoemission spectroscopy (IPES) is as the name implies the inverse to photoemission. The involved process is inverse to the photoemission: an incident electron loses a discrete amount of energy and falls from a continuum state to an unoccupied state accompanied by the emission of a photon. IPES provides the information about the undisturbed by the core hole energy distribution of unoccupied states in CB similar to SXA, but in contrast to SXA the process is not in resonance with a core transitions.

The last technique mentioned in the Table 2.1 is the Auger electron spectroscopy (AES). The Auger process is initiated by creation of a core hole by beam of high energy electrons (which have a primary energy in the range 2 - 10 keV) or by the monochromotized photon beam. The ionized atom that remains after the removal of the core hole electron can relax back to a lower energy state. An electron falls from a higher level to fill the initial core hole and the energy liberated in this process is simultaneously transferred to a second electron. A fraction of this energy is required to overcome the binding energy of this second electron, the remainder is retained by the emitted Auger electron as kinetic energy which is measured in the experiment. AES is a surface-sensitive spectroscopic technique used for elemental analysis of surfaces. It offers high sensitivity (typically 1% of a monolayer) for all elements except H and He and provides the quantitative compositional analysis of the surface region of specimens, by comparison with standard samples of known composition.

2.2 One-electron appoximation.

The process involved in soft X-ray spectroscopy can be described in the one-electron approximation by two steps. This means that processes of the electron excitation and the photon emission are considered independent from each other.

The initial state of the SXS process is given by the incoming photon with the energy $\hbar\omega_{in}$ and the solid in the ground state of energy E_i. An absorption of the photon with the energy $\hbar\omega_{in}$ causes the excitation to the intermediate state with the energy of $E_m = E_i + \hbar\omega_{in}$. By emission of a photon with the energy $\hbar\omega_{out}$ the excited state decays into the final state with the energy $E_f = E_m - \hbar\omega_{out}$. In quantum theory transition probabilities per unit time for both processes follow from "Fermi's Golden Rule":

$$W_{ab} \propto \frac{2\pi}{\hbar} \left|\langle b \left|H\right| a\rangle\right|^2 \delta(E_b - E_a \pm \hbar\omega) \tag{2.1}$$

where "+" and "-" are for emission and absorption, respectively. The prefactor differs for emission and absorption as will be discussed below. The δ-function describes the energy conservation during the process and selects the allowed final states.

The interaction Hamiltonian between the photon and electrons of the atom neglecting the electron spin can be written in following way [41]:

$$H = \sum_i \left[-\frac{e}{2mc}(\mathbf{p}_i \cdot \mathbf{A}(r_i,t) + \mathbf{A}(r_i,t) \cdot \mathbf{p}_i) + \frac{e^2}{2mc^2}\mathbf{A}(r_i,t) \cdot \mathbf{A}(r_i,t) \right] \tag{2.2}$$

Here the sum runs over all electrons and $\mathbf{A}$ is a field operator acting on electron i with the momentum $\mathbf{p}_i$ located at r_i. The operator $\mathbf{A}$ is a superposition of the photon creation and the photon annihilation operators. The number of the photons changes by one in a single absorption or emission process. The $\mathbf{A}\cdot\mathbf{A}$ term in eq.2.2 does not contribute to this process in the first approximation, as it changes the total number of photons by 0 or ± 2. Because of the tranversality of the field operator ($\nabla \cdot \mathbf{A} = 0$), $\mathbf{p}\cdot\mathbf{A}$ can be replaced with $\mathbf{A}\cdot\mathbf{p}$. Then only terms of the form $\mathbf{p}\cdot\mathbf{A}$ have to be considered to describe the absorption of the photon and the following fluoresccence process.

Thus, the interaction Hamiltonian of a photon and the electron system of the solid can be rewritten:

$$H = \sum_i \left[-\frac{e}{mc}(\mathbf{p}_i \cdot \mathbf{A}(r_i) \right]. \tag{2.3}$$

The vector potential is different for emission and absorption, given in the normalilzation volume V by

$$\mathbf{A}_{emis} = \sqrt{\frac{(n_{\mathbf{k},\alpha}+1)\hbar}{2\omega V}}\epsilon_\alpha e^{-\mathbf{k}\cdot\mathbf{r}} \quad and \quad \mathbf{A}_{abs} = \sqrt{\frac{n_{\mathbf{k},\alpha}\hbar}{2\omega V}}\epsilon_\alpha e^{+\mathbf{k}\cdot\mathbf{r}}, \tag{2.4}$$

where ω is the angular frequency, $\mathbf{k}$ is the wave number, the ϵ_α is the polarization vector and $n_{\mathbf{k},\alpha}$ is the photon occupation number in the initial state of the process.

The other difference in the transition probabilities for the absorption and emission processes is in the creation of the photon. The number of states available for the photon

of energy $\hbar\omega$ increases with ω^2. The emitted photon is part of the final state and the emission rate is larger than the absorption transition rate by this factor.

Keeping these facts in mind one can write the transition probability in detail as:

$$W_{ab} \propto \omega \left| \int \Psi_b^* \omega \mathbf{r} e^{i\mathbf{kr}} \Psi_a dr \right|^2 \delta(E_b - E_a \pm \hbar\omega), \tag{2.5}$$

where Ψ_a and Ψ_b are wave functions of the initial and the final states.

Within dipole approximation, one can assume (kr)$\ll 1$, in the expression $e^{i\mathbf{kr}} = 1 + i(\mathbf{kr}) + \frac{i(\mathbf{kr})^2}{2!} + \ldots$ one can thus neglect all terms except the first one. This approximation is valid for soft X-rays. As an example, consider $\hbar\omega$=100eV: for core electrons $r \approx 10^{-9}m$, $\lambda \approx 1.24\mathring{A}$, thus $(\vec{kr}) \approx 6 * 10^{-3}$. The transition probability is futher simplified:

$$W_{ab} \propto \omega \left| \int \Psi_b^* \mathbf{r} \Psi_a dr \right|^2 \delta(E_b - E_a \pm \hbar\omega). \tag{2.6}$$

The average intensity of the emission/absorption is obtained after summarizing all initial and final states which have the same energy difference $\hbar\omega$ and on all directions of the polarization vector.

The wave function of an electron in the central field of the nucleus can be represented as:

$$\Psi_{nlm} = R_{nl}(r) \times Y_{lm}(\vartheta) e^{im\varphi} \tag{2.7}$$

where $Y_{lm}(\vartheta)e^{im\varphi}$ is a spherical function, $R_{nl}(r)$ is a radial part of the wave function, n is the main quantum number, l is an angular quantum number, m is a magnetic quantum number.

From the behavior of the wave functions it is found that the probability of transitions is significant only for transitions between the states where angular and magnetic quantum number change as:

$$\Delta l = \pm 1 \quad and \quad \Delta m = 0, \pm 1 \tag{2.8}$$

This is the expression of the **dipole selection rules** which are very important for the soft X-ray spectroscopy as core levels have well defined atomic symmetry and thus determine the states between which transitions are allowed.

Let us consider the emission process separetely. The initial state for the emission process is the vacancy on the core level and characterized by the atomic wave function of the electron. The final state is the vacancy in the VB and described by the wave function of the valence electron. Thus the intensity of the emission band is:

$$I(\omega) \propto \omega^3 \sum | \int \Psi_{nlm}^* \mathbf{r} \Psi_k dr|^2 \delta(E_{nlm} - E_k - \hbar\omega). \tag{2.9}$$

For the explanation of emission spectra of solids the density of states (DOS) can be used. The DOS is simply the number of states per volume unit in the energy range from E to E+dE. It can be expressed through the integral over the **k** - space between surfaces of constant energies E and E+dE:

$$N(E)dE = \frac{1}{8\pi^3} \int d^3k, \quad dk = \frac{dE}{\Delta_{\mathbf{k}} E}, \quad N(E) = \frac{1}{8\pi^3} \int_S \frac{dS}{|\Delta_{\mathbf{k}} E|} \tag{2.10}$$

where S is the surface of a constant energy. Then

$$I(E) \propto \omega^3 \sum_n \int_S \frac{|P(E,\mathbf{k})|^2}{\Delta_\mathbf{k} E_n(\mathbf{k})} dS$$
$$where\ P(E,\mathbf{k}) = \int \Psi^*_{nlm} \mathbf{r} \Psi_k dr \tag{2.11}$$

where the sum is taken over all Brillouin zones with energy E. The gradient operator is applied to the difference between energies of the core electron and an electron in the VB. As core states in solids have atomic character they have no dispersion in **k**:

$$\Delta_\mathbf{k} E_0(k) = 0. \tag{2.12}$$

The value $|P(E,\mathbf{k})|^2$ is the transition probability averaged on **k**. It is constant over the surface S. Then

$$I(E) \propto \omega^3 \overline{P(E)} N(E). \tag{2.13}$$

The energy distribution of the intensity in the emission spectrum gives information about the energy distribution of the density of valence states (VBDOS) taking into account the transition probability.

A good approximation is to assume that the crystal potential in the Hamiltonian has a spherical symmetry form within spheres inscribed to the unit cells and it is constant between these spheres [42]. The crystal wave function can be represented in this appoximation by the linear combination of solutions of the Schroedinger equation of the eigenergy value equal $E(\mathbf{k})$:

$$\Psi_{\vec{k}}(\vec{r}) = \sum_{l,m} C_{lm}(k) \times R_\vartheta(r) \times Y_{lm}(\vartheta, \varphi), \tag{2.14}$$

where $|C_{lm}(k)|^2$ are coefficients of the decomposition.

The wave function of the core electron of the atom in the solid can be written as the one for the free atom:

$$\Psi_{nlm}(\vec{r}) = R_{nl}(r) \times Y_{lm}(\vartheta, \varphi). \tag{2.15}$$

After the substitution of these wave functions to the expression for the transition probability (eq. 2.6) the integral transforms into the sum of integrals and each of them includes the core level wave function and one set of spherical harmonics from the valence electron wave function. Dipole selection rules lead to the separation of the total DOS N(E) into the partial DOS N_l(E) which describes states with the certain symmetry:

$$N(E) = \sum_l N_l(E) = \sum_l \sum_n \int_S \frac{|C_l(\mathbf{k})|^2}{|\Delta_\mathbf{k} E_n(\mathbf{k})|} dS. \tag{2.16}$$

After averaging over **k** the partial DOS can be expressed by:

$$N_l(E) = \overline{C_l(E)} N(E) \tag{2.17}$$

where $\overline{C_l(E)}$ defines the contribution of states with a given symmetry to the total DOS.

Further, the intensity of the emission is then defined as the sum of the partial DOS multiplied with the corresponding probability of the transition:

$$I_l(E) \propto \omega^3(aN_{l-1}(E)\overline{P_{l,l-1}(E)} + bN_{l+1}(E)\overline{P_{l,l+1}(E)}) \tag{2.18}$$

where l defines the symmetry of the initial core state and the coefficients a and b take into account the angular momentum parts of the transition probability. The $\overline{P(E)}$ can be expressed by the radial part of the wave function of the initial and the final states:

$$\overline{P_{l,l\pm1}(E)} = |\int_0^\infty R_{nl}(r)R_{\vartheta,l}(E,r)r^3dr|^2. \tag{2.19}$$

Thus, the intensity of the emission is:

$$I_K(E) \propto \omega^3 N_p(E)\overline{P_{s,p}(E)} \quad for \quad K-band \tag{2.20}$$

$$I_L(E) \propto \omega^3(aN_s(E)\overline{P_{s,p}(E)} + bN_d(E)\overline{P_{p,d}(E)}) \quad for \quad L-band. \tag{2.21}$$

Transition probabilities can be calculated. For metals, for instance, symmetry considerations indicate that in the range of small **k**, where electrons can be regarded as nearly free, N(E) is proportional to $E^{1/2}$ as wave functions can be represented as plane waves. It was shown earlier [43] that for K-band the transitions probability is proportional $\mathbf{k}^2$, for L-band it does not depend on **k**. For small **k** one obtains:

$$I_K(E) \sim E^{3/2} \quad I_L(E) \sim E^{1/2}. \tag{2.22}$$

In conclusion, there are general advantages of SXS spectroscopy. First, the technique is element specific due to the fact that of core level is localized in the vicinity of the atom. This enables the study the local electronic structure at the atomic site. Second, the SXS method is chemical sensitive as the states from the CB and VB which participate in the chemical bonding are probed. Third, the unique information about the symmetry of the states in the bands is obtained. The method is bulk sensitive in the photon-in-photon-out mode.

2.3 Resonant inelastic X-ray scattering in broad band materials.

The 'emission-following-the-absorption' approximation can break down for several reasons. If the life time of the intermediate states is short compared to the interaction time between the atom and the photon, the entire process has to be treated as a one step scattering event.

The whole process should be described as one scattering act, where the absorption and emission of a photon are no longer independent:

$$|i\rangle + \hbar\omega_{in} \rightarrow |f\rangle + \hbar\omega_{out} \tag{2.23}$$

In Fig. 2.2 the initial, intermediate and final states of the scattering process in a single electron picture are shown schematically. One can see that the occupation of the core level

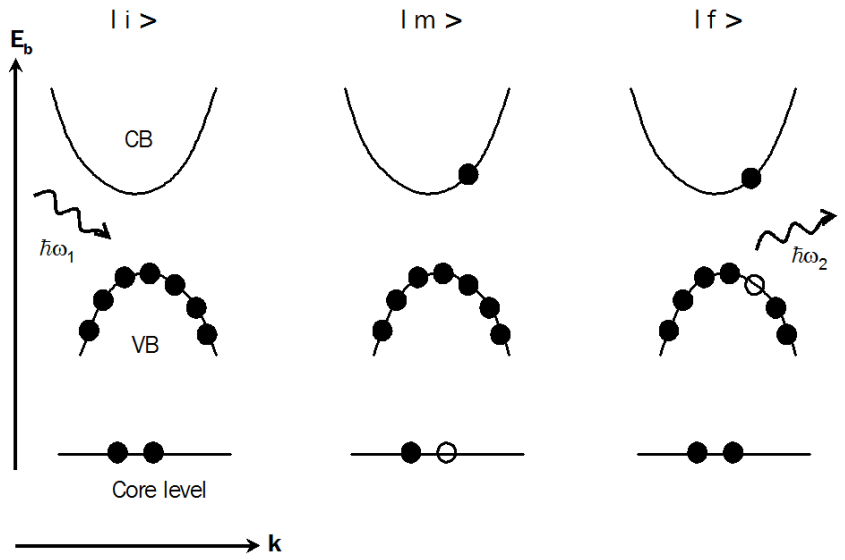

Figure 2.2: Initial **i**, intermediat **m** and final **f** states of an inalastic x-ray scattering act in a single electron picture.

and the number of the photons do not change in initial and final states. It means that there is no crystal symmetry breaking (due to the core vacancy) in the one-step process. The transition probability in this case is described by the Kramers-Heisenberg formula for the differential cross section [41]:

$$\frac{d\sigma}{d\omega_2 d\Omega} \propto \frac{\omega_2}{\omega_1} \sum_f \left| \frac{e^2}{2mc^2} \langle f|\mathbf{A}_2 \cdot \mathbf{A}_1|i\rangle + \frac{e}{mc} \sum_m \left\{ \frac{\langle f|\mathbf{A}_2 \cdot \mathbf{p}_2|m\rangle \langle m|\mathbf{A}_1 \cdot \mathbf{p}_1|i\rangle}{E_m - E_i - \hbar\omega_1 - i\Gamma_m/2} + \frac{\langle f|\mathbf{A}_1 \cdot \mathbf{p}_1|m\rangle \langle m|\mathbf{A}_2 \cdot \mathbf{p}_p|i\rangle}{E_m - E_i + \hbar\omega_2} \right\} \right|^2 \cdot \delta(\omega_1 - \omega_2 - \omega_{fi}) \tag{2.24}$$

The meaning of most of the symbols are clear from figure 2.2, $d\Omega$ is a solid angle element, Γ_m is the life time of the intermidiate state and $\hbar\omega_{fi} = E_f - E_i$. The sum over all electrons i in the Hamiltonian (see eq. 2.2) is made: the only nonzero contributions from $\mathbf{p}_1 \cdot \mathbf{A}_1$ acting on the electron promoted from the core level into CB, and $\mathbf{p}_2 \cdot \mathbf{A}_2$, acting on the VB electron filling the core vacancy are taken into account. The first term is the "normal" inelastic scattering, the second term is the so-called "anomalous" x-ray scattering [44]. This term is called the resonant term, as there is a resonance when the $\hbar\omega_1 = E_m - E_i$. In a solid the states are continous and the resonance condition can be fulfilled if $\hbar\omega_1$ is at or above the absorption threshold. In this case, the main contribution comes from the $\hbar\omega_1/\Gamma_m$ term and the cross section of the resonant scattering has typically 10^6 order [45]. In this case the resonant term dominates over the non-resonant term by the order of $\left[2\hbar(\omega_1 - \omega_2)/\Gamma_m\right]^2$.

Under resonance conditions all terms can be neglected except for the anomalous res-

onant one in order to calculate the cross section:

$$\frac{d\sigma}{d\omega_2 d\Omega} \propto \frac{\omega_2}{\omega_1} \sum_f \left| \frac{e}{mc} \sum_m \frac{\langle f \left| \mathbf{A}_2 \cdot \mathbf{p}_2 \right| i \rangle \langle i \left| \mathbf{A}_1 \cdot \mathbf{p}_1 \right| m \rangle}{E_i - E_m - \hbar\omega_1 - i\Gamma_m/2} \right|^2 \cdot \delta(\omega_1 - \omega_2 - \omega_{fi}) \qquad (2.25)$$

Ma [36] described the core level states as a delocalized state of a nearly dispersionless band. This lead to the conservation of the crystal moments in the intermediate state. Eisebitt [35] started with the well localized core state and proposed that the sum in the eq. 2.24 has to run over all equivalent lattice sites within the coherent photon field due to the uncertainty of the atomic site of the core hole in the intermediate state. This leads to the momentum conservation rule for the scattering process (i.e. both come to the same result).

The main rule obtained for the soft x-ray region, where the photon momentum tranfer can be neglected, is:

in the final state the momentum of the electron in the CB has to be equal to the momentum of the hole in the VB.

This **k**-selectivity enables to some extent the mapping of the band structure. When the electron has enough energy to reach the CB states, the resonant condition can be fulfilled. In this case, the largest contribution to the emission spectrum is due to the resonant term. The non-resonat contribution depends on the life time width Γ_m of the intermediate state. In the limit $\Gamma_m \to 0$, off-resonant states are insignificant. By choosing the excitation energy $\hbar\omega_1$ different states can be made to resonate. These resonant states have certain **k** values for the CB electron, determined by the band structure $E(\mathbf{k})$. The valence hole in the final state has to have the same crystal momentum as the CB electron. This condition forces transitions from VB states only with certain **k**. Such a band mapping was demonstrated on graphite [37] and SiC [39].

It is conceivable, that the excited electron in the intermediate state can participate in other scattering events during the intermediate state lifetime. In particular, electronelectron and electronphonon scattering can alter the momentum and energy of the excited electron. As the momentum transfer from/to these phonons or electrons is not accounted for in the RIXS experiment, such processes give rise to a k-unselective contribution to the RIXS. If such a process occurs, the excitation energy no longer determines which states are preferentially probed. Two time scales are of importance: the intermediate state lifetime as typically given by the core hole lifetime and the electronphonon scattering rate. In the intermediate state there is a competition between the core hole decay without an additional scattering event and a decay after an additional scattering event. While k-unselective contributions of different relative magnitudes have been observed in all RIXS experiments, the attempt to qualitatively investigate and explain the k-unselective contribution has been made for Si 2p RIXS [46]. The estimation of the excitation energy dependence of the k-selective contribution of the Si 2p emission into the RIXS intensity is in agreement with the experimental data. It was demonstrated that it decreases drastically at the photon energies 1 - 2 eV above the CB_{min}. Thus, for the band mapping the near threshold energies should be used.

2.4 Many electron effects in strongly correlated materials.

A core hole is involved into the final state of SXA and initial state of SXF. The measured spectra in absorption and emission processes reffered to the system with or without the additional core hole potential. It is now generally assumed that the final state determines the SXA and SXF spectra [47]. That means that in the absorption the CB DOS in the presence of the core hole is mapped, while the SXF measures the ground state VB DOS. This so called **final state rule** is not theoretically proven, but it has a lot of experimental support.

In the Chapter 5 the SXA and SXF spectra of Sc will be discussed in relation with hybridization effects in the chemical bond. The nature of the electronic structure and chemical bonding in 3d transition metal (TM) compounds is currently of great fundamental and technological interest because these compounds show many unique electronic and magnetic properties. The properties of TM are usually analyzed taking into account the correlations between the highly localized 3d electrons, the charge transfer and covalent bonding (hybridization) between the TM atom and its nearest-neighbor atoms [48]. All of these effects are directly reflected in characteristics of the absorption and fluorescence of TM 3d states for a compound.

The 3d electronic configuration is well probed in SXA by excitation of metal 2p core electrons to unfilled 3d electron states. The 2p excitations of the 3d atoms are usually considered as the intra-atomic ones, that are strongly localized within the TM ions with formal [Ar]$3d^n$ ground-state electronic configurations, and are mainly described in various ionic multiplet approaches [49, 50, 51]. At the same time it is apparent that the TM 3d electrons participate in covalent bonding to an extent which depends strongly on the ligand electronic structure. This hybridization between the TM 3d electrons and ligand valence electrons leads to delocalization of the 3d states and thus lowers the dominant role of the 3d electron correlations. The subtle interplay between hybridization and 3d correlations in the electronic structure can be studied by high-resolution SXA, core-to-core and VB-to-core SXF at TM 2p edges.

Scandium is located at the beginning of the series of the 3d TM's and the ground state electronic configuration of its atom is [Ar] $3d^14s^2$. The Sc atom has usually a valence of three in its compounds and, therefore, in a simple ionic model there are no 3d electrons nominally in the ground state. This leads to the expectation that the role of d-d electron correlations is not large for Sc compounds and, consequently, spectral changes along the series of different ligands will be mainly caused by changes of the character of the chemical bonding between the scandium and ligand atoms, the Sc-ligand coordination and distances.

The Hamiltonian for atomic multiplets can be written as [49, 50]:

$$H = H_0 + \mathbf{L} \cdot \mathbf{S}(p) + \mathbf{L} \cdot \mathbf{S}(d) + g(i,j). \tag{2.26}$$

H_0 contains the kinetic term and the electron-nuclei interaction. It gives the avarage energy of the multiplet and does not contribute to the multiplet splittings. The multipliet splitting is caused by the spin orbit coupling of the 2p and 3d electrons, $\mathbf{L} \cdot \mathbf{S}(d)$, and

by the Coulomb repulsion term, $g(i,j)$. This two electron operator can be expressed in terms of spherical harmonics and divided into radial and angular parts. The radial part, $R^K(l_1l_2;l_3l_4)$, is divided into a direct Coulomb term, $F^K(l_1l_1;l_2l_1)$, and an exchange term, $G^K(l_1l_2;l_2l_1)$. The angular part of $g(i,j)$ results in the selection rules and gives the possible K values. For the direct Coulomb term no odd K values are allowed. The maximum K value is two times of the minimum l value. For the p^5d^1 configuration the possible terms are F^0 and F^2, for the d^2 configuration - the F^4. The K values in the exchange term are equal $|l_1-l_2|$, $|l_1-l_2+2k|...l_1+l_2$. For the p^5d^1 configuration the possible terms are G^1 and G^3. It means that for the p^5d^1 configuration only four interactions must be taken into account: F^0,F^2, G^1 and G^3. F^0 only contributes to the average energy and is taken into H_0. These Coulomb, exchange and spin-orbit parameters for different metals can be evaluated from *ab initio* calculations (see, for instance, [52]).

The ground state of Sc^{+3}, d^0, consists of one single state ^1S. In an absorption process governed by dipole selection rules only the ^1P final state contributes within the LS-coupling scheme. Thus in the SXA spectrum only one peak would appear. Turning on the spin-orbit coupling of the 2p core hole, but still neglecting the spin-orbit coupling with the 3d electrons and the Coulumb repulsion term, leads to the well known two peaks shape of the SXA spectrum with the intensity ratio 2 : 1, denoted as L_3 and L_2 edges. This is caused by a situation which is intermediate between LS and jj coupling, which results in tranforming $^1P(LS)$ into ^1P, ^3P and ^3D (jj) terms, where both triplet terms have equal energy. As the direct Coulomb and exchange terms are not negligible, the L_3 edge is splitting further into a small leading peak predominantly of triplet character and a main peak. The triplet peak appears in the SXA spectra of d^0 compounds energetically below the main L_3 peak.

The effect of the crystal field results in a futher splitting of the main absorption peaks. In the simple cubic field the 3d states are split into the e_g and t_{2g} symmetry. This splitting can be directly related to the dependence of the d orbitals on their spatial orientation: the d-orbitals are directed in between the ligand atoms (t_{2g}) or into the direction to the ligand atoms (e_g). An e_g electron has strong antibonding character and the energy of the state is higher then for the t_{2g} electron which interacts only weakly with the surrounding.

After the absorption of the incident photon, the system can relax into the different final states. Let us consider the transition of the 3s electron into the 2p core hole. The final state is $3s^13d^1$ configuration and within the LS-coupling consists of the singlet $^1D_2$ and triplet $^3D_{1,2,3}$ states. As the initial state of the SXF process has the total angular momentum of $J=1$, the dipole selection rule gives ΔJ=0,$\pm$1. Thus final states with J=0, 1, 2 are allowed. In the LS-coupling in Sc^{3+}, these are the following transitions:

$$p^5d^1(^1P_1) \longrightarrow 3s^13d^1(^1D_2)$$

$$p^5d^1(^3P_1) \longrightarrow 3s^13d^1(^3D_{1,2})$$

$$p^5d^1(^3D_1) \longrightarrow 3s^13d^1(^3D_{1,2})$$

Thus the excitation into certain intermediate states will be followed by transitions into different final states. As a result, SXF will exhibit a strong primary photon dependence near the excitation threshold. Going far above the excitation edge the excited electron is

decoupled from the system and the fluorescence spectrum represents the non-resonant 3s to 2p lines.

Strong excitation dependence of fluorescence spectra was observed in many ionic materials, like CaF_2 [40], LaF_3 [53]. This dependence was also observed but less pronounced in materials with weaker ionic character of the bond. This is thought to be a result of a weaker coupling of the core hole and d electrons due to the more effective screening of the core hole by common electrons.

The character of the chemical bonding is directly reflected in the VB state distribution. By measuring the energy of photons emitted after the electron transition from the excited state to the final state, one should be able to recognize the chemical state of the element in the material. If Sc is in pure 3+ state in a compound, there would be no occupied states with Sc 3d character. If the charge transfere is not complete, some of the d electrons are still in the vicinity of the Sc core and hybridize with ligand states.

The observed fluorescence is then weak but not zero. The primary photon energy dependence of the SXF spectra reflects two antagonistic processes: a coupling between the 2p core hole and 3d excited electron and the screening of the 2p core hole by the valence electrons. The stronger the covalent character of the bonding the less pronounced the excitation dependece of the SXF spectra. This spectral behavior can be a qualitative indication of the charater of the chemical bond in the material under question. The quantitive analysis of the excited states is the subject of Chapter 6.

Chapter 3

Experimental setup

3.1 Synchrotron radiation.

To study the electronic structure of solids by resonant soft X-ray spectroscopy a source of highly monochromatic and intense radiation with tunable energy is necessary. BESSY II is such a source. With respect to most properties the synchrotron radiation is by far superior to conventional light sources, such as X-ray tubes or discharge lamps. The radiation is characterized in general by the following terms: spectral range, photon flux, photon flux density, brilliance, and the polarization. The photon flux is the overall flux collected by an experiment and reaching the sample, the photon flux density is the flux per area at the sample and the brilliance is the flux per area and opening angle.

The interplay of several systems is necessary in order to produce synchrotron radiation (Fig.3.1) [54]. The third generation source BESSY II is based on a 240 m circumference storage ring. The injection system consists of a 50 MeV racetrack microtron and a 10 Hz booster synchrotron which ramps the electron beam of 70 kV to its final operation energy of maximal 1.7 GeV. The accelerating process takes 50 ms. After this primary system accelerates the electron beam it is stored in the ring for several hours. The total current in the storage ring of 250 mA can be obtained by successive injection of electrons, accelerated in multiple accelerating cycles. The path of electrons in the storage ring is controlled by different types of magnetic lenses. Radiation is emitted when the path of the electron is bent by a magnet and the electron is accelerated. Different types of magnets are used at BESSY. A dipole magnet forces the electron beam to turn and the radiation is emitted tangential to the path of the electron beam. A multipole magnet (insertion device (ID)) bends the electron beam path into a sinusoidal curve and radiation is emitted at every single bend. Three types of the electron beam path and resulting angular and a spectral distributions of the emitted radiation are show schematically in Fig. 3.2. Undulators are IDs with a periodic magnetic structure producing a weak magnetic field. This relatively weak periodic field forces the electrons to oscillate with a small amplitude. This allows to achieve a small angular distribution of emitted photons. In combination with a tightly confined electron beam, this leads to radiation with relative narrow spectral width, as the radiation in each oscillation can interfere. as a result, the emitted power is concentrated in harmonics of narrow spectral width The wiggler is a special magnet with alternating directions of the strong magnetic field and the trajectory of an electron beam through

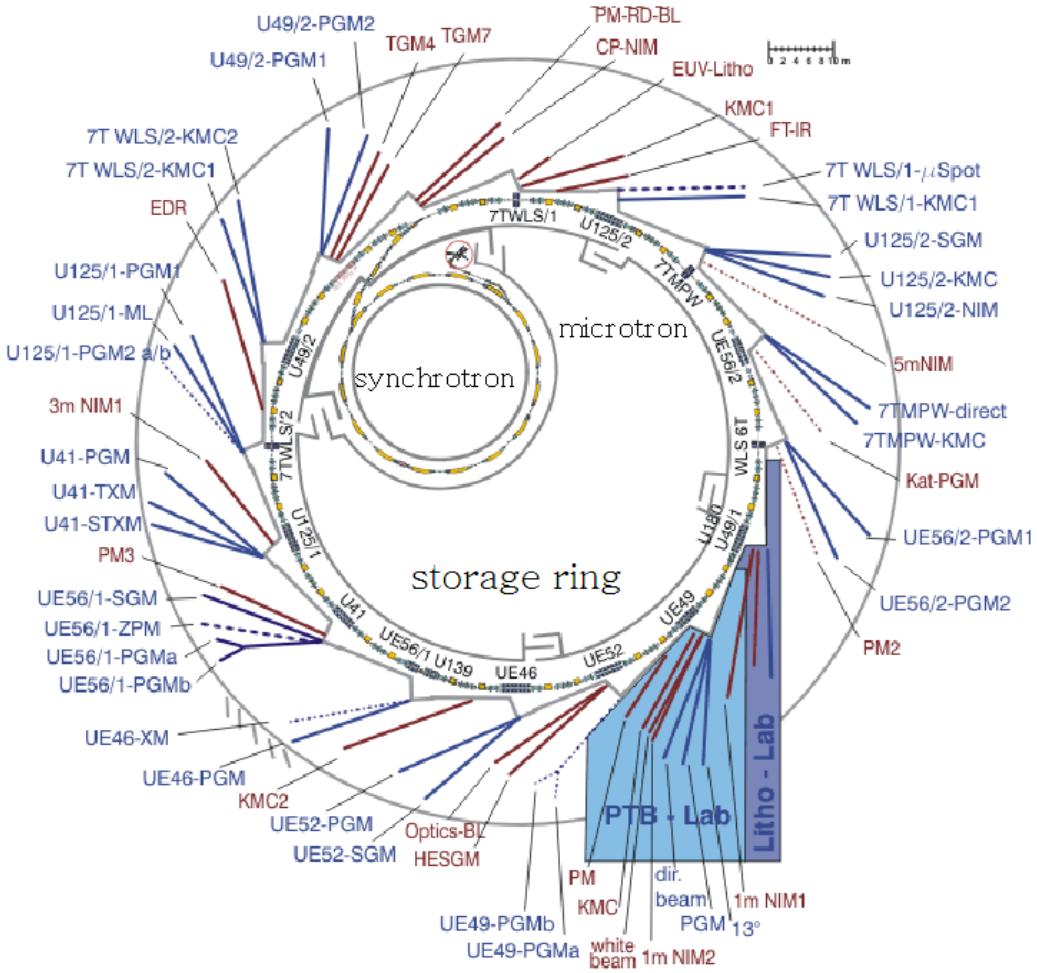

Figure 3.1: Electron source, accelerator and storage ring: production of synchrotron radiation at BESSY. In Fig. 3.3 the beamlines available at BESSY are listed together with their brilliance and spectral range of operation. Reproduced from www.bessy.de

a wiggler has a large amplitude. The photon flux as well as the central intensity of the radiation emitted by the wiggler is comparable to the radiation from the bending magnet but more intensive by a factor N, where N is the number of poles within the wiggler (N is in order of 30). Because of the cross sections at the locations of the wigglers are 3 or 4 times larger as in the bending magnet, the brilliance of is of a factor 10 more intense than of the bending magnet. An electron beam energy lost to synchrotron radiation is compensated in a radiofrequency cavity.

Optical elements direct the radiation in the beamline systems (Fig.3.4). It is a set of optical elements to tune and direct the radiation to an experimental end-station where the research work utilizing the X-rays is carried out. Several beamlines can share one ID and the premirror directs the radiation into a certain beamline. Several types of monochromators are installed at BESSY II: normal-incidence gratings; grazing-incidence spherical, plane and toroidal gratings, a double crystal monochromator and a zone plate monochromator. Behind the monochromator the photons with well defined energy are

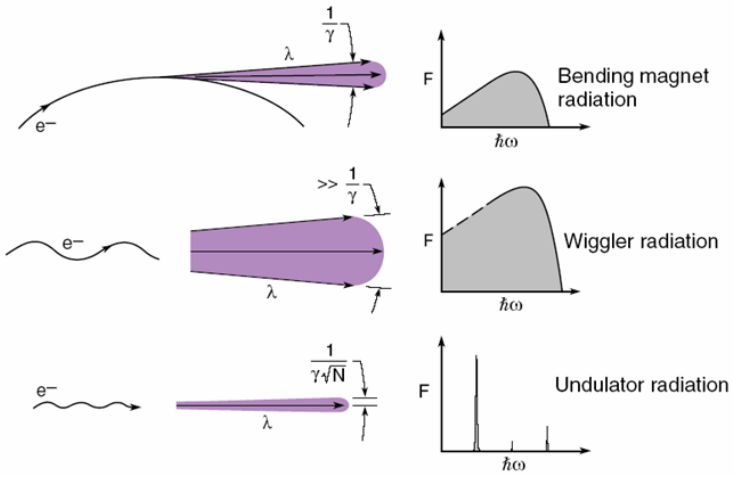

Figure 3.2: Different types of magnets producing the radiation at BESSY. Reproduced from [54].

often focused by mirrors into a spot on a sample. The size of the spot depends on the magnet type and the optical elements of the beamline (slits and mirrors). Since many beam lines and monochromators can be set up at a storage ring many experiments can be carried out simultaneously. At each beamline the wavelength of the light and other experimental requirements can be individually set.

These properties make the synchrotron radiation a most versatile tool. The high brilliance of synchrotron radiation at BESSY is essential for investigations which require the high spatial and/or spectral resolution. As the radiative decay of the core hole which is monitored in soft X-ray fluorescence spectroscopy typically has a low probability and the solid angle that can be accepted in a secondary spectrometers is small ($5{\cdot}10^{-5}$ times the full solid angle), the high brilliance of the synchrotron radiation is essential for this technique (see Section 3.3). The high flux (above 10^{13} photons per sec per 0.1% spectral band width) in a small spot in vertical direction is needed to realize a measurement with the resolving power of the secondary spectrometer of at least $E/\delta E = 500$.

3.2 Soft X-ray absorption spectroscopy.

The distribution of unoccupied electronic states was measured in various material systems by soft X-ray absorption spectroscopy. The probability for the core electron to transfer to unoccupied states after the absorption of the incoming photon is monitored as a function of the primary photon energy in the energy range close to the binding energy of the core electron. The most direct method to measure the absorption coefficient of a material is a transmission measurement. In the soft X-ray region (30 - 1000 eV) the penetration depth of the photons is of the order of 100 nm. This limits the number of materials which can be prepared as a thin film for such measurements. Fortunately, indirect methods can be used in order to monitor the absorption process. Following the core electron excitation,

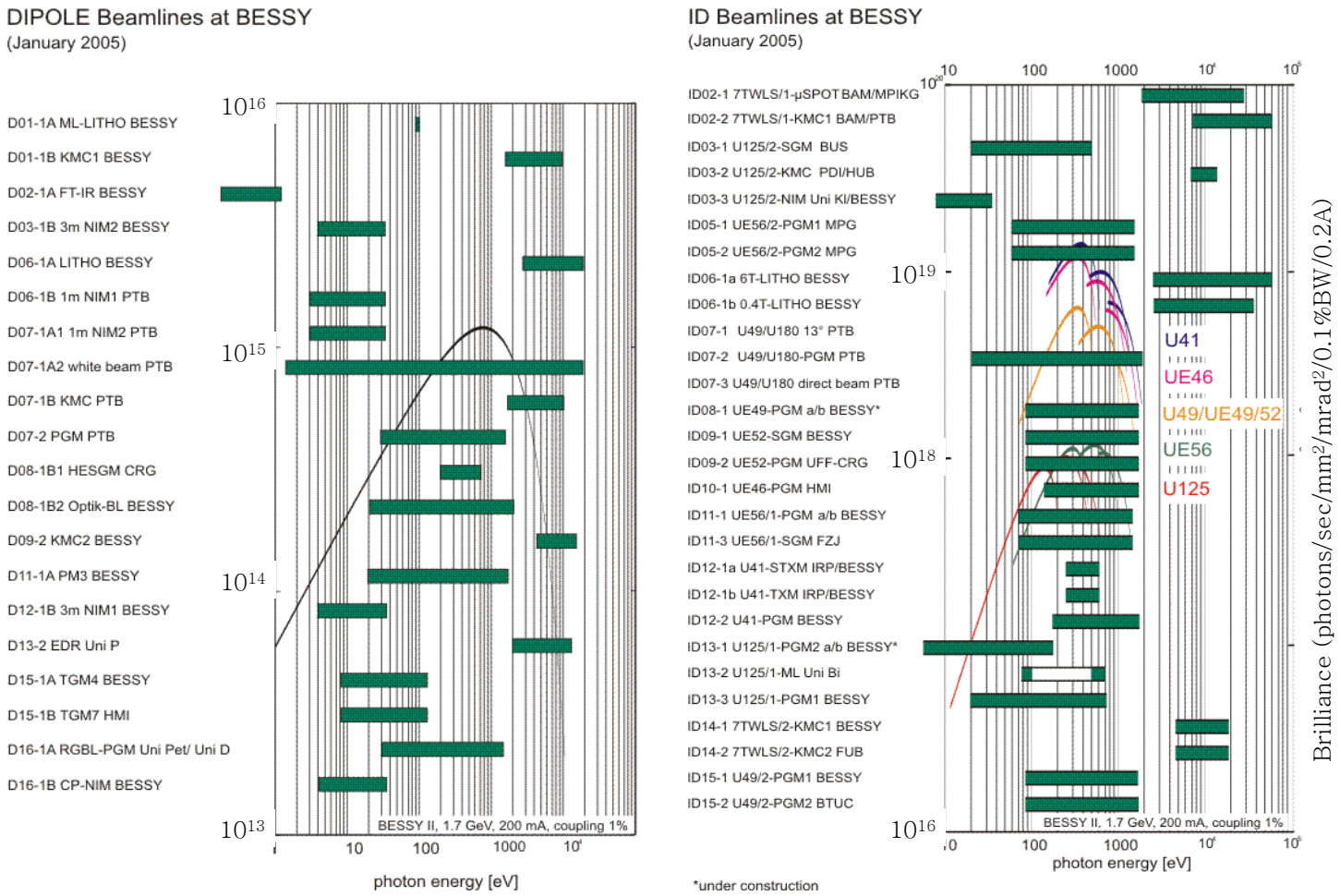

Figure 3.3: Dipole and undulator beamlines at BESSY: brilliance and spectral range of operation. Reproduced from www.bessy.de. The beamlines used in this work are UE125/1-PGM, U49/2-PGM, UE56/1-SGM, UE52-SGM.

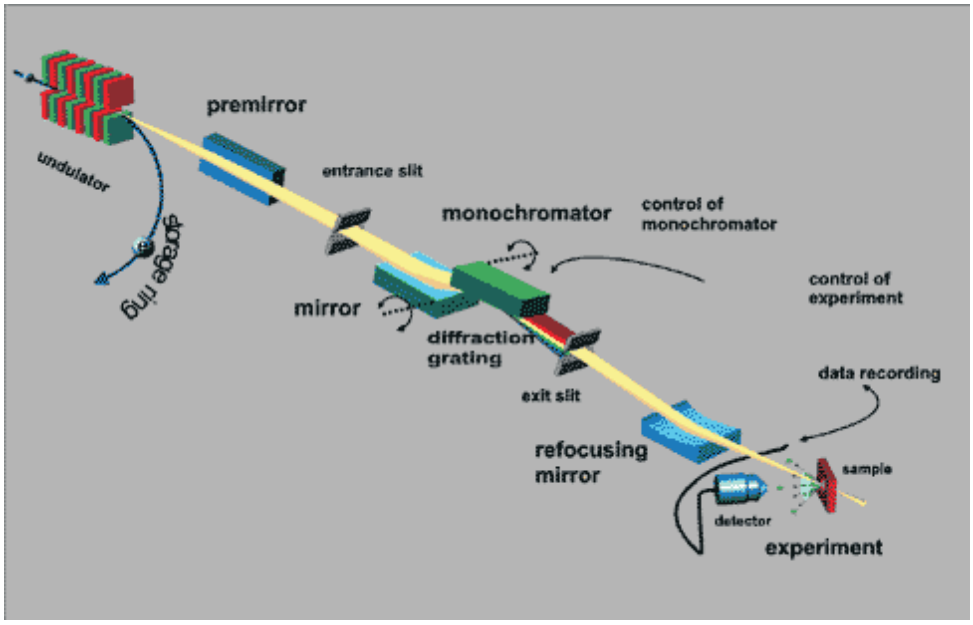

Figure 3.4: Typical path of the light beam from the source to the sample at BESSY. Reproduced from www.bessy.de

the core vacancy can decay in different ways. These secondary processes can lead to the emission of electrons (total electron yield, TEY-SXA) or secondary photons (fluorescence yield, FY-SXA), which are detected. The intensity of these signals reflects the absorption properties of the core electron, if a correct detection geometry is chosen [55].

The radiative decay of the core hole state generally competes with the non-radiative Auger channel. The efficiency of radiative or non-radiative processes usually is denoted as the yield of the decay channel. The fluorescence yield Y_x^i gives the fraction of states that decay by the specific radiative decay channel **i** for the excited core hole state **x**. Yield (Y_x^i), probability (W_x^i) and rate (Γ_x^i) of the decay channel are related as follows:

$$Y_x^i = \frac{W_x^i}{W_x + W_A} = \frac{\Gamma_x^i}{\Gamma_x + \Gamma_A} \tag{3.1}$$

where W_x and Γ_x (W_A and Γ_A) are the total probability and the total rate of all radiative (of all Auger) decay channels possible for the excited state (assuming that only these two types of channels exist). Y_x^i strongly depends on the material: in Fig.3.5 dependencies of the fluorescence yield of K- and L-shells (averaged over the three subshells) on the atomic number are shown. Auger channels dominate for the decay of shallow core vacancies. With increasing energy of the core hole the fraction of the fluorescence decay increases and finally becomes dominant. The main contribution however is given by radiative transitions involving deeply bound core electrons, e.g., the radiative decay of the 1s core hole by transition of the electron from the 2p core level. Such decays are referred to as "core-to-core" transitions.

As the attenuation length of the electrons is much smaller than the photon penetration depth in the soft X-ray range (see Fig. 3.6), the TEY signal provides information from

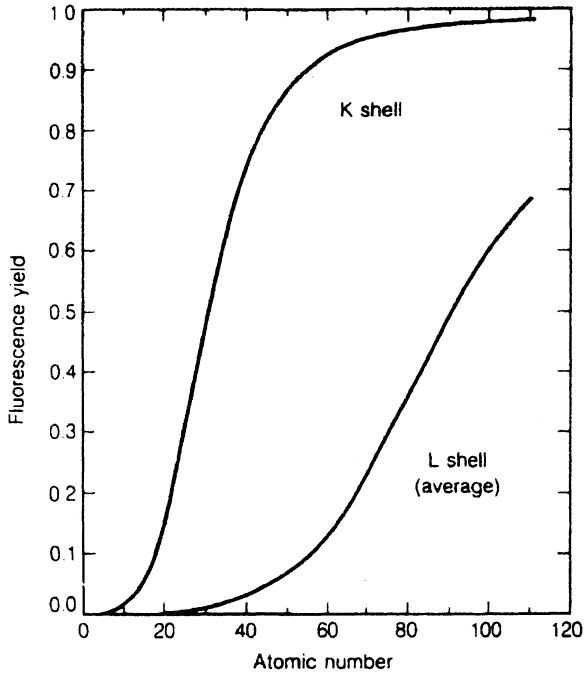

Figure 3.5: Fluorescence yields for K and L shells for $5 \leq Z \leq 110$. The L shells curve is an average over the effective yields of L_1, L_2 and L_3. Fig. is reproduced from [56].

the near surface region of the material under investigation. The intensity of the signal is proportional to the linear absorption coefficient. In this work, TEY-SXA is measured by detecting the drain current from the sample, the single Auger decay is amplified further by the cascade of electron excitations in the solid. Problems to realize TEY measurements occur when the sample is an insulator or not well conducting, resulting in charging when irradiated by X-rays. Another property of the TEY mode is the small information depth.

To obtain bulk information, the FY-SXA technique is more suitable, as the escape depth of the secondary photons is comparable with the penetration depth of the primary light. These measurements are a little bit more complicated to realize as one has to be aware about possible saturation of the FY-signal [55]. Special experimental geometry conditions have to be used to avoid non-linearity between the measured intensities and the absorption coefficient. Also, the FY signal is typically weaker than the TEY. This is due to the fact that the probability of the radiative core decay typically much smaller than the non-radiative decay in the soft X-ray range.

Diffuse elastic scattering due to surface roughness can prevail in the measured total FY signal. In complex materials absorption signals from different elements can overlap with each other. In some cases, one can measure outgoing photons with energies in a certain window to separate elastically scattered light from the inelastic or to specificate the fluorescence from certain atoms. This modification of the FY-SXA method is named partial fluorescence yield (PFY) and is realized by using an energy selective photodetector.

In principle, any core shell could be regarded as the starting point for the study of the electronic structure. There are two major restrictions which limit the number of available

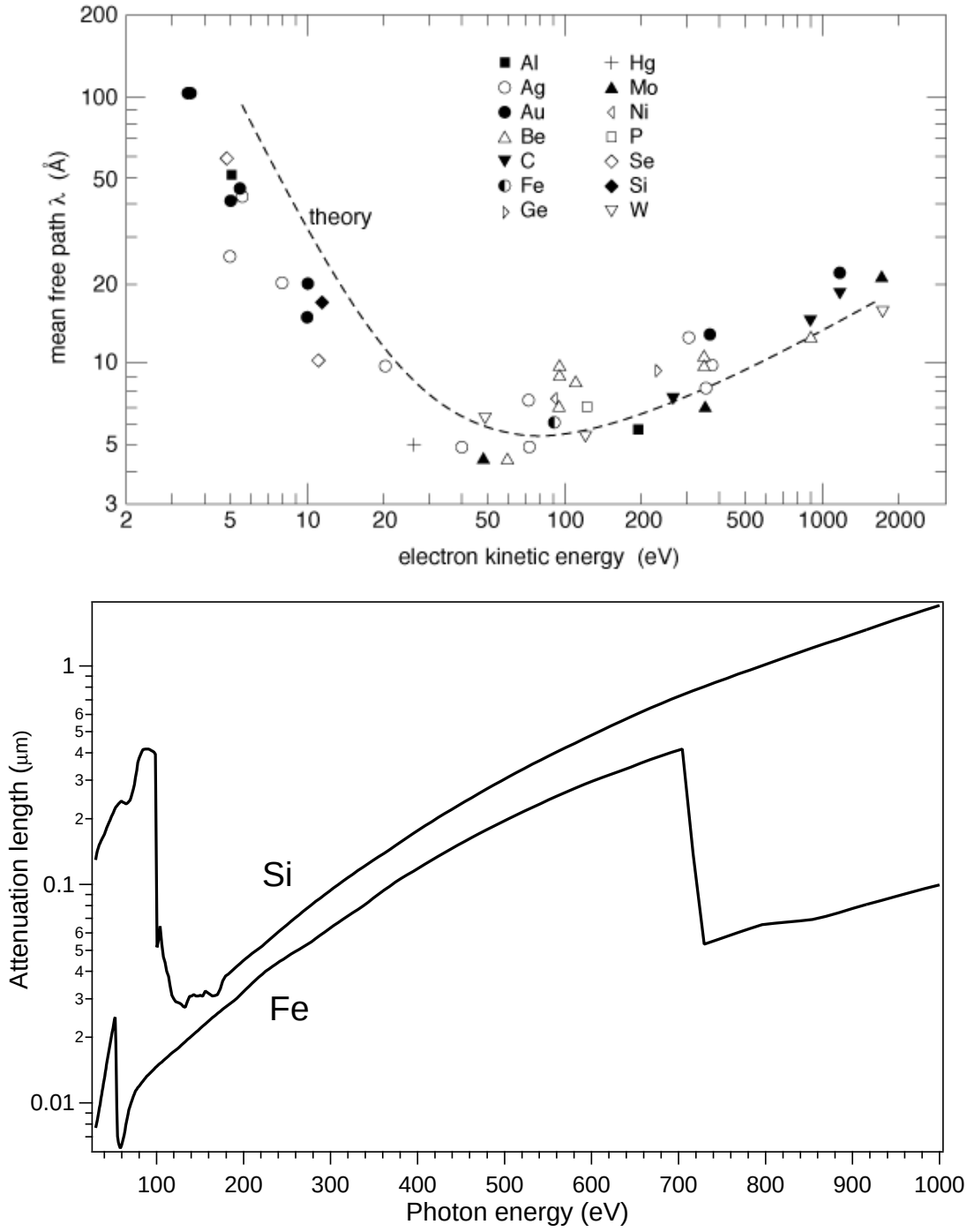

Figure 3.6: Top: Universal curve representing the energy dependence of the inelastic mean free path of electrons. Reproduced from [57]. Bottom: Calculated attenuation length of the photons in Si and Fe. Calculation are made using the program at www.http://www-cxro.lbl.gov/.

core states. First, as it was mentioned above, is the low radiative rate of low Z elements. The additional Auger channel of the decay restricts the core levels useful for the study of the VB structure by the emission spectroscopy. Second, the finite lifetime of an excited state related to the uncertainty in the energy of an excited state according to Heisenberg's uncertainty principle:

$$\Delta t \times \Delta E \leq h. \tag{3.2}$$

With the increasing binding energy of an electron the lifetime of a core hole in those levels generally decreases. The measured transition energies are thus broadened. This broadening can obscure the fine structure of VB DOS. This washing out of the fine structure generally increases with increasing core level binding energy. In combination with competing rates of decay channels there are the K shells of the light elements of the first row in the periodic table of the elements and also the first elements of the second row (Na, Mg, Al and Si) and the $L_{2,3}$ shells of elements of the 3d transitions metals which are most suitable for study by soft X-ray spectroscopy.

3.3 Soft X-ray fluorescence spectroscopy.

Soft X-ray fluorescence spectra reflect the density of the occupied states in some approximation. The intensity of outgoing photons can be recorded as a function of energy with a Rowland type of spectrometer [58, 59]. In the setup used at BESSY two spherical gratings are used in grazing incidence geometry for energy dispersion in the soft x-ray energy range (30-1000 eV). Below 1000 eV Bragg reflection is not longer practicable since the wavelength is longer than the crystal plane spacing of most natural crystals. On the other hand above 10 eV conventional transmission optics fails as all materials strongly absorb in this region. That is why gratings have to be used to monochromatize radiation in this energy range. Above 30 eV the grazing incidence geometry has to be applied as the reflectivity decreases drastically for steeper angles.

A schematic picture of the Rowland spectrometer is shown in Fig. 3.7. In this set-up the incident synchrotron radiation excites the fluorescence. The fluorescence radiation illuminates the secondary monochromator through an entrance slit of some tens of μm in width and is detected by a position sensitive photodetector after it has been dispersed by the spherical grating. The entrance slit, the center of the grating of radius R and the detector are situated on the "Rowland circle" of the radius R/2. The result of this arrangement is that the radiation of different wavelengths is focused at different points of the Rowland circle. To detect the dispersed radiation this spectrometer is equipped with a multichannel plate detector that can be moved along the Rowland circle with the help of x/y- and rotational tables. The radiation source is defined by an entrance slit of variable width. By the variation of the slit size it is possible to choose between high throughput or high energy resolution. The crucial parameters (radius, grating constant and blaze angle) are listed in Table 3.1. The slit-limited resolution of a Rowland spectrometer is given by

$$\Delta\lambda = 1.1 * \frac{wd}{mR}, \tag{3.3}$$

where w is the width of the entrance slit, m is the order of diffraction, d is the groove separation. To be able to reach the slit width determined resolution ($\delta\lambda/\lambda \approx 10^{-3}$) the spatial

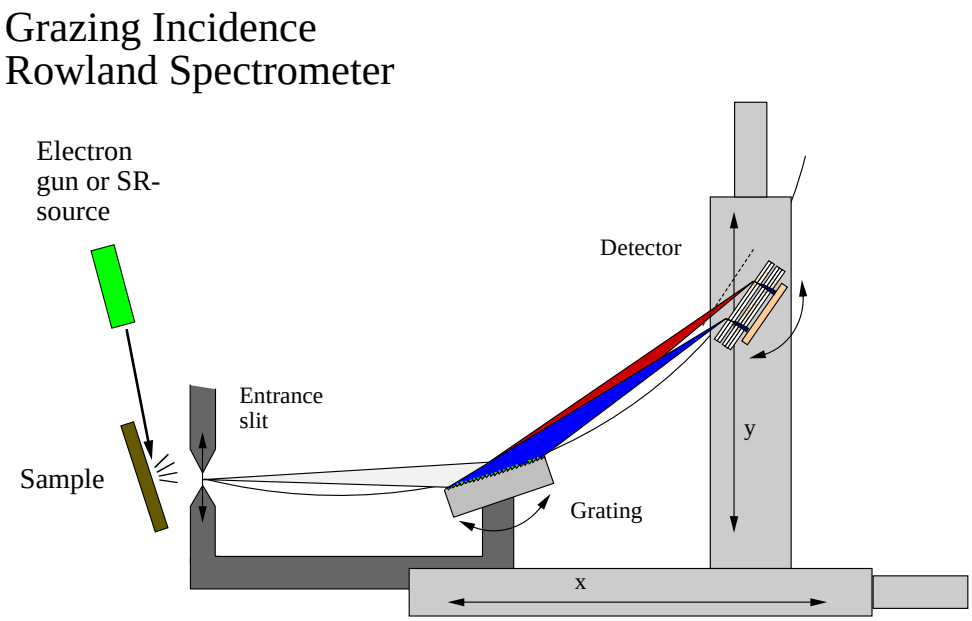

Figure 3.7: Principle set-up of a Rowland spectrometer. Entrance slit, detector and the spherical grating are set on a circle with a diameter equivalent to the grating radius.

resolution of the detector must be sufficiently high and abberation must be sufficiently small.

The multichannel-plate detector is equipped with a resistive anode read-out, allowing detection with 2D spatial resolution. The detection of photons is sketched in Fig.3.8. When a soft X-ray photon hits the top plate of the detector a secondary electron is created. To increase the probability of the electron yield the material with a very small work function for electrons (CsI) is evaporated on the surface of the topmost channel plate. If the electron is emitted upwards it is pushed back by the negative potential applied to a grid above channel plates. In the channels the electrons are multiplied and accelerated in the direction to the anode. The distribution of electrons striking on the resistive anode below the fifth channel plate is within good approximation Gaussian. Its center is determined from the current measured separately at the four corners of the anode.

In a Rowland spectrometer, the surface of the position sensitive detector is usually placed tangential to the Rowland circle. In such geometry a spacial resolution of 50 μm can be achieved in the dispersion direction of the spectrometer.

Grating	Blazed for energy (eV)	Radius (m)	Line density(mm^{-1})	Angle of incidence (deg.)
1	50–300	3.71	600	86.31
2	200–1000	5.0	1200	87.26

Table 3.1: Destinated energy range and crucial parameters of the gratings in the Rowland spectrometer.

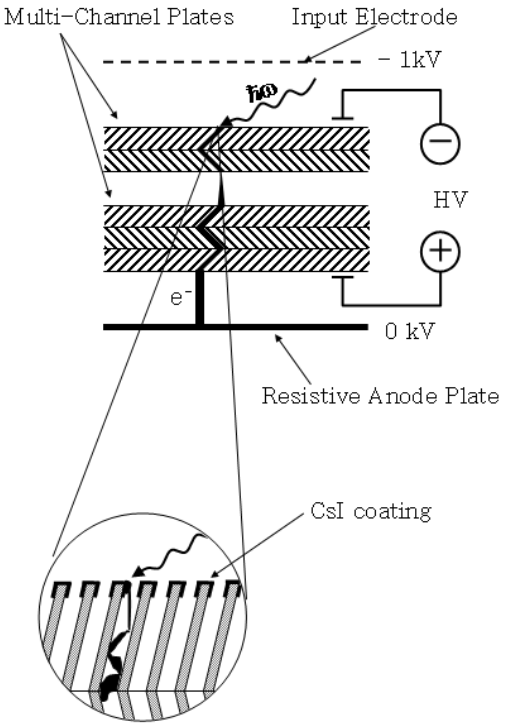

Figure 3.8: Principle of the photon detection with a multi-channel plate detector with resistive anode read-out. The position where electron strikes on the anode is determined via the current measured at the corners of the anode.

Chapter 4

Si nanoclusters in a SiO_2 matrix.

This chapter is dedicated to the investigation of the electronic structure of Si nanoclusters in a SiO_2 matrix by photon-in photon-out soft x-ray spectroscopy. The energy shift of the Si 2p core levels as a function of the local oxygen coordination number in the SiO_x system is exploited. As a result, information about the suboxide environment at the interface between the nanoclusters and the SiO_2 matrix as well as on the occupied and unoccupied electronic states in the core of the Si nanoclusters is extracted.

4.1 Samples and experimental details.

The Si nanocluster arrays in SiO_2 have been prepared by Dr. J. Heitmann in the group of PD Dr. M. Zacharias in Max Planck Institute of Microstructure Physics (Weinberg, 2, 06120, Halle, Germany)[5, 60]. The method used is the growth of a SiO/SiO_2 superlattice with subsequent high temperature annealing in N_2 atmosphere. Si nanoclusters as small as 1.5 nm in diameter can be produced with a narrow size distribution in this way. Annealed samples initially consisted of 45 periods of $SiO(d)/SiO_2(5nm)$, d=5, 4, 3, 2nm, on a quartz substrate.

While the optical properties of such structures are directly accessible by optical spectroscopy in the visible or infrared spectral range, the underlying electronic structure is difficult to probe directly. The electrically isolating glass matrix hampers efforts to perform transport measurements and tunneling spectroscopy. A direct study of the electron band structure by photoelectron spectroscopy is impossible as the energy of photoemitted electrons is uncontrollably affected by inhomogeneous charging of the samples. The soft X-ray fluorescnece method overcame these difficulties as the photons with the energy around 100eV are used for the excitation of the secondary emission.

Annealed samples were investigated at the BESSY UE125-PGM and U49/2-PGM1 beamlines. The incident photon energy resolution was set to 50 meV, a secondary soft x-ray spectrometer of Rowland type was set to 300 meV resolution. As the Si $2p_{3/2}$ and Si $2p_{1/2}$ binding energies increase by 1 eV for each silicon-oxygen bond formed as compared to bulk silicon [61], this energy resolution allows selectively to excite pure silicon or different oxides. The resulting spectra represent the partial s and d density of electronic states in the valence band locally at the Si atoms. The fact that the local information can be obtained with chemically sensitivity means that the electronic structure of the

Si nanoclusters can be seperated form the suboxides and the SiO_2 matrix. The local contribution of the unoccupied states of s or d symmetry from the Si atoms is accessible via SXA spectroscopy by measuring the partial fluorescence yield detected in the Rowland spectrometer. While this mode of operation is tedious resulting in low count rates due to the low solid angle coverable by the secondary spectrometer, it is absolutely crucial in this material system due to the possibility to discriminate against diffuse, elastic scattering of the incident beam. Without this suppression, the energy dependence of the reflectivity dominates the fluorescence yield. As both the magnitude and spectral shape of the elastic contribution depends on the experimental geometry as well as the roughness of the sample surfaces, total fluorescence yield spectra are not interpretable with respect to the density of electronic states without detailed modeling of these effects.

4.2 Core-shell model and sub-oxide evaluation.

Transmission electron microscopy and photoluminescence spectroscopy have shown that Si nanoclusters of controllable size and spacing are formed upon annealing of the SiO/SiO_2 superlattices (schematically shown in Fig. 4.1). As it will be shown below, the spectroscopic evidence in this work indicates that the core of the particles consists of crystalline Si. On the lengthscale of a few interatomic distances a transition between the Si core and the surrounding SiO_2 has to occur, and one can expect local configurations corresponding to suboxides to be present.

The studied material is considered to consist of a centered core, where Si atoms have mostly Si as first neighbors. This "Si-core" is surrounded by the sub-oxyde layer, where silicon can have oxygen as 1^{st}, 2^{nd} and 3^{rd} neighbors ("sub-oxide transition region"). The whole structure is built into the stochiometric SiO_2 matrix (see Fig. 4.2).

In a random bonding model (Fig. 4.3), sub-oxide configurations are denoted as Si Si_xO_{4-x}, with x describing the relative silicon to oxygen occupancy for a given, fourfold coordinated Si atom. Over this transition layer with varying x, the electronic structure will vary. The thickness and composition of this transition layer thus determines the effective potential well confining electrons and holes in the nanoclusters, which is of basic importance for the resulting optoelectronic properties. Knowledge of this potential shape would enable quantitative models of the confinement energy as a function of particle size and interface structure. Information on the presence of the various possible silicon oxides adjacent to a Si particle may also help to refine the synthesis procedures.

A series of SXE spectra as a function of incident photon energy were recorded for all samples. The excitation energy was chosen in such a way that Si atoms in different intermediate structures were selectively excited. The selective excitation can be realized due to the well established chemical shift of the binding energy of the Si 2p core electron caused by the presence of oxygen atoms. This shift was measured by photoemission of Si(100) with a thin layer of oxide and is about 0.9 eV for every O atom (see Fig. 4.4 reproduced from the [62]).

In Fig. 4.5 – Fig. 4.8 data for the sample with an initial SiO layer of 5, 4, 3 and 2 nm thickness are shown respectively. The strong elastic peak at emission energies equal to the excitation energy has been clipped for clarity. A general behavior was observed for all

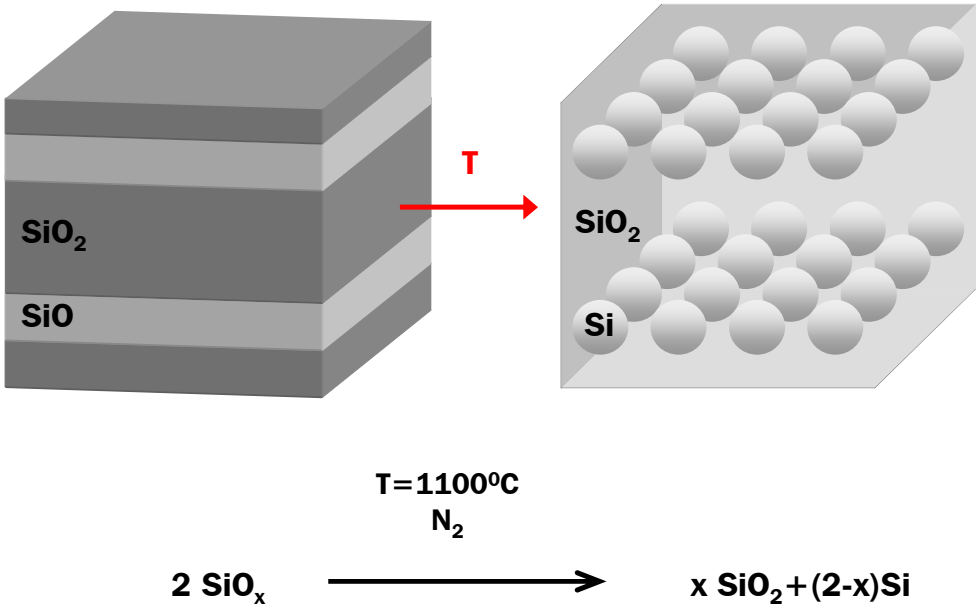

Figure 4.1: Samples are prepared by alternating evaporation of SiO powder in a vacuum under a pressure below 10^{-7} mbar or in oxygen atmosphere under a oxygen partial pressure of 10^4 mbar. This changes the stoichiometry x of SiO_x alternatively between 1 and 2 [5]. The thickness of the SiO layers is varied between 2 and 5 nm. The SiO_2 layers had a thickness of 5 nm. The number of periods grown in this fashion by J. Heitmann was 45 [5]. The evaporated samples were annealed at 1100 ^{0}C under N_2 atmosphere. This leads to the phase separation and, as it was shown by TEM, Si cluster formation in SiO_2 matrix.

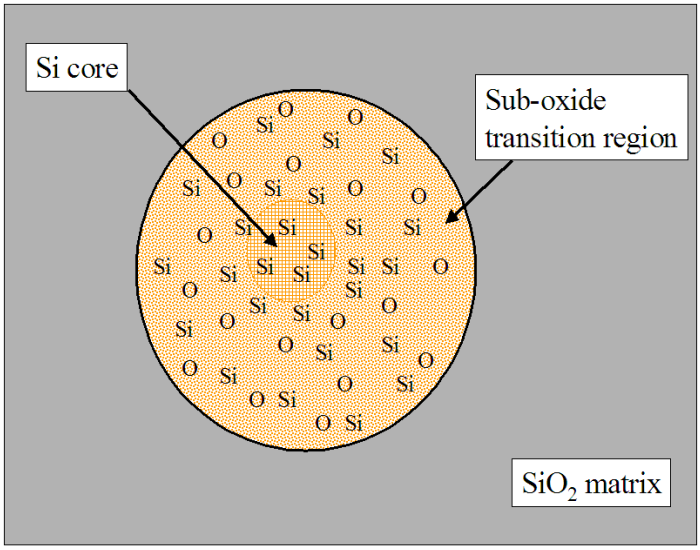

Figure 4.2: "Core-shell model" used for the description of the annealed superlattice samples: "Si *core*" is the region of the sample where every Si atom has only Si as (1^{st}-)neighbors; "SiO_2 matrix" is stochiometric SiO_2; "transition region" is volume of the sample where presence Si has O as 1^{st}, 2^{nd} or 3^{rd} nearest neighbor is assumed.

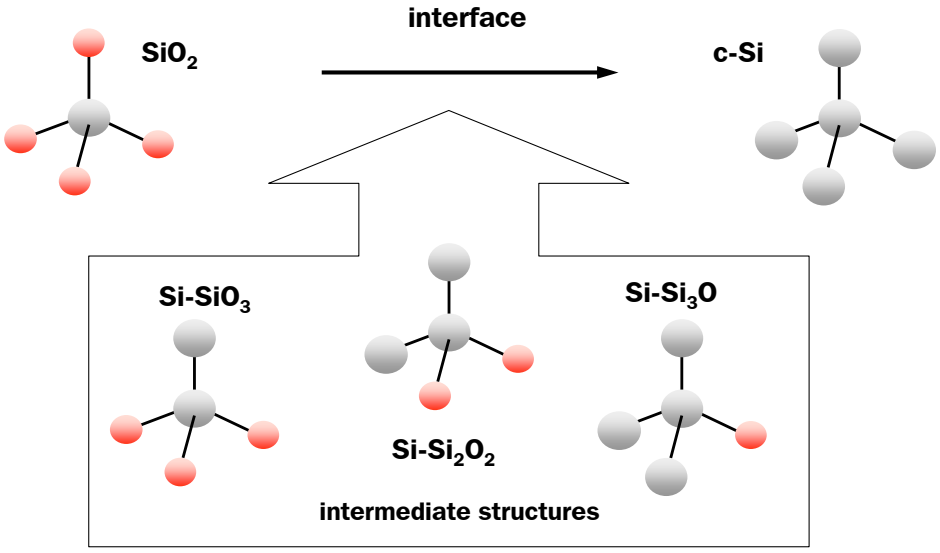

Figure 4.3: "Random bonding model": the transition region in the mixture of intermediate structures where O atoms substitute Si atoms in the fourfold coordination structure.

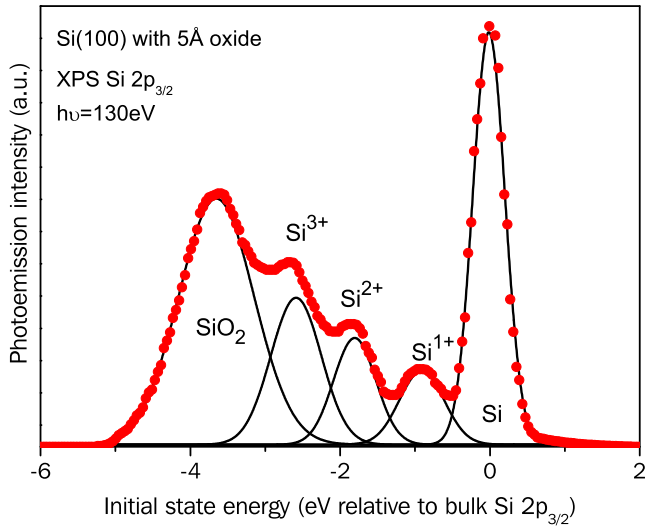

Figure 4.4: Si $2p_{3/2}$ photoemission spectrum measured on Si(100) with 5$\mathring{A}$ oxide layer. The solid line is Gaussian fitting. Every peak corresponds to the 2p binding energy of Si atom in certain intermediate structure. Reproduced from the [62].

samples with different Si nanoparticle sizes. With the lowest excitation energy the $2p_{3/2}$ core level of crystalline Si can be excited. The SXE spectrum resembles the spectrum for crystalline Si, which is superimposed as a dashed line. The deviation between the SXE spectrum for the nanoclusters and crystalline silicon in the region around 96 eV emission energy can to some extent be explained by momentum conservation effects which emphasize specific parts in the Brilloin zone in bulk crystalline Si [63]. Such effects can be expected to be reduced when the electronic wavefunctions are confined to regions of a few nanometers in size. On the other hand, the spectrum of the nanoclusters is distinctly different from the one of amorphous silicon, where the peaks at 89.5 eV and 91.5 eV emission energy merge to one structure due to the lack of long range order [64]. These observations demonstrate that from the viewpoint of the resulting electronic structure, the core of the nanoclusters does not consist of amorphous silicon, but has a high degree of crystallinity. This result is in agreement with high resolution transmission electron microscopy images, which show well ordered columns of atoms[65].

At 100.6 eV excitation enrgy the $2p_{1/2}$ level is reached and the spectrum is the sum of Lα and Lβ emission, but still related only to the Si atoms without a chemical bond to an oxygen neighbor. With further increase in the primary energy Si atoms with more oxygen neighbors were excited. The SXF spectra are then a superposition of the valence band emission from all Si atoms with a 2p binding energy below or equal to the excitation energy. The spectra with excitation energies from 100.6eV and 101eV are virtually identical, indicating that suboxides with stoichoimetry Si-Si_3O_1 are not present. A slight change of the emission spectrum can be observed when raising the excitation energy to 102eV. Spectra excited at 103 and 104 eV are significantly different from the low energy excited spectra. They cannot be described by a superposition of the spectrum excited at 101eV and the well known SiO_2 spectrum, which is obtained for excitation energies equal to 108 eV when the Si atoms in the stochiometric SiO_2 matrix is excited. This spectral shape suggests the presence of small amounts of sub-oxides with a stoichiometry Si-Si_xO_{4-x}, $x \leq 2$. The observations are consistent with a relatively sharp interface region with only few sub-oxides present. For the samples with 3 and 2nm initial SiO layers the changes in the spectral shape are stronger (Fig. 4.7 and 4.8): the intensity of the emission peak around 92eV decreases relative to the peak at 89eV at higher excitation energies (spectra e,f) compared to the low energy excited spectra (a,b). These modifications reflect the changes in the relative volume of the transition region between the crystalline Si core and the surrounding matrix. For the smallest crystals it contains suboxides over a shell with a volume e.g. comparable to the nanocrystal core volume.

The amount of sub-oxide around the Si core was evaluated by analysing its respective contribution to the SXE spectra on the basis of their different spectral shape. For every sample the emission spectrum excited at 100.6 eV was reffered to Si atoms with only silicon atoms as neibours. Then the difference between the "core-related" spectrum and other emission spectra corresponds to Si atoms from the transition region. The procedure is demonstrated in Fig. 4.9 for the sample with the 4 nm thick initial SiO layer where the SXE spectra excited at 100.6 eV and 103 eV and their difference are plotted.

The same procedure was made for every excitation energy. The relative contribution of the core intensity to the emission spectrum at different excitation energies for the 4nm SiO layer are listed in the Table 4.1. One can see that the sub-oxide contribution increases

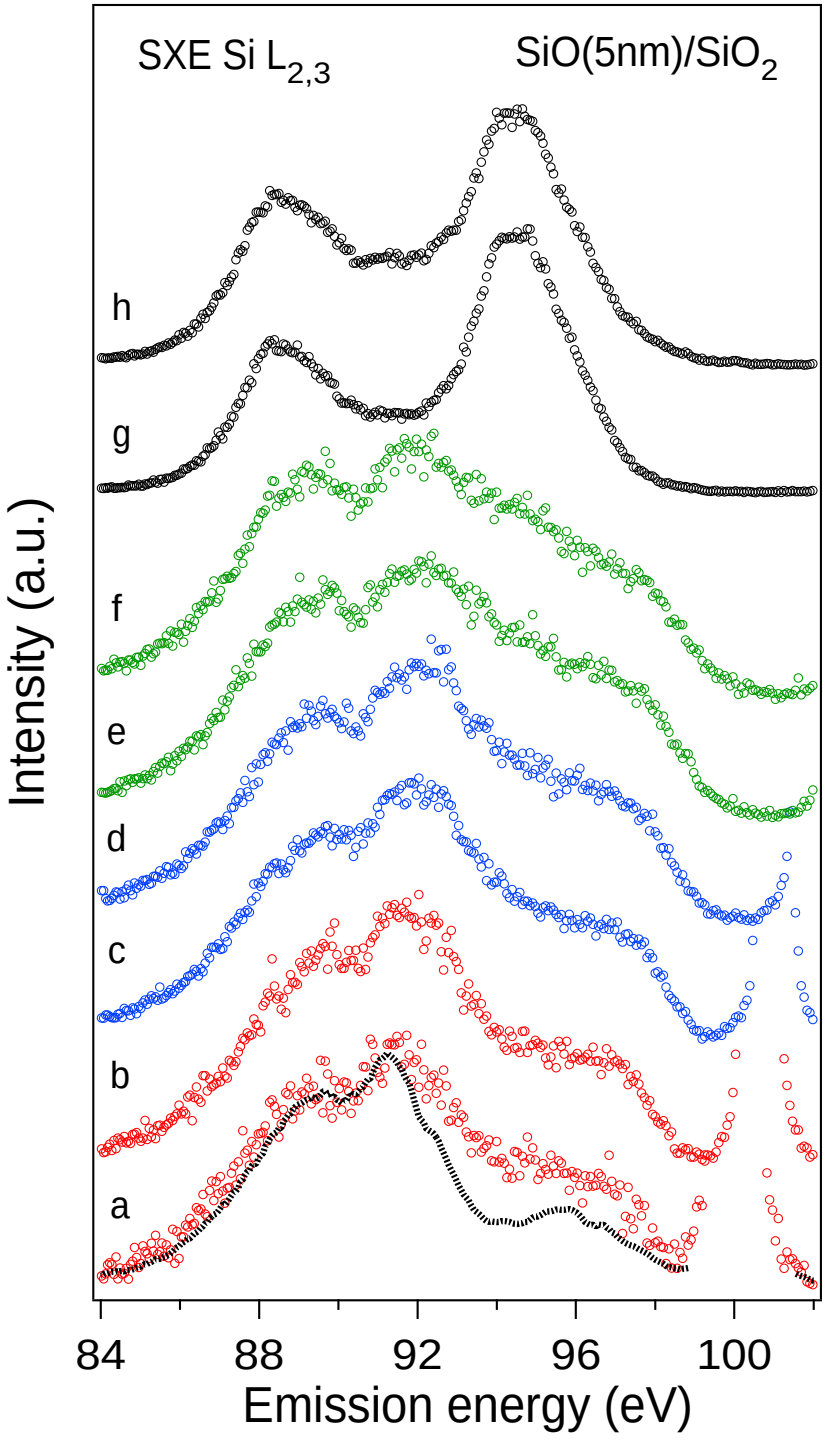

Figure 4.5: Series of SXE spectra as a function of incident photon energy recorded for the sample with an initial SiO layer of 5 nm thickness. Excitation energies are 100 eV (a), 100.6 eV (b), 101 eV (c), 102 eV (d), 103 eV (e), 104 eV (f), 108 V (g) and 120 eV (h). Different colors are used to mark spectra with similar shape. Spectrum of c-Si (black curve superimposed to the spectrum excited at 100eV) is shown for comparison. Elastic peaks are clipped for clarity.

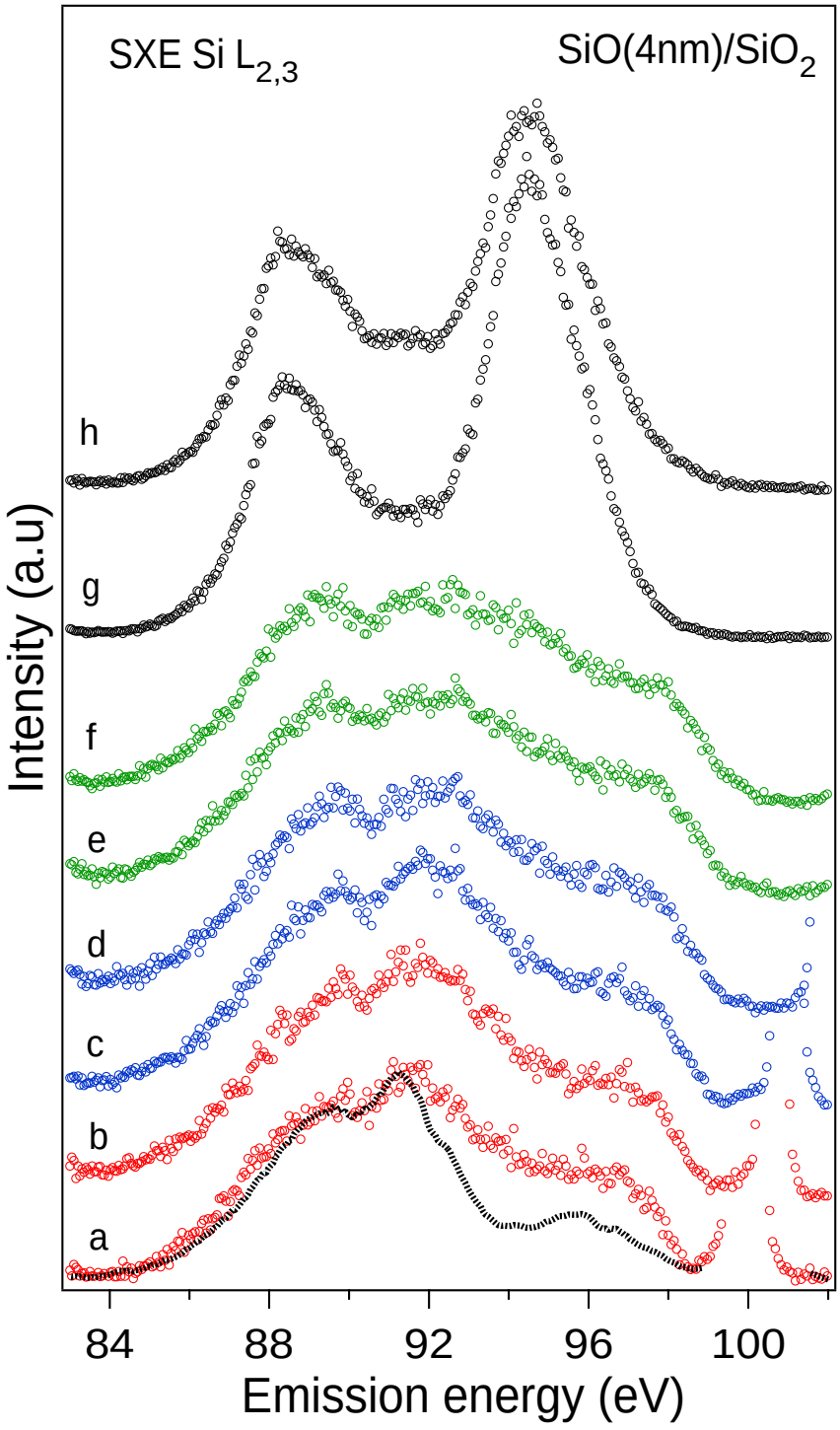

Figure 4.6: Series of SXE spectra as a function of incident photon energy recorded for the sample with an initial SiO layer of 4 nm thickness. For the explanation of notations see Fig. 4.5.

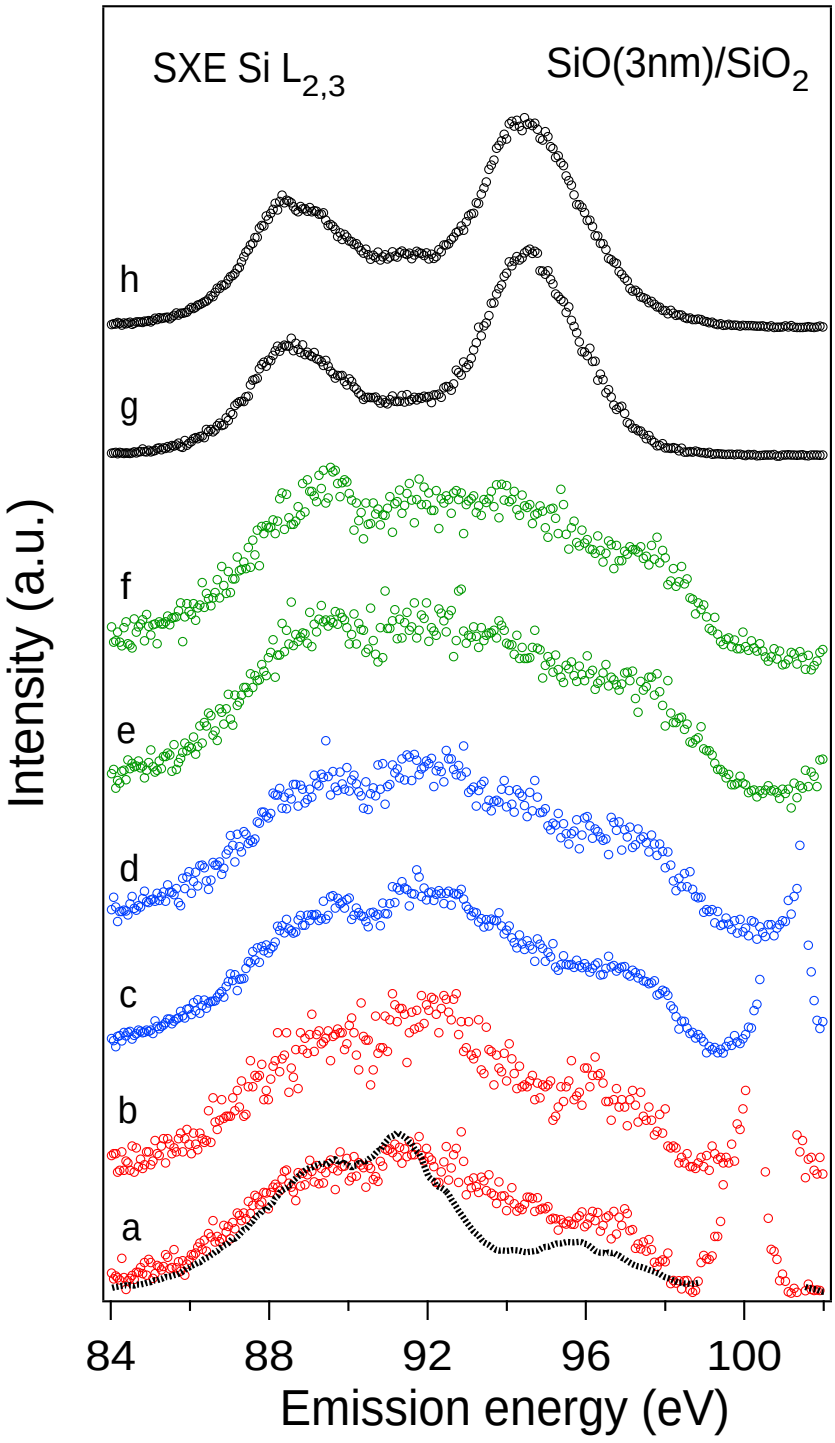

Figure 4.7: Series of SXE spectra as a function of incident photon energy recorded for the sample with an initial SiO layer of 3 nm thickness. For the explanation of notations see Fig. 4.5.

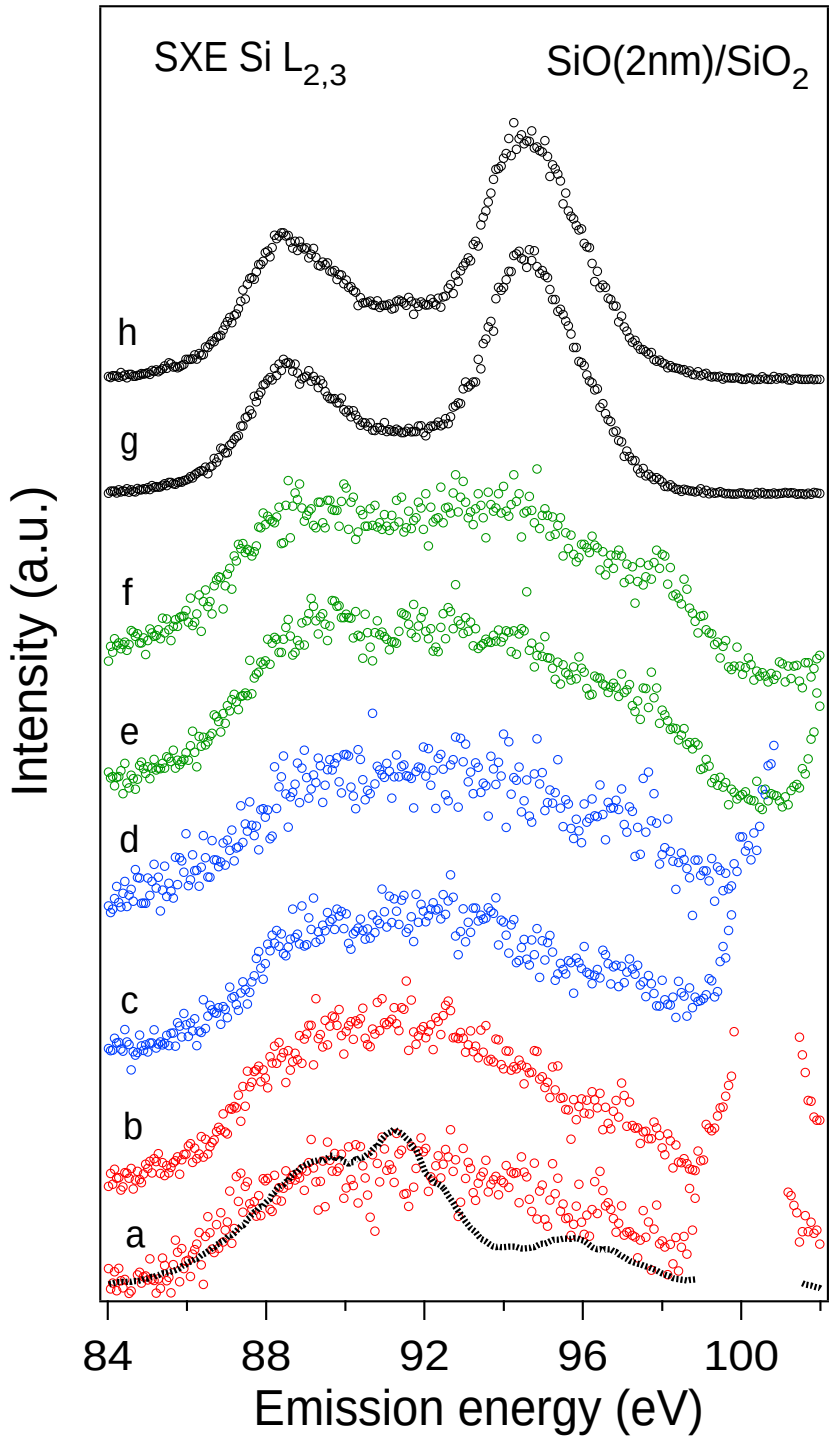

Figure 4.8: Series of SXE spectra as a function of incident photon energy recorded for the sample with an initial SiO layer of 2 nm thickness. For the explanation of notations see Fig. 4.5.

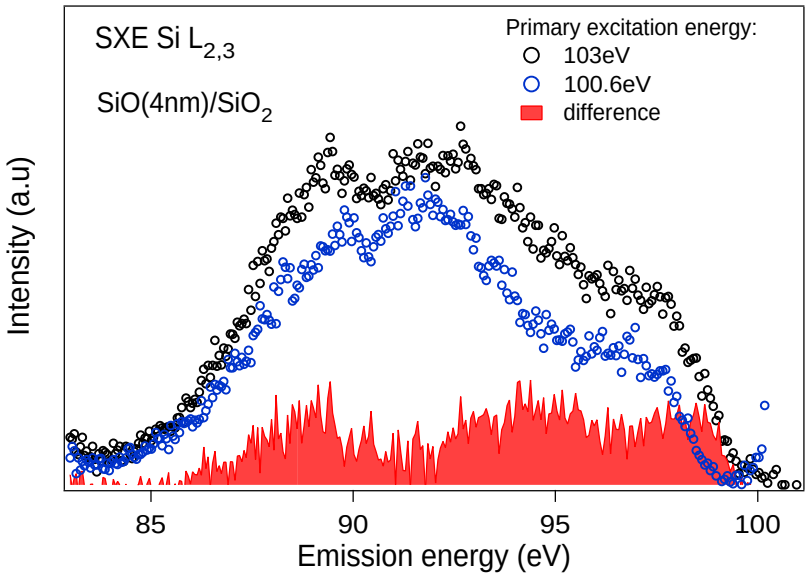

Figure 4.9: SXE spectra of the sample with 4nm initial SiO layer excited at 100.6eV and 103eV and the difference between them.

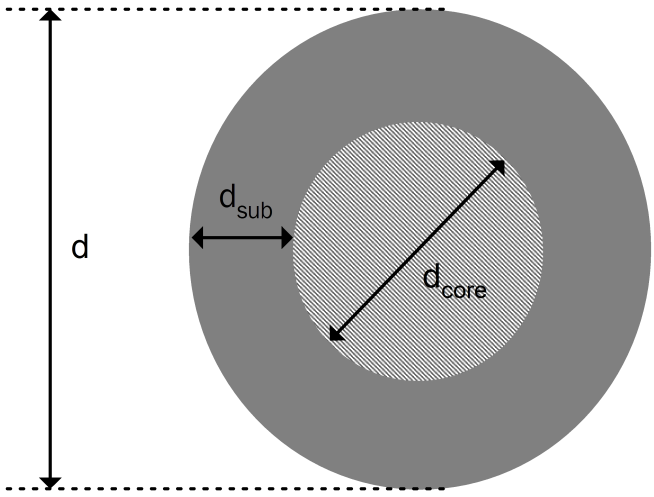

Figure 4.10: Parameters used to described the sample: d is thickness of the initial SiO layer, d_{core} is the diameter of the Si core, d_{sub} is the thickness of the suboxide layer.

Excitation energy (eV)	100.6	101	102	103	104	108
Si-Si_4 contribution (%)	100	100	86	79	72	<2

Table 4.1: Contribution of the Si core to the intensity of the emission spectrum as a function of the primary photon energy (±20%). The values are calculated from the experimental data for the sample with the initial SiO layer of 4 nm thickness.

if the excitation energy increases, but the low energy spectra are free of this contribution. The maximum contribution of the sub-oxide into the emission intensity does not exceed 30% at 104 eV and at higher energies emission from the SiO_2 absolutely prevails in the spectrum.

From these data the average sub-oxide thickness relative to the initial SiO layer was calculated. The only approximation is made is that the Si L fluorescence efficiency of the oxides and pure Si is proportional to the number of silicon atoms per unit volume in these materials. For the Si-Si_2O_2 intermediate structure excited at 103 eV the efficiency is equal 2. Then the amount of the suboxide can be calculated as:

$$K_{sub} = \frac{2 * (1 - A_{core})}{2 * (1 - A_{core}) + 1 - A_{core}}, \tag{4.1}$$

where A_{core} is the intensity contribution from the Si core and the K_{sub} is the relative volume of the suboxide.

Further, if one assumes that the final structure has the total size equal to the initial thickness of SiO layer (see Fig. 4.10), the diameter of Si-core (d_{core}) and the thickness of the sub-oxide layer (d_{sub}) can be calculated from the following relation:

$$\begin{aligned} d_{sub} &= \frac{d}{2}(1 - \sqrt{1 - K_{sub}}) \\ d_{core} &= d - 2d_{sub} \end{aligned} \tag{4.2}$$

where d is the thickness of the initial SiO layer.

The results are summarized in the Table 4.2 together with the uncertainties originating from the experimental errors. From this measurements one can see, that the final size of the Si-core is smaller then the initial SiO thickness, but the sub-oxide layer is small relative to the Si-core diameter. This result is in agreement with previous published results from the MPI work reporting a decreasing size distribution for decreasing size, e.g. layer thickness [5, 60, 66]. A Gaussian size distribution of (2.8 $\pm$0.2) nm and (3.3$\pm$0.35) nm estimated from dark field images of the respective two samples prepared with slightly different layer thickness were reported [60]. A recent study using energy filtered transmission electron microscopy on silicon nanocrsytals grown under the same conditions as the presented samples (but not from layered precursors) indicates the presence of a 1 nm thick transition layer around Si nanocrystals of 2.0 nm to 3.4 nm diameter in a SiO_2 matrix [67].

4.3 Size dependence of the electronic structure of the Si core.

As c-Si is an indirect semiconductor, the strong photoluminescence observed in the nano-sized Si particles is an outstanding behavior for this material. Indirect transitions from the bottom of the conduction band to the top of the valence band can become more probable due to the changes in the electronic structure when the size of the structure decreases. New boundary coditions due to the size reduction of the strucutre can effect the electronic

D_{SiO}, (nm)	Si-core contribution to the 103 eV spectrum (%)	Sub-oxide content, relative to the initial size of SiO layer (%)	Diameter of the Si core ±20 % (nm)	Thickness of the suboxide layer ±20 % (nm)
5	77	37	4.0	0.5
4	79	35	3.2	0.4
3	77	37	2.4	0.3
2	82	30	1.6	0.2

Table 4.2: Size-dependent compositional and geometric parameters of the silicon naoncrystals as determined from the SXE spectra.

states in different ways. First, different effective masses are precribed to electrons and holes at certai points of the of Brilloin zone. This defines the size-dependence of the energy of the state and the nanostructured material could become a direct semiconductor under these conditions. Second, electronic states at the top of the bands become less defined in k-space and the overlap of the corresponding CB and VB wave functions increases giving rise to an increased transition propability. These two effects are sketched in Fig. 4.11.

PL measurements on the samples demonstrated not only the strong efficiency, but also size dependence of the maximum of the PL signal: it moves to higher energies with decreasing initial thickness of layers, corresponding to a decreasing Si-core size [65]. This observation can be explained in terms of quantum confinement theory. As the size of a particle decreases, the electronic states have to fulfill the new boundary condition of the modified quantum well. This results in reasing of the energy of the states, so that the energy gap between VB maximum and CB minimum increases, in the first approximation. Also the shape of the electronic bands can change under the quantum confinement conditions. From the PL measurements the information about the total opening of the band gap with decreasing particle size was obtained [5].

More detailed information concerning any size induced changes in the top occupied and lowest unoccupied bands of the Si can be obtained by the SXS method, as by this technique electronic states in valence and conduction bands are probed separately from each other. The details of the electronic structure within the Si *core* of the nanoclusters as a function of nanocluster size can be investigated by measuring the selective excitated spectra of Si 2p emission band at the primary photon energy corresponding to the binding energy of the 2p electron of Si atom with exclusively Si as nearest neibours.

4.3.1 Electronic structure of Si clusters: Unoccupied states

The absorption probability for the incident photons can be monitored by total-electron yield (TEY) or fluorescence yield (FY) methods. The present samples are not conductive and the TEY can not be effectively measured. The FY can be recorded but the diffuse reflection of the incident x-rays is strong. As a result, the total fluorescence yield contains information about both the real and imaginary part of the refrective index. Futhermore, it will depend on geometrical parameters such as geometry and sample surface roughtness. The recorded FY spectra for different cluster sizes are shown in Fig. 4.12. Two wide

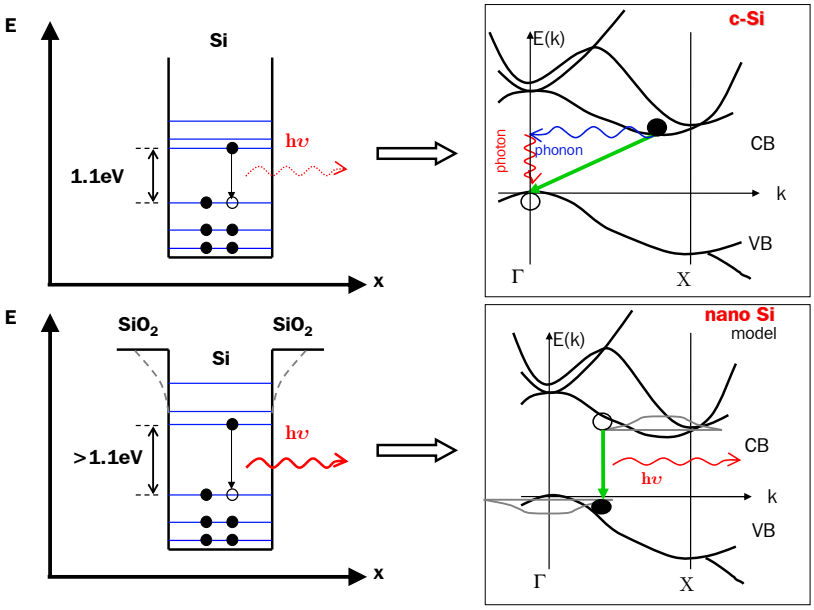

Figure 4.11: As cSi is an indirect semiconductor, PL is not very effective recombination process in this material. As far as the real size of the sample decrease the electronic states changes to fit new conditions: the states at different points in BZ move apart from each other in energy. The presence of SiO_2 matrix can modify the boundary conditions and this should be reflected in the electronic structure of the Si *core*. Another effect of the size limitation is the increase of the uncertainty of the k-vector in small structures.

valleys correspond to the reflection from the $2p_{3/2}$ and $2p_{1/2}$ of Si. One can see that the maximum of the reflection does not move drastically with the size. The shape of the reflection spectrum is not well known and strongly influenced by the sample quality and the experimental conditions. From these measurement it is diffucult to extract the absorption coefficient of the Si atoms which is hidden under the strong energy dependence of the reflection of the primary photons.

Si 2p absorption was successfully recorded by partial fluorescence yield (PFY), accepting only characteristic x-ray fluorescence in the photon energy range between 86 and 97 eV in the Rowland spectrometer as a yield signal. The PFY-SXA spectra as a function of particle size are presented in Fig. 4.13. As mentioned earlier, the spectral resolution of 300 meV in the secondary spectrometer allowed to discriminate against diffuse reflection of the incident x-ray beam, visible as intense peak in Fig. 4.14. The spectrum obtained from the bulk crystalline silicon wafer is superimposed. Geometric fluorescence yield saturation effects [55] influence the spectral shape to some extent but are kept constant, so that spectra of different samples can be directly compared.

The unoccupied (s+d)-DOS is not dramatically different from bulk crystalline Si. The Si $2p_{3/2}$-$2p_{1/2}$ spin orbit splitting of 0.6 eV which is clearly visible in bulk crystalline silicon (edge inflection points at 99.8 eV and 100.4 eV) can be observed in the Si nanocluster samples down to the smallest size. This indicates that inhomogeneous broadening e.g. due to particle size variation is small. In comparison, bulk amorphous silicon (a-Si:H) SXA spectra do not exhibit such spin-orbit splitted structure. These observations are

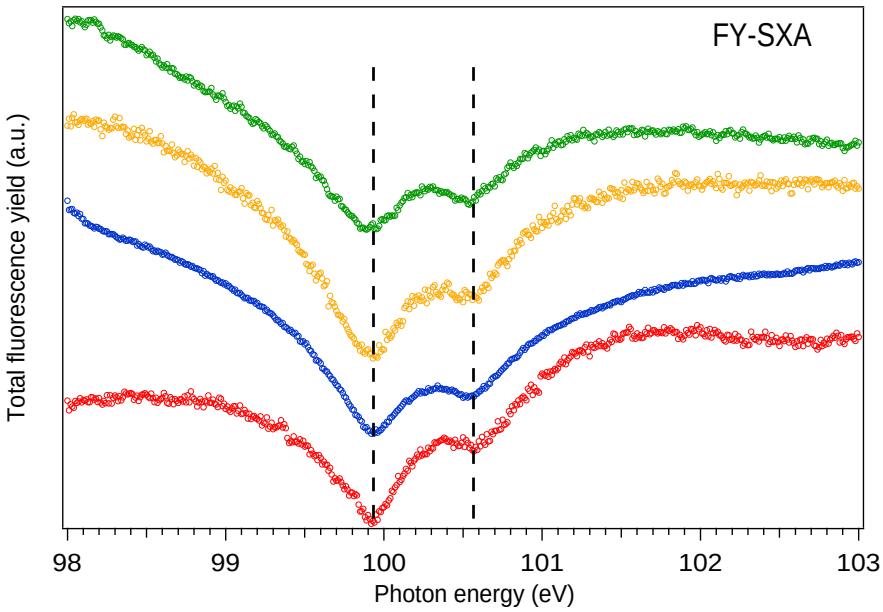

Figure 4.12: FY-SXA spectra are shown as a function of nanocluster size: 5nm (red), 4nm (blue), 3nm (orange), 2nm (green) are the initial thicknesses of the SiO layer. Vertical lines mark the reaks corresponding to the reflection min at the energies equal to the binding energy of $2p_{3/2}$ and $2p_{1/2}$ of c-Si.

consistent with the formation of Si nanoparticles containing a core of crystalline silicon. The most obvious change in the soft x-ray absorption spectra is a shallower onset in the nanocluster samples. Again, this behavior is identical to porous silicon [1] and silicon nanoclusters on surfaces [68]. In contrast to the case of porous silicon, a strong quantum confinement shift of the conduction band minimum with decreasing nanocluster size can not be detected. An onset of the absorption edge for the 3 and 2 nm samples of about 90 and 140 meV, respectively, to lower photon energies as compared to the bulk silicon crystal is measured.

4.3.2 Electronic structure of Si clusters: Occupied states

Spectroscopic results on annealed samples with 5, 4, 3, and 2 nm initial SiO layer are presented in Fig. 4.14. The occupied electronic states in the valence band are reflected by SXE spectra excited at 100.5 eV incident photon energy. Again, the spectrum of bulk crystalline Si has been superimposed for easier comparison of the changes in the electronic structure. At 100.5 eV excitation energy only 2p core levels of Si atoms without oxygen neighbors are excited and thus the observed spectra reflect the (s+d)-DOS in the valence band of the Si nanocluster core. The (s+d)-DOS observed for the nanoclusters of all sizes indicate the presence of crystalline Si, with its characteristic 3 peak structure (peaks around 89.7 eV, 92.2 eV, 95 eV). The detailed shape of the spectra differs from the SXE spectrum of the crystalline Si wafer and changes with the particle size. The peak around 98 eV emission energy is more "step-like" in the Si nanoclusters as compared to the "peak-

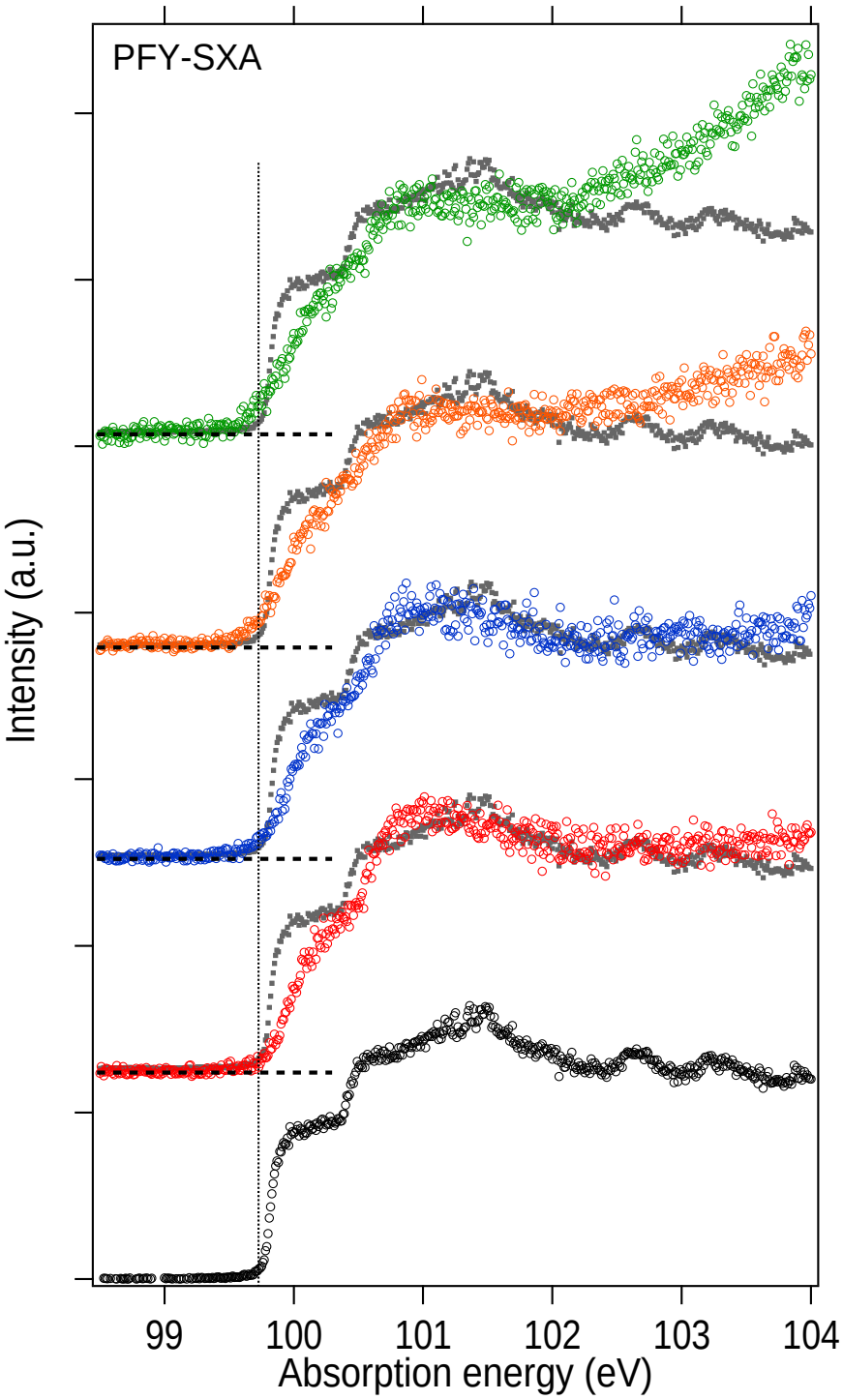

Figure 4.13: PFY-SXA spectra are presented as a function of nanocluster size: 5nm (red), 4nm (blue), 3nm (orange), 2nm (green) are the initial thicknesses of the SiO layer. A spectrum of bulk crystalline Si (black) has been superimposed for comparison. Vertical line marks the CB edge of the c-Si.

like" shape in bulk crystalline Si. Similar changes in the SXE spectral shape have been observed for nanoporous silicon in the past, where they could be attributed to a changes in the (s+d)-DOS due to quantum confinement. In addition the existence of an inelastic feature on the low energy side of the elastically scattered x-rays should be noted. It also exists in pure quartz. This feature makes a quantitative determination of the energy of valence band maximum in the nanoclusters difficult. Nevertheless it is clear from the spectra that the position of the valence band maximum moves to lower energies with decreasing particle size, as expected in a quantum confinement model. The maximum shift, seen in the 2 nm sample, is 0.5±0.1 eV relative to bulk silicon, while the shift in the 3, 4, and 5 nm nanocluster samples amounts to 0.3±0.1 eV. These findings are in good agreement with the diameter dependence obtained for passivated silicon nanocrystals on a germanium surface [69].

The presence of the transition region may influece the electrinic behavior of the cluster. This influence can be significant for nanostructures having a large surface to volume ratio.

4.3.3 Theoretical considerations.

In a quantum confinement model based on the effective masses of the bands in crystalline silicon and using experimental findings for porous silicon [1] and deposited nanocrystals [68], one would expect about one third of the total increase in band gap to be due to a shift of the conduction band. An effect of this magnitude should be clearly detectable by PFY-SXA measurements. In contrast, the onset of the absorption edge for the 3 and 2 nm samples was observed at about 90 and 140 meV to lower photon energies as compared to the bulk silicon crystal, respectively. In combination with the effects in the valence band, this still amounts to an increase of the total band gap by 0.36±0.1 eV over the value for crystalline bulk silicon for these samples. This overall change in the band gap is in agreement with the observed shift of the photoluminescence peak positions in the samples, which shift by 0.35 eV when going from 6 nm particles to 2 nm particles. The fact however, that this shift is almost entirely due to a change in the occupied electronic states within the Si core is surprising and incompatible with a simple quantum confinement model based on the bulk Si band structure. In the following, two possible explanations for such a behavior are discussed: strain effects and the influence of excitonic states on the absorption spectra.

Strain effect.

The geometry of the approximately spherical nanoclusters requires a strongly curved interface to the surrounding matrix, which is formed by a suboxide region, as discussed above. Calculations for Si_{10} clusters in a β-cristobalite SiO_2 matrix including structural relaxation indicate the presence of strain in the clusters (14%)and the immediately adjacent oxide matrix (8 - 9$\mathring{A}$ transition region is formed)[67]. In order to investigate whether strain effects may be responsible for the present observations, Si L SXA spectroscopy on biaxially strained silicon, grown as a thin film on SiGe, have been performed. In this case, a shift of the conduction band edge to *higher* energies by 40 meV for a change of biaxial strain of 0.4 % was observed. An effect with this magnitude and sign is in agreement with

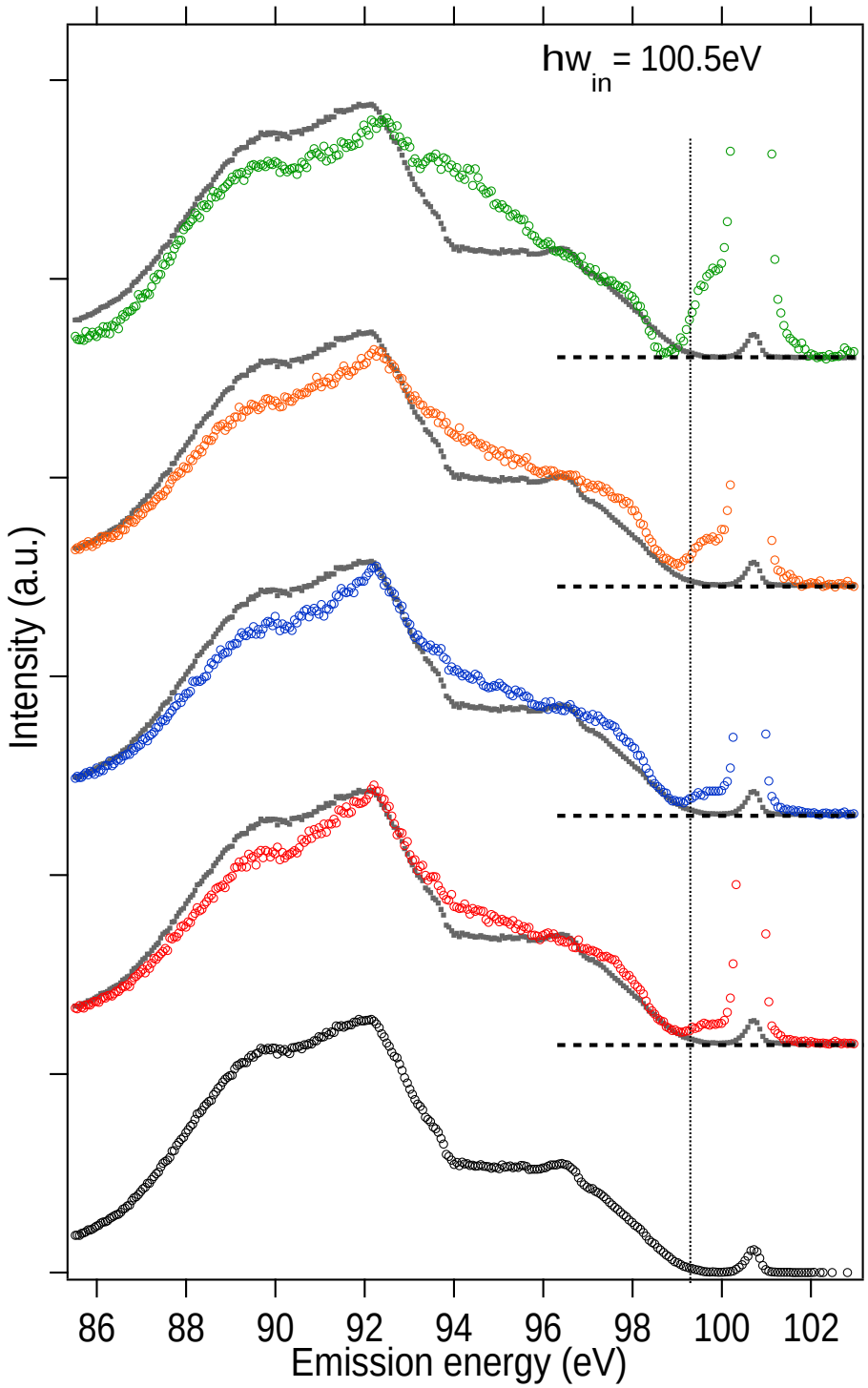

Figure 4.14: SXE spectra excited at 100.5eV are presented as a function of nanocluster size: 5nm (red), 4nm (blue), 3nm (orange), 2nm (green) are the initial thicknesses of the SiO layer. A spectrum of bulk crystalline Si (black) has been superimposed for comparison. Vertical line marks the VB edge of the c-Si. Elastic peaks are clipped for clarity.

theoretical expectations [70]. While this planar model system is certainly much simpler than the situation in the nanoclusters, this result nevertheless suggest that strain effects can not explain the non-existent shift of the conduction band minimum to higher energies in the Si nanoclusters.

Electron correlation.

Interaction between the electron excited into the conduction band and the core hole will lower the total energy of the electronic system and may give rise to an excitonic state. Such a core exciton is different from a Mott-Wannier-type and a Frenkel-exciton in that the core hole can neither move through the crystal nor hop from one nanocrystal to another [66]. Nevertheless, the exciton energy will be influenced by the size of the nanocluster if the spatial confinement is on the order of the exciton radius and below [71]. The Hamiltonian describing the electron-hole interaction can be written as:

$$\widehat{H} = -\frac{\hbar^2}{2m_e}\nabla_e^2 - \frac{\hbar^2}{2m_h}\nabla_h^2 - \frac{e^2}{\epsilon\left|r_e - r_h\right|} \tag{4.3}$$

where m_e and m_h are effective masses of the electron and the hole, ϵ is the dielectric constant of material. In this case the electron and the hole interact with each other via shielded Coulumb forces. From an analytical solution of the Schrodinger equation, the lowest eigenvalue is

$$E^* \cong E_g + \frac{\hbar^2\pi^2}{2R^2}\left[\frac{1}{2m_e} + \frac{1}{2m_h}\right] - \frac{1.8e^2}{\epsilon R} \tag{4.4}$$

where R is the radius of the cluster [71]. One can see that the Coulomb term shifts the energy to lower energy as R^{-1}, while the quantum confiment effect shifts it to the higher energy as R^{-2}. The band gap is expected to increase for the small clusters, but the effect can be slowed by the excitonic effect in materials with large band gap where the Coulomb intraction is strong.

For hydrogen passivated Si quantum dots, the excitons were found to be confined by the quantum dot dimension and not by the Coulomb interaction for diameter D<4 nm [72, 73]. For Si, the associated energy reduction due to Coulomb interaction in the excitonic state can be parameterized as $E_C = 3.572\backslash eD$ in atomic units (D in Bohr radii, E in Hartrees), translating to E_C=$1\backslash D * 454(meV\backslash nm)$ when the dielectric constant ϵ=11.4 of bulk Si is used [71, 72].

The statistic dielectric constant ϵ is defined as the integral over absorption spectra and thus depends on the dipole transition matrix element between the final and initial states. As the size of the cluster decreases the matrix element should change. The effect on ϵ of reduction the size of R was reported and calculated theoretically [72]. The screening dielectric constant which effectively measures the reduction of the Coulomb potential of an electron or hole due to screening by the medium can be written in a simple analytical form [72]:

$$\epsilon(R) = 1 + \frac{\epsilon - 1}{1 + (\alpha/R)^l} \tag{4.5}$$

	(a)	(b)	(c)	(d)	(e)
D_{Sicore}(nm)	CBM shift ±0.03	1/3 QC infinite	E_{exc}, ϵ_{bulk}=11.4	E_{exc}, ϵ_{nano}(D)	E_{exc}, ϵ_{nano}(D) & $\delta\Sigma$ & ϵ_{SiO_2}
4.0	0.00	0.10	-0.11	-0.14	-0.19
3.2	0.00	0.15	-0.14	-0.18	-0.24
2.4	-0.09	0.38	-0.19	-0.27	-0.34
1.6	-0.14	0.60	-0.28	-0.48	-0.62

Table 4.3: Comparison of the experimental shift of the absorption edge (a) with the theoretical calculations: quantum confinement prediction in effective mass approximation assuming infinite barriers and no excitonic contribution (b); exciton contribution, without[71] (c) and with[72] (d) size dependent dielectric constant within the nanocrystal; exciton contribution including the image contribution to the exciton binding energy and ϵ(SiO2)=3.9 (e)[74]. The excitonic contributions have to be subtracted from column (b) for comparison with the experimental result in (a). All energies are in eV.

where α=6.9$\mathring{A}$ and l = 1.37. A smaller effective dielectric constant in nanoclusters will lead to a correspondingly larger energy contribution; values calculated on the basis of Refs [71, 72, 74] are listed in Table 4.3.

Although a singular spectral feature due to a transition into an excitonic final state in PFY-SXA spectra cannot be resolved, such transitions can nevertheless determine the overall spectral shape at the absorption threshold and may lead to the observed shift to lower energy for the smallest nanoclusters. The existence of core excitons for x-ray transitions is in line with the observed population of valence excitonic states upon optical pumping [66]. Apparently, the interplay of the bandstructure and size of the Si nanoclusters is such that excitonic and quantum confinement contributions are of similar size and can thus cancel each other, as predicted by L. Brus in 1986 [71]. One can not expect quantitative agreement between calculations based on free, hydrogen passivated nanoclusters and the present nanoclusters, which are covered by a layer of suboxide within a SiO_2 matrix. Furthermore, details of the concept of the dielectric constant and its magnitude in nanosized structures is still a matter of recent theoretical debates [72, 75, 73, 74, 76, 77, 78] and the immobility of the core hole is not taken into account in the current model. Nevertheless, the excitonic contribution explains the observed trends in the experimental data, i.e. a small and even negative shift of the onset of the x-ray absorption edge in conjunction with a sizeable quantum confinement shift at the valence band maximum. Interestingly, the x-ray absorption edges of non-embedded nanostructures such as porous silicon and hydrogen passivated nanoclusters show a stronger size-dependent shift to higher energies as observed here, while the changes in the occupied states are in agreement [1, 68], suggesting a possible influence of the nanocrystal to matrix interface on the exciton properties in the silicon core.

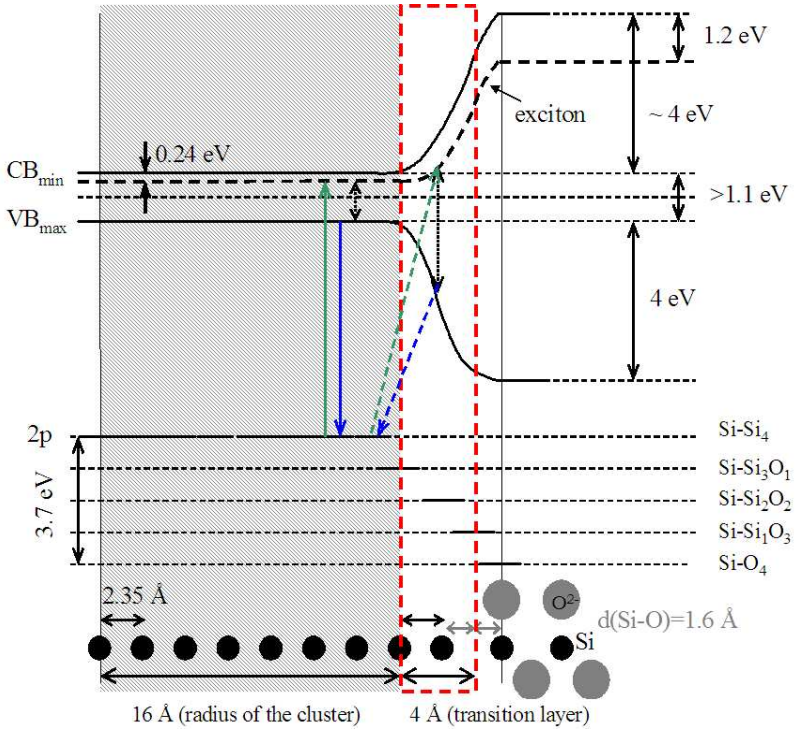

Figure 4.15: The energy diagram of the cluster with the transition region for the sample with 4 nm initial SiO layer based on the present SXS and XPS /SXA [79] data. The absorption (green lines) and emission processes (blue lines) are marked.

Tunneling effect.

We would like to discuss the possibility of non-local electronic transitions and their influence on the interpretation of the results. As wavefunctions do not stop abruptly at an interface, transitions between atoms located at different sides of an interface may be feasible. Such tunneling was observed previously in thin a-Si layers on SiN_x and SiO_x as the downward shift of the absorption edge [79]. The probability of such tunneling transition is difficult to estimate but is thought to be below 1%. The electron transition between the states of the nc-Si and the states of the Si atom in the transition region may occur as well. With the lowest photon energy only the 2p electron of the Si atoms in the core can be excited. With increasing photon energy this electron can tunnel to the transition region additionally to the direct transition to the higher unoccupied states of the nc-Si (green lines in Fig. 4.15). These tunneling would be observed as an absorption structure at photon energies above the real nc-Si 2p edge. The recombination process can occur by the decay of the electron from the VB of the Si atom in the transition region to the core hole of the nc-Si atom (blues lines). This will be observed as an additional high energy feature in the emission spectra. If described processes are present, the opening of the band gap with the size decreasing is measured to be larger than the real value (dotted black arrows). From this point of view, we assumed that the tunneling processes can give intensity to the measured spectra but the energy positions of the absorption edge and the emission band edge corresponds to the direct transitions inside the Si-core.

4.4 Conclusions.

In conclusion, a series of Si nanoclusters embedded in an insulating SiO_2 matrix have been characterized with respect to their electronic structure. In contrast to optical spectroscopy, the size dependent changes in the electronic structure are determined separately for the valence band and the conduction band. Up to now, such disentangled information on nanosized silicon materials has only been available for non-buried nanostructures accessible by electron spectroscopy. Based on the spectroscopic signatures, the embedded nanoclusters are identified as core-shell structures with a thin layer of suboxide (Si-Si_xO_{4-x}, x$\leq$2) covering a predominantly crystalline silicon core. The thicknesses of these two regions have been determined as a function of nanocluster size. Within the silicon core, quantum confinement widens the band gap due to a shift of the occupied states to lower energies. In the unoccupied states, Coulomb interaction of excitonic states counterbalances the quantum confinement effects. The overall change in the bandgap is in agreement with photoluminescence results, corroborating the involvement of excitonic states in this process. These experimental data contribute to an improved theoretical description of the electronic properties of matrix embedded nanocrystals which takes details of the confining potential well - as given by the suboxide transition region and the matrix oxide- into account.

Chapter 5

MoS_2 sub-nanometer diameter nanotubes.

In this chapter investigations of the electronic structure of semiconducting nanotubes with a diameter of less then one nanometer are presented. Nanotubes (NTs) $Mo_xS_yI_z$ of such a small diameter were grown in the Jozef Stefan Institute, Ljubljana, Slovenia [16, 17, 80, 18]. The geometric structure of the NTs varies with the S and I content. To study how the electronic structure of the tubes changes with the geometry SXS was used and the atomic selectivity of the method exploited by measuring resonant inelastic scattering at the S 2p excitation threshold.

Samples.

The first description of the synthesis of single-wall MoS_2 nanotubes (SWNTs) was reported in 2001 [16]. $MoS_2I_{1/3}$ NTs were grown by a catalyzed transport method using C_{60} as a growth promoter in the reaction which was added to MoS_2 powder in a transport tube. The reaction was run typically for 22 days at 1010 K in an evacuated silica ampule at a pressure of 1023 Pa with a temperature gradient of 6 K/cm. Iodine was used as a transport agent. Approximately 15% (by weight) of the starting material was transported by the reaction to form SWNTs, with the rest remaining in the form of layered material. The transported material was subsequently washed with toluene to remove the C_{60}. The material grows in the form of bundles oriented perpendicular to the substrate surface, consisting of individual MoS_2 nanotubes. The bundles usually terminate in a sharp tip, forming sharp needles, with each bundle containing 500,000 ordered nanotubes. A well-pronounced self-assembly of the bundles indicates an attractive interaction among the nanotubes [16].

Energy-dispersive x-ray spectroscopy (EDX) and x-ray fluorescence spectrometry have shown the chemical composition of the bundles to be $MoS_2I_{1/3}$. The stability of the MoS_2 bundles at normal ambient conditions was evident from electron microscopy and diffraction, as well as from other techniques. A high-resolution transmission electron microscopy (HRTEM) investigation of the bundles along their longitudinal direction revealed a hexagonal close-packing of identical nanotubes with the center-to-center distance between two tubes of 0.961 nm. HRTEM images taken approximately perpendicular to the nanotube

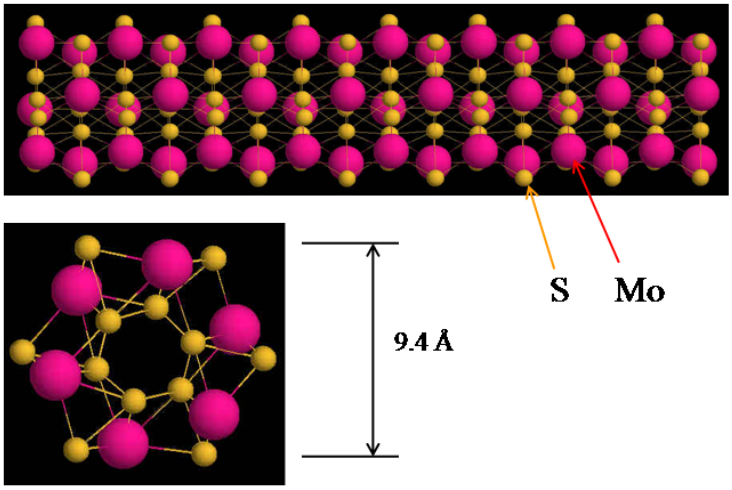

Figure 5.1: Model of the MoS_2-$I_{1/3}$ tubes from the diffraction measurements [80] (purple - Mo, yellow - S). Reproduced from http://optlab.ijs.si/SpLABFiles/Nnotubes/MoS2.html.

axis revealed the ordered structure of individual nanotubes, as well as their regular stacking arrangement within the bundle. Based on diffraction measurements the geometrical structure shown in Fig. 5.1 was proposed [80]. One can image the tube as a rolled-up bulk S-Mo-S trilayer. The iodine is proposed to connect atoms between different tubes.

A follow-up study designed to find other one-dimensional transition-metal chalcogenide-based nanowires and nanotubes resulted in the discovery of a new nanowire material with the formula $Mo_6S_3I_6$ reported in [17]. The material can be synthesized in a single step by direct synthesis from the elements and is functionally similar to $MoS_2I_{1/3}$. The bulk of the material has a fur-like appearance, with individual needles having a diameter of about 50 – 1000 nm and a wide range of lengths up to 5 mm. It is composed of identical small-diameter nanowires 0.94 nm in diameter, weakly bound in bundles, which can be handled in the same way as carbon NTs. The advantage over the $MoS_2I_{1/3}$ NTs is that the new material can be dispersed in organic solvents such as methanol, ethanol, isopropanol, acetone, benzene or toluene using an ultrasonic bath. The material is not brittle and the individual needles are not easily broken on handling. Particularly its reproducibility, ease of handling and its functional properties open the way for widespread study and functionalizing of these NTs.

Based on the analysis of diffraction data [80], the skeleton structure shown in Fig. 5.2 was proposed: it consist of the Mo_6 trigonal cluster and a "shell" of I and S atoms. Atoms connected to Mo atoms do not participate in bridging to neighboring tubes. Those sites can be occupied by S or I atoms. Atoms which do not have Mo as their closest neighbor are bridging atoms and are predominantly iodine. The diffraction pattern shows that there is no S - I bond forming (from the absent of closest I S neighbours). Changing the synthesis parameter produced similar NTs with varying S and I content. The I atoms which are substituted by the S atoms are non-bridging atoms. In the next sections, spectroscopic results on $Mo_6S_3I_6$ and $Mo_6S_{4.5}I_{4.5}$ NTs are discussed.

Nanotubes were investigated by atom-selective photon-in photon-out spectroscopies, namely by SXA and SXF. The experimental results were compared to 2H-MoS_2 bulk

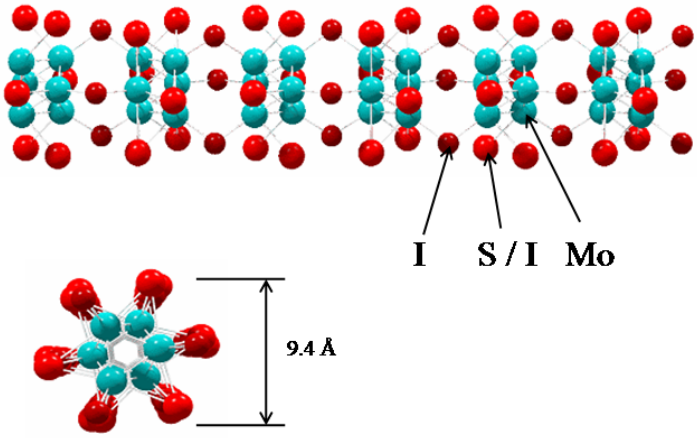

Figure 5.2: Skeleton structure of the $Mo_6S_3I_6$ nanotube: cyan atoms are Mo, red atoms have mixed population of S and I (side view - top, top view - bottom). Red atoms between the Mo_6 cluster are bridging atoms and have the predominant I population. Reproduced from http://complex.ijs.si/research/nanoscience.html

material. For a better understanding of experimental data theoretical calculations of the electronic structure by DFT were carried out in the Jozef Stefan Institute by I. Vilfan for the $Mo_6S_3I_6$ NTs with the following sequence of atoms in the repeating block:

$$Mo_3S_3 - Mo_3I_3 - I_3.$$

In addition, DFT calculations of model structures for the bulk material and MoS_2-$I_{1/3}$ were performed using the StoBe package [81] at BESSY.

Both SXA and SXF spectroscopies were performed in a photon-in photon-out mode and hence are insensitive to electrical charging of the nanotubes. As discussed in details in Ch.2, the basic process involved in both techniques is the excitation of a S 2p core electron into empty states in the CB and the subsequent relaxation when an electron from the VB recombines with the core hole. Only states which can participate in dipole transitions with the S 2p core hole are probed, i.e. S s- and d-states and Mo-S molecular orbitals which have significant s- and d-character with respect to the excited S atom. The production of the core vacancy as a function of the incoming photon energy is measured in SXA and reflects the density of s- and d-symmetry unoccupied states in the CB. The energy resolved SXF measurements of the emitted photons after the electron-hole recombination monitor the occupied states in the VB having s- and d-character.

$MoS_2I_{1/3}$ was investigated at the BESSY UE56/1-SGM beamline, the beamline energy bandwidth was set to 150 meV. $Mo_6S_3I_6$ and $Mo_6S_{4.5}I_{4.5}$ were investigated at the BESSY U49/2-PGM1 beamline, the beamline energy width was set to 80 meV for SXA. Bulk 2H-MoS_2 material was measured at both beamlines as a check of reproducibility. S $L_{2,3}$ SXF was recorded in a Rowland-type soft x-ray fluorescence spectrometer with 600 l/mm spherical grating of 3710 mm radius and 2D-detection at an appropriate off-Rowland angle to obtain the entire spectrum in a parallel mode. The size of the entrance slit was set to achieve an SXF energy resolution equal to 0.5 eV (at BESSY UE56/1-SGM) and 0.8 eV (at BESSY U49/2-PGM1) as measured by the energy width of the elastically reflected

light from the primary monochromator. SXA was monitored in total fluorescence yield (FY) mode using a GaAs:P photodiode as detector. Saturation effects were avoided by using a normal-in grazing-out geometry [55].

5.1 Electronic structure of 2H-MoS_2.

MoS_2 belongs to a class of semiconducting layered compounds with a trigonal prismatic coordination of atoms. In the most common 2H polytype the hexagonal unit cell consists of two S-Mo-S sandwich layers. The bonding in the trilayer has covalent character. The interaction between the adjacent S layers belonging to different sandwiches is very weak and of van der Waals type.

Calculations [82] demonstrated that the principal valence band structure of this compound is composed of 4d orbitals of Mo as well as 3p and 3s orbitals of S. The 4d states of Mo are split into non-degenerate a_{1g} and doubly degenerate e_g bands in the ligand-field of the trigonal-prismatic surrounding and are strongly hybridized with the S p states. The lowest group in the band corresponds to the completely occupied S 3s states. The band close to the maximum of the VB is built of S 3p and Mo a_{1g} and the Fermi level is located at the upper edge of the Mo band. Mo 4d states hybridized with empty S 3p and 3d states dominate the bottom of the CB. Experimentally, the value of the band gap in the 2H-MoS_2 is 1.2 eV [83] and theoretical calculations based on the local density approximation predict an indirect band gap for this material equal to 0.89 eV [82].

The band structure can be described as following. The top of the VB and the bottom of the CB are at the Γ point and at the midpoint of the ΓK line, respectively. Along the ΓA axis the band dispersion at the top of the VB around the Γ point is relative large reflecting the extension of wave functions near the Fermi energy over several trilayers [84]. The band structure of the 2H-MoS_2 as calculated by I. Viffan is shown in Fig. 5.3. The presence of the unoccupieted sub-band (for MoS_2 5.8 eV above the top of the VB) is a characteristic property of these transition metal compounds. The s and d density of states of sulfur are shown as well.

In Fig. 5.4 the SXA and high energy excited SXF spectra of the 2H-MoS_2 are presented. The insert shows the larger photon energy range SXF spectrum including the most intense, low lying S 3s states. The spectra in the narrow photon energy window reflect the energy range in the vicinity of the top of the VB and bottom of the CB, where states are most sensitive to the changes in the chemical bonding. The intensity of the emission is very low reflecting the weak S s- and d-character of the states at these energies. This is consistent with the dominant character of S 3p and Mo d-states at the top of the VB from the electronic structure calculation [82]. The solid lines are a simulation of the non-resonant spectra based on the band structure calculation, taking into account the spin-orbit splitting of the S 2p core level, broadening due to lifetime effects, instrumental resolution, and the energy dependence of the transition matrix elements (see below eq. 5.2). It can be seen from the comparison of the experiment with the theory (see densities in Fig. 5.3) that the spectra reflect essentially the S s and d density of electronic states in the VB and CB. It should be also mentioned that the shape of SXF spectrum is better described by the S s DOS than by S d DOS: the theoretical spectrum in Fig. 5.4

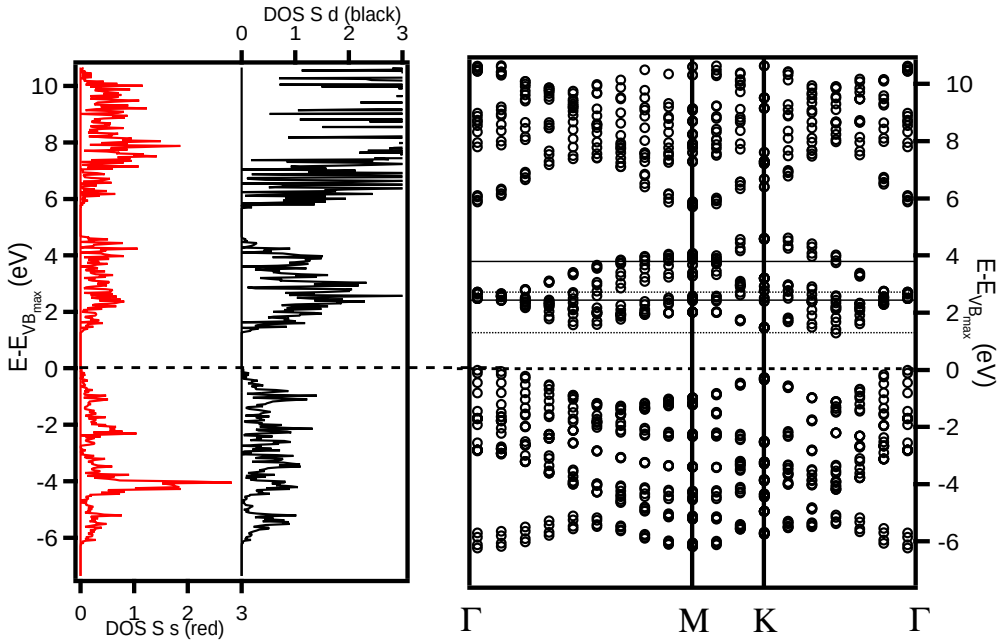

Figure 5.3: Part of the band structure of 2H-MoS_2 (right) and S s and d density of states (left). Dotted blue line marks the top of the VB, solid lines - excitation energies for the band gap probing RIXS measurements (see below).

was obtained with a s:d DOS ratio of 1:0.1. The theoretical absorption spectrum is the combination of S s and d densities of states with a 1:1 ratio.

The agreement between experiment and theory is rather good: the shape and the energy width of the theoretical spectra are very close to the experimental values, especially for the occupied states. One should mention that the theoretical calculation gives the energy bands 16% narrower in energy than was measured in the experiment and the size of the band gap is smaller than the experimetal value due to shortcoming of the local density approximation. Some disagreement between the experimental and the theoretical absorption spectrum based on the unoccupied DOS can be explained by electron correlation effects (see Sec.2.4). The most likely explanation of the disagreement is the presence of the core hole in the final state of the absorption process. While the final state of the absorption process contains a core hole and an excited electron in the CB, the DOS calculation does not take this into account. The presence of a core hole is known to shift spectral weight to lower energies in SXA spectra [48] and it is at the lowest energies where we observe the strongest discrepancies between SXA spectrum and the ground state DOS calculation. Such effects are observed possibly indirectly as the available empty states are S states hybridized with the Mo d states which are in turn strongly localized and non-degenerate due to the crystal field.

In Fig. 5.5 RIXS spectra of 2H-MoS_2 are shown as a function of the primary photon energy ($\hbar\omega_{in}$). The excitation energy dependence of spectra reflects the shape and occupation of different points in the band structure as was described in detail in Section

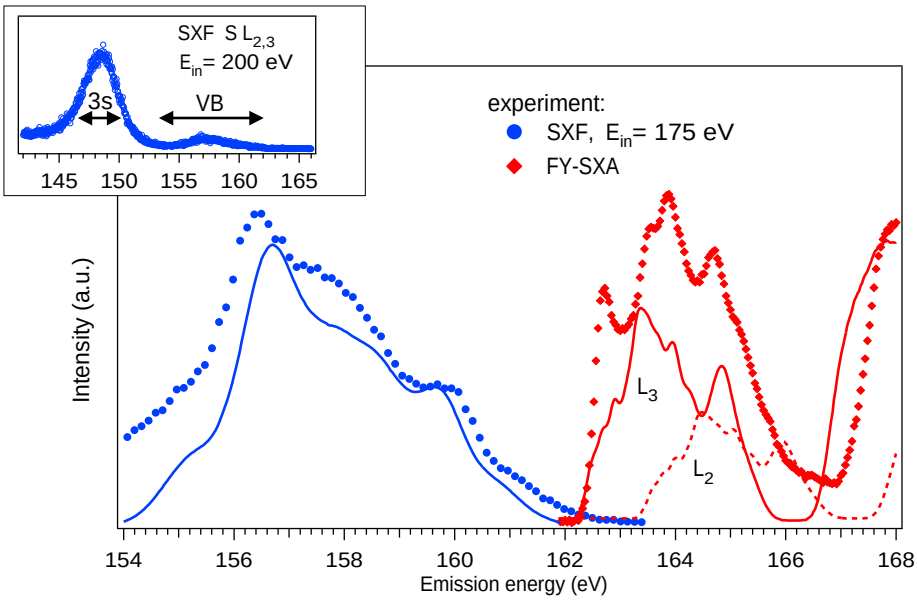

Figure 5.4: SXA (red) and SXF (blue) experimental (dot lines) and theoretical non-resonant (solid lines) spectra of 2H-MoS_2.

2.3. At $\hbar\omega_{in}$ = 162.35 and 162.50 eV the core electron is excited into states close to the bottom of the CB, thus transitions occur resonantly from states close to the Γ-K midpoint of the VB. At $\hbar\omega_{in}$=163.35 eV the resonant excitation moves closer towards the K point. Starting at $\hbar\omega_{in}$=163.70 states in the vicinity of the top of the VB at the Γ point and states in the Γ-A direction arrear in fluorescent spectra. Additionally, at $\hbar\omega_{in}$=163.70 eV the $2p_{1/2}$ level is excited and the measured spectrum contains additional intensity, shifted to the higher emission energies. Changes in the shape of the spectrum excited with $\hbar\omega_{in}$=167.70 eV (above the second band gap) are related to the excitations to states above the minimum of the second subband: the contribution of L_3 emission intensity to the fluorescence band increases again. Energy positions of some specific points of the band structure of the bulk MoS_2 measured in experiment are compared to the theoretical values in Table 5.1.

Thus, the electronic structure of 2H-MoS_2 bulk material is well characterized experimentally and the findings are in agreement with electronic structure calculations.

Point	VB_{max} (Γ)	midpoint Γ-K	VB_{bottom}	CB_{min}
Experiment	0 (161.4)	-1.5 (159.9)	-7.5 (153.9)	1.1 (162.5)
Theory	0	-1.2	-6.2	1.3

Table 5.1: Energy position of some specific points of the band structure of bulk 2H-MoS_2 relative to the VB_{max} measured by RIXS and SXA and theoretical values (in eV). Experimental data are estimated to have an uncertainty of $\pm 0.5eV$ (RIXS) and ±0.1 eV (SXA) due to the limited instrumental resolution.

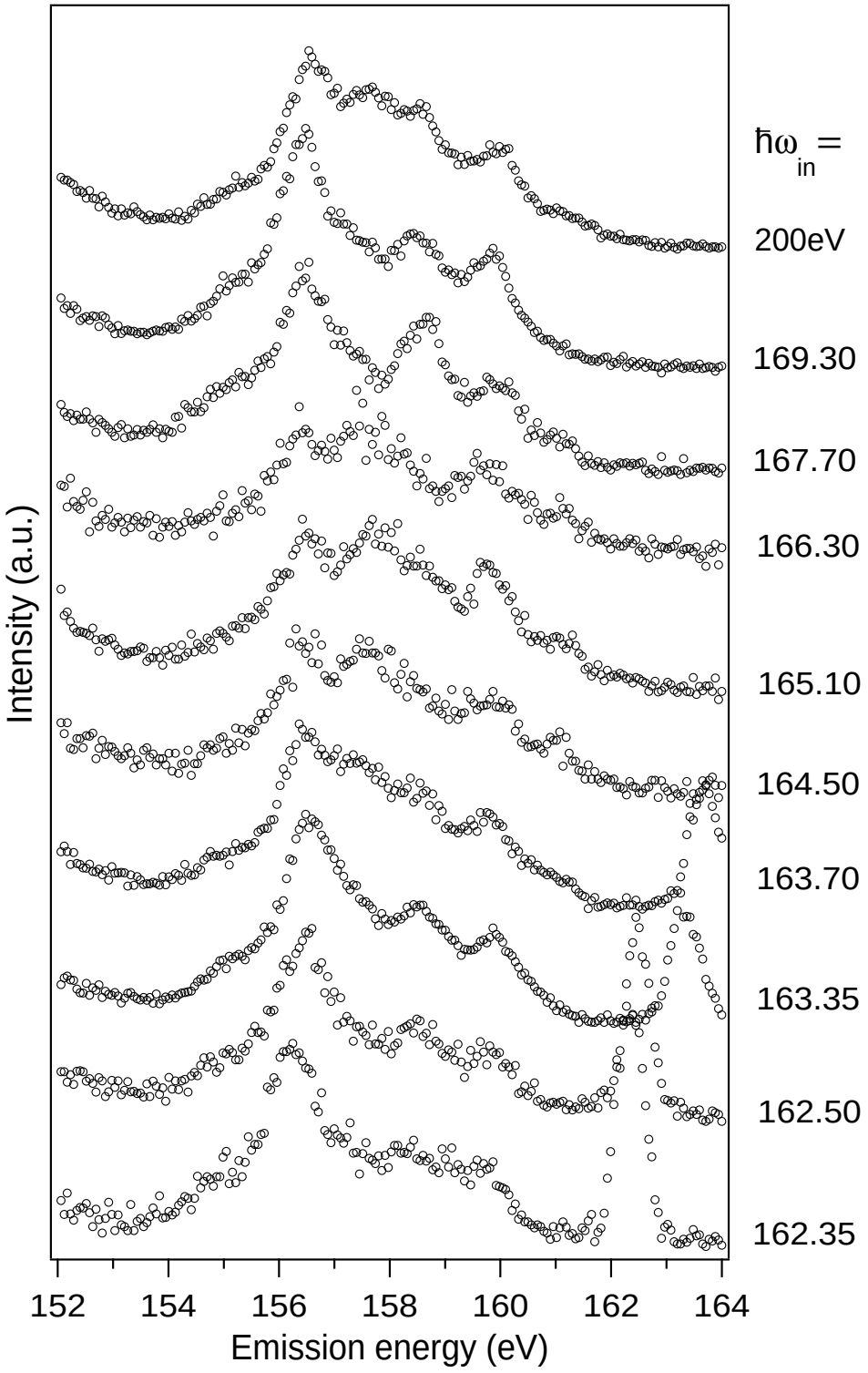

Figure 5.5: RIXS spectra of bulk MoS_2 recorded with different excitation energies corresponding to the specific features in the SXA spectrum (see Fig.5.3). Intense peaks at high energies in spectra excited with energies close to the absorption threshold are due to elastically scattered primary photons. For $\hbar\omega_{in}$= 162.50 eV this peak has been divided by two.

5.2 Electronic structure of Mo-S-I nanotubes.

5.2.1 $MoS_2I_{1/3}$ nanotubes.

Turning from the bulk to the subnanometer diameter NTs, one may expect changes due to i) different overlapping of the Mo and S states inside the tube, ii) changes in electron-electron correlation due to the different overlap of the electron wavefunctions, iii) effects of quantum confinement and, possibly, iv) inter-tube interaction within a bundle. Indeed, the SXA and SXF spectra of $MoS_2I_{1/3}$ NTs are clearly different from the bulk spectra (see Fig. 5.6 and Fig. 5.7).

The most notable changes in spectra of NTs compared to the bulk can be seen in the immediate vicinity of the band edges. The peak at 162.5 eV in the absorption spectrum, which can be observed in the bulk material, disappears in the NTs. In SXF, spectral signal weight at high energies, corresponding to the states at the top of the VB, is strongly increased in the NTs. While, the top of the VB and the bottom of the CB are dominated by Mo states, indicates that these states are observed via their overlap with the S site and that they are affected most when going from bulk to the NTs.

The position of the top of the VB for the $MoS_2I_{1/3}$ NTs can be measured from the spectrum recorded with $\hbar\omega_{in}$ =164.00 eV, below the $2p_{1/2}$ threshold (in Fig. 5.7), and with $\hbar\omega_{in}$ =162.50 eV for the bulk material shown in Fig. 5.6. The VB maximum for the NTs is observed at higher emission energies, compared to the 2H-MoS_2. In conjunction with the absence of the low energy peak in the SXA spectra of $MoS_2I_{1/3}$ NTs, the total reduction of the band gap in the NTs compared to the bulk is measured to be 0.8 eV. From these measurements in conjunction with the bulk 2H-MoS_2 band gap of 1.2 eV [83] a band gap of 0.4 $\pm$ 0.2 eV for the $MoS_2I_{1/3}$ NTs is determined. This is in agreement with the prediction of a smaller gap in the NTs as compared to the bulk material which, however, was for tubes of significantly larger diameter ($\geq$ 2 nm) [13]. This is counter intuitive with respect to a simple quantum confinement model, which does not take bond angle distortion into account.

In Fig. 5.7 RIXS spectra for $MoS_2I_{1/3}$ NTs are shown. In general, the shape of the spectra is significantly different from the corresponding bulk spectra. Compared to the 2H-MoS_2 spectrum at $\hbar\omega_{in}$=162.35 eV, the peak around the $\hbar\omega_{out}$=161.5 eV, close to the top of the VB, is more intense in the corresponding NTs spectrum at $\hbar\omega_{in}$ =163.40 eV. The shape of the RIXS spectra does not change significantly with the energy up to $\hbar\omega_{in}$ = 164.68 eV, when the $2p_{1/2}$ threshold is excited. The SXF spectra change when the photon energy reaches 167.75 eV where the intensity of the low energy peak around 156 eV emission energy increases. The weak excitation energy dependence indicates the "flattening" of the band structure of the NTs in agreement with the theoretical predictions [13, 85]. The existence of a second set of bands separated by a second gap from the lower energy unoccupied states in $MoS_2I_{1/3}$ NTs similar to the 2H-MoS_2 band structure is also well observed in the experiment. The theory also predicts a decrease of the band gap with a reduction of the diameter for this type of the tubes. This is possibly governed by the character of the bonding between S and Mo. This material has a covalent bonding and the S-Mo bond is a hybridized orbital, thus electrons can redistribute over it when the geometry changes. This is in contrast to the situation in carbon NTs where the π-orbitals

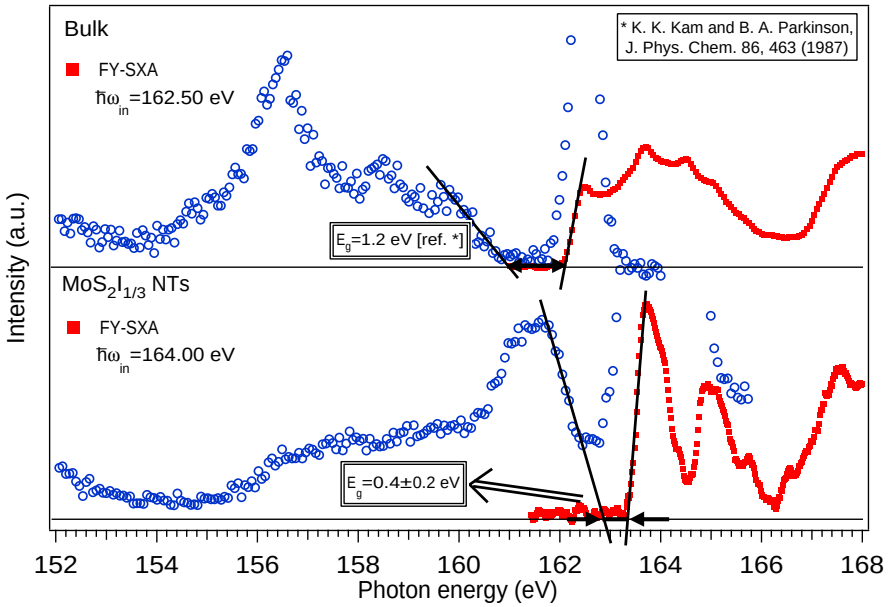

Figure 5.6: SXA (red) and low energy excited SXF (blue) spectra of $MoS_2I_{1/3}$ nanotubes. The bulk spectra are shown for comparison. Black solid lines mark slopes of the spectra for the definition of the size of the band gap.

of carbon atoms are equivalent and saturated, so that charge transfer from one atom to another does not occur.

5.2.2 Model calculations.

In order to understand the main changes in the electronic structure between bulk and $MoS_2I_{1/3}$ NTs, electronic structure calculations of model structures were performed. As noted in [16] the most drastic change in the local geometric arrangement of the $MoS_2I_{1/3}$ NTs as compared to the bulk is the S-Mo-S bond angle. Only the most simple model structure containing this bond angle as a parameter, namely a three atom S-Mo-S cluster, was considered. Based on the electronic structure calculations the probability of electronic transitions from the 2p core level to the unoccupied states in the CB was computed to simulate SXA spectra and from the valence band to the 2p core hole to simulate SXF spectra. The calculations were made using the software package StoBe, based on the Linear Combination of Gaussian Type Orbitals - MO solution of the Kohn-Sham DFT equations [81].

From the consideration of the proposed structure for the MoS_2-$I_{1/3}$ NT (see Fig. 5.1 on page 50) the presence of two types of nonequivalent sulfur atoms (belonging to the inner and to the outer shells) is obvious. A shift in the binding energy of the S 2p core electron may exist due to the inequivalent sites. XPS measurements on MoS_2-$I_{1/3}$ [86] demonstrated the presence of two S 2p sets of peaks separated by about 1.8 eV. As XPS is very surface sensitive, the identification of the origin of the two XPS peaks is not clear:

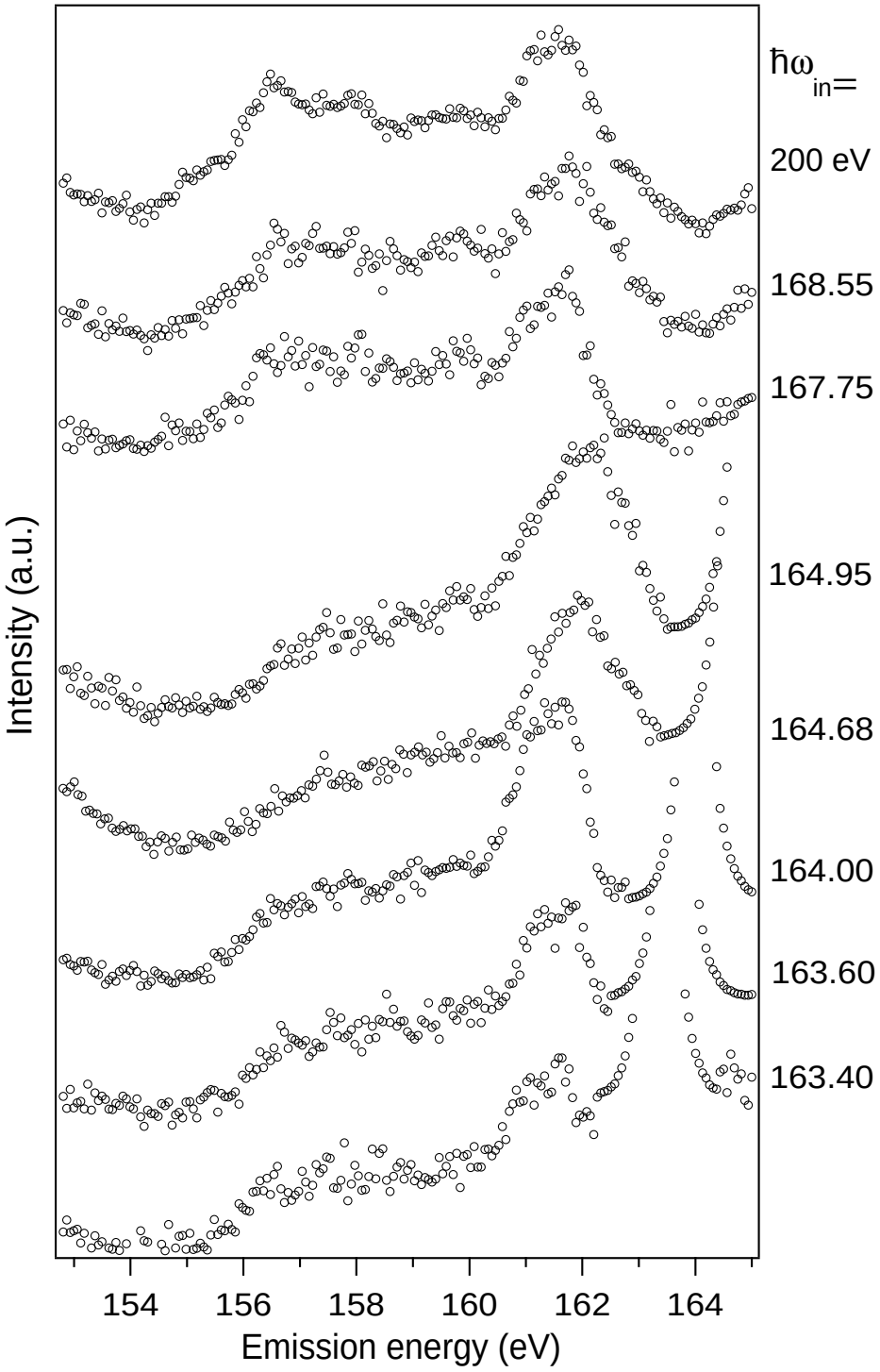

Figure 5.7: RIXS spectra of $MoS_2I_{1/3}$ NTs recorded with different excitation energies corresponding to the specific features in the SXA spectrum (see Fig.5.6). For $\hbar\omega_{in} \leq$ 164.95 eV the intense elastic peaks have been divided by 25 and clipped.

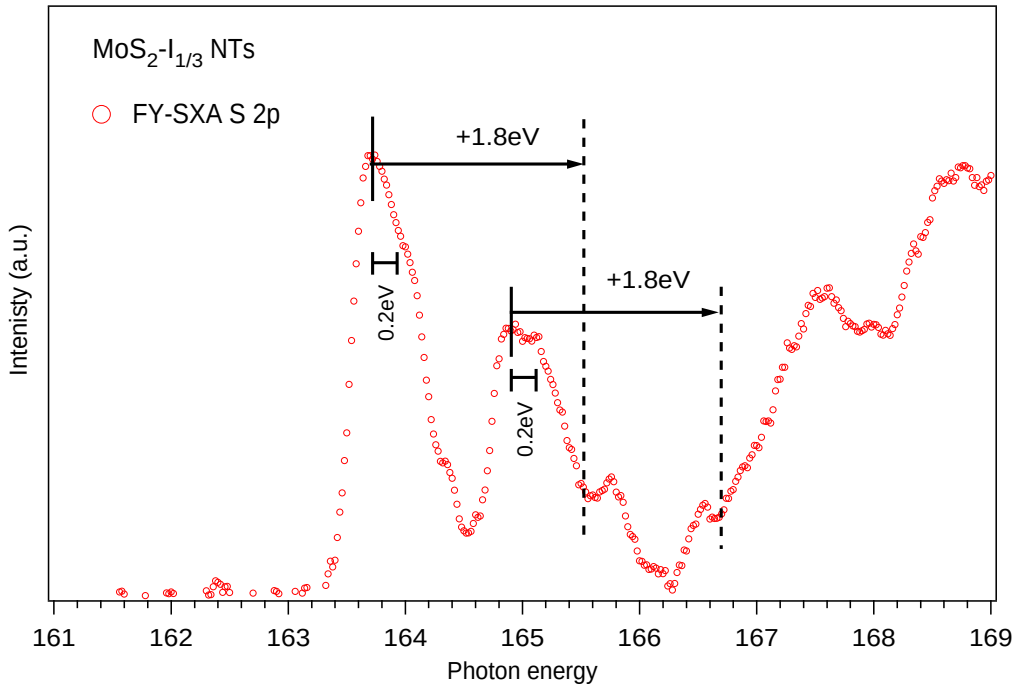

Figure 5.8: FY-SXA spectrum of MoS_2-$I_{1/3}$ NTs. The energy positions of the absorption peaks due to the presence of the nonequivalent sulfur atom are marked by dashed lines.

this shift may also be due to sulfur atoms at the surface of NT bundles vs. sulfur atoms inside a bundle. Out FY-SXA spectra are able to provide some insight into this question. If the different atomic position of the sulfur atom within each NT causes the 1.8 eV shift of the energy of the 2p core electron, two absorption spectra should be observed, shifted relative to each other by 1.8 eV. In Fig. 5.8 the FY-SXA spectrum of MoS_2-$I_{1/3}$ NTs is shown. Lines mark the position of main peaks which are 1.1 eV separated and thus can not be assigned to non-equivalent S atoms, but to the spin-orbit partners of the each sulfur atom. The positions of the peaks shifted by 1.8 eV are marked by the dashed line: there are no strong features in the experimental spectrum observed at those photon energies. From this consideration we conclude that the difference in the 2p electron binding energy in two different sulfur atoms is considerably smaller than 1.8 eV. It could be estimated to be 0.3±0.1eV from the presence of shoulders at the high energy side of the absorption peaks. The energy shift observed in the XPS measurements may be due to probing the surface S atoms. This analysis supports the suitability of the model structure for the MoS_2-$I_{1/3}$ NTs with equivalent sulfur atoms for simulation of emission and absorption spectra neglecting an energy shift of the binding energy of the S 2p electron as this small value is not known precisely.

The bulk material was modeled with a S-Mo-S angle of 82^0 and a S-Mo bond length equal 2.417 $\mathring{A}$ [82]. The $MoS_2{-}I_x$ NTs were modeled with the smaller S-Mo-S angle of 63^0 suggested in [16], keeping the bond length constant. The calculated spectra were convoluted with a Gaussian function with a FWMH of 0.3 eV for SXA and 0.5 eV for SXF to account for the life-time broadening of the core hole and the experimental energy

resolution. The presence of the core hole in the final state of the absorption process and the hole in the VB in the non-resonant emission process was taken into account in these calculations. The 1.1 eV spin-orbit splitting of the $2p_{3/2}$ and $2p_{1/2}$ levels was taken into account assuming a 2:1 branching ratio. The resulting theoretical model spectra are plotted in Fig. 5.9 together with the experimental data. The calculations are in rather good agreement with the measured intensities and reproduce the main features of the experimental spectra. The simple model obviously cannot describe effects resulting from the crystalline structure of the bulk and the NTs. Nevertheless, the main trend in the SXA and SXF spectra when going from the bulk to the NTs is predicted: the SXF spectrum exhibits increased spectral weight at the top of the VB whereas the peak at 162.5 eV is absent in the SXA spectrum.

The good agreement between the calculated spectra and both the experimental SXA and SXF spectra suggests that the simple model captures the essential effects in the changes of the local electronic structure between bulk MoS_2 and subnanometer MoS_2-$I_{1/3}$ NTs. The redistribution of electron density in the tubes compared to 2H-MoS_2 bulk material is interpreted due to the S-Mo-S bond distortion. A charge distribution analysis in the ground state (see Fig. 5.10) was made. The distribution of the electronic states which would give a contribution to the high energy peak in the SXF spectrum (state with binding energy of 2 eV below the top of the VB) was calculated for both model structures. The positions of Mo and one of the S atoms were fixed and the second S atom was moved to simulate the bond angle changing in the tube compared to bulk. Thus the electron density between the fixed atoms could be directly compared. This analysis shows that electron density is redistributed from the S atoms toward the Mo atom due to the change in bond angle: the electron density changes locally at the sulfur site with bond angle.

Although the theoretical spectra give correctly the general character of the experimental changes, the relative intensity of different features is not well reproduced. The high energy part of the emission spectra and the low energy peak in the absorption spectra for both models are underestimated by the theory. The simplicity of the model can explain the disagreement. For bulk material spectra simulated on the basis of DFT calculations using the complete structure of Fig. 5.4 is better reproduced the shape of the experimental emission spectrum:a consequence of taking into account all atoms of the unit cell and the strong hybridization between them.

5.2.3 $Mo_6S_{9-x}I_x$ nanotubes, x=6, 4.5.

The geometrical structure of $Mo_6S_{9-x}I_x$ NTs changes drastically compared to the $MoS_2I_{1/3}$ NTs discussed in the previous sections (see Fig. 5.1 on page 50 and Fig. 5.2 on page 51). The electronic structure of $Mo_6S_{9-x}I_x$ NTs is expected to change with x mostly due to the substitution of the non-bridging iodine atoms by sulfur atoms. This may lead to a modification of the bonding between S and Mo. Such changes in the bonding should be detectable by measuring the S $L_{2,3}$ fluorescence.

The common behavior of the electronic bands of tubes of this type predicted by the theory is the weak dispersion of electron bands as shown later in Fig. 5.15. This means that the electron correlation effects can be expected to influence the experimental results more strongly than in the bulk material.

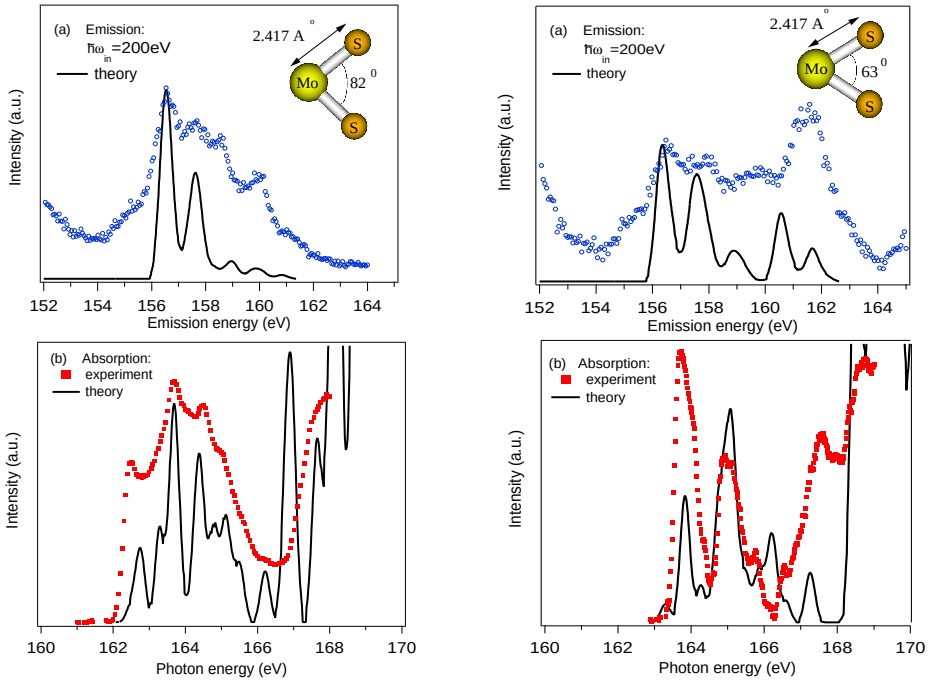

Figure 5.9: Experimental (marks) and calculated (solid) spectra of 2H-MoS_2 (left) and $MoS_2I_{1/3}$ NT (right) trimer model structures.

In Fig. 5.11 non-resonant SXF and FY-SXA spectra measured on $Mo_6S_{9-x}I_x$ (x=6 and 4.5) and $MoS_2I_{1/3}$ are shown. Corresponding spectra for bulk material are shown for comparison. One sees that both SXF and SXA spectra of NTs differ from the bulk spectra significantly. The changes are similar to MoS_2-$I_{1/3}$: in NTs there are more states at the top of the VB and less at the bottom of the CB. The band gap is much smaller in the NTs than in the bulk material and also seems to change with the stoichiometry. There are also remarkable differences between spectra from $Mo_6S_{9-x}I_x$ and MoS_2-$I_{1/3}$ NTs. In the spectra of $Mo_6S_{9-x}I_x$ NTs the intensity of the high energy part of the emission spectra decreases relative to the low energy part compared to the MoS_2-$I_{1/3}$ NTs and there is a low energy (162 - 163.5 eV) contribution in absorption spectra in the case of the $Mo_6S_{9-x}I_x$ tubes. These changes may be due to the stoichiometry changes in the $Mo_6S_{9-x}I_x$ NTs compared to the MoS_2-$I_{1/3}$ NTs. The intensity of the high energy contribution to emission spectra correlates with the intensity of the low energy part of absorption spectra: it increases with the decrease of the low energy intensity corresponding to the empty states at the bottom of the CB.

The electronic structure of $Mo_6S_3I_6$ NTs and bulk MoS_2 was calculated by I. Vilfan with the WIEN2k program lapw1. The photoelectron spectra can be directly compared to the DOS taking into account the photoionization cross section for different states [87]. In this case S p and Mo d states dominate in the signal at the top of the VB. In the case of X-ray fluorescence, the probed states are the S s and S d which are very weak in the VB and CB of MoS_2.

The PES spectra of bulk MoS_2 and $Mo_6S_3I_6$ were measured at Elettra (Italy) by the

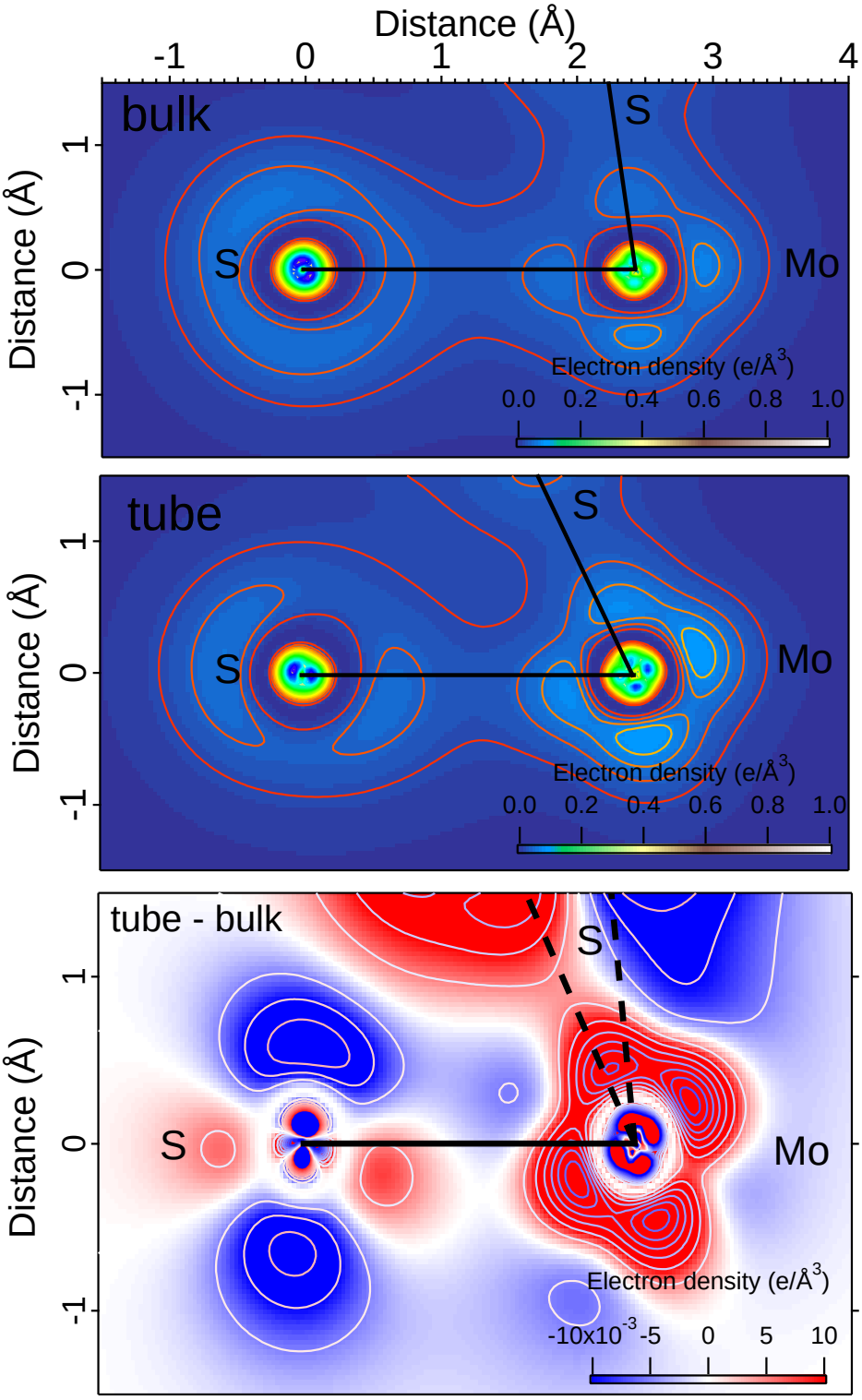

Figure 5.10: Charge distribution of occipied states in the vicinity of the top of the VB in the ground state for 2H-MoS_2 and $MoS_2I_{1/3}$ trimer model structures and the difference between them. The electron density in the area between Mo and the S atoms at (0,0) are to be compared.

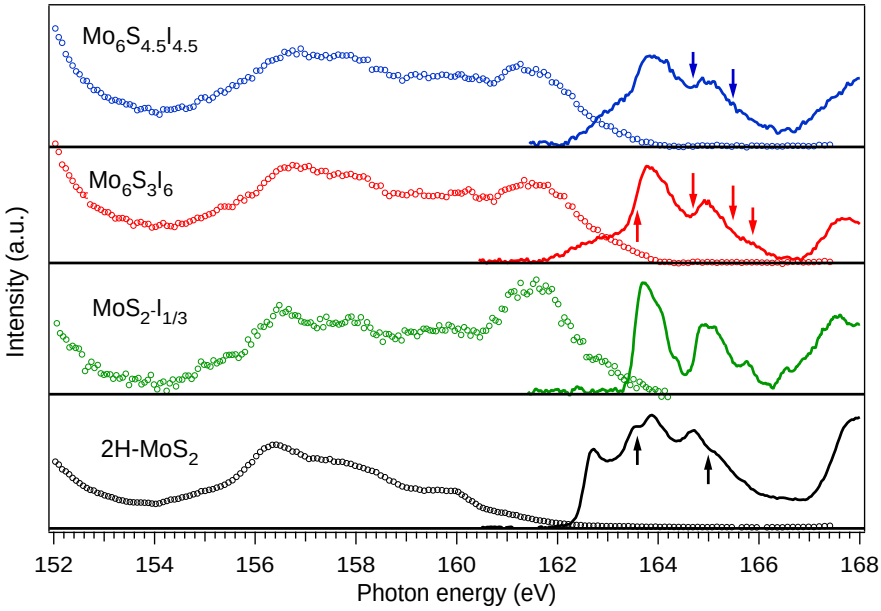

Figure 5.11: Non-resonant SXF spectra (marks) and FY-SXA spectra (solid) of $Mo_6S_{9-x}I_x$ for x=6 (red), 4.5 (blue), $MoS_2I_{1/3}$ (green) and 2H-MoS_2 (black). The excitation energy was 175 eV for $Mo_6S_{9-x}I_x$ NTs and bulk, 200 eV $MoS_2I_{1/3}$ NTs. Arrows mark the photons excitation energies at which the resonant spectra were measured.

group of D. Michailovich [86, 88]. In Fig. 5.13 the PES and non-resonant SXF spectra for the bulk MoS_2 are shown together with the spectra simulated on the basis of LPDOSs (also shown). For the simulation of the SXF spectra the spin-orbit splitting of the S 2p level (1.1 eV) and the experimental energy resolution were taken into account. The dipole matrix elements for transitions were calculated by I. Vilfan as well (plotted in Fig. 5.12) and included in the simulation. The energy dependence of the corresponding matrix elements for the MoS_2 can be well fitted to the calculated values as following (energy in eV):

$$M_s = 0.0267 + 0.0003 \times (E - E_F) - 2.61e^{-5} \times (E - E_F)^2 - 4.18e^{-7} \times (E - E_F)^3 + 1.92e^{-8} \times (E - E_F)^4 + 4.42e^{-10} \times (E - E_F)^5 \quad \text{for the selection rule l-1,} \tag{5.1}$$

$$M_d = 0.0292 + 0.0014 \times (E - E_F) + 3.65e^{-5} \times (E - E_F)^2 + 4.59e^{-7} \times (E - E_F)^3 \quad \text{for the selection rule l+1.} \tag{5.2}$$

The theoretical spectra were aligned in energy scale to fit the width of the VB and the energy position of pronounced peaks measured by the XPS. The emission energy scale is aligned to the binding energy scale based on the position of the theoretical spectrum.

The photoelectron spectrum of the bulk 2H-MoS_2 is well reproduced from the Mo d-DOS and S p-DOS with the photoionization ration 1:0.3. The shape of the non-resonant fluorescence spectrum is well reproduced on the base of the S s- and d-DOS with the

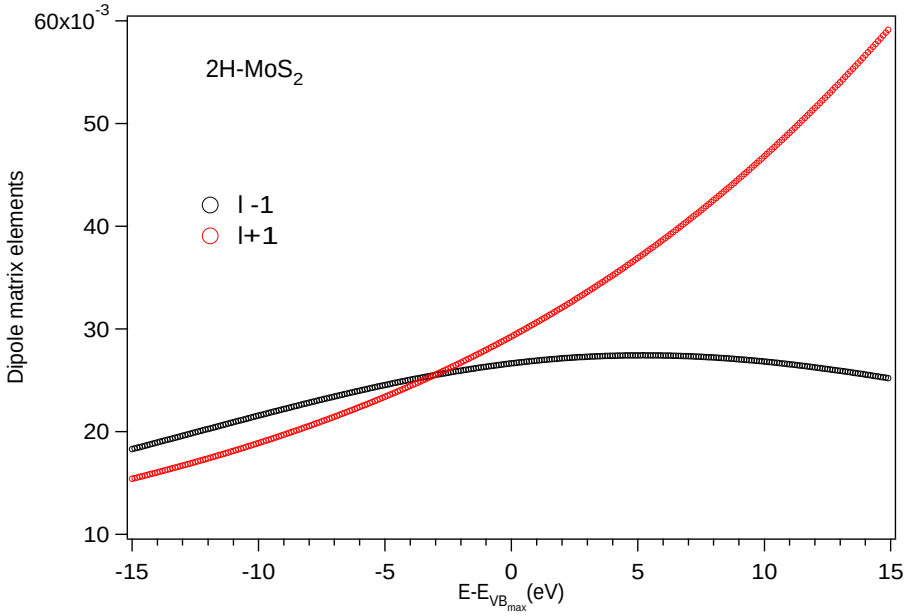

Figure 5.12: Dipole matrix elements calculated for bulk MoS_2 by I. Vilfan.

ration 1:0.1 taking into account the energy dependence of matrix elements. The only feature that is not reproduced is the feature at 157.5 eV in the experimental spectrum. The width of the theoretical band is about 16% less then the measured one.

On the basis of the band structure calculation, we have simulated RIXS spectra by taking into account k-conservation, the dipole selection rule and atomic selectivity. Here additionally the lifetime of the S 2p core hole (70 meV [89]) and the experimental uncertainty in photon energy were also taken into account. Simulated RIXS spectra together with the experimentally obtained spectra of 2H-MoS_2 are shown in Fig. 5.14. The agreement between the experiment and the theory is reasonable: the theoretical spectra resemble the shape of the experimental data, the main peaks of the experimental spectra are well reproduced.

In all spectra the low emission energy part has mostly s-character and the high energy part has an increasing d-character. At 163.6 eV excitation energy states from the whole VB (see Fig. 5.3 on page 53) participate in the transitions to the $2p_{3/2}$ level and the middle part of the VB (5.2 eV $< E_b <$ 2.5 eV, 157 eV $< \hbar\omega_{out} <$ 159 eV) is dominated by the transition to $2p_{1/2}$. The contribution from the $2p_{3/2}$ transitions to the 163.6 eV excited spectrum is dominant. The maximum $\hbar\omega_{out}$ of the $2p_{1/2}$ contribution in 163.6 eV spectrum coincides with the position of the corresponding $2p_{3/2}$ contribution.

At 165.0 eV excitation energy states of the VB close to Γ point and low binding energy states around E = −6 eV give contributions into the transition VB→$2p_{3/2}$ and states mostly from the middle part of the VB into transitions VB→$2p_{1/2}$. In the 165.0 eV excited spectrum contributions from both L_2 and L_3 emission bands are nearly equal and the peak around the 158 eV is mainly due to the L_2 contribution.

For $Mo_6S_3I_6$ NTs the band structure was calculated using the same parameters as for bulk MoS_2. The result is shown in Fig. 5.15 together with the S s, d and Mo d densities of

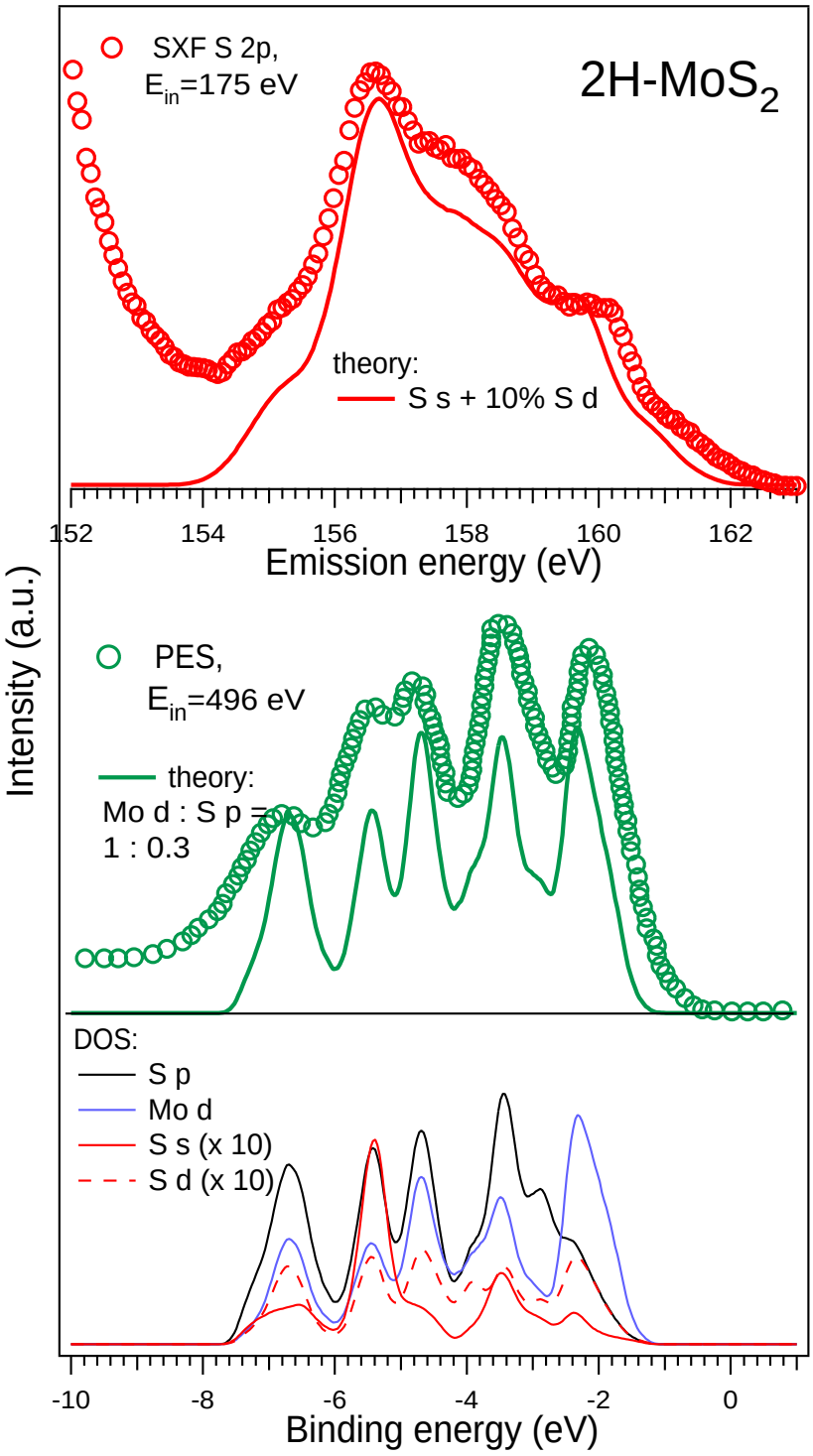

Figure 5.13: PES and non-resonant SXF spectra of bulk 2H-MoS_2 and spectra simulated based on the DFT band structure calculations (marks - experiment, lines - theory). The PES data reproduced from the [86]. The theoretical DOS is also shown: S s and S d DOS are 10 times magnified.

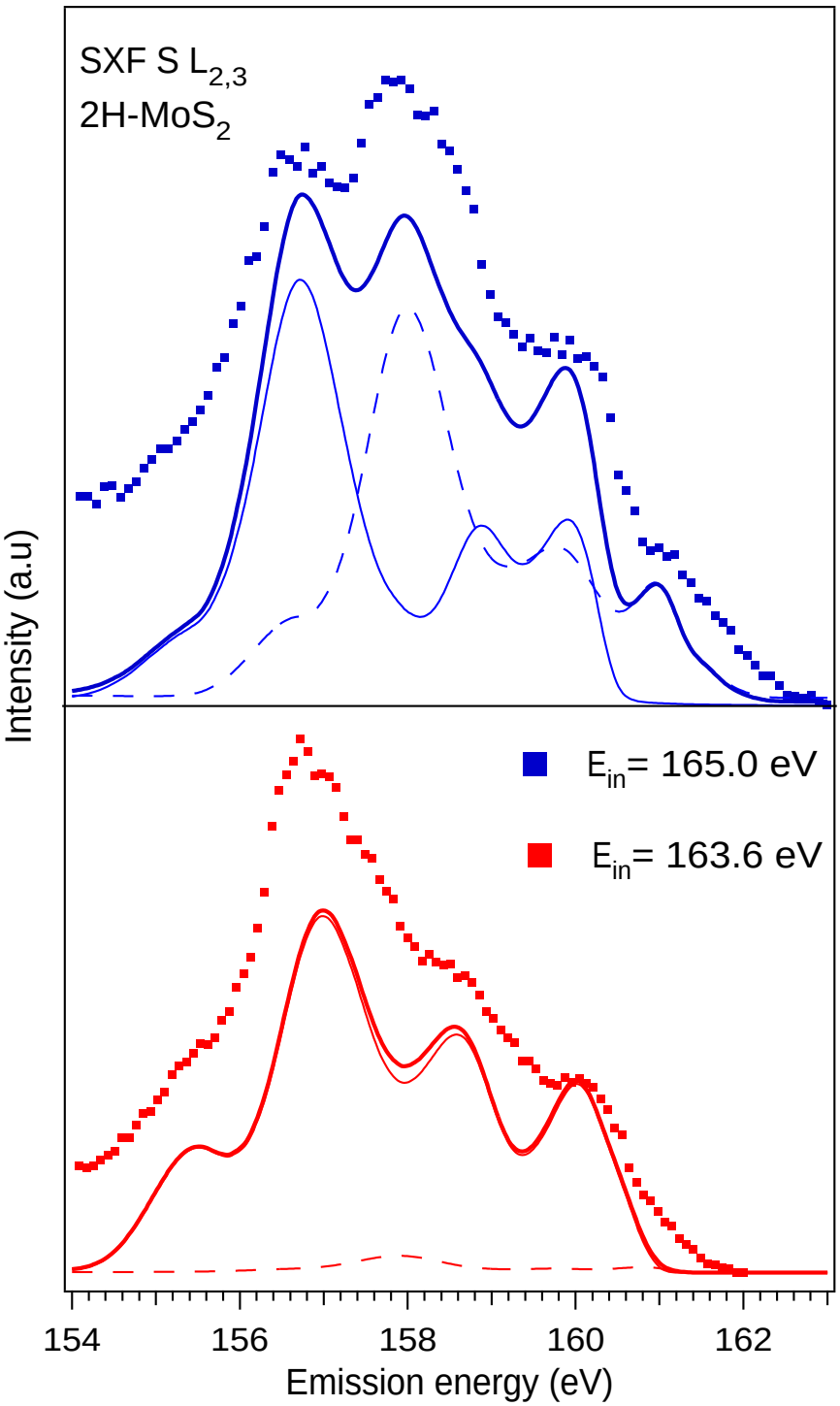

Figure 5.14: Resonant emission spectra measured at $\hbar\omega_{in} = 163.6$ eV and 165.0 eV of 2H-MoS_2 (markers are experimental data, solid line - simulations: thin line - L_3 contribution, dashed line - L_2 contribution).

states. Again, the bands generally exhibit weak dispersion and there is the second empty sub-band 4.2 eV above the top of the VB.

The states forming the VB and CB are S p, Mo d and I p states in this case. The photoelectron VB spectrum is shown in Fig. 5.16 together with the spectrum simulated based on local densities of states with the ratio Mo d : S p : I p = 1 : 0.3 : 0.2 according to the photoionization cross section. The shape of the PES is well reproduced, the width of the experimental spectrum is about 15% broader in energy than the DFT calculations predict.

The states which are observed in the SXS experiments are not very intense, while matrix elements and dipole selection rules made the experiment most sensitive to the sulfur states of s- and d-symmetry. Especially in the energy range 2 eV above the Fermi energy the density of s and d states of S is very low in the nanotubes. The intensity of d states relative to s states decreases compared to the bulk. As electron correlation effects are expected to be weaker for excitation far above the threshold, the non-resonant spectra were compared to the theoretical density of states.

The non-resonant SXF spectrum excited at 175 eV is shown in Fig. 5.16 together with S $L_{2,3}$ emission spectra simulated on the basis of the electronic structure for the skeleton structure corresponding to the $Mo_6S_3I_6$ stoichiometry. The theoretical emission spectrum calculated from the S s- and d-DOS (with the ratio 1:0.1) taking into account the energy dependence and intensities of the matrix elements is shown as a dashed red line. The values of the matrix elements for $Mo_6S_3I_6$ NTs were calculated by I. Vilfan (see Fig. 5.17) and are well fitted by the following functions (energy is in eV):

$$M_s = 0.0259 + 0.0004 \times (E - E_F) - 2.14e^{-5} \times (E - E_F)^2 - 4.38e^{-7} \times (E - E_F)^3 + 9.94e^{-9} \times (E - E_F)^4 + 2.24e^{-10} \times (E - E_F)^5 \quad \text{for the selection rule } \mathsf{l\text{-}1}, \tag{5.3}$$

$$M_d = 0.0269 + 0.0012 \times (E - E_F) + 3.34e^{-5} \times (E - E_F)^2 + 4.23e^{-7} \times (E - E_F)^3 \quad \text{for the selection rule } \mathsf{l{+}1}. \tag{5.4}$$

The theoretical spectrum resembles the experimental one by general shape. The width of the theoretical spectrum is about 30% less than the experimental one. In the case of bulk MoS_2, this discrepancy was only 16%. From the sulfur s- and d-DOS and adding 2.5% of Mo d DOS the similarity between the shape of the experimental non-resonant emission spectrum and the theoretical spectrum can be increased (red solid line). The black solid line is the resulting simulated spectrum (S s + 10%S d +2.5% Mo d) and stretching the energy scale. From the comparison of the stretched theoretical spectrum with the experimental one can see that the ratio between the high (161.2 eV) and low (156.7 eV) emission energy part can be reproduced. Nevertheless, the peak at 158.6 eV is overestimeted and the feature at 160.6 eV is not reproduced.

In Fig. 5.4 on page 54 the FY-SXA spectrum of bulk MoS_2 is compared to the theoretical absorption spectrum based on the ground state DFT calculations. The underestimation of the low energy absorption peak at 162.5 eV may be explained by the presence of the core hole which is not included in this approximation. But the general shape and the width of the experimental data are well reproduced. This implies that the electron correlation effects are not strong in bulk MoS_2.

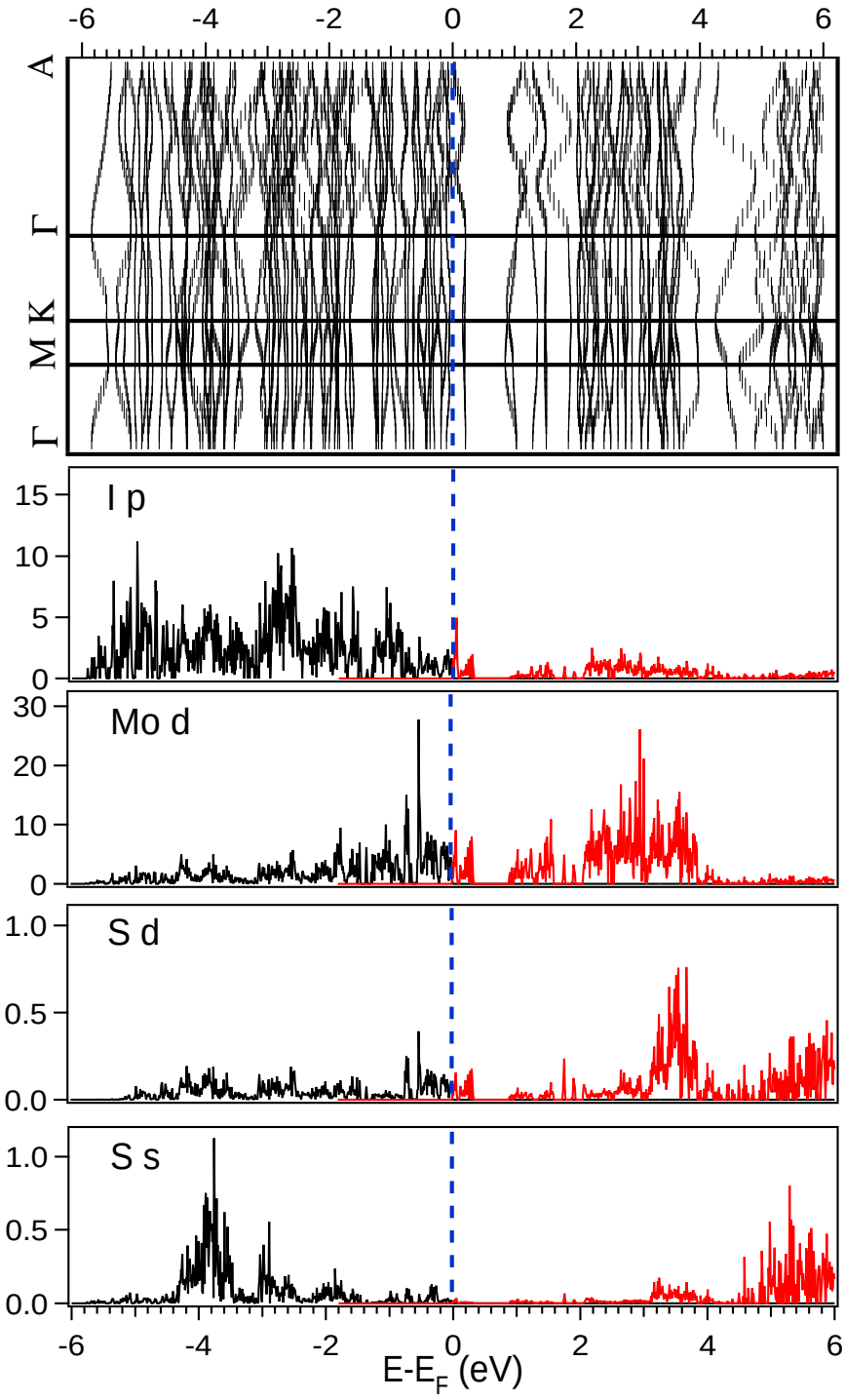

Figure 5.15: Band structures and S s, d and Mo d DOS calculated using the WIEN2k package for the structure shown in Fig. 5.2 on page 51. Dashed blue lines mark the top of the VB. Symmetry labels correspond to the hexagonal unit cell containing three $Mo_6S_3I_6$ nanowires, oriented parallel to the hexagonal c axis. The unit cell dimensions are a = b = 16.385 $\AA$ and c = 11.9230 $\AA$. The structure was calculated using an R3 space group, in which the wires are displaced relative to each other by 1/6 of the hexagonal lattice constant c [80].

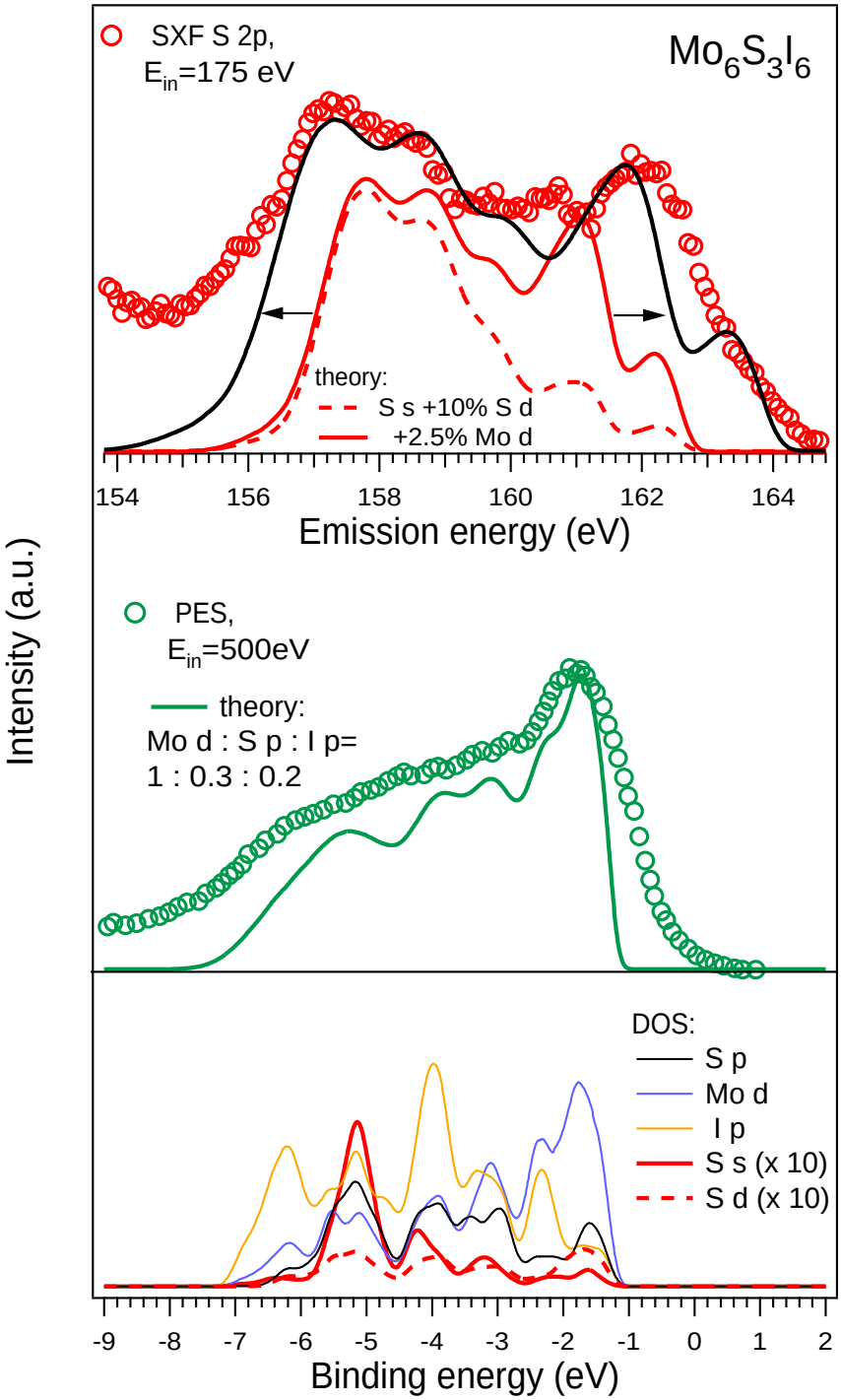

Figure 5.16: PES and non-resonant SXF spectra of $Mo_6S_3I_6$ NTs and spectra simulated based on the DFT band structure calculations (marks - experiment, lines - theory). The PES data are provided by D. Vbranic [88]. The theoretical DOS is also shown: the S s and d DOS are 10 times magnified. Black line is the simulated SXF spectrum (S s + S d + 2.5%Mo d) 30% elongated in energy scale.

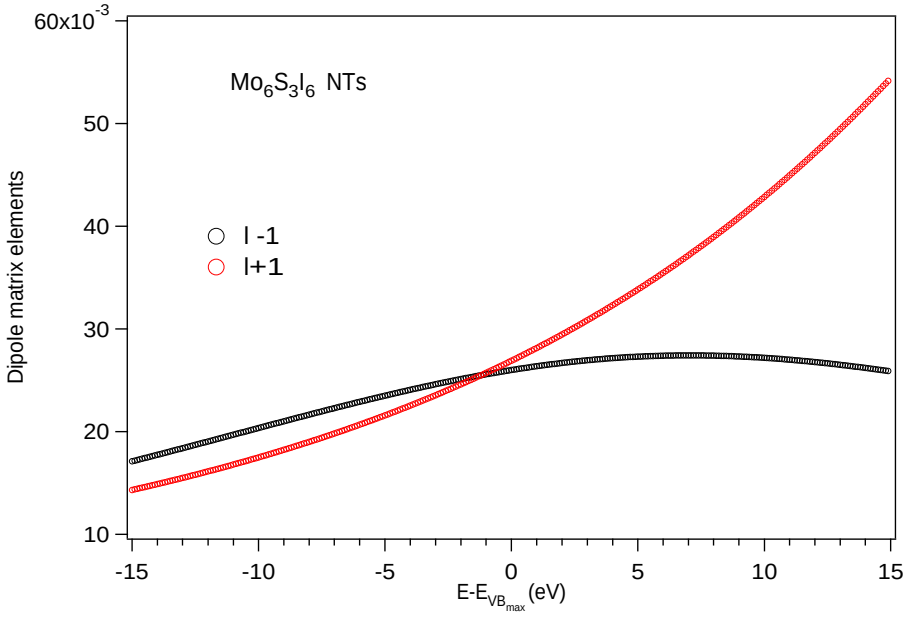

Figure 5.17: Dipole matrix elements calculated for the $Mo_6S_3I_6$ NTs by I. Vilfan.

In Fig. 5.18 the FY-SXA spectrum of $Mo_6S_3I_6$ NTs is compared with the S $L_{2,3}$ absorption spectra simulated on the basis of the different local partial unoccupied DOS calculated for this structure (shown as well). The lower density at the bottom of the CB ($E\text{-}E_F \geq 2.6$ eV, corresponding to 161.8 eV $\leq \hbar\omega \leq$ 163.6 eV in the absorption energy scale) compared to the top of the CB (2.6eV $\leq E\text{-}E_F \leq 4$ eV; 163.6 eV $\leq \hbar\omega \leq$ 166 eV) and the presence of the sub-gap ($E\text{-}E_F \approx 4.2$ eV; $\hbar\omega \approx 166.4$ eV) are reproduced. There is, however, a large disagreement between the theoretical curves and experimental data in this case. Two strong peaks in experimental SXA spectrum (at 163.4 and 164.5 eV) may correspond to the two peaks in the spectrum based on the sulfur d-DOS, but the energy of these states is about 1.7 eV higher relative to the bottom of the CB than experimentally measured.

There are some possible explanations of the disagreement between the experimental data and the theoretical results. First, due to the one-dimensional confinement the electronic states near the Fermi energy may become rather localized and the excited electron does not leave the system. The additional spectator electron may influence the system, so that the observed binding energies differ from the energies in the ground state. Furthermore, the influence of the core hole can be expected to be stronger in such a confined situation in comparison to the bulk MoS_2 case. The DFT calculation is also made for the system in its ground state and does not reproduce the excited state observed. Second, the material under investigation could contain other Mo-S components, like bulk MoS_2 or others. The measured spectra in this case are mixed with spectra from all sulfur contained impurities. The degree of tube-like material in the sample is currently under investigation.

In Fig. 5.19 the experimental RIXS spectra from $Mo_6S_3I_6$ excited at the photon energies marked by arrows in Fig. 5.11 on page 63 are shown. The main effects of

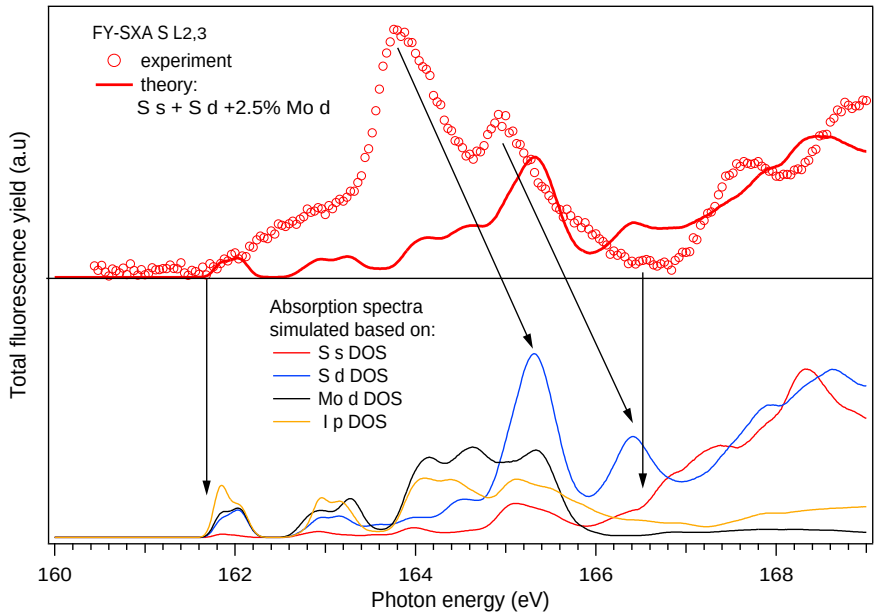

Figure 5.18: FY-SXA spectrum of $Mo_6S_3I_6$ and S $L_{2,3}$ absorption spectra simulated based on the DFT band structure calculations for the skeleton structure corresponded to the $Mo_6S_3I_6$ stoichiometry (marks - experiment, solid line -theoretical spectra). Arrows mark the features in the experimental spectrum which can be identificated with the features of the theoretical spectrum.

the resonant excitation experimentally observed for the $Mo_6S_3I_6$ NTs are the following: additional intensity arrears at $\hbar\omega_{out} > 162.3$ eV in the 164.7 eV excited spectrum, the intensity at this energy increases and broaden, for the spectrum at 165.5 eV, a further significant increase of intensity at $\hbar\omega_{out} < 159$ eV is appearent in the 165.9 eV excited spectrum. Similar to bulk MoS_2 the excitation energy dependence of the fluorescence spectra of the $Mo_6S_3I_6$ NTs may be explained by the interplay between two contributions related to the spin-orbit splitting of the S 2p core level. For instance, in the 165.9 eV excited spectrum an increase of intensity may be due to reaching the second sub-gap.

Although the RIXS spectra were not simulated on the basis of an electronic structure calculation, an interesting observation is made: the shape of the low energy excited spectra resemble the Mo d DOS (see blue line in Fig. 5.16 and red solid line in Fig. 5.19). Based on this similarity we propose that some kind of a non-local resonant inelastic scattering is observed at the excitation energies close to the threshold, similar to charge transfer excitations which are e.g. observed in vanadates [90]. As a majority of the states in the VB and CB close to the Fermi energy have strong Mo d character, the inelastic scattering occurs dominantly for those states. The enhancement of the fluorescence from certain S states which are strong hybridized with Mo d states may occur.

The electronic structure of the $Mo_6S_{4.5}I_{4.5}$ NTs has not been calculated yet. The RIXS spectra excited at the photon energies marked in Fig. 5.11 on 63 are shown in Fig. 5.20. There are some differences between the spectra from $Mo_6S_{9-x}I_x$ NTs for x=6 and 4.5. In the spectrum excited at 164.7 eV the intensity of the low energy part (155 eV $\leq$ E $\leq$

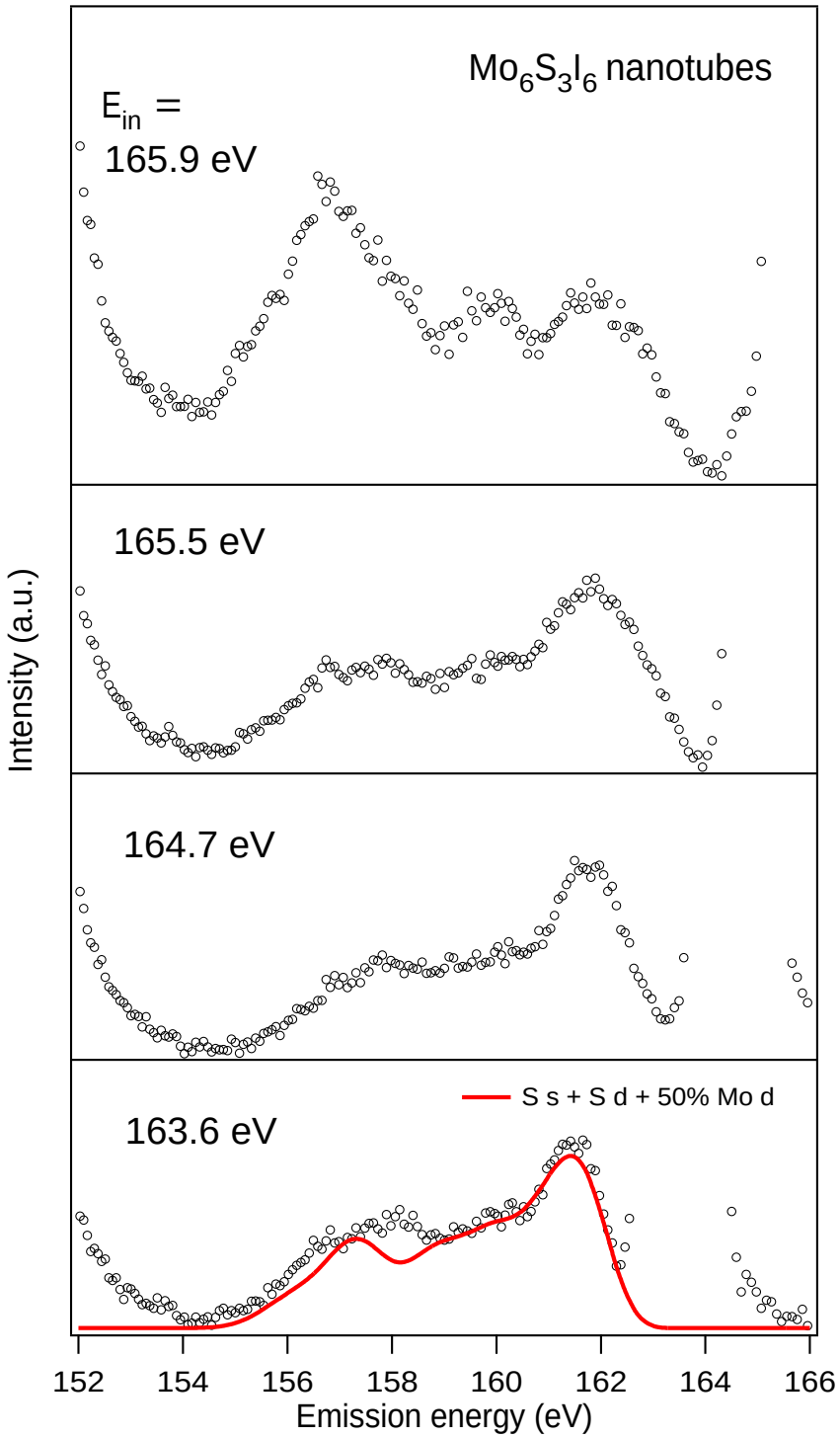

Figure 5.19: Resonant emission spectra of $Mo_6S_3I_6$ measured at photon energies marked in Fig.5.11 on page 63. Elastic peaks are clipped. Marks are the experimental data, red line is the sum of S s and d with 50% of Mo d DOS.

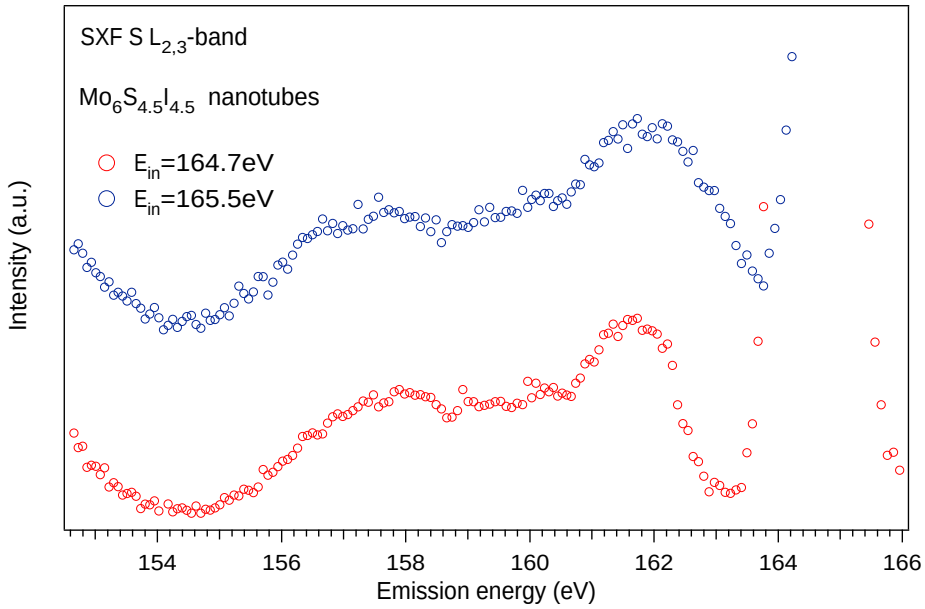

Figure 5.20: RIXS spectra of $Mo_6S_{4.5}I_{4.5}$ measured at energies marked in the Fig.5.11. Elastic peaks are clipped.

159 eV) increases in the spectrum of $Mo_6S_{4.5}I_{4.5}$ NTs relative to the intensity of the high energy peak compared to the corresponding spectrum of the $Mo_6S_3I_6$. SXF spectra of the $Mo_6S_{4.5}I_{4.5}$ NTs excited at 165.5 eV and 175 eV are very similar to the corresponding spectra of the $Mo_6S_3I_6$ NTs in shape, but about 0.2 eV broader. This can indicate a metallic character of the bond in those NTs.

Further work on the detailed explanation of the experimental result on $Mo_6S_{x-9}I_x$ is needed. Calculations of the electronic structure of the nanotubes in ground state and in excited state of the most realistic model structure in order to include electron correlation effects would be highly valuable. However, the treatment of both the full structure as well as correlation effects is a formidable theoretical challenge.

5.3 Conclusions.

The electronic structure of the small diameter Mo-S-I NTs differs significantly from the bulk material due to the modification of the geometrical structure. The most affected parameters are the bonding between the S and other atoms and presence of iodine atoms. In general, changes in the electronic structure of the $Mo_xS_yI_z$ NTs compared to the bulk material have the following tendencies:

1. The density of sulfur and hybridized to sulfur states at the bottom of empty band decreases and at the top of the occupied band increases.

2. The band structure of the NTs is characterized by weak dispersion, as a consequence, the shape of the experimental absorption and emission spectra are strongly influenced by electron correlation effects compared to the bulk material. Strong

electron correlation effects are observed in both absorption and fluorescence spectra of the NTs.

3. The band gap decreases in NTs compared to the bulk. For the $MoS_2I_{1/3}$ we could quantify the band gap as 0.4±0.2 eV. $Mo_6S_3I_6$ and $Mo_6S_{4.5}I_{4.5}$ appear to be metallic.

These tendencies are in agreement with the theoretical predictions. It is likely that the discrepancies between experiment and theory are due to correlation effects. Only in a 3 atoms cluster calculation we could include the effect of the core hole. Such a treatment would be desirable for realistic structurel models.

Chapter 6

Electronic structure of Sc compounds.

In this chapter the analysis of effects of the chemical bonding observed experimentally in the SXA and SXF spectra of Sc is presented. A set of Sc compounds was investigated where the local surrounding of the central Sc atom and the character of the bond is different. On the basis of the analysis of the electron density at the Sc site the chemical state of the Sc atom in $Sc_3N@C_{80}$ fullerene is evaluated.

6.1 Bonding in transition metal complexes.

Ionic crystals which contain transition metals (TM) may be considered as a set of linked polyhedrons according to the Pauling rules [91]: *A coordinated polyhedron of anions is formed about each cation, the cation-anion distance determined by the sum of ionic radii and the coordination number by the radius ratio.* The electronic structure of such crystals is in first approximation defined by the electronic structure inside the polyhedron. In the polyhedron the anions build a coordinated complex around the TM cation. The geometry of the anion coordination is determined by the bonding between the TM and the anions.

Bonding in TM complexes has a character different from ionic compounds like sodium chloride and from the covalent compounds like methane [91, 92]. Here ions/atoms are bonded via a two-center, two-electron bond, but both electrons stem from one of the atoms. This type of bond is known as a *donor-acceptor* or a *coordination* bond. In TM complexes the electron acceptor is a metal ion and a ligand is usually the donor for the bond. The properties of the complex are strongly dependent on the type of the ligand and the coordination geometry.

In this work the Sc complexes were investigated to clarify the ligand influence on the electronic structure in such complexes. In most of the studied complexes, the Sc ion has octahedral coordination (O_h) (see Fig. 6.1); ScB_2 is a bilayered material of AlB_2 type [93] with trigonal-prismatic Sc coordination; in $Sc(C_5H_5)_3$ (see Fig. 6.2) (read "cyclopentanienyl ", below marked as 5MR (5-Membered-Ring)) and in $Sc_3N@C_{80}$ the Sc ion is assumed to have a linear coordination of ligands . As ligands in O_h coordination single ions like F^{1-}, Cl^{1-}, O^{2-} and molecules $(NO_3)^{1-}$, $(CO_3)^{2-}$, $(SO_4)^{2-}$, $(CH_3CO{=}CHCOCH_3)^{1-}$

(read "acetylacetonate" (see Fig. 6.3), below marked as (acac)) were probed.

A general point about the bonding in TM complexes is the behavior of the orbitals participating in the bonding. The 3d orbital of the metal is much closer to the nuclei than either 4s or 4p orbitals. Though hardly core-like, the radial extension of the 3d orbital is not large and its overlap with ligand functions is correspondingly small. Another parameter defining the bonding is the energy of the contributing orbitals. Orbital energies for the metal in high oxidation states are expected to be ordered like following:

$$ligand\ donor\ function\ <\ metal\ 3d\ <\ metal\ 4s\ <\ metal\ 4p.$$

Based on both these grounds it is argued that the 4s metal orbital is a dominant contribution to the bonding. This orbital is spherically symmetric and the attractive forces are undirected. The ligand-ligand repulsive forces define the angular geometry of the complex in a very rough picture. Although 3d metal electrons do not play a significant role in the formation of the metal-ligand bond, they interact with the bonding electrons: the d electrons are affected by the bonding electrons and the bonding electrons are affected by the d electrons. The first effect is addressed by the crystal-field theory (CFT).

CFT considers the behavior of d electrons in negatively charged anionic environment which is typically simplified as an array of negative point charges. d electrons have to avoid each other and are repelled by the crystal field (CF). Depending on the symmetry of the CF the energy of d orbitals is raised and they split into groups according to their angular symmetry. For the octahedral CF, energies of orbitals oriented between the point charges in coordination planes (d_{xy}, d_{xz}, d_{yz} (t_{2g})) increase less than energies of orbitals oriented toward the point charges ($d_{x^2-y^2}$ and d_{z^2} (e_g)). In tetrahedral CF the picture is slightly different: the energy of **e** orbitals increases less than the energy of $\mathbf{t}_g$ orbitals.

The total energy splitting of orbitals may be estimated from

$$\delta \approx \frac{\langle r^4 \rangle}{R^{-5}} \tag{6.1}$$

where r is the radius of the d orbital and R is the metal-ligand internuclear distance [94]. A large crystal field splitting energy is provided by ligands with high negative charge and small radius, and by metal cations with a large oxidation number.

The energy splitting of the orbitals depends not only on the CF splitting parameter, but also on the inter-electron repulsion between the d electrons within the particular environment. The d-d electron repulsion is less in a complex then in the free ion (so called "nephelauxetic effect") due to the fact that the average distance between the d electrons is larger in a complex than in the ion. As 4s/4p metal orbitals are more penetrating close to the nucleus, an increased electron density on these orbitals due to the charge transfer from the ligand, causes this density to enter into the region between the nucleus and the d-orbitals. Consequently, the 3d electrons are more screened from the nucleus in complexes with larger electron donation from the ligand to the metal atom. This results in a decrease of the binding energy of d electrons and extension of their radial distribution. The nephelauxetic effect also depends on the ligand: the d-d repulsion decreases as more negative charge is transferred from the ligand to the metal ion.

Thus, the value of the CF splitting parameter is a measure of the interaction between the metal d electrons and their molecular environment. For a certain metal, ligands

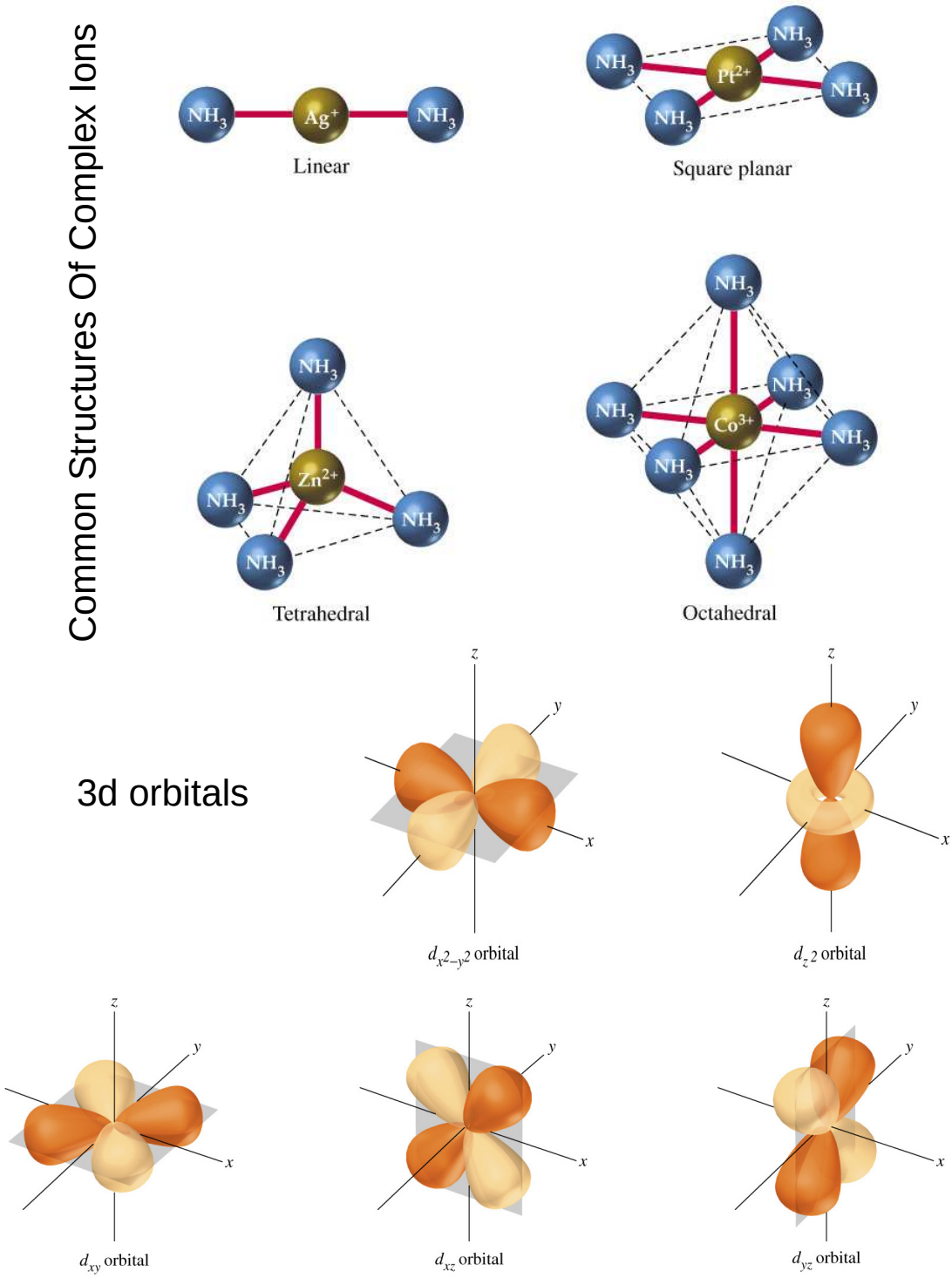

Figure 6.1: Top: The most common coordination structure of complex ions. Bottom: An angular distribution of atomic 3d orbitals. Reproduced from http://www.chem.utk.edu/yang/chap22a.ppt

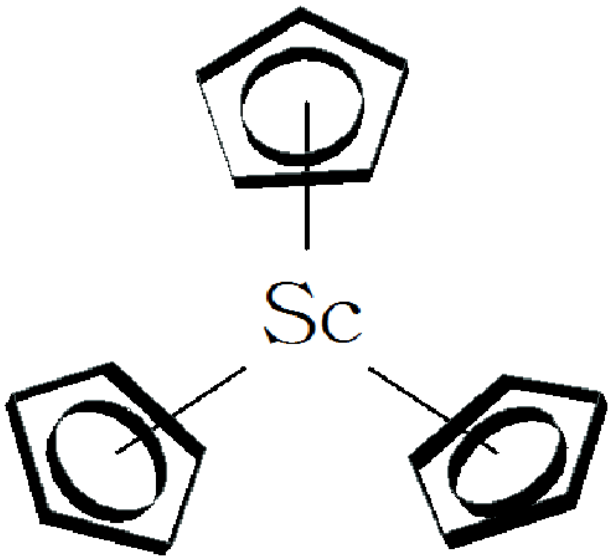

Figure 6.2: Structure of $Sc(5MR)_3$.

can be ordered according to the magnitude of the CF they create into the so called "spectrochemical series" [92]:

$$CF\ increasing\ \rightarrow$$
$$I^{1-} < Br^{1-} < Cl^{1-} < F^{1-} < O^{2-} < NH_3 < CO. \tag{6.2}$$

One can see that the splitting of the d orbitals strongly depends on the size of the ligand (it decreases with size, for the halogen ions for example r(F^{1-})=1.33$\mathring{A}$; r(Cl^{1-})=1.81$\mathring{A}$; r(Br^{1-})=1.96$\mathring{A}$; r(I^{1-})=2.20$\mathring{A}$ [91]) due to the changes of the bond length. Nevertheless, the experimentally observed fact that the negatively charged ligands cause less splitting of d orbitals than the neutral ligands (see Eq.6.2) is not easy to understand from the CF point of view. This is the point were the CF theory stops to explain the spectrochemical series due to the simplification of ligands as point charges. Another interesting observation is that the oxygen anion causes a larger energy splitting of d orbitals than the fluorine although it has slightly larger ionic radius (1.36 $\mathring{A}$) [91] and weaker electronegativity. Those effects are matter of a consideration of the bond formation between the metal and the ligand, as the MeO^6 polyhedrons are differently connected to each other compared to MeF^6.

To understand the ligand influence on the electronic structure of TM compounds the bonding in the complex may be regarded from the point of view of molecular orbital (MO) creation. As an example, the MOs of the TM complex with O_h coordination are considered below using the linear combination of atomic orbitals (LCAO) approximation. MOs are built from the metal orbitals (3d, 4s, 4d) and the ligand group orbitals (σ and π) which are combined s and p ligand orbitals classified according to the octahedral symmetry.

The schematic picture of the result of the combination of different ligand and metal orbitals into the bonding MO is shown in Fig. 6.4. MOs are constructed according to their symmetry and direction. Not all metal orbitals can build a σ bond with the ligand orbitals, for instance, d_{xy} does not match to any ligand group orbital and develops into

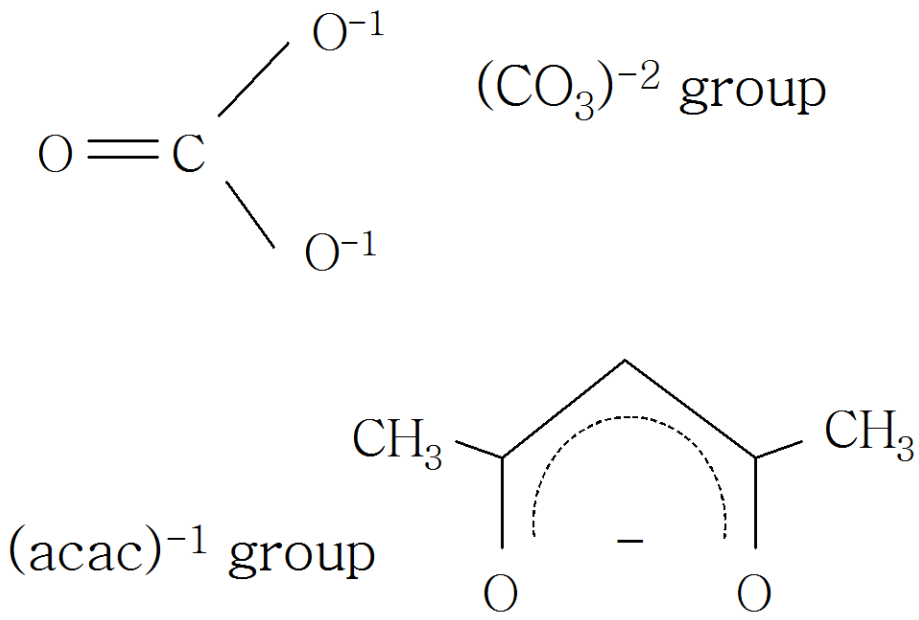

Figure 6.3: Structure of the CO_3^{1-} and $(acac)^{1-}$ ligand groups.

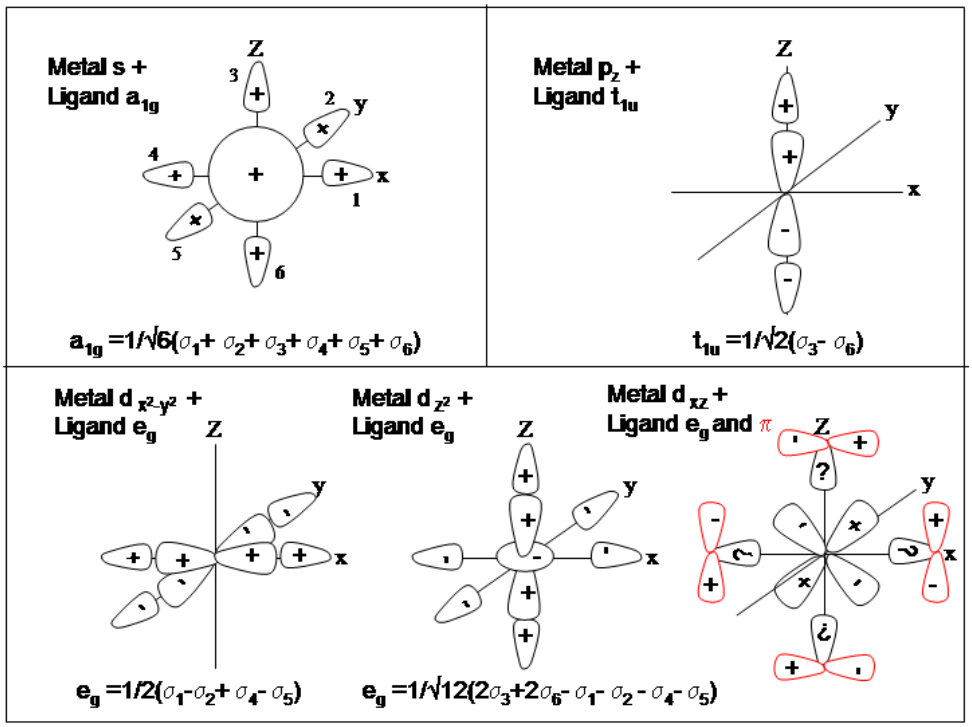

Figure 6.4: Interaction between the metal s, p and d orbitals and corresponding ligand σ and π group orbitals.

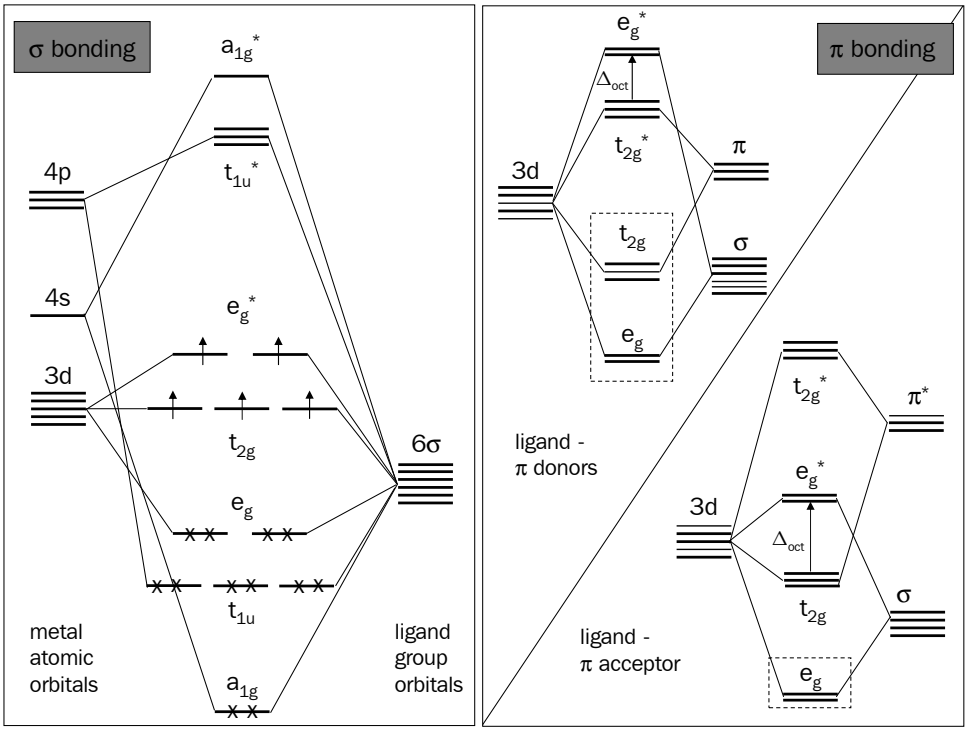

Figure 6.5: Schematic drawing of the metal-ligand σ and π bonding in O_h symmetry. Crosses and boxes marks MO with electron occupation from the ligand group, arrows - from 3d metal orbitals. Δ_{oct} marks the crystal field splitting parameter. Reproduced from [92].

the non-bonding t_{2g} MO in first approximation.

The schematic diagram of metal-ligand σ and π bonds in O_h symmetry and the electron occupation are shown in Fig. 6.5. Each ligand acting as a σ donor offers a lone pair of electrons, regardless of whether the ligand is formally negatively charged or neutral. These 12 electrons are shared by the metal and the ligand and marked by crosses. In addition to these electrons there are electrons originating from the d^n metal configuration (marked as arrows). According to the *Aufbau* principle, metal d electrons occupy the non-bonding t_{2g} and antibonding e_g^* orbitals. Thus the lowest six MOs provide an account of the bonding via *attractive forces* between the metal and ligands. The higher five MOs originate from the d metal atomic states and their interaction with the 2p hole is the matter of consideration in the CF theory. These electrons are *repelled* by the ligands. These orbitals are moved to higher energy for increasing interaction with the ligand. This understanding gives insight into the spectrochemical series by noting that the energy splitting of both bonding e_g and antibonding e_g^* orbitals are closely related to the ability of the ligand to donate electrons into the complex.

Significant π bonding occurs between metal t_{2g} orbitals and p-like ligand orbitals normal to the local metal-ligand vector due to the symmetry (see ligand orbitals in red in Fig. 6.4). On the right side of Fig. 6.5 two diagrams for the π bonding are shown, for the case of ligand as π donor and as π acceptor. For the π donor ligand the greater increase in energy of the e_g^* orbital compared to t_{2g}^* is explained by the stronger antibonding

interaction (overlapping) of metal orbitals with σ than with π ligand orbitals. In CFT the same splitting of the d electrons are due to the different direction of the d orbitals to the point changes (toward or between). The energy splitting (Δ_{oct}) is less for a ligand which is both σ and π donor than for a pure σ donor: greater σ bonding increases the energy of the e_g^* MO, while greater π bonding increases the energy of the t_{2g}^* MO and hence decreases Δ_{oct}. This trend is responsible for the ordering in the specrochemical series where halogens provide smaller Δ_{oct} than the π-neutral ammonia ligand (Eq. 6.2).

An ordering in MOs for the ligand π acceptor is different and the Δ_{oct} is associated with the energy gap t_{2g}-e_g^*. The greater the π acception of the ligand the lower the energy of the t_{2g} MO and the greater Δ_{oct}. The position of the CO ligand in the higher end of the spectrochemical series is ascribed to their strong π-accepting role in the complex. Overall, consideration of the bonding in the TM complexes from the point of view of molecular orbitals predicts that Δ_{oct} will be smaller for π donor ligands and larger for π acceptor ligands than in π neutral species. This is in agreement with experimental observations.

From above, the detailed consideration of the formation of the MO in coordinated compounds is helpful in understanding their electronic structure: in general, the CF splitting parameter should be considered as a parameter of the whole system including the metal configuration, the ligand type and the bonding character between them.

Although d orbitals overlap little with the ligand orbitals in TM complexes, they influence the metal-ligand bonding. Apart from the repulsion of d electrons by bonds, they affect in turn the bonds: all d electrons repel the bonding electron density. The efficiency of this interaction depends on the geometry and position of d orbitals: for instance, for metal ion in O_h coordination the t_{2g} orbitals are more weakly influenced by this effect than the e_g orbitals due to direction of the last one toward ligands. This can explain the experimentally observed increase of the bond length with the number of d electrons in TM complexes [92].

As electron density on the Sc site is strongly influenced by the molecular surrounding due to the interaction of 3d electrons with the ligand states, the chemical-sensitive and atom-selective methods of SXS are well suitable to probe any modifications in the local Sc surrounding and the Sc−ligands bonging.

6.2 Correlation effects in X-ray absorption spectra.

The measurements presented here were carried out at the U49/2-PGM1 beamline and the Russian-German beamline (RGBL) at BESSY (Germany). The SXA spectra were recorded by TEY, FY and transmission detection modes depending on the sample. Photon energies in the range of the fine structure of absorption spectra were calibrated using the known positions of the 1s $\rightarrow \pi^*$, v=0 transition (400.88 eV) in the spectrum of N_2 [95] and the first narrow peak (683.9 eV) in the F 1s absorption spectrum of K_2TiF_6 [96]. The beamline primary photon energy resolution was 60 meV at Sc 2p absorption edge.

The experimentally obtained Sc 2p SXA spectra of different Sc compounds are shown in Fig. 6.6. Both surface sensitive TEY-SXA and bulk probing FY-SXA spectra are plotted for the direct comparison for every sample except Sc_2O_3 (the FY-SXA spectrum was not measured). Some FY-spectra may suffer from the saturation effects due to the

Sample	pos. a	FWHM a	pos. b	FWHM b	pos. a*	FWHM a*	pos. b*	FWHM b*
ScF_3	402.56	0.20	404.37	0.21	406.81	0.17	408.59	0.29
$Sc(NO_3)_3$	401.97	0.28	403.70	0.32	406.16	0.31	407.89	0.48
Sc_2O_3	401.86	0.17	403.59	0.25	406.11	0.21	407.82	0.42
$Sc(5MR)_3$	401.90	0.18	403.55	0.27	406.10	0.24	407.77	0.45
$ScCl_3$	401.88	0.18	403.56	0.20	406.07	0.21	407.73	0.35
$Sc_2(SO_4)_3$	402.22	0.26	403.86	0.28	406.37	0.33	408.03	0.41
$Sc_2(CO_3)_3$	402.04	0.36	403.70	0.29	406.19	0.26	407.82	0.47
ScB_2	402.09	0.41	403.72	0.28	406.28	0.40	407.90	0.47
$Sc(acac)_3$	401.98	0.50	403.50	0.55	406.18	0.40	407.73	0.69
$Sc_3N@C_{80}$	402.10	0.52	403.52	0.41	406.32	0.36	407.74	0.58
Sc			402.26	1.47			406.69	1.95

Table 6.1: Spectroscopic characteristics from SXA spectra of Sc compounds. The experimental error is estimated to be ±0.06 eV. The decomposition precision is estimated to be ±0.05 eV.

uncertainty in the sample thickness and the geometry of measurements. ScF_3 and Sc metal were thermally evaporated *in situ* onto a Cu substrate directly before measurements, $Sc_3N@C_{80}$ was grown on a Si-wafer, the rest of samples were powders. Some of the samples are expected to be unstable in air or under photon radiation. For those samples SXA spectra were measured several times at different positions of the beam.

The results are shown in Fig. 6.6. SXA spectra measured in two modes differ from each other most significantly for $ScBr_3$. In this work the influence of the ligand nature reflected in the experimental spectra are discussed, concentrating on such characteristics of the spectra as energy splitting of the main peaks (representing the CF splitting parameter, described in the previous section) and the energy width of the peaks. Every spectrum was decomposed into individual peaks and their characteristics were compared. Corresponding peaks in FY and TEY spectra had the same parameters in the peak fitting procedure and the average (from FY and TEY) value is used for further analysis. There is a significant difference between the TEY- and FY-SXA spectra of $ScBr_3$ which can be due to radial damages of the sample. This material is not discussed further.

SXA spectra from Sc compounds have a general shape which consists of three groups of peaks: weak peaks or a shoulder at low photon energies and two groups of a similar "two-peak" structure. The structure represents the electron transitions to the empty d states from $2p_{3/2}$ and $2p_{1/2}$ core levels, the energy shift between two groups corresponds to the spin-orbit splitting of the 2p levels. Two peaks inside the group correspond to the transitions to d orbitals of different energy. The energy of the intermediate states is defined by the CF and by the bonding to the ligand (**a** and **b**; **a*** and **b***). The absorption peak at lower photon energy in the group (**a** and **a***) corresponds to the d orbital which interacts weakly with the ligand orbitals. The absorption peak at higher photon energy in the group (**b** and **b***) corresponds to the d orbital which interacts strongly with the ligand orbitals. For metal Sc the SXA spectrum resembles the unoccupied DOS (see below Fig.

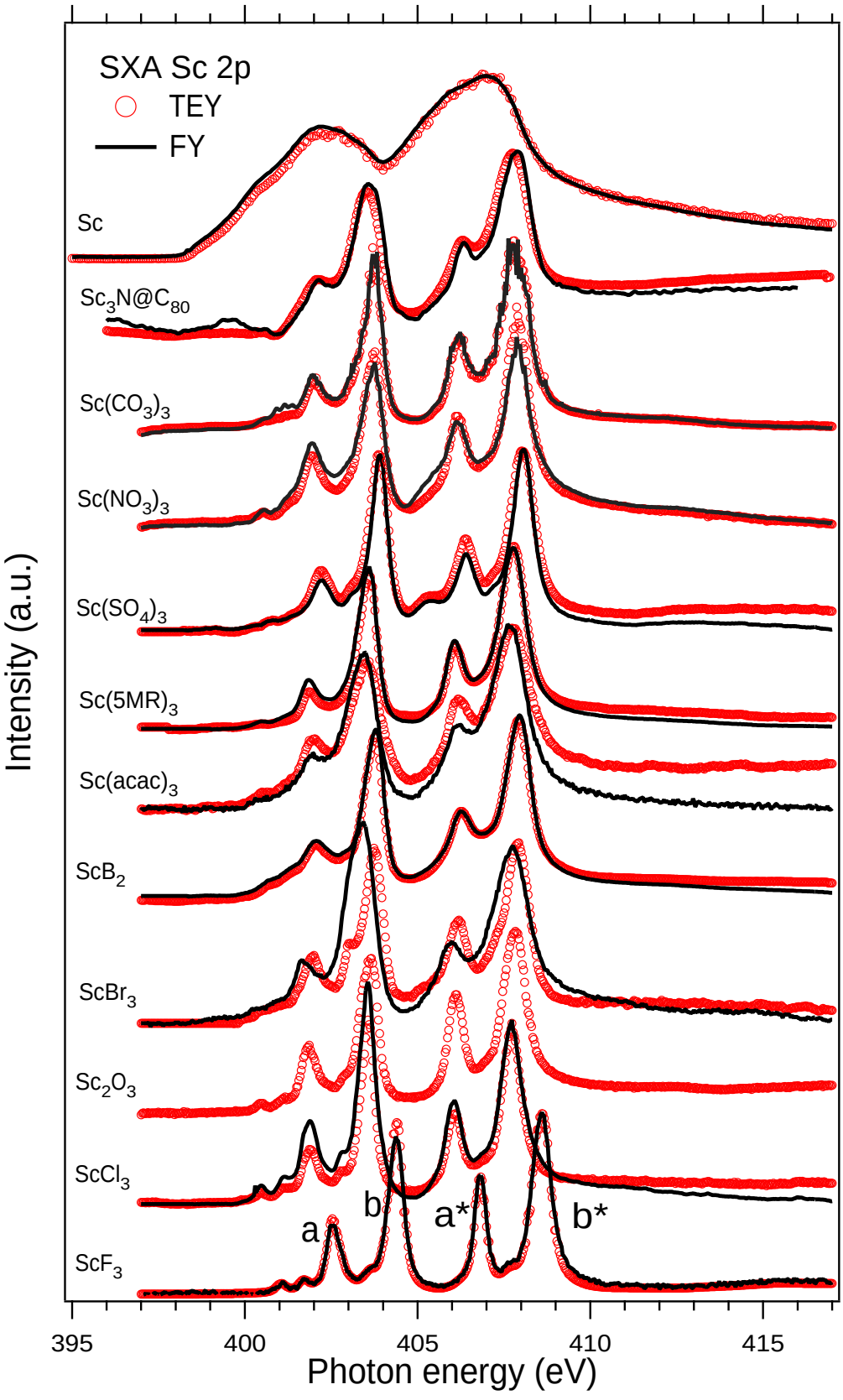

Figure 6.6: TEY-(circles) and FY-SXA (solid lines) spectra of different Sc compounds.

Sample	CG (eV)	a-b (eV)	a*-b* (eV)	I(b*/b)	I(a*/b*)	Atom	EN
ScF_3	408.11	1.81	1.77	1.06	1.63	F	3.98
$Sc(NO_3)_3$	407.50	1.73	1.72	1.19	2.20	N	3.04
Sc_2O_3	407.42	1.73	1.71	1.22	1.66	O	3.44
$Sc(5MR)_3$	407.51	1.65	1.67	1.23	2.83		
$ScCl_3$	407.37	1.68	1.66	0.94	2.23	Cl	3.16
$Sc_2(SO_4)_3$	407.63	1.64	1.66	1.02	2.47	S	2.58
$Sc(CO_3)_3$	407.53	1.66	1.63	1.17	2.51	C	2.55
ScB_2	407.49	1.63	1.62	1.07	2.53	B	2.04
$Sc(acac)_3$	407.42	1.51	1.56	1.29	2.25		
$Sc_3N@C_{80}$	407.50	1.42	1.42	1.15	3.03		

Table 6.2: Spectroscopic characteristics from SXA spectra of Sc compounds and characteristics of the some atoms in the ligand group. CG is the energy position of the center of gravity of the SXA spectrum. EN is the electronegativity [91]. The experimental error is estimated to be ±0.06 eV.

6.7.).

From Fig. 6.6 one recognizes that the SXA spectra change depending on the ligand. The characteristics of the experimental SXA spectra are listed in Tables 6.1 and 6.2.

Based on present spectroscopic data the ligands can be ordered according to the position of the center of gravity of the L_2 absorption band as following:

$$\begin{aligned} &photon\ energy\ decreasing\ \rightarrow \\ &F^{1-} > S0_4^{2-} > CO_3^{2-} \approx NO_3^{1-} \approx (5MR)^{1-} \\ &\approx fullerene \approx B^{1-} > O^{2-} \approx (acac)^{1-} > Cl^{1-}. \end{aligned} \tag{6.3}$$

The low energy shift corresponds to the decrease of the ionicity of the Sc-ligand bond in absence of effects of CF and d–d interactions. The ionicity of the bond between two atoms can be estimated as:

$$percent\ ionic\ character = 1\ -\ e^{0.25\times\Delta\chi} \tag{6.4}$$

where $\Delta\chi$ is the difference between values of the electronegativity of atoms. The order of the complex ligands may correspond to an effective charge on the connecting ion due to the bonding inside the ligand.

Looking closer at the spectral characteristics one sees that other most noticeable modifications are changes of the width of the peaks and the a – b energy splitting. The energy splitting and the width of the absorption peaks reflect the parameters of the bonding between the Sc ion and the ligands. The electronic structure is strongly influenced by the geometry of the complex. Any non-perfection of the polyhedron can cause changes in the spectral shape and the energy position of the peaks. To identify such effects theoretical calculations have to be provided. The present analysis is made assuming the perfect coordinated polyhedrons in the Sc complexes.

Taking into account the experimental error due to the limited photon energy resolution the studied ligands can be organized into several series according to the changes of different parameters of L_2 absorption line like following:

$$a^* - b^* \text{ energy splitting decreasing} \rightarrow \tag{6.5}$$
$$F^{1-} > NO_3^{1-} \approx O^{2-} > (5MR)^{1-} \approx Cl^{1-} \approx S0_4^{2-} \approx CO_3^{2-} \approx B^{1-} > (acac)^{1-} > full,$$

$$a^* \text{ width increasing} \rightarrow \tag{6.6}$$
$$F^{1-} < Cl^{1-} \approx O^{2-} \approx (5MR)^{1-} \approx CO_3^{2-} < NO_3^{1-} \approx S0_4^{2-} \approx full < B^{1-} \approx (acac)^{1-},$$

$$b^* \text{ width increasing} \rightarrow \tag{6.7}$$
$$F^{1-} < Cl^{1-} < S0_4^{2-} \approx O^{2-} < (5MR)^{1-} \approx CO_3^{2-} \approx NO_3^{1-} \approx B^{1-} < full < (acac)^{1-}.$$

In general, several observations can be made. First, the fluorine ion causes the strongest ligand field where Sc 3d electrons suffer most pronounced correlation effects, not in agreement with the spectrochemical serie (Eq. 6.2) and recent publication [49]. Second, an energy splitting of the d-orbitals in compounds with single halogens as ligands can be correlated with their electronegativity. The increase of the width of the peaks in oxide compared to fluoride and chloride needs detailed considerations. Third, the effective charge of the oxygen ion, the structure of the ligand group and an interaction between the scandium ion and the whole ligand group are possible reasons for the changes in characteristics of absorption spectra.

6.2.1 Complexes with octahedral coordination.

In complexes with O_h coordination peaks **a** and **a*** in SXA spectra correspond to the electron transitions into the states with t_{2g} symmetry and **b** and **b*** peaks correspond to the transitions into the states with e_g symmetry.

Single halogens as ligands: F^{1-}, Cl^{1-}, O^{2-}.

From the comparison of spectra of ScF_3, Sc_2O_3 and $ScCl_3$ one can see that the there are two main tendencies. First, the energy splitting of the peaks a and b (a* and b*) decreases from the ScF_3 to the $ScCl_3$ consistent with the increase of the ionic radius of the ligands (which causes the increase of the bond length between the Sc and the ligand and is related to the decrease of the electronegativity of the ligand) (see Tables 6.2 and 6.3). This disagrees with previous experimental observations summarized in the spectrochemical series 6.2. The smaller t_{2g} - e_g energy splitting and the broadening of the peaks in SXA spectra of Sc_2O_2 compared to ScF_3 was observed early by de Groot [49]. The SXA spectra were successfully simulated based on the multiplet atomic calculation assuming a weaker CF in oxide than in fluoride taking into account solid state effects.

Second, the width of the peaks increases in oxide compared to fluorine and chlorine. The second effect can not be explained from the simple consideration of the parameters of the Sc-ligand bond.

Ligand	Ionic radius ($\mathring{A}$)	Bond length ($\mathring{A}$)	Bond ionicity (%)
F^{1-}	1.33	2.01	92
O^{2-}	1.36	2.11	73
Cl^{1-}	1.81	2.58	53
N^{3-}	1.48	1.99	54

Table 6.3: Parameters of the bond between the scandium ion and simple halogens as ligands [91, 97, 98, 99, 100].

Looking closely at the parameters of the SXA spectra one can see that the width of the high energy peaks of oxide increases more than the width of the low energy peaks. This observation can have different explanations but it is obvious that the width of the peaks is determined by the interaction between the atomic orbitals of scandium and ligand: the low energy peaks change less as the corresponding t_{2g} orbitals are directed between ligands and do not overlap strongly with the MOs in contrast to the e_g orbitals which are more affected by changes in the bonding MOs. The increase of the width of the high energy peaks in oxide may be related to more effective charge transfer from the 2p valence state of oxygen ion than from the other ligands due to a more effective interaction between Sc 3d states with oxygen 2p states than with the chlorine 3p states. Other possible explanation is the deformation of the octahedral coordination of the Sc ion in the oxide and changing of the Sc-oxygen bond length in one direction. To clarify reasons for the above spectral changes in the absorption spectra of Sc complexes detailed theoretical calculation of the MOs and simulations of the SXA spectra are needed.

Complex ions as ligands: NO_3^{1-}, CO_3^{2-}, $S0_4^{2-}$, $(acac)^{1-}$.

From the series 6.7 and 6.8 one can see that the width of peaks b* for the compounds with the complex ligands connected to the Sc through the oxygen atom does not change significantly compared to the oxide except for $Sc(acac)_3$, where peak a* becomes broadened relative to the oxide.

The t_{2g} - e_g energy splitting is consistent with the change of the electronegativity of the central atom in the ligand complex (N > S > C). Due to the increasing difference in the electronegativity the ionicity of the bond between the oxygen atom and the central atom of the complex increases, the effective charge between them moves closer to the oxygen atom. The broadening of peak a* may be related to the increase of the covalent radius of the central atom in the ligand (C ≈N ($0.7\mathring{A}$) < S (1.0 $\mathring{A}$)) and the increase of the size of the whole ligand complex.

The ligand causing the most drastic modification of the spectrum in this group is $(acac)^{1-}$: it is a didentate ligand (occupying with two oxygen atoms two sites in the octahedral coordination of the Sc atom) and builds the perfect octahedral coordination [101]. It can be compared to the CO_3^{2-} as the bridging oxygen atom bonded to the carbon atom in the ligand: both the a*-b* splitting and the width of peaks change. It should correspond to the increase of the size of the group and reduction of the effective negative charge on the connecting oxygen atom in $(acac)^{1-}$ compared to the CO_3^{2-} group (see Fig. 6.3).

6.2.2 Complexes with non-octahedral coordination.

The increase of the energy and the energy splitting of the d orbitals strongly depend on the environment, particular on the symmetry of the crystal field. For instance, for the same metal and the same bond length, the energy splitting of the d orbitals caused by the certain ligand in the octahedral coordination is more than in the tetrahedral coordination ($\delta_{tet} = 4/9\ \delta_{oct}$) [92]. That is why the modification of the d orbitals of the Sc ion in non-octahedral coordination cannot be directly compared to the oxide. $Sc(5MR)_3$, ScB_2 and $Sc_3N@C_{80}$ could be compared to each other as Sc in those complexes has a ligand coordination close to linear. From this general consideration one can expect that d orbitals split into two main groups: one, directed in one coordination axes toward the ligand group and the rest, directed between the ligands. In SXA spectrum the low energy peak would correspond to the last group, the high energy peak would correspond to the d orbital directed to the ligand.

Sc in diboride has 6-coordination of B. The CF has a well defined symmetry and the energy of the Sc d orbitals would increase as:

$$\begin{aligned} &orbital\ energy\ increasing \rightarrow \\ &d_{xy}, d_{x^2-y^2} < d_{xz}, d_{zy} < d_{z^2}. \end{aligned} \tag{6.8}$$

The low electronegativity of the B atom (2.0 Pauling units) [91] and the large Sc-B distance of 2.34 $\mathring{A}$ may be a reason for a weak generated CF (see serie 6.6). The large width of the absorption peaks (see series 6.7 and 6.8) must indicate the strong covalent character of the bond in ScB_2.

In fullerene Sc is bonded to a 5MR of the fullerene cage and to a nitrogen atom. The absorption spectrum of fullerene can contain two different absorption structures. The binding energies of Sc $2p_{3/2}$ and N 1s in the fullerene was measured by XPS [102] ([30]) and are equal to 400.9 (401.2) and 396.4 eV (396.9 eV), respectively. The band gap in this fullerene is estimated to be 0.8 eV from the offset of the ultraviolet-visible-near infrared spectra [102], 1.0 eV from the He I photoemission measurements [30] and about 2 eV from theoretical calculations [31]. Based on the XPS data one can expect Sc 2p absorption edge appearing between 400.9 eV and (401.2 + 2=)408.2 eV and N 1s absorption edge between 396.4 eV and (396.9+2+5=)403.9 eV (2 eV for the maximum possible band gap value and 5 eV for the possible position of the nitrogen empty states above the minimum of the CB). From the present SXA measurement the position of the Sc 2p absorption edge is difficult to define due to the atomic-like effects in the absorption spectra. Concerning the N 1s edge, it can be seen in Fig. 6.6 that the TEY-SXA spectrum of the fullerene does not have any noticeable feature at the photon energy range estimated above. The FY-SXA spectrum of the fullerene has a peak-like feature at the photon energy of about 399.57 eV which can be identified as a nitrogen absorption feature. The absent of the corresponding peak in the TEY-SXA spectrum might be due to the enchantment surface sensitivity of this mode. The photoabsorption cross section of Sc 2p and N 1s core levels are equal to 2.5 Mb and 0.7 Mb, respectively [87]. As far as there are three scandium atoms to every nitrogen atom in the fullerene, assuming roughly equal fluorescence yield for the core hole decay of Sc 2p and N 1s, the intensity ratio between the Sc 2p and N 1s FY-SXA spectrum is estimated to be 11:1. The SXA spectrum recorded by Alvarez et al.

[30] has also the feature about 398.8 eV which might be seen as originating from the N 1s absorption as it is not observed in the SXA spectrum of $Sc_2@C_{84}$. Unfortunately, no comments are made in the publication concerning this fact.

The N 1s absorption should be also observed in $Sc(NO_3)_3$. As the nitrogen in NO_3^{1-} ion has 3+ charge, the binding energy of the 1s core electron is shifted to the higher energies in this case by several eV. The energy position of the strong N $2\pi^*$ resonance observed in $NaNO_3$ is equal to 405.5±0.2 eV as measured by SXA [103]. As the NO_3^{1-} ion can be regarded as quasi-isolated molecularlike group, the binding energy of the N 1s electron does not change significantly in the Sc nitrate compared to the Na nitrate and the peak corresponding to the N 1s absorption must be observed at the photon energies close to the 405.5 eV. Indeed, there is a shoulder at 405.2 eV in the SXA spectrum of $Sc(NO_3)_3$ which may be the N 1s absorption feature.

The geometrical structure of $Sc_3N@C_{80}$ was measured by X-ray diffraction [102]. From this study it is known that the shortest Sc–N and Sc–C distances are equal 1.966 $\mathring{A}$ and 2.188 $\mathring{A}$, respectively. The electronegativity of the N is comparable to the chlorine, the ionic radius of N^{3-} (1.48 $\mathring{A}$) is smaller than the radius of Cl^{1-} ion.

The increase of energy of the Sc d orbitals according to the simple consideration of the bond formation in the Sc_3N cluster ($\sigma = N(sp^2)+S(d)$) has the same order as in ScB_2. The bond to the carbon cage may be realized via a π-bonding to the C 2p orbitals and should be weaker than the σ-bond to the nitrogen. The broadening of the peaks in SXA spectrum of fullerene indicates, first, the complex splitting of Sc d orbitals in combined CF generated by the nitrogen and the cage (which cannot be resolved in presented measurements) and, second, strong overlap between the Sc d orbitals and carbon or nitrogen orbitals. The smallest splitting of the symmetry related peaks (a and b) is the sign of the weakest CF, caused by the nitrogen and the carbon cage.

In $Sc(5MR)_3$ the CF is symmetric and the bonding is realized by Sc d orbitals and carbon 2p orbitals, the last, probably, acting as a strong π-acceptor. The splitting of the peaks is rather strong and the peaks are rather narrow. These observations indicate that in this compound the (5MR) causes rather strong CF.

The further quantitative analysis should be based on more detailed theoretical calculations of the MO formation in the ground and excited states in each particular Sc compound.

6.2.3 Sc metal.

The need to prepare Sc metal film *in situ* in ultrahigh vacuum can be realized from the comparison of absorption spectra in Fig. 6.7. As Sc oxidizes very fast in air, to prove the purity of the metal another sample was prepared as a thin film by electron-beam evaporation onto a 900$\mathring{A}$ thick Ti film and measured by transmission at the Russian-German beamline (BESSY) additionally. From the comparison of Sc 2p SXA on metal one can see that they are very sensitive to vacuum conditions under which Sc films are prepared. Spectra measured 10 min after the preparation in both TEY and FY modes are similar to the one obtained by the SXA in transmission detection mode in ultrahigh vacuum conditions and thus represent true Sc spectra. After 50 min in the photon beam at a pressure of 2×10^{-8} mbar the sample is clearly oxidized.

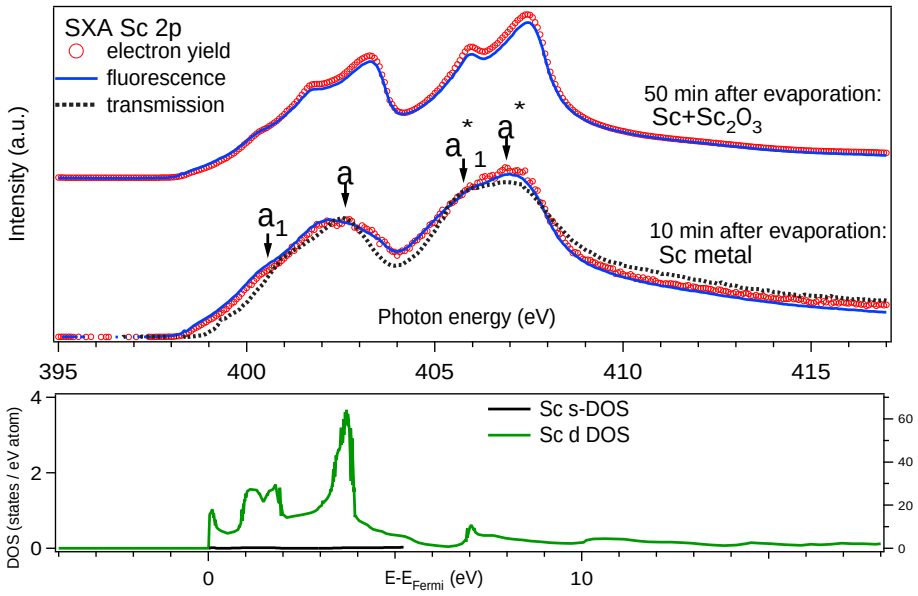

Figure 6.7: Top: TEY-SXA (circles) and FY-SXA (solid line) spectra of the fresh prepared layer of Sc (after 10 min, for the transfer from the preparation chamber through the vacuum) and 50 min under the photon radiation in 10^{-8} mbar. The SXA spectrum measured by the transmission mode at 10^{-9} mbar (dots) is shown for comparison. Bottom: Theoretical density of d states in hexagonal Sc [104].

The CB of Sc is formed by the d states near the Fermi energy while 5eV above the Fermi energy the hybridized 4s and 4p states dominate. As the transition probability from the 2p state to the 4s and 4p states is much smaller than to the 3d states and the density of states of the 4s band is considerably lower than that of the 3d band, the structure of the $L_{2,3}$ absorption spectrum is more closely related to the empty 3d states [105]. Two main absorption bands are caused by the $2p_{3/2}$ and $2p_{1/2}$ electron transitions to empty 3d electron states. Peaks a_1 and a_1^* correspond to the feature in the empty DOS at 1 eV$\leq E_{bin} - E_{Fermi} \leq$2 eV, peaks a and a* correspond to the feature at 3 eV$\leq E_{bin}$-$E_{Fermi} \leq$4 eV (E_{bin} is the binding energy of electrons, E_{Fermi} is the Fermi energy), the shoulder at 399.4 eV may correspond to the states at the Fermi energy. The obtained Sc 2p absorption spectrum of Sc metal correlates well in its spectral shape with that obtained previously by Fink et.al [105].

The shape and the energy position of spectral features are not exactly the same as predicted by the theoretical calculation of the ground state in Sc. There are four main effects which are recognized to influence the shape of the X-ray absorption spectrum of transition metals. They are, the energy dependence of the single-particle transition matrix elements, atomic multiplet effects within the ground state wave function, the Coulomb and exchange interactions between the core hole and the d electrons (which can be divided into the monopole-like attractive potential and the higher-mutipole Coulomb) and exchange interactions [105, 106].

The origin of the energy dependence of the matrix elements is the energy dependence

of the radial part of the atomic d wave function. Those wave functions overlap strongly with those centered on nearest neighbors. The amplitude of the bonding-like d states in the core region will decrease and the amplitude of the antibonding-like d states will increase. Since the bottom of the d band has bonding character and the top of the d band has antibonding character, the transition matrix element is expected to increase with energy. Thus, the energy dependence of the matrix elements only renormalizes the intensity inside the band.

The atomic-like behavior of the d state may cause the atomic multiplet effects within the ground state wave function. However, the success of the one-electron band theory in describing the VB structure rules out large effects due to the electron correlation in the d band.

The core hole effect plays a significant role for the strongly correlated materials as can be seen from the consideration of the SXA spectra of the Sc compounds above. The significance of this effect in the absorption spectra of the metallic scandium may be recognized from the following fact: the intensity ration of the peaks around 1.5 and 3.5 eV relative to the Fermi energy in theoretical DOS of Sc is closer to the value obtained by the Bremsstrahlung isochromat spectroscopy, where no core hole is created, (see BIS spectrum in Fig. 6.8, reproduced from [107], and SXA spectrum in Fig. 6.7) than to the value obtained by X-ray absorption. Nevertheless, there is some unclarity on how the core hole effect influences the d states. The theoretical calculations including the core hole in the intermediate state often predict a behavior opposite from the experimental observations: the predicted lower energy shift of the peaks contradict the experimentally observed higher energy shift [105]. Other experimental observation which cannot be explained only by the core hole influence are a strong deviation of the intensity ratio between L_3 and L_2 absorption band from the statistical (2:1), the different line shape of L_3 and L_2 absorption bands and a strong change in the apparent spin-orbit splitting between L_3 and L_2 edges relative to that observed in 2p XPS. Thus, the core hole effect does influence the SXA spectra of transition metals but may interact with other effects like atomic exchange and solid-state band-structure effects.

It was proposed by Speier at el. [107] that the shape of the Bremsstrahlung isochromat spectra of Sc can not be fully described as empty d-DOS due to the strong 2p - 3d exchange effect. This atomic-like effect can lead to the significant transfer of weight from the L_2 to L_3 edges if the $\langle 2p3d\,|1/r_{12}|\,3d2p\rangle$ is comparable to the spin-orbit coupling of 2p state. Those effects are observed in Sc where the spin-orbit splitting is equal 4.7 eV [108]. However, the atomic exchange effect can not explain the difference between the L_3 and L_2 line shape. Thus, the detailed shape of the $L_{2,3}$ absorption edge of the Sc neither can be fully explained on the basis of a purely atomiclike picture nor on the basis of the structure of the empty DOS with small modifications due to the energy dependence of the matrix elements. The intensity ratio between the L_3 and L_2 edges, the shape of the SXA spectrum and the difference between the shape of L_3 and L_2 edges were explained by a combination of all these effects rather successfully, but it still failed to describe the line shape of the SXA spectrum in detail, especially for the early TM [106].

For outlining a qualitative difference between the absorption and emission spectra of Sc atom in strongly and in weakly correlated complexes, the goal of the present work, no further theoretical calculation are necessary. Such complex considerations are desirable

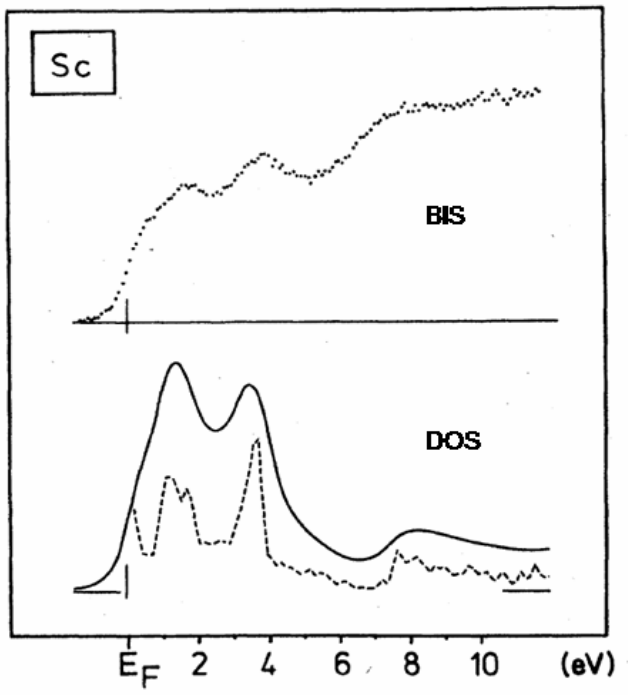

Figure 6.8: Comparison between the Bremsstrahlung isochromat spectra of Sc and the theoretical ground state DOS. Reproduced from [107].

for the deeper understanding of an electronic structure response on the X-ray excitation and relaxation processes in the transition metal complexes.

6.3 Correlation and resonant effects in X-ray fluorescence spectra.

Resonance effects reflecting the localization of Sc d electrons and interaction with the ligand are observed by SXF spectroscopy. The core excitation and decay processes occur coherently in RIXS. The energy difference between incident and emitted photons corresponds to the energy of a final state excitation. The observed energy dispersion in the SXF spectra of strongly ionic TM compounds can be explained by the fact that intermediate states of various energies populate the same well defined final states. In ionic-covalent bonding materials the excited electron can occupy different states due to the de-localization of electrons and less resonant effects are observed. This section demonstrates that the resonant effect are clearly observable in both core-to-core and VB→2p transitions in Sc_2O_3 and vanish in metallic Sc and in covalent $Sc_3N@C_{80}$. A quantitative analysis of RIXS spectra is provided.

After the excitation of the 2p electron to localized empty d states the core vacancy can decay in different radiative and non-radiative processes. For the Sc metal, Sc_2O_3, $Sc(acac)_3$ and $Sc_3N@C_{80}$ two types of radiative processes were monitored by measuring the intensity and energy distribution of the fluorescence occurring after the 3s electron

transitions to the 2p hole (core-to-core transitions) and after the electron transitions from the VB to the 2p hole. Both processes compete with the non-radiative decay (Auger process), which can take place if the core electron excitation is energetically possible due to the presence of the band gap. As the 2p core level is split into two levels due to the spin-orbit interaction, two emission lines are expected to be observed with the intensity ratio ($2p_{3/2}$:$2p_{1/2}$) equal to 2:1 due to the statistical electron occupation. As the $2p_{1/2}$ hole has an additional probability to decay via the Coster-Kronig process, the $2p_{3/2}$:$2p_{1/2}$ intensity ratio increases if the 2p spin-orbit splitting is larger then the band gap.

The atomic character of the Sc d states plays an important role in the process of the core hole decay. Threshold excited core-to-core transitions in Sc can be considered as a two step process: in the first step an electron from the Sc 2p core level is promoted to a empty 3d orbital and in the second step a 3s electron fills the 2p vacancy. In the final $3s^{-1}3d$ state the Coulomb and exchange interaction between 3s and 3d electrons can be directly measured. Tuning the excitation energy to different $2p^{-1}3d$ excited states one can determine how these interactions are influenced by the CF.

6.3.1 Sc metal.

The electronic structure of Sc metal is schematically sketched in Fig. 6.9 based on XPS data [87], theoretical calculations [104] and present measurements. The $3s \rightarrow 2p_{3/2}$ transitions results in the fluorescence of photons with the energy of 348.4 eV (L_l emission band), the $3s \rightarrow 2p_{1/2}$ transitions results in the fluorescence of photons with the energy of 353.1 eV (L_η emission band). The valence band of the Sc metal is built by $4s^2 3d^1$ electrons. The 4s→2p transition has very little probability according to the calculation of the transition matrix elements. The VB $3d \rightarrow 2p_{3/2}$ transitions results in the fluorescence of photons with the energy 395 eV$\leq \hbar\omega_{out} \leq$399 eV ($L_\alpha$ emission band), the VB $3d \rightarrow 2p_{1/2}$ transitions results in the fluorescence of photons with the energy about 399.7 eV$\leq \hbar\omega_{out} \leq$403.7 eV ($L_\beta$ emission band).

In metallic Sc no resonance effects due to the interaction of the core hole and the 3d states are expected, as the d states are screened from the core hole in the metal. The experimentally obtained RIXS spectra are shown in the Fig. 6.10 (primary excitation photon energies indicated in the SXA spectrum at the top part of the figure). The excitation dependence of the fluorescence spectra is not a simply excitation of 2p core level and 3s to 2p decay. The relative intensity of the L_l and L_η lines is excitation energy dependent and reflects the existence of the competing Auger decay channel for the $2p_{1/2}$ vacancy and the absorption probability of the different 2p core levels.

At 416 eV where both core levels can be excited. The intensity ratio of the resulting emission lines (L_l : L_η = 2:0.4) is different from the statistical electron occupation of sub-levels (2:1). The width of emission lines excited at 416 eV is also different (FWHM(L_l)=1.0 eV, FWHM(L_η)=1.3 eV). This can be explained by the intense Coster-Kronig decay of the $2p^{-1}_{1/2}$ state to the $2p^{-1}_{3/2}\epsilon^1$ (where ϵ is an electronic state in the CB) as electrons in metal are nearly free. The width of the bands is defined by the experimental energy resolution (0.8 eV), by the energy width of the 3s semi-core level (as it is larger than the width of the 2p core level) and by the lifetime of the core hole. The life time of the $2p^{-1}_{1/2}$ state is shorter then the lifetime of the $2p^{-1}_{3/2}$ state due to the fact that the Coster-Kronig

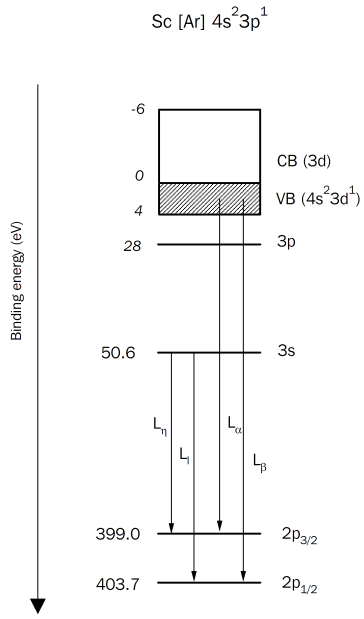

Figure 6.9: The sketch of the electronic structure of the Sc metal based on the XPS, SXE and theoretical data.

process is allowed in metal with the band gap equal to zero.

For the low photon energy excitation (to the states in the vicinity of the Fermi energy) the intensity of the L_l band relative to the L_η is consistent with the energy dependence of the excitation probability of the 2p core electron measured by SXA: the intensity of the L_η line increases when the absorption is strong (Fig. 6.11).

Additionally, one observes a peak shifted by about 0.8 eV to higher energy relative to the L_η line at 400.5 eV (10% of the intensity of the main line,) at 401.8 eV (19%) and at 403.4 eV (21%). Similar peak shifted by about 0.8 eV to the higher energies relative to the L_η emission line can be observed at 407.6 eV excitation energy (45%). This may be the sign of electronic correlation effects, which can be seen as the response of the electronic system to the presence of the electron in the conduction band.

VB RIXS spectra of Sc metal excited with the same photon energies as core-to-core spectra are shown in Fig. 6.12. In general, at low energies the $2p_{3/2}$ core level is excited and the L_α band occurs. When the $2p_{1/2}$ level is excited, the L_β band appears. The shape of the emission spectrum excited at low photon energies resembles the Sc d DOS [104]. The width of the theoretical DOS is about 4 eV, which is narrower than the experimental one (about 7 eV) due to the experimental energy resolution (about 0.8 eV) and a low-energy tail (388eV $\leq \hbar\omega_{out} \leq$ 395eV) due to the Auger effect in the VB typical for metal X-ray emission bands. The small kink in the low-energy tail (α at 391.6 eV, about 6.2 eV apart from the maximum of the L_α line) is an interesting feature as no prominent peaks are expected in the intensity reflecting the broadening due to the final state lifetime. In the high energy excited spectrum the high energy satellite (β, 400.6eV $\leq \hbar\omega_{out} \leq$ 408.6eV) is due to a spectator vacancy in the initial state (double excitations at high excitation energies).

The experimentally obtained low energy excited SXF spectrum of Sc metal is similar

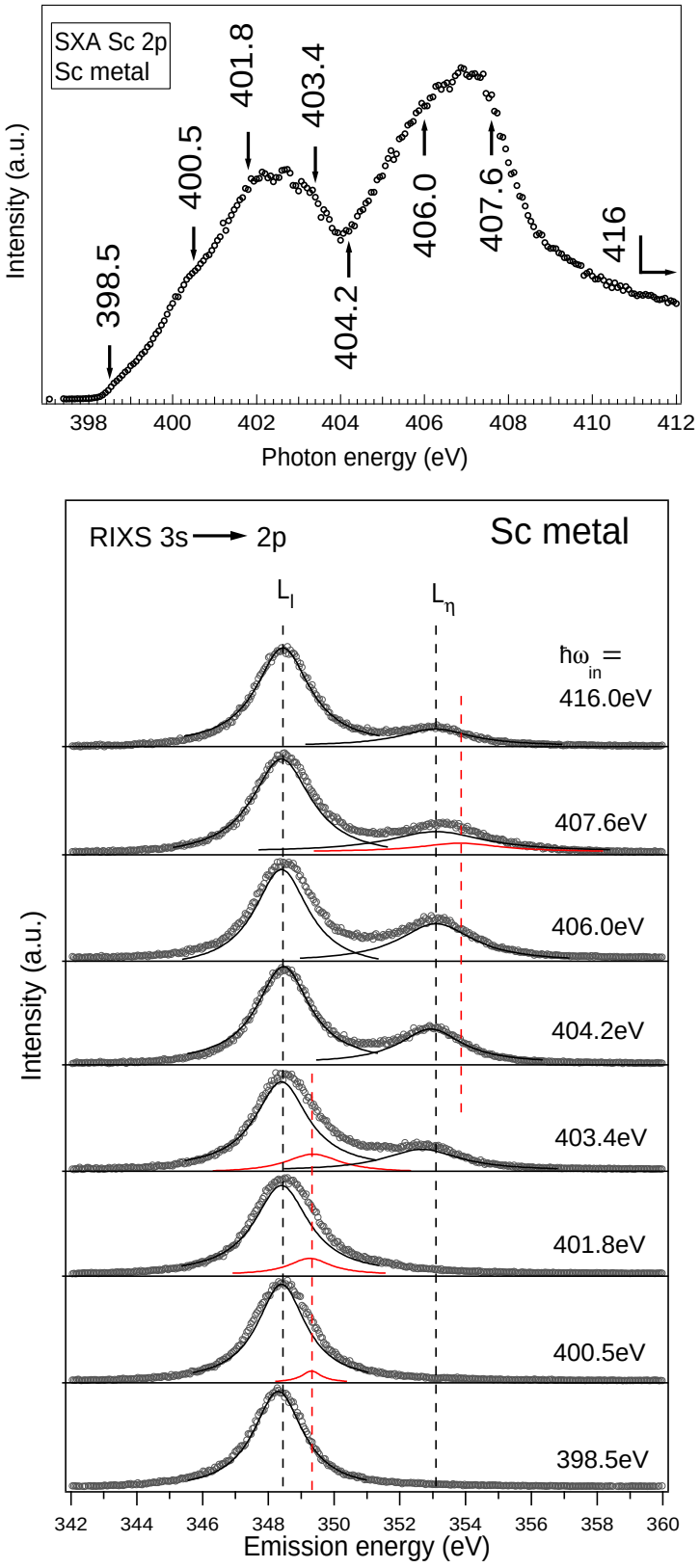

Figure 6.10: RIXS core-to-core (3s→2p) spectra of Sc metal excited at photon energies indicated in SXA spectrum above by arrows.

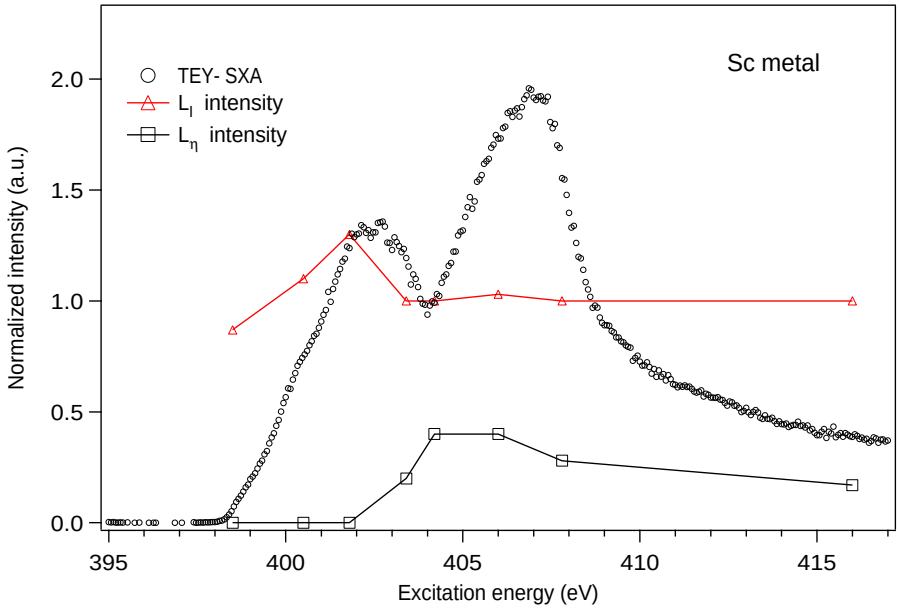

Figure 6.11: Comparison between the TEY-SXA spectrum the excitation energy dependence of the intensities of L_l and L_η emission lines of Sc metal. The intensities of the emission lines are normalized to the incoming flux and to the measurement time.

in the shape and in the energy width to the X-ray photoemission spectrum (PES) shown in Fig. 6.13 reproduced from [109]. From PES measurements the VB width is estimated to be equal to 8.3 eV. The kink E in the PES of Sc metal occurs 7.9 eV below the A feature. As far as the tailing at the bottom of the VB measured by PES on TM Sc through Fe [109] is seems to be a physical effect which till now is not reproduced by band structure calculationsthe, the highly successful interpretation of high-energy PES in terms of initial-state density has been done (see, for instance, [110]).

The relative intensity of L_α and L_β bands in the high energy excited spectrum is again different from the statistical ratio (measured L_α:L_β=2:0.6) due to the existence of an additional Auger relaxation channel for the $2p_{1/2}$ vacancy. The ratio (3.3) differs from the corresponding ratio of the core-to-core lines (5.0). It was demonstrated by J. Kawai [111] that the intensity ratio of L_α and L_β emission lines of transition metal compounds can be strongly influenced by the self-absorption. The L_3 and L_2 absorption edges are at the high energy side of L_α and L_β lines, respectively. The TM L fluorescence emitted in a solid will be absorbed by another atom of the same element before they escape from the surface to the vacuum. Thus, a part of the intensity of L_β is absorbed by the L_3 edge. The line shape of L_β itself is modified by the L_3 absorption edge. This leads to the underestimation of the intensity of the L_β line relative to the intensity of the L_α emission line, the measured L_α:L_β ratio is then *higher* than the true value.

In contrast to VB fluorescence, the core-to-core lines do not suffer from self-absorption as the emitted fluorescence can be absorbed only by shallow electrons. Then the L_l:L_η ratio should represent the true probability of the radiation decay of the 2p holes influenced only by the Coster-Kronig process. An interesting fact is that the L_α:L_β ratio (3.3) observed

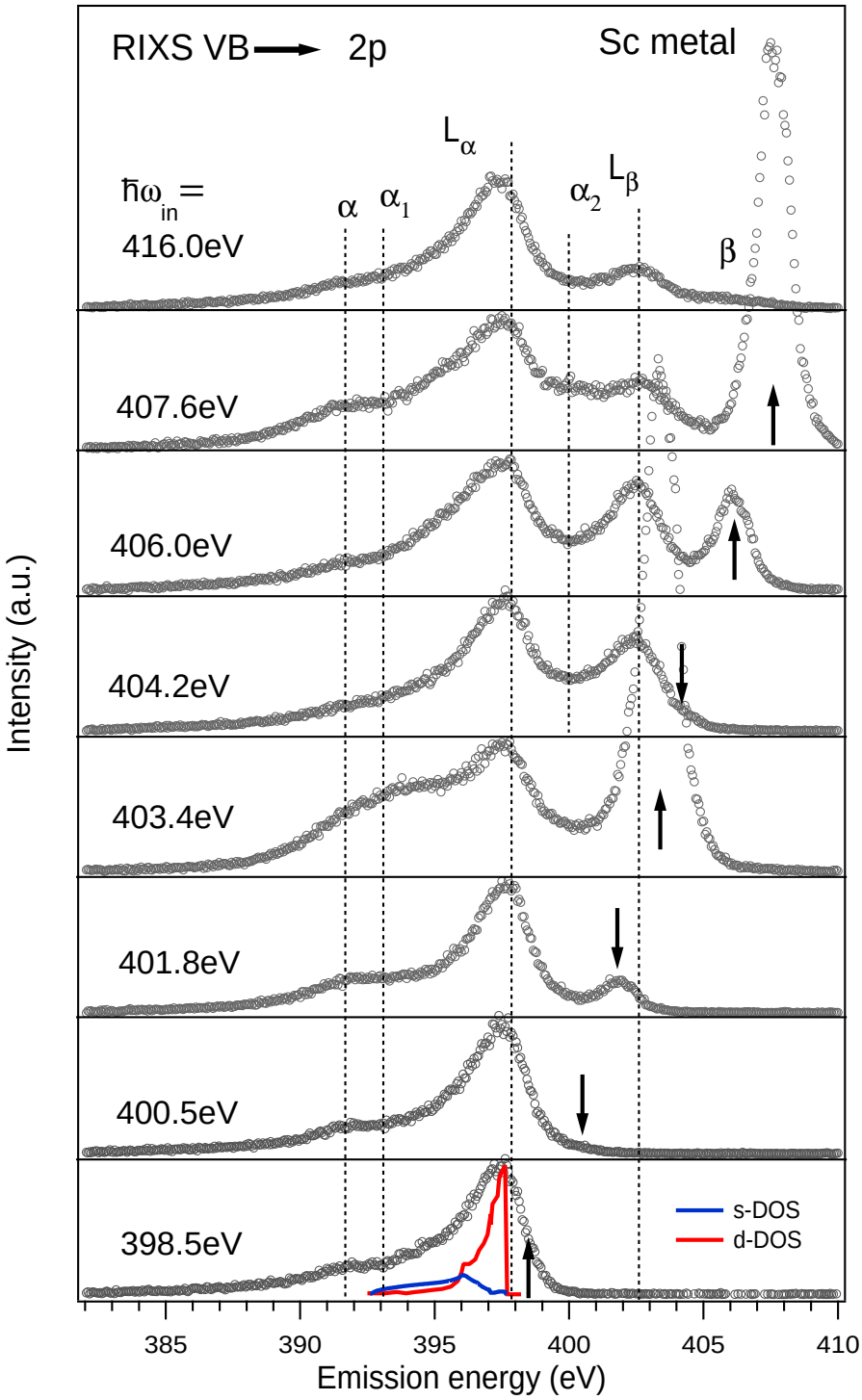

Figure 6.12: RIXS (VB→2p) spectra of Sc excited at photon energies indicated in SXA spectrum in Fig. 6.10. Arrows mark the position of the elastic peaks, lines - positions of the non-resonance inelastic peaks and satellites. The red and the blue lines are the theoretical d and s density of states of Sc [104].

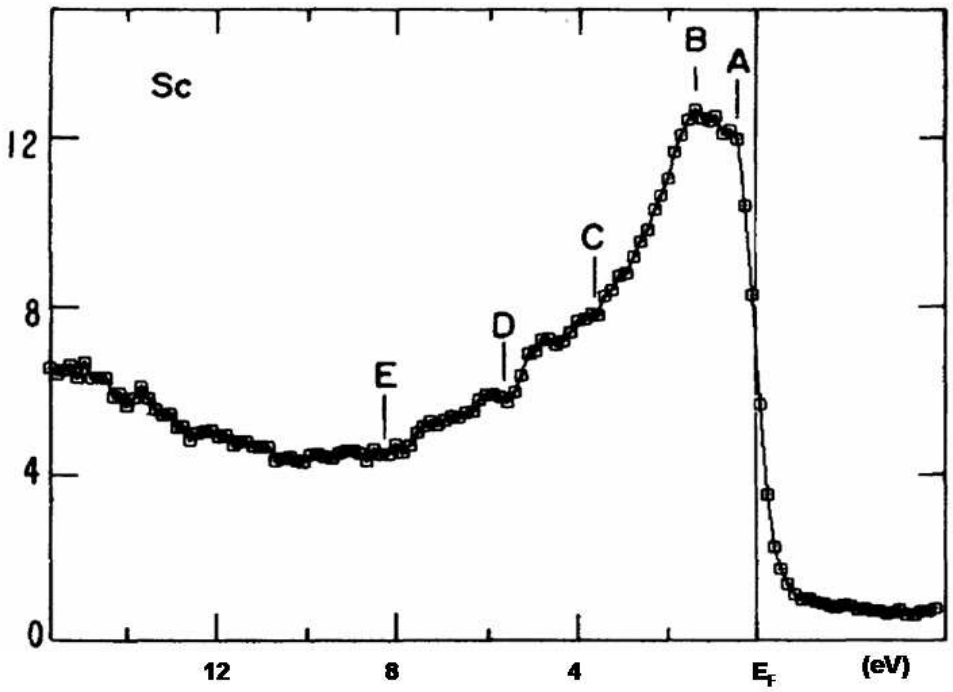

Figure 6.13: X-ray photoemission spectrum of the VB region of Sc. Reproduced from [109].

in Sc metal is *lower* than the L_l:L_η (5.0). The consideration above clearly excludes the self-absorption effect as a reason for the difference in intensity ratio. The similar difference in intensity ratios due to core-to-core and VB-to-core transitions was observed by Pease [112, 113] and it was explained by the enhancement of the Coster-Kronig width in certain TM. The effect which influences the L_α:L_β ratio is the 2p - 3d exchange interaction effects [113]. The decrease of the intensity ratio for VB transitions compared to core-to-core transitions means that such exchange effects are strong in Sc metal.

There are two excitation energy dependent features at 393 and 400 eV (marked as α_1 and α_2, respectively, in Fig. 6.12) clearly amplified at excitation energies 403.4 (α_1) and 407.6 eV ($\alpha_{1,2}$). An interesting observation is that those peaks appear at the same excitation energies at which the L_l and L_α high energy satellites appear, but are at the low energy side of the L_3 and L_2. Usually, a high energy satellite of the X-ray emission band assigned to the spectator vacancy in the initial state and a low-energy satellite are referred to the final-state effects like a presence of an additional electron in the conduction band. The excitation energies at which the satellites are enhanced may correspond to the narrow feature about 3.4 eV above the Fermi energy in the Sc DOS shown in Fig. 6.7. To explain the photon energy shift of the satellites relative to the main lines, their intensities and the excitation energy dependence a simulation of the X-ray absorption and resonance emission taking into account initial and final state effects may be helpful.

The last observation which can be mentioned here is the excitation energy dependence of the intensity of the elastic peak. The intensity of the elastic peak depends strongly on the geometry and the surface structure of the sample. The presented measurements of Sc

metal were carried out in fixed geometry and every spectrum took about 2 min. This and the fact, that very weak elastic scattering is observed at the 400.5 eV excitation energy, gives a hope that the total intensity of the elastic peak corresponds to the probability of the resonance recombination process. The intensity of elastic peaks again follows the probability of core electron excitation measured by the SXA.

6.3.2 Sc_2O_3.

The early TM are governed by the d-d interaction as the band gap is defined by the splitting of the d states (Mott-Hubbart insulators), for late TM compounds the band gap is located between the empty d states and the filled ligand states (charge-transfer insulators). Sc in d^0 configuration has no d electrons indicating that the entire Sc_2O_3 compound is a charge-transfer insulator.

A Sc ion in the oxide has nominally $[Ar]4s^03d^0$ configuration. The VB consists of O 2p states. The binding energy of $2p_{3/2}$ level is shifted to higher energies relative to the metal by 2.9 eV, the energy difference between the binding energy of Sc $2p_{3/2}$ and $2p_{3/2}$ electrons in Sc oxide measured by XPS is equal to 4.4 eV [108]. The decrease of the energy separation between $2p_{3/2}$ and $2p_{3/2}$ XPS lines is an interesting observation as the spin-orbit interaction is a pure atomic behavior and in first approximation not influenced by the surrounding. Similar changes in the energy separation of 2p components was observed in Co oxides [114]. The different energy separation of the TM 2p core lines in different compounds can have a physical reason due to the different electron exchange interactions or can be due to the final-state effects influencing the photoemission process itself. Unfortunately, no declaration of the reason of this observation was made before.

A schematic picture of the electronic structure of the Sc_2O_3 based on the XPS [108, 115] and present SXE data is shown in Fig. 6.14.

With the excitation energies close to the 2p threshold core-to-core transitions occur in the presence of an electron excited into the narrow d states. In Fig. 6.15 a schematic diagram of intermediate and final states in the energy scale above the ground state are shown.

The RIXS from Sc compounds is usually considered as the charge transfer transitions. The ground state is a hybridization state between the d^0 and the charge transfer state d^1L^{-1}, where L^{-1} denotes the ligand hole. In Fig. 6.16 the schematic diagram of the charge transfer process between the ligand states and Sc empty valence states is shown. When the 2p electron is excited into the continuum the presence of the 2p core hole influences the electronic states of the Sc ion in such a way that the energy of empty states lowers. The hole can be screened by outer electrons (a) by an occupation of the atomic-like 3d states or (b) by an occupation of states in the broad 4s4p band. Low energy satellites of the 2p line and VB of TM compounds were observed by XPS [116] and are explained as the results of different screening of the 2p core hole ("local" screening by d electrons and "nonlocal" screening by 4s4p electrons). Such processes will also influence the X-ray transitions and may be observed by SXF.

Indeed, the relation between the high energy hump of the Cu L_α emission line and the high binding energy satellite of the $2p_{3/2}$ XPS line was proposed by J. Kawai et al. [117] based on the correlation in appearance of those features in different Cu compounds.

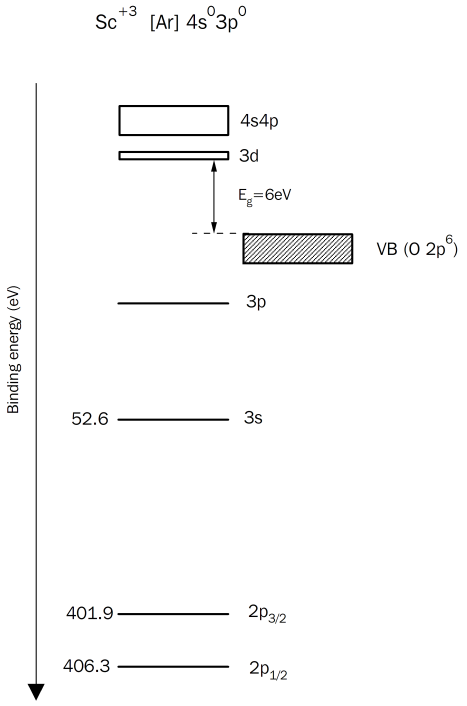

Figure 6.14: The sketch of the electronic structure of the Sc_2O_3 based on XPS, SXE.

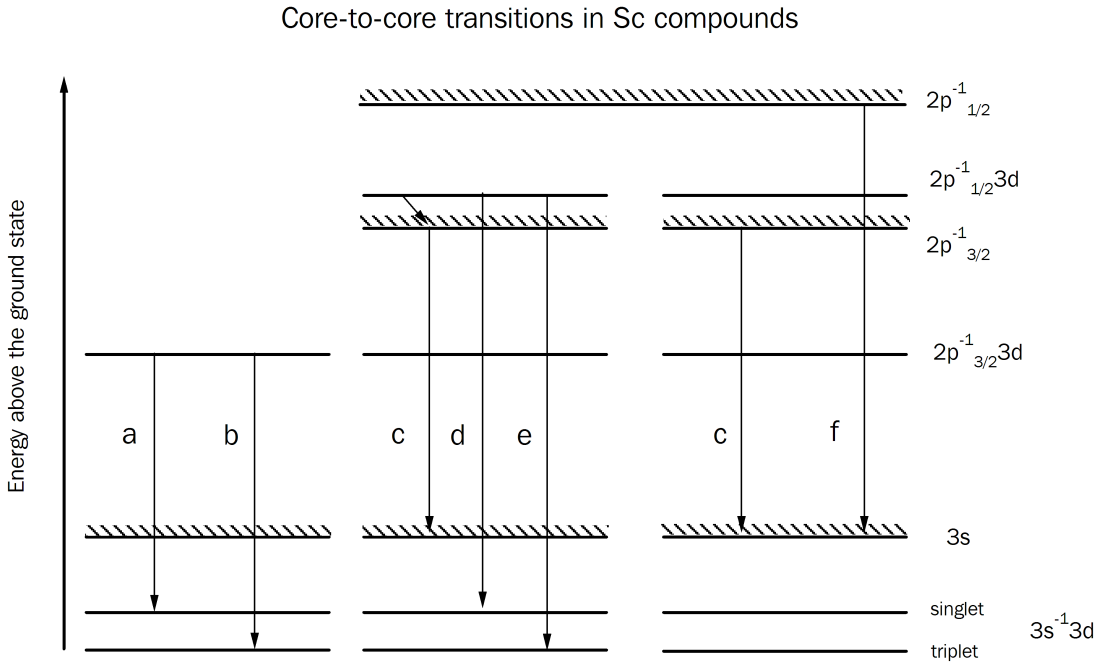

Figure 6.15: Schematic energy picture of states and transitions in Sc compounds with strong ionic bonding.

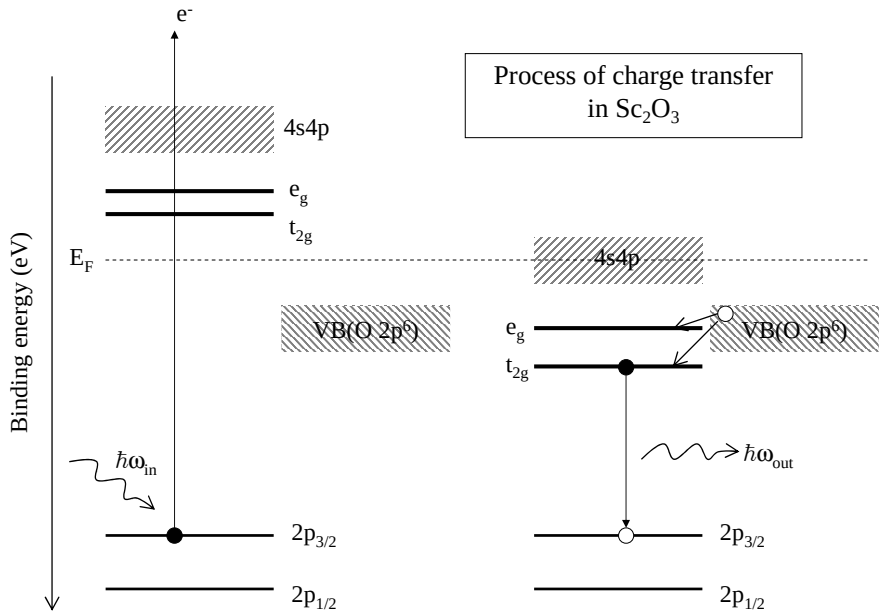

Figure 6.16: Schematic energy picture of the process of charge transfer in Sc_2O_3 after the absorption of the high energy photon.

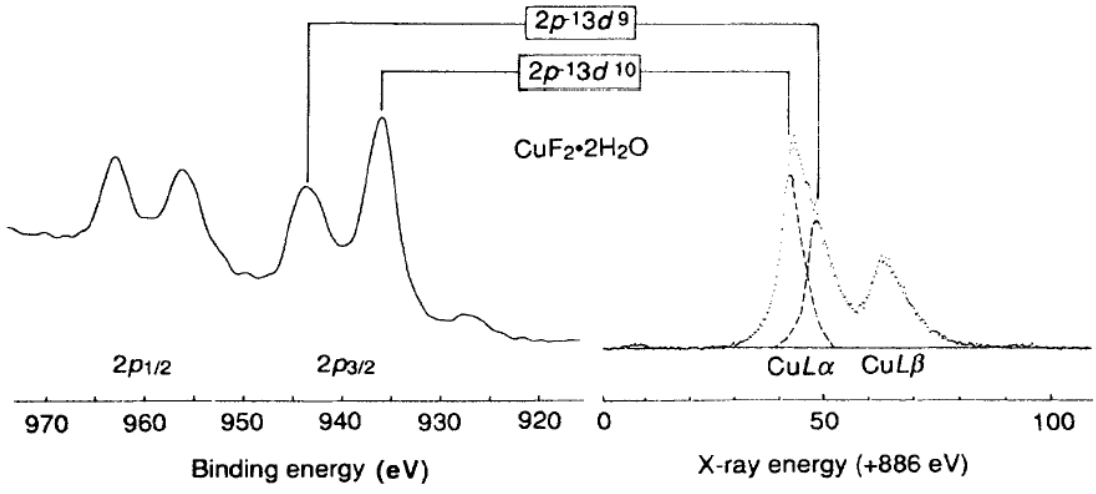

Figure 6.17: Relation between the Cu L_α emission and $2p_{3/2}$ XPS line. Reproduced from [117].

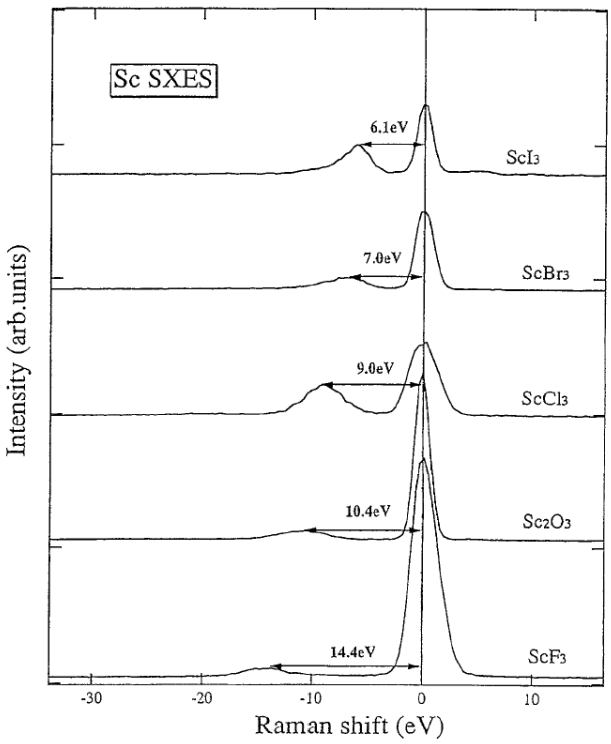

Figure 6.18: Relation between the energy separation between the elastic peak and the inelastic feature in SXF spectra of different Sc compounds. Reproduced from [118].

The high energy hump of the emission line was explained as the transition between poorly screened states and not due to the electron transition between multiple-hole states. It was also concluded that the L_α main line originates from the charge-transfer effect in strong ionic compounds. The main observation is illustrated in Fig. 6.17.

As was seen from the analysis of the SXA spectra, the Coulomb and exchange interaction between electrons in the final state can be strong for TM compounds with ionic character of the bonding . Tuning the excitation energy to different excited states one can determine how these interactions are influenced by the ligands. The excitation energy dependence and the energy shift between the elastic and inelastic peaks in Sc compounds also reflects the chemical state of the Sc ion: it was observed before that the energy loss decreases according to the electronegativity of the ligand in Sc halides [118]. The energy loss can be understood as the energy difference between the recombination peak and the inelastic peak defined by the interaction between the d^0 and the d^1 configurations. This interaction strongly correlates with the character of the bonding between the Sc ion and the ligand (see Fig. 6.18): the more ionic the bonding between the Sc and the ligand the larger the Raman shift of the inelastic feature in the SXF spectra of Sc halides. Unfortunately, no more information about the experimental details are reported.

Starting from the rather ionic Sc_2O_3, the SXA spectrum is well understood and peaks are assigned to transitions of certain intermediate states (Fig. 6.19). The RIXS 3s→2p spectra excited at the photon energies indicated in the Fig. 6.19 are shown in Fig. 6.20: non-resonant SXF transitions $3s\rightarrow 2p_{3/2}$ and $3s\rightarrow 2p_{1/2}$ are measured at the high primary

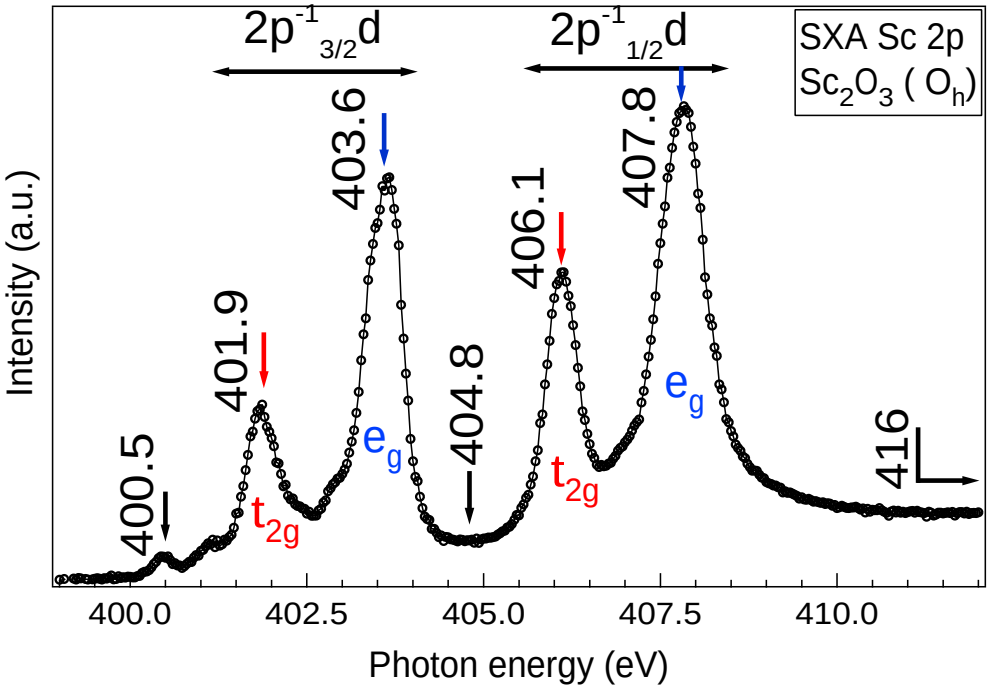

Figure 6.19: TEY-SXA spectrum of Sc_2O_3. Absorption peaks are marked according to the splitting of Sc d states in the O_h coordination of O^{-2} ions. Arrows indicate the excitation photon energies at which RIXS spectra were measured.

energy excitation spectrum (416 eV), the result of the decay of the $2p^5t^1_{2g}$ intermediate states are measured at 401.9 and 406.1 eV, the result of the decay of the $2p^5e^1_g$ intermediate states are measured at 403.6 and 407.8 eV.

The high energy excited spectrum consists of two lines similar to the core-to-core spectra of Sc metal. In contrast to the metal spectra, L_l and L_η lines in the oxide are broader and have nearly the same width (1.5±0.2 eV FWHM). The same width is consistent with the fact that the apparent 2p spin-orbit splitting (4.4 eV, Sc 2p XPS) is less then the band gap (6 eV) and the Auger decay of the $2p_{1/2}$ via the Coster-Kronig process does not happen in the oxide. The increase of the linewidth in the oxide compared to the metal can have different reasons. First, this can reflect the decrease of the lifetime (LT) of the 3s hole in the final state in the oxide compared to the metal. Second, the width of the emission line can be influenced by the optical phonons. From the simple consideration, the width of the fluorescence line (W) can be evaluated:

$$LT(2p, initial\ state)^2 + LT(3s, final\ state)^2 + exp.\ resolution^2 = W^2. \qquad (6.9)$$

The experimental resolution provided by the setup is estimated to be 0.8 eV or better. The energy width of the 3s hole is then estimated from the equation 6.9 to be 0.6 eV in the metal and 1.3 eV in the oxide. The electron density is situated in the vicinity of anion in the ionic compound. As the probability of the Auger decay decreases inverse to the distance, the non-radiative decay is less probable in the oxide than in the metal. From this point of view, the width of the 3s level should decrease in the cation compared to

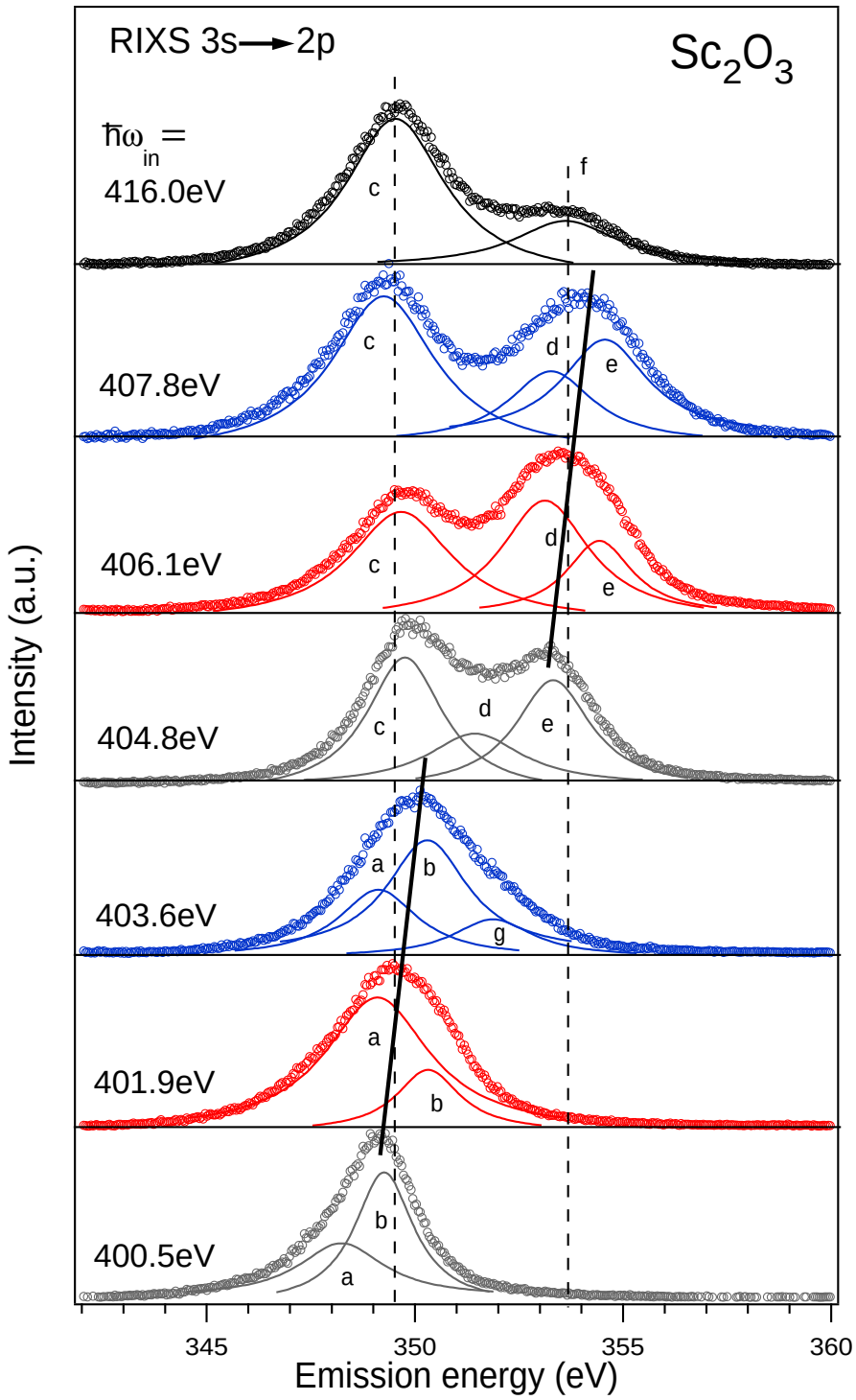

Figure 6.20: RIXS core-to-core (3s→2p) spectra of Sc_2O_3 excited at photon energies indicated in Fig. 6.19 by arrows. Dotted lines mark the energy position of the non-resonant peaks as measured from the SXF spectrum excited at the photon energy of 416 eV (marked as c and f). Solid lines mark the energy dispertion of resonant peaks.

the neutral atom. To explain the experimentally observed increase of the linewidth in the oxide further theoretical consideration are necessary.

The drastic difference in the width of the 2p XPS line (0.74 eV in Cu and 2.42 eV in CuO) was reported in [119]. It related not to the lifetime of the 2p hole, but to the difference in hole-phonon coupling strengths in these materials. In contrast, no phonon broadening was observed in the Cu 1s→$2p_{3/2}$ core-to-core X-ray emission lines and the width of the emission lines is in agreement with the theoretical calculations assuming just lifetime broading for transitions between deep core levels [120]. The lifetime of semi-core levels can depend on chemical state of the atom, but as it was mention above it should increase in the oxide compared to the metal. From the XPS measurements [108], the absolute value of the width of the Sc 2p line doesn't change drastically in the oxide (72 meV) compared to the metal (57 meV). This means that the interaction with optical phonons are not strong for the Sc 2p hole. The possible reason of the experimentally observed broading of the emission line in the oxide is drastic increase of the phonon interaction of the 3s hole in the oxide compared to the metal. To confirm this conclusion the Sc 3s linewidth must be measured by XPS (not available at the present time).

The L_l:L_η intensity ratio is 2:0.6 = 3.3, which is lower than in the corresponding ratio for Sc metal (5.0) but still higher then the theoretical ratio (2.0). It is closer to the theoretical limit due the energetically forbidden Coster-Kronig decay of the $2p_{3/2}$ hole as it was describe above. The difference from 2.0 value is due to the strong 2p-3d exchange interaction in the oxide.

The energy splitting of the L_l and L_η lines (4.1±0.2 eV) is less than in Sc metal (4.7±0.2 eV) and consistent with the difference in the 2p binding energies in the Sc metal (4.7 eV) and in the Sc oxide (4.3 eV) measured by XPS [108]. The dependence of the spin-orbit splitting values on the binding energy of the $2p_{3/2}$ electron is observed in the transition metals. The splitting value increases by about 0.027 eV per 1 eV increase of the binding energy. It can be understand from the simple assumption that the orbit contracts when its energy increases due to the increase of the nuclei charge. This causes stronger interaction between electrons and as a results the *larger* energy splitting. The binding energy of $2p_{3/2}$ electron of Sc in the oxide measured by XPS is higher by 2.9 eV than in the metal. This would give 0.08 eV increase in the spin-orbit splitting. The experimental observation that the energy separation of the emission lines *decreases* by 0.6 eV. It means that the change in the energy separation of the emission lines is dominated by the final state effects, like the presence of the core hole and the multielectron exchange interaction. The reduction of the energy splitting must be due a less effective screening of the 2p core hole in the oxide than in the metal.

One can see that the shape and the energy position of the RIXS spectra are strongly excitation energy dependent. The energy dependence of core-to-core transitions can be understood from the schematic energy diagram shown in Fig. 6.15 on page 99. For the quantitative analysis every RIXS spectrum was decomposed into components on the emission energy scale (the results are shown in Fig. 6.20). An initial Voigt curve fitting showed that in most cases the Lorenzian components dominates the spectral shape similar to the result on CaF_2 from [121].

Analysing the results of the decomposition one can identify the non-resonant peaks (staying at the constant photon energies: c and f) and the resonant peaks (showing an

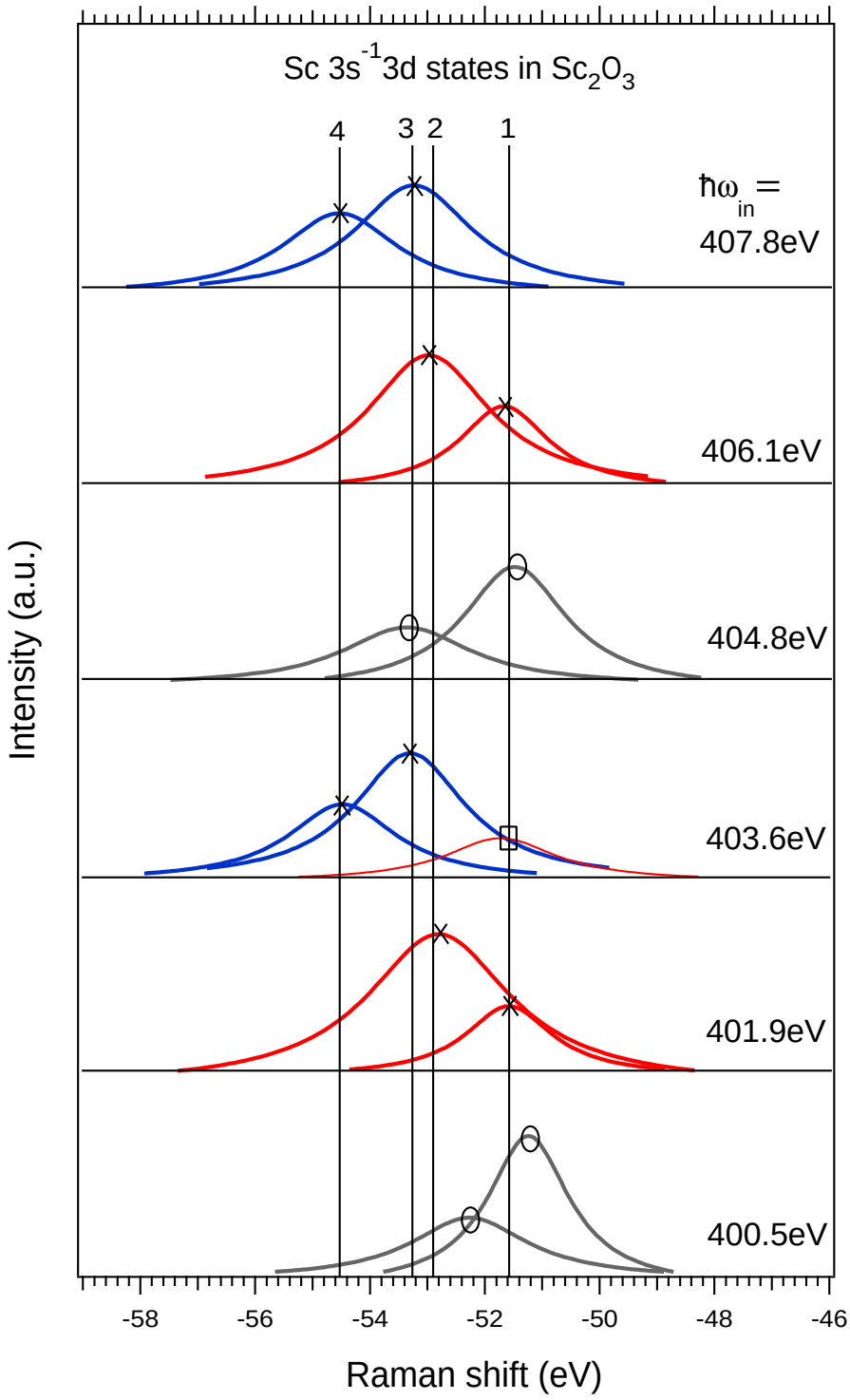

Figure 6.21: Resonant part of RIXS 3s→2p spectra of Sc_2O_3 plotted on the Raman shift scale. Solid lines mark the final states: 1 - $3s^{-1}3t_{2g}$ triplet, 2 - $3s^{-1}3t_{2g}$ singlet, 3 - $3s^{-1}3e_g$ triplet, 4 - $3s^{-1}3e_g$ singlet.

energy dispersion: a, b, d and e). One can see that starting from the 404.8 eV spectrum the non-resonant $2p_{3/2}$ contribution into the spectrum due to the Coster-Kronig Auger decay of the $2p_{1/2}$ hole increases (peak c). The energy position of the peak c in the spectra excited at the photon energies in the vicinity of the L_2 edge is different from the energy position of the peak c excited at 416 eV by $\pm$0.2 eV. This energy shift of the emission line might be due to the weak exchange interaction between the $2p_{3/2}$ hole and the 3d states occupied by the $2p_{1/2}\rightarrow$3d transition. This state can be different from the state excited with the photon energies in the vicinity of the L_3 edge as the 3d state can be additionally excited due to the energy liberated after the Costa-Kronig decay of the $2p_{1/2}$ hole.

Taking the c peak away, one can plot the resonant peaks on the Raman shift scale (E_{emiss}-$\hbar\omega_{in}$). Every resonant emission peak can be decomposed into two peaks which might correspond to the transitions into the singlet and triplet $3s^{-1}3d$ final states (see Section 2.4). At the low excitation energies the $2p_{3/2}$ level is excited and 2 intermediate states can be occupied ($2p^5_{3/2}t_{2g}$ and $2p^5_{3/2}e_g$). The resulting emission reflects transitions into the final states $3s^{-1}t_{2g}$ and $3s^{-1}e_g$. When the excitation energy of $2p_{1/2}$ core level is reached, the relaxation of the other 2 intermediate states ($2p^5_{1/2}t_{2g}$ and $2p^5_{1/2}e_g$) results in transitions into the same final states. Measuring the energy position of the peaks a, b, d and e at the Raman scale one can see that the emission peak excited at the photon energies corresponding to the maximum of the absorption peaks correspond to the transition to the well defined final states (as they appear at the constant loss energies within the experimental error, marked with crosses in Fig. 6.21). Peaks excited at the intermediate photon energies (400.5 and 404.8 eV) appear at the different energies at the Raman scale (marked with circles in Fig. 6.21). The situation when the energy of excited electron is different by some eV from the energy necessary for the transition to the well defined intermediate state might result in changing of the energy of the final state due to the additional excitation of valence electrons. The spectrum excited at the 403.6 eV photon energy also contains the high energy peak (peak g in Fig. 6.20) which at the Raman close to the $3s^{-1}3t_{2g}$ triplet state (marked with the square in Fig. 6.20). The reason for the final state with the energy corresponding to this specific state to be created is to be clarified further.

The final states energies in Sc_2O_3 are measured as the average value of the energy position of resonant peaks at the Raman shift energy scale and are equal to 51.5 (1), 52.9 (2), 53.2 (3), 54.5 (4) $\pm$0.2 eV. The energy splitting between the $3s^{-1}t_{2g}$ and the $3s^{-1}e_g$ states (1 and 3 energy position for triplet states or 2 and 4 for the singlet states) is 1.6$\div$1.7 eV, which is roughly equal to the $2p^{-1}t_{2g}$ – $2p^{-1}e_g$ splitting measured by the SXA (1.7 eV). The energy splitting between the singlet and the triplet final states is equal to 1.4$\pm$0.2 eV.

A further quantitative analysis of effects possibly changing the energies of the final states in Sc_2O_3 is necessary to clarify the reason of effects observed in this work.

The emission spectra due to the transition from the VB involving a charge transfer process are less clear than the 3s$\rightarrow$2p transitions. VB RIXS spectra on Sc_2O_3 are shown in Fig. 6.22.

The high energy excited spectrum reflects the transitions at the Sc site when the electron is promoted to the continuum. The two peaks at 392.1 and 395.8 eV cannot be assigned to the non-resonant L_3 and L_2 emission lines due to two observations. First,

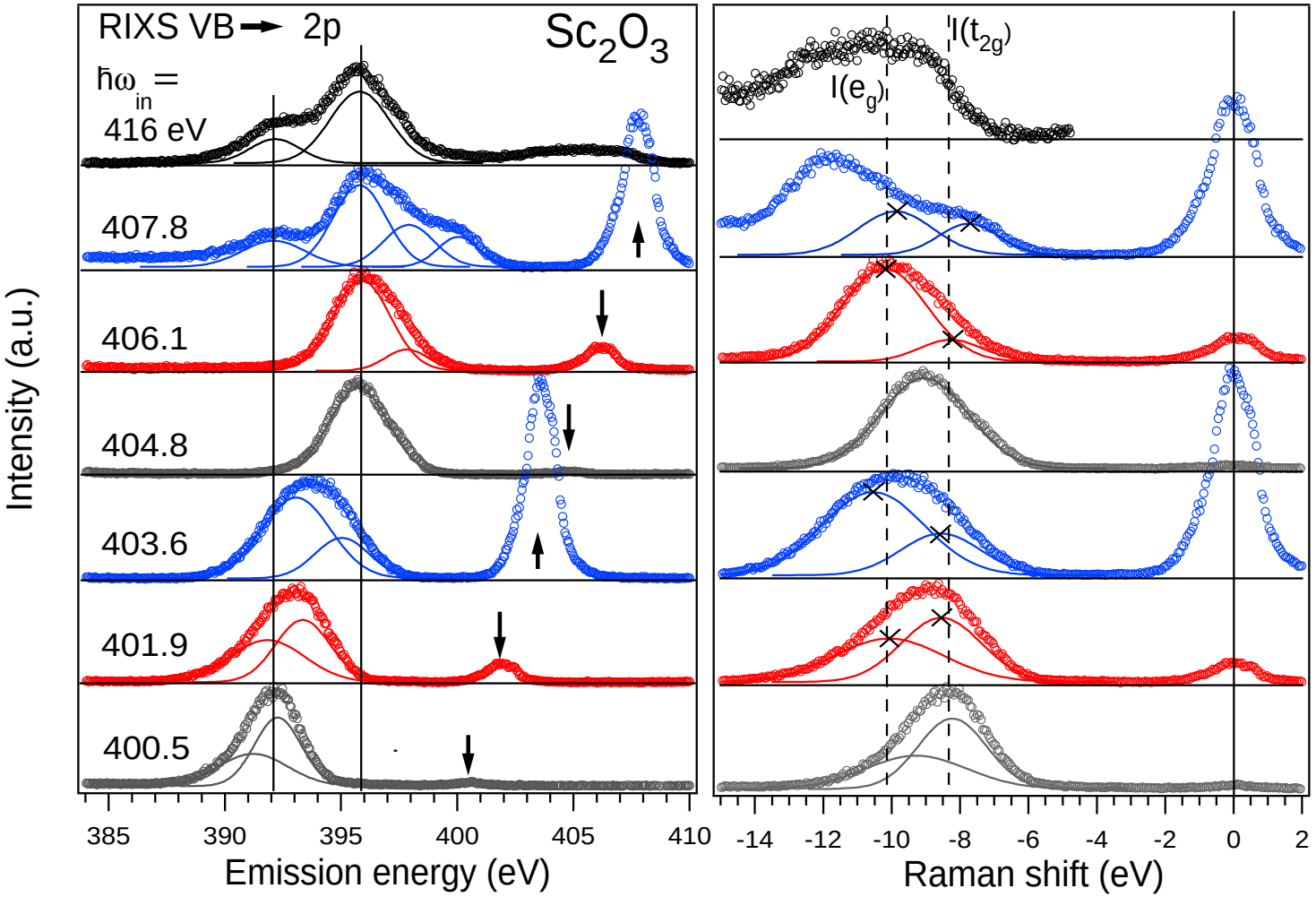

Figure 6.22: (left) RIXS (VB→2p) spectra of Sc_2O_3 excited at photon energies indicated in the SXA spectrum in Fig. 6.20 (top). Arrows mark the position of the elastic peaks, solid lines mark the positions of the non-resonance inelastic peaks. (right). The same spectra plotted versus the Raman shift. The solid line marks the elastic peak, dotted lines mark the position of resonance peaks in loss energy scale, crosses mark the energy position of the Gaussian components of the resonant inelastic part of spectra.

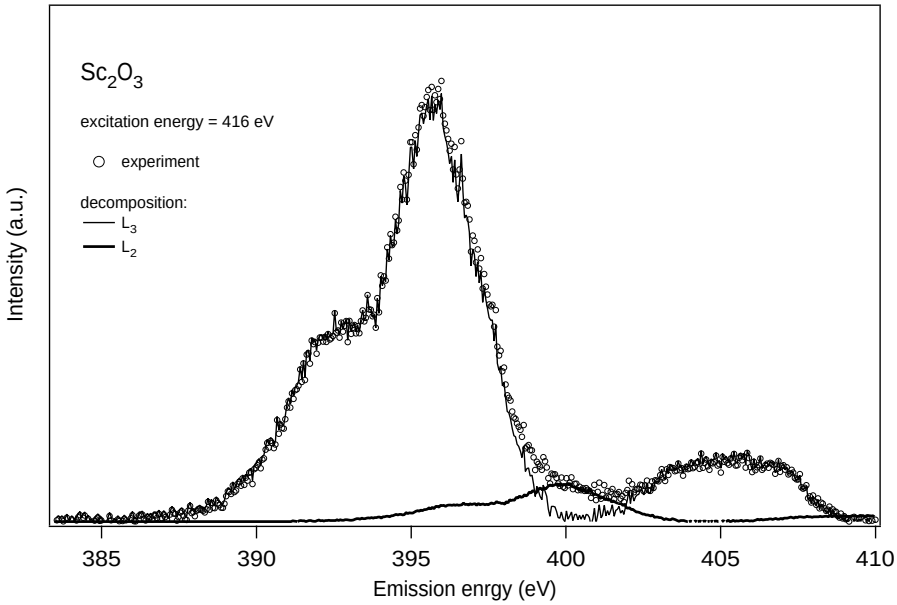

Figure 6.23: The result of the decomposition of the emission spectrum of the Sc_2O_3 excited at 416 eV into L_3 and L_2 emission bands.

the energy difference between those peaks (3.7±0.2 eV) is significantly smaller than the L_l-L_η shift (4.1 eV, see Fig. 6.20). Second, the relative intensity is equal to 1:3 drastically different from the observed L_l:L_η intensity ratio (2:0.6, see Fig. 6.20).

The emission spectrum excited at 416 eV was decomposed into L_α and L_β bands of the same shape using the known spin-orbit shift (the energy difference between the position of b and b* SXA peaks in Fig. 6.6, equal to 4.2 eV). The resulting intensity ratio is 2:0.18 = 11.0 which is much higher than the measured L_l and L_η ratio for the oxide (3.3). Because of the high value for the resulting intensity ratio and its opposite behavior to Sc metal, the final identification of the emission peaks in the high energy excited spectrum cannot be made.

As the situation in Sc can to same extent be expected to be similar to Cu mentioned above [117], the two low energy peaks may correspond to VB transitions occuring between states with a different screening. The high energy feature (402 - 408 eV) may be (i) the inelastic scattering from the $2p_{1/2}$ or (ii) due to the double excitations or (iii) due to the transition from an unscreened state (which is about 11.4 eV above the screened state according to the $2p_{3/2}$ main line - satellite energy separation [116]).

The position of the two peaks at 392.1 and 395.8 eV are marked with solid lines on the left side of Fig. 6.22. From the comparision of the position of emission features appearing at low excitation energies with the energy position of the non-resonant peaks one can recognize that there is also a feature that moves with the excitation energy. The same RIXS spectra are plotted on the right side of Fig. 6.22 but on the Raman shift scale together with the peaks obtained by the Gaussian decomposition of the spectra which are referred to the resonant inelastic scattering. One can see that resonant peaks stay at the same energy relative to the elastic peak, the relative intensity of their Gaussian

components changes with the incident photon energy.

This resonance behavior of the emission spectra was observed in TM compound in the past [122, 123, 124, 125]. The excitation energy dependent fluorescence is proposed to represent transitions to the non-bonding states of the final state configuration in the TM compounds. The RXES spectra are mainly explained as consisting of three parts: they correspond to the bonding, nonbonding and antibonding states, respectively. The bonding and antibonding states originate from strongly hybridized $3d^0$ and $3d^1L^{-1}$ states, while the nonbonding state originates from other unhybridized states. From the change of the spectral intensity in RXES with the excitation energy the character of the spectral features of the fluorescence spectra was established.

Similar to the results on Sc halides reported in [125], the excitation energy dependent fluorescence can be assigned to the transition between non-bonding states in Sc_2O_3. The two components of this part of the spectra are due to the CF splitting and correspond to the t_{2g} (the high photon energy component) and e_g (the low photon energy component) states. The assignment can be made based on the intensity enhancement of those components dependent on the excitation energy. The enhancement of different components is consistent with the resonant excitation of relevant intermediate states for the excitation energies below $2p_{1/2}$. Thus, the state at which loss low energy component is strong at the photon energy corresponding to the excitation into the $2p^{-1}_{3/2}t^1_{2g}$ state (401.9eV) and the high loss energy component corresponds to the excitation to the $2p^{-1}_{3/2}e^1_g$ (403.6eV). The analysis of the excitation energy dependence of the resonant peaks for the photon energies exceeding the $2p_{1/2}$ threshold is complex. From the Fig. 6.20 it is obvious that the Coster-Kronig decay of the $2p_{1/2}$ take place at the excitation energy of 406.1 eV (peak c). As the band gap in the oxide is large than the spin-orbit splitting, this experimental observation means that the Coster-Kronig process involves the electron excited into the d states. From this consideration, the absent of the emission peak at the 392.1 eV in the VB spectrum excited at the 406.1 eV and its appearing in the VB spectrum excited at 407.8 eV is not clear. The average energy position of the $I(t_{2g})$ component is 8.3±0.7 eV in the energy loss scale, the average energy position of the $I(e_g)$ component is 10.0±0.4 eV. The energy splitting between $I(t_{2g})$ and $I(e_g)$ components is 1.7±0.2 eV, which is close to the $2p^{-1}t_{2g}$ – $2p^{-1}e_g$ splitting measured by the SXA. The elastic peak becomes stronger at the excitation into the e_g states and weaker at the other energies.

The direct comparison of the resonant behavior of the X-ray fluorescence spectra measured on Cr and CrO_2 was reported by E.Z. Kurmaev et al. [126]. The general character of the changes in the spectral shape and the excitation energy dependence of elastic and inelastic features are similar to the results presented in this work. The advantage of the present investigation is the additional information obtained by recording the excitation energy dependence of the core-to-core transition for both Sc metal and Sc oxide. The experimentally observed excitation energy dependence of 3p→2p and VB→2p transitions in Sc_2O_3 must be considered together and a common explanation of the complex relaxation process found. The fact that 3p→2p and VB→2p transitions demonstrate qualitatively different excitation energy behavior and have different characteristics (the linewidth and the energy position) in the oxide and in the metal can be used for the further analysis of the chemical state of the Sc atom in different compounds.

6.3.3 $Sc(acac)_3$.

From the chemistry point of view the energy shift of the resonant inelastic feature from the elastic peak and the enhancement of the crystal field caused component at different excitation energies can be parameters for the evaluation of the effective charge and the hybridization status of the Sc atom in compounds. To test the chemical sensitivity of VB RIXS spectra for $Sc(acac)_3$ were recorded. This compound is very similar to Sc_2O_3 in structure regarding the local chemical surrounding of the Sc atom but as it can be seen from the absorption spectrum both compounds are significantly different in the electron distribution.

RIXS spectra of $Sc(acac)_3$ excited at the primary photon energies indicated in the SXA spectrum are shown in Fig. 6.24. A picture very similar to the oxide excitation energy dependence is observed. The high energy excited spectra are nearly identical, as expected, due to the fact that non-resonant core-to-core spectra are not sensitive to the chemical state of Sc. The energy position of the non-resonant peaks (L_l and L_η) in the high energy excited spectrum of $Sc(acac)_3$ are equal to 349.3 and 353.6 eV, the widths are equal to 1.4 eV FWHM, the L_l/ L_η intensity ratio is equal to 4.0. The most pronounced difference between Sc oxide and (acac) is the relative contribution of the non-resonant part to the spectra.

All spectra can be decomposed into components similar to the oxide case and the non-resonant part can be extracted. The resulting resonant peaks plotted versus the (E_{emiss}-$\hbar\omega_{in}$) energy are shown in Fig. 6.25. The assignment of the components of the resonant part of the fluorescence can be made based on the intensity enhancement of the components with the excitation energy and their energy position on the loss energy scale. The final states energies in $Sc(acac)_3$ are measured as the average position of the components excited at different photon energies and are equal to 51.9 (1), 53.0 (2), 53.2 (3), 54.3 (4) ±0.2 eV. The energy splitting between the singlet and the triplet component is 1.2±0.2 eV. The energy splitting between the $3s^{-1}3t_{2g}$ and the $3s^{-1}3t_{2g}$ final state is 1.3±0.2 eV which is smaller than the $2p^{-1}t_{2g}$ – $2p^{-1}e_g$ splitting measured by SXA (1.5 eV).

In Fig. 6.26 the VB RIXS spectra of $Sc(acac)_3$ excited at the primary photon energies corresponding to the resonance peaks in the SXA spectrum are shown. The high energy excited spectrum is significantly different from the oxide: there is no double structure observed in the low energy part of the spectrum and the relative intensity of low and high energy structures decreases. This behavior can be explained by the stronger hybridization of the d states with the O 2p states compared to the oxide: the increase of the width of the absorption peaks in (acac) support this interpretation. At the energies close to the excitation threshold the observed emission spectra have a shape close to a Gaussian and no singlet and triplet component could be resolved. On the right of Fig. 6.26 the same RIXS spectra are plotted on the Raman shift energy scale. The dotted lines indicate the possible position of $I(t_{2g})$ and $I(e_g)$ components estimated from the excitation energy behavior of the RIXS spectra (6.0 and 7.2±0.5 eV). The energy separation between the $I(t_{2g})$ and the $I(e_g)$ peaks is equal to 1.2 eV which is less to the $I(t_{2g})$ - $I(e_g)$ splitting measured for the oxide (1.7 eV).

The intensity of the resonant peak relative to the non-resonant contribution decreases

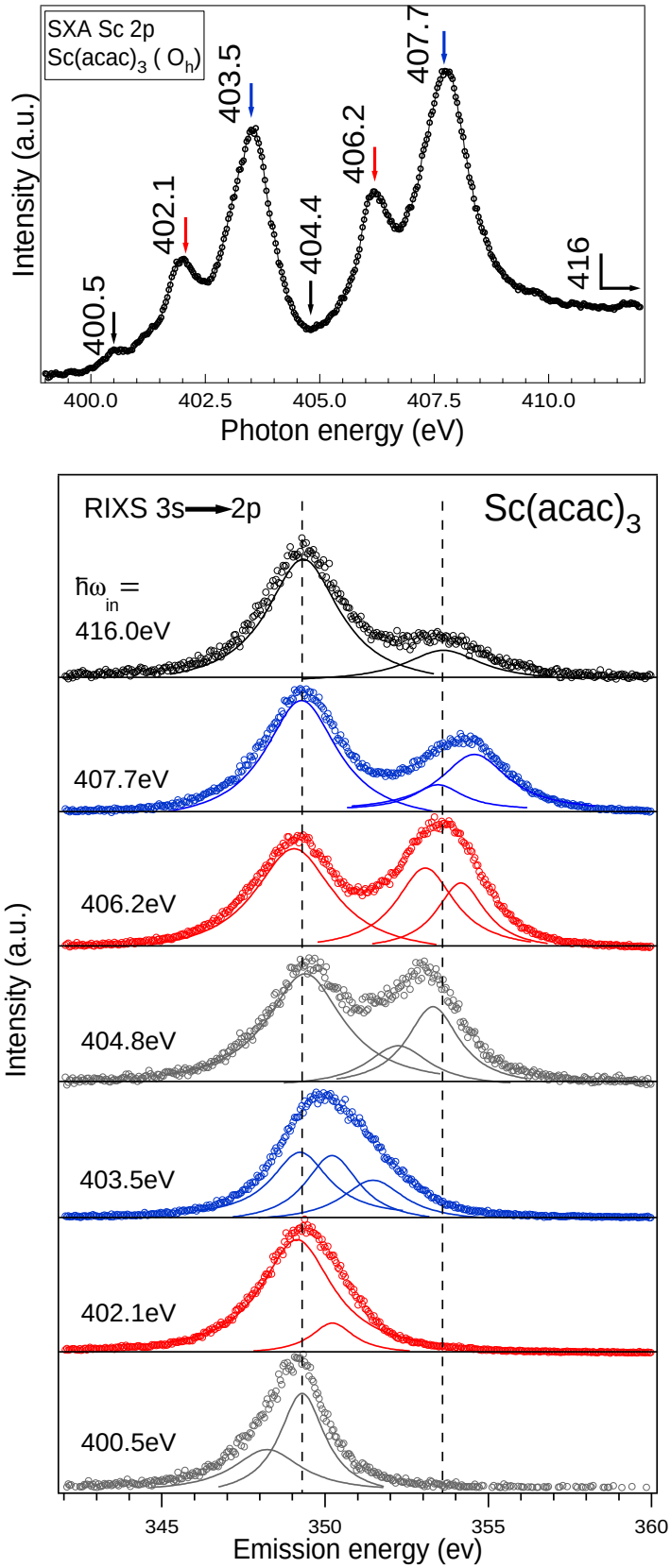

Figure 6.24: RIXS core-to-core (3s→2p) spectra of $Sc(acac)_3$ excited at photon energies indicated in SXA spectrum above by arrows.

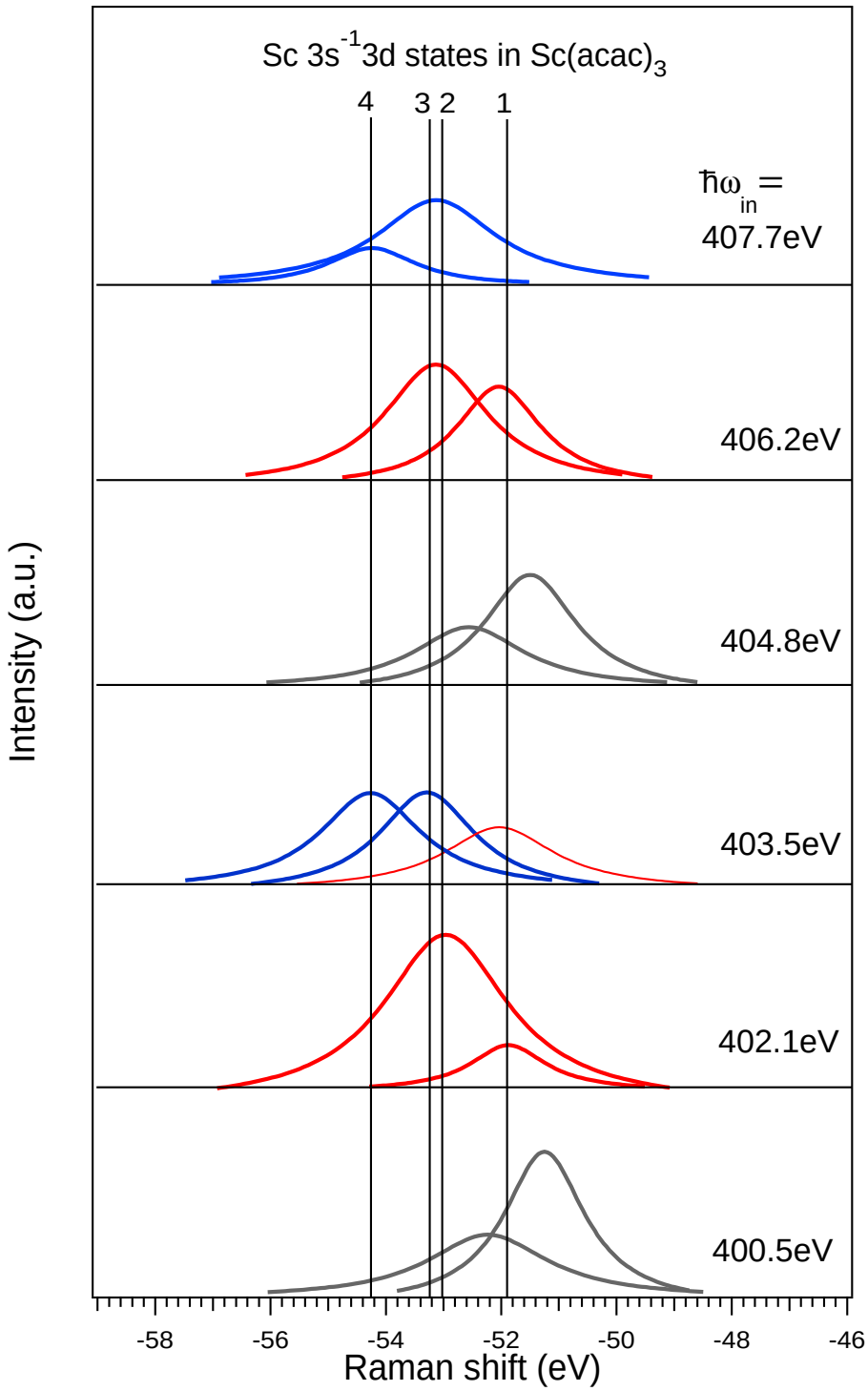

Figure 6.25: Resonant part of RIXS 3s→2p spectra of $Sc(acac)_3$ plotted on the final state energy scale. Solid lines mark the final states: 1 - $3s^{-1}3t_{2g}$ triplet, 2 - $3s^{-1}3t_{2g}$ singlet, 3 - $3s^{-1}3e_g$ triplet, 4 - $3s^{-1}3e_g$ singlet.

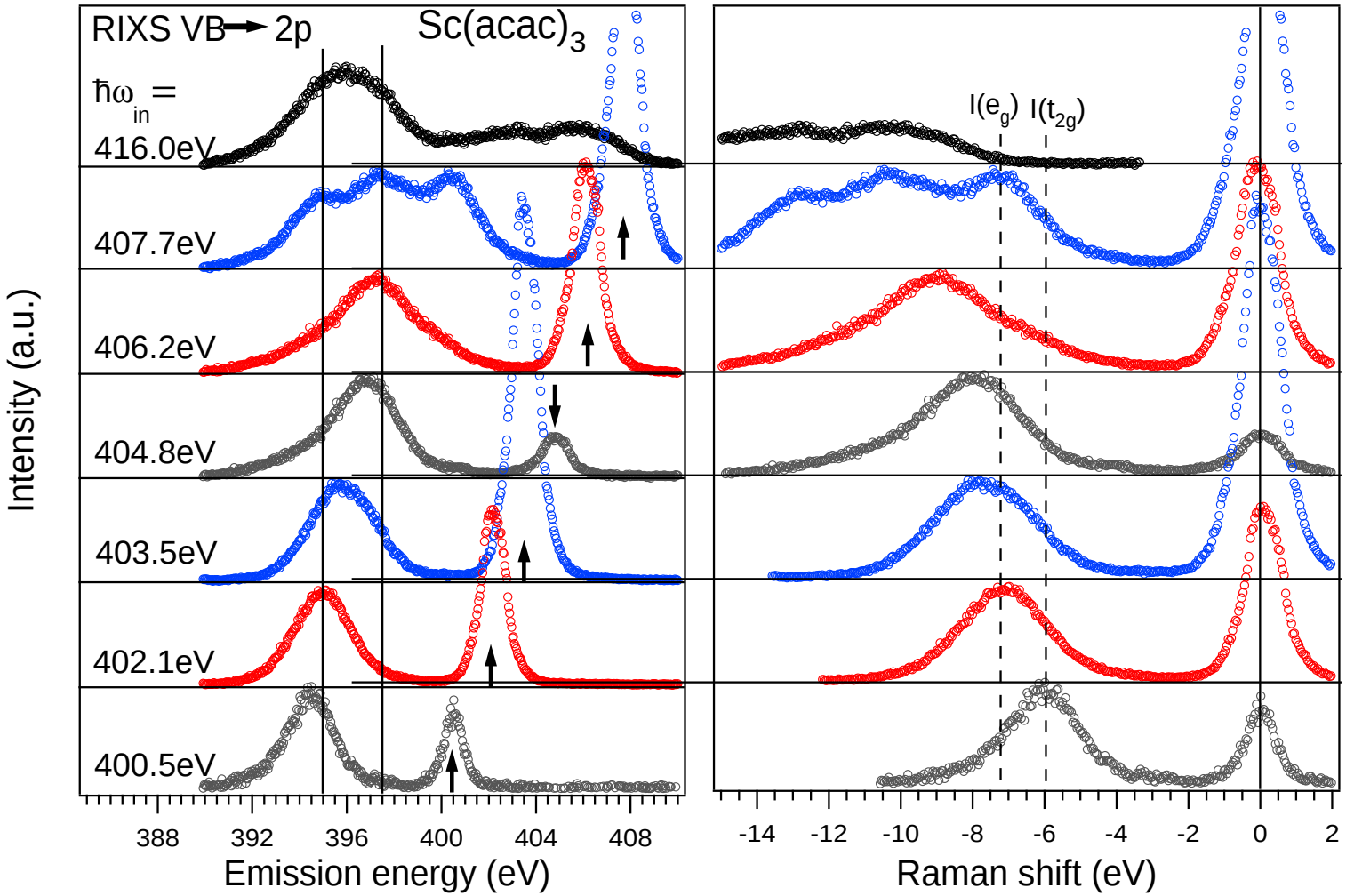

Figure 6.26: (left) RIXS (VB→2p) spectra of $Sc(acac)_3$ excited at photon energies indicated in SXA spectrum in Fig. 6.24 (top). Arrows marks the position of the elastic peaks, solid lines mark positions of the non-resonance inelastic peaks. (right). The same spectra plotted versus the Raman shift. The solid line marks the elastic peak, dotted lines mark positions of resonance peaks in the loss energy scale.

compared to the oxide. The non-resonant peak around the $\hbar\omega_{out}$=395 eV can be observed already at low excitation energies of 402.1 and 403.5 eV.

The effective charge transfer can be traced according to S. Shin et.al [118] by measuring the Raman shift of the resonant component in the RIXS spectra. The energy position of the lowest loss energy component relative to the elastic peak in oxide and (acac) are measured to be equal to 8.3eV and 6.0eV, respectively. The relative shift for the oxide reported by S. Shin [118] (10.4 eV) is not in agreement with the value measured in the present work for the oxide but may correspond to the average value between the I(t_{2g}) and the I(e_g) Raman shift as those two components are not resolved in the measurements of S. Shin at el.. The Raman shift of the loss energy component for the $Sc(acac)_3$ is measured for the first time. As was discussed above, based on the analysis of the SXA spectra, the charge transfer from the metal to the ligand is less in the (acac) than in the oxide. This conclusion is supported of the reducing of the Raman shift in the (acac) compared to the oxide similar to the tendency observed by S. Shin in Sc halides (see Fig. 6.18 on page 101).

6.3.4 $Sc_3N@C_{80}$.

As observed from the comparison between the fluorescence spectra of Sc_2O_3, $Sc(acac)_3$ and Sc metal the main effects of the changing of the character of the chemical bonding from the ionic to the covalent - ionic / metallic are the splitting of the spin-orbit component, the decrease of the line width of the core-to-core transitions and stronger non-resonance behavior of the VB emission spectra. Based on these observations, some conclusions can be make about the chemical state of the Sc atom in the $Sc_3N@C_{80}$.

Core-to-core spectra of $Sc_3N@C_{80}$ excited at the primary photon energies indicated in the SXA spectrum are shown in Fig. 6.27. The width of the non-resonant L_l and L_η peaks measured at the 416 eV excitation energy are both 1.2±0.2 eV, which is smaller than in the oxide. Their relative intensity and the energy splitting are close to the value of the spectra of Sc metal. The excitation energy dependence of the core-to-core spectra is much weaker and the relative intensity of the non-resonant contribution increases compared to the oxide.

All spectra can be decomposed into Lorenzian components and the non-resonant part of spectra can be identified. The resonant contribution to the emission is plotted in the conventional way versus the Raman shift in Fig. 6.28. No singlet and triplet components are resolved. The final states energies in $Sc_3N@C_{80}$ are measured as the average value of the peak position on the loss energy scale and are equal to 52.5 and 53.4 ±0.2 eV. The energy splitting between $3s^{-1}3d_1$ and $3s^{-1}3d_2$ is equal to 0.9 eV, where $3d_1$ is the group of Sc d orbitals interacting weakly with ligands and $3d_2$ is the group of Sc d orbitals interacting strongly with ligands (as discussed before in the subsection 6.2.2). All those observations indicate that the bonding of the Sc atom in the fullerene has a strong covalent character and less ionic than the Sc - O bonding in $Sc(acac)_3$.

In Fig. 6.29 RIXS spectra of $Sc_3N@C_{80}$ excited at photon energies marked in Fig. 6.27 are shown. As the nitrogen 1s core level is very close to the scandium 2p core level in energy, both of them can be excited. The expected low fluorescence yield of the N 2p→1s transitions (see discussion above concerning the SXA spectrum of the fullerene in the

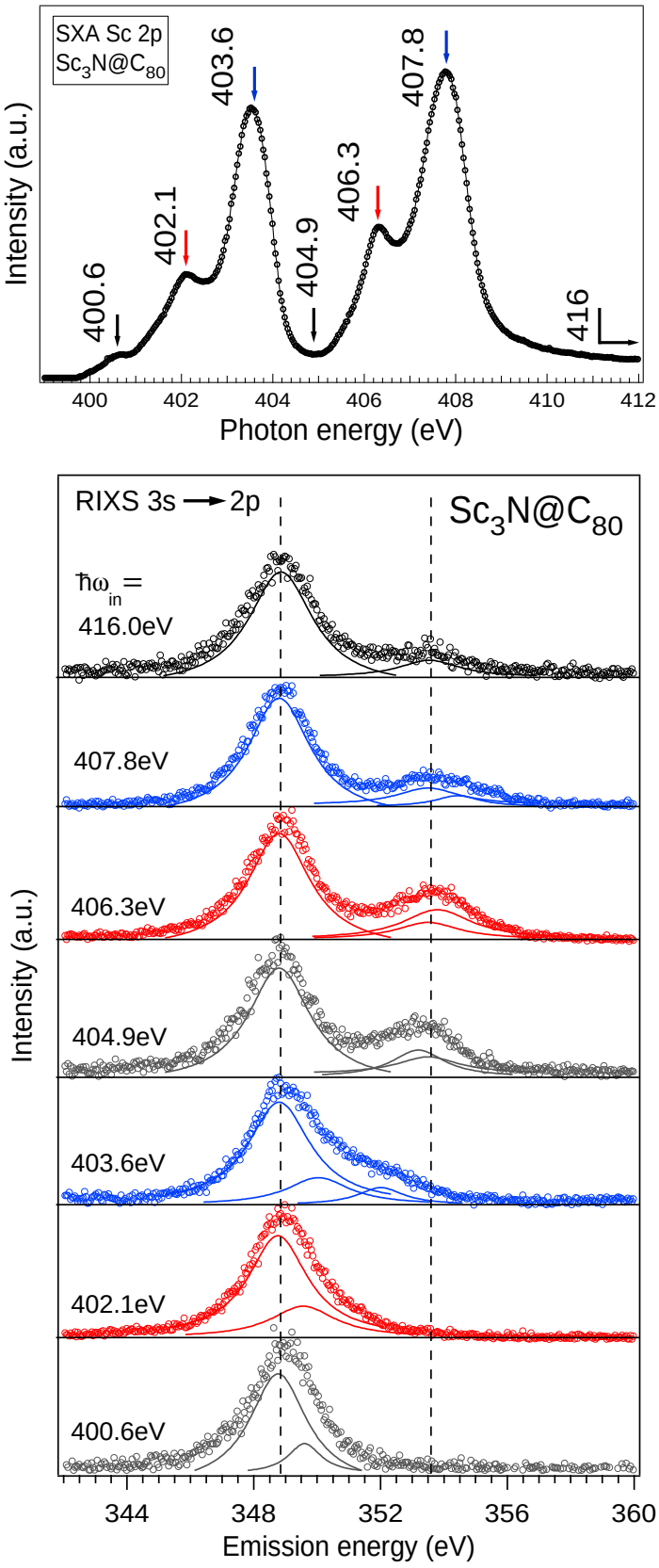

Figure 6.27: RIXS core-to-core (3s→2p) spectra of $Sc_3N@C_{80}$ excited at photon energies indicated in the SXA spectrum above by arrows. Dotted line mark the energy position of the non-resonant L_l and L_η line.

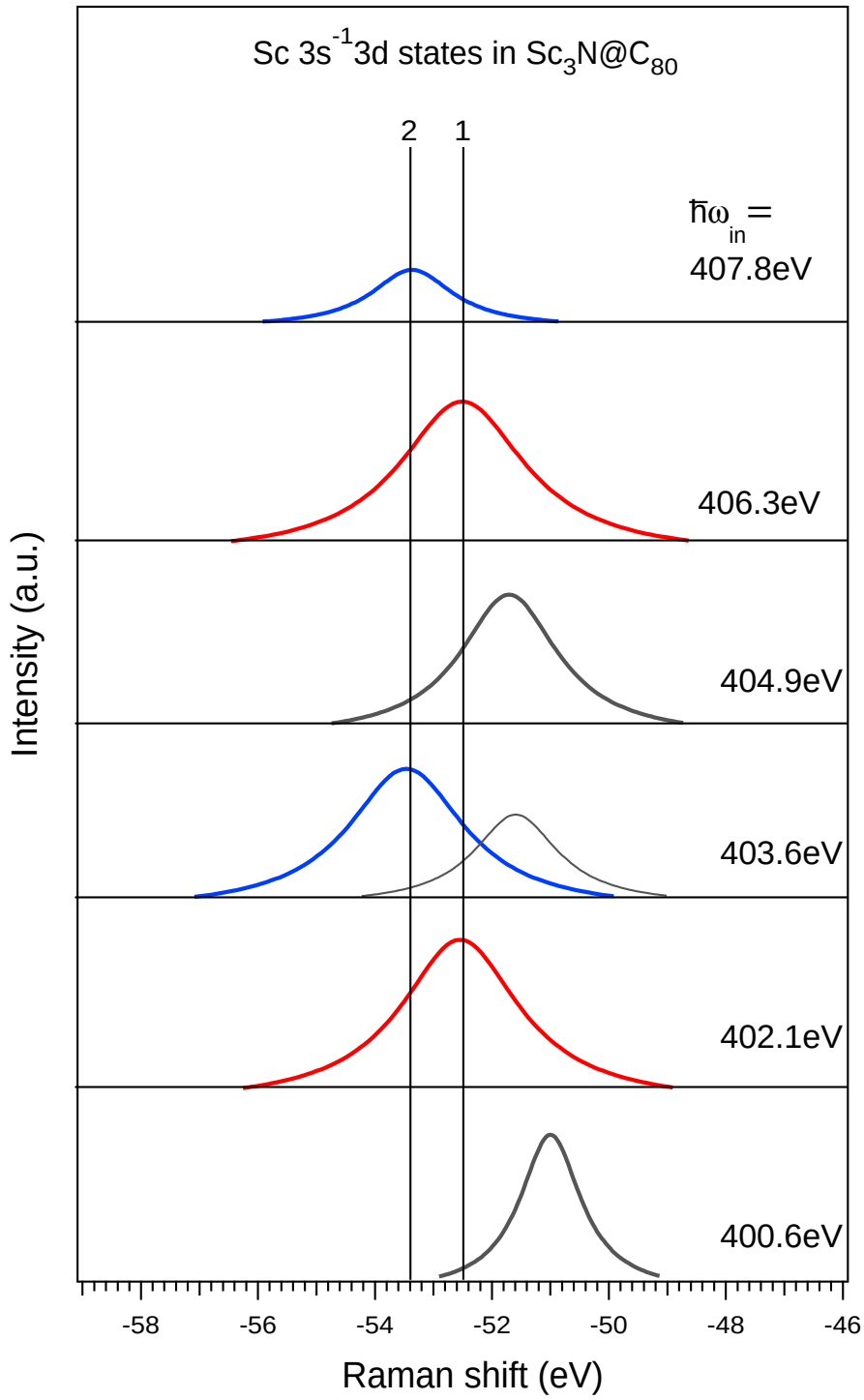

Figure 6.28: Resonant part of RIXS 3s→2p spectra of $Sc_3N@C_{80}$ plotted on the Raman shift scale. Solid lines mark the final states: 1 - $3s^{-1}3d_1$, 2 - $3s^{-1}3d_2$, where $3d_1$ is the group of Sc d orbitals interacting weak with the ligands and $3d_2$ is the group of Sc d orbitals interacting strong with the ligands.

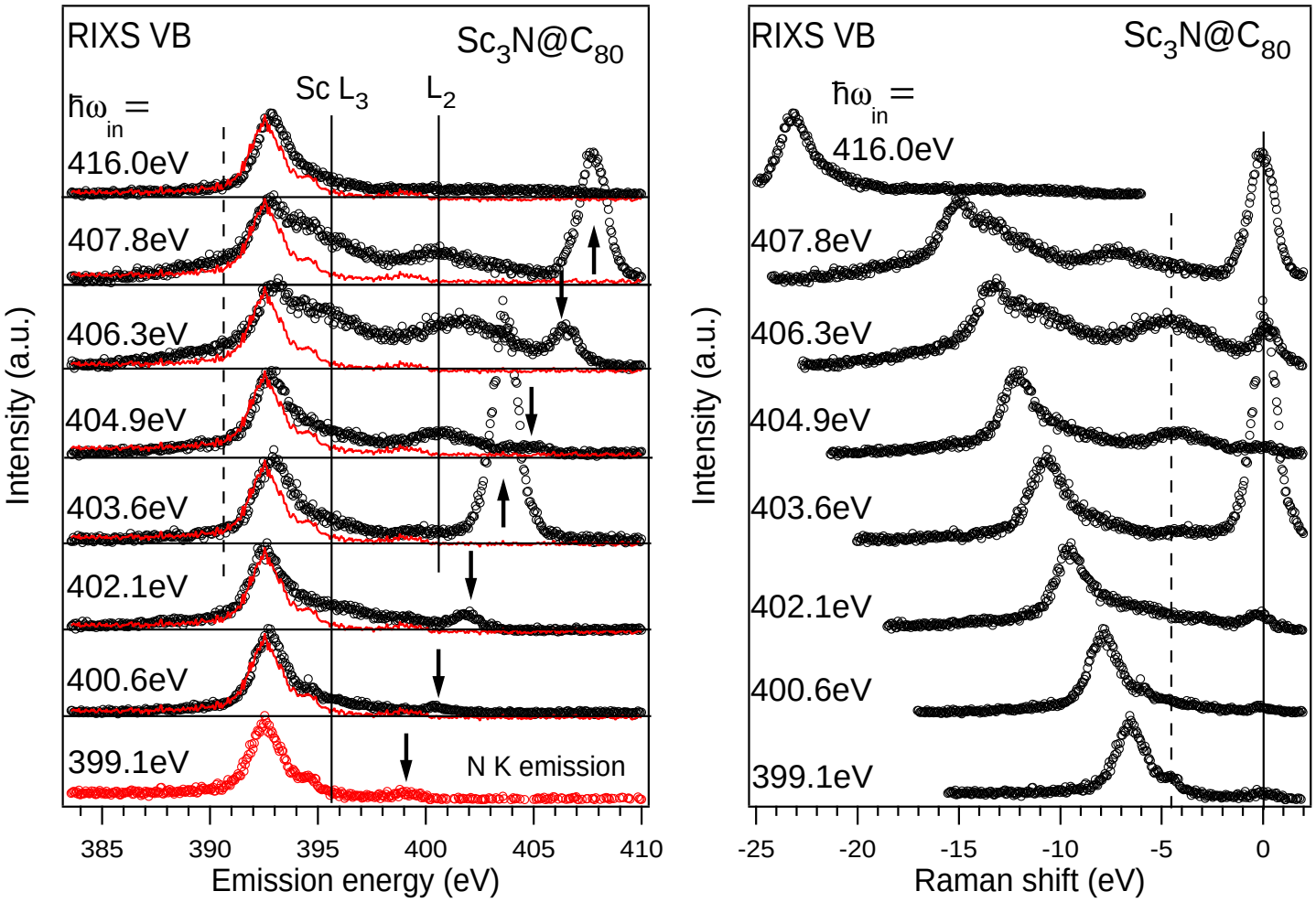

Figure 6.29: (left) RIXS (VB→2p) spectra of $Sc_3N@C_{80}$ excited at photon energies indicated in SXA spectrum in Fig. 6.27. Red spectrum is N K-emission. Arrows marks the position of the elastic peaks, solid lines mark positions of the Sc L_3 and L_2 emission bands. Dashed line marks the position of the low energy satellite of the Sc L_3 emission band. (right) The same spectra plotted versus the Raman shift. The solid line marks the elastic peak, the dotted line marks positions of resonance peaks in the loss energy scale.

section 6.2.2) was a prerequisite to observe strong Sc L-emission lines. Nevertheless, the fluorescence spectrum excited at the 399.1eV has to be identified as the N K-emission due to two facts. First, the shape of the spectrum does not change with the excitation energy variation. Second, no spin-orbit partner appears at the excitation energies exceeding the Sc $2p_{1/2}$ threshold. From the figure one sees that the N K-emission dominates at the low excitation energies. The significant contribution from the Sc first observed in the spectra excited at 402.1eV. Overlapping of the Sc L-emission and N K-emission lines in photon energies makes more detailed analysis of the energy dependence of the Sc fluorescence impossible.

The same VB RIXS spectra are plotted at the right side of Fig. 6.29 but in the Raman shift energy scale. The weak resonant feature can be identified at the photon energy equal to 4.5±0.2 eV in the loss energy scale.

Another interesting behavior is the long high energy tail of the Sc L-emission spectrum. This can be the C states which are observed due a strong hybridization between Sc and C atoms as the top of the VB formed by carbon states. No long high energy tail is observed for the N K band, as the nitrogen atom does not chemically bond to the cage.

Density functional calculations have been performed on $Sc_3N@C_{80}$ to examine the bonding between the scandium atoms and the fullerene cage [32]. The encapsulation of the Sc_3N unit is a strongly exothermic process that is accompanied by a formal transfer of six electrons from the scandium atoms to the fullerene cage. It was found that the Sc_3N unit is not trapped in a specific position within the inner surface of the C_{80} cage, which is an unusual fullerene that lacks pyracylene patches. Thus, free rotation of the Sc_3N group within the C_{80} cage is expected. Despite the electronic transfer from the Sc_3N unit to the carbon cage, $Sc_3N@C_{80}$ was estimated to have relatively large electron affinities and ionization potentials. This prediction is supported by the 13C NMR measurements that suggest that the trimetallic nitride may freely rotate inside the cage [102]. The sign of strong hybridization between the cage and scandium observed in the RIXS spectra of $Sc_3N@C_{80}$ mentioned above may be additional support of the idea of a free rotation of the Sc_3N unit inside the carbon cage. The character of the chemical bonding and the charge transfere from to furellene might be quantitatively established from the experimental data presented in this work in future by using the theoretical calculations [32, 127].

6.4 Conclusions.

To summarize, the strong correlation between the chemical state of the Sc atom and the characteristics of the X-ray emission and absorption lines is observed. The energy splitting and the width of the absorption peaks corresponding to the transition to the intermediate state with a different symmetry governed by the ligand coordination can be coupled to the characteristics of the Sc-ligand bond. The decay of those intermediate states was monitored by measuring the intensity of the 3s→2p and VB→2p transitions. The high energy excited core-to-core spectra of in the raw Sc metal - $Sc_3N@C_{80}$ - $Sc(acac)_3$ - Sc_2O_3 differ from each other by the increasing of the relative intensity of the counterpart contributions and of the width of the peaks and by the decreasing of the L_η – L_l splitting. To summarize, the spectral characteristics are put together in the Table 6.4. The relative

Sample	E(L_l)	w(L_l)	E(L_η)	w(L_η)	I(L_η)/I(L_l)	I_{res}/I_{nonres}
Sc_2O_3	349.5	1.4	353.6	1.5	0.28	1.40
$Sc(acac)_3$	349.3	1.4	353.6	1.4	0.25	1.10
$Sc_3N@C_{80}$	348.8	1.2	353.5	1.2	0.15	0.25
Sc metal	348.4	1.0	353.1	1.3	0.17	0.20

Table 6.4: Spectral characteristics of core-to-core spectra. E is the position of the maximum in eV, w is the width of the Lorenzian peaks in eV, I is the intensity, I_{res}/I_{nonres} is the intensity ratio of the resonant peaks to the non-resonant peak in the SXF spectrum excited at the photon energy corresponding to the d state strongly interacting with ligands ($2p^{-1}_{1/2}t_{2g}$ for Sc_2O_3 and $Sc(acac)_3$, $2p^{-1}_{1/2}3d_2$ for $Sc_2N@C_{80}$) and 407.6 eV for Sc metal.

intensity of spin-orbit component depends on the chemical state in an indirect way, as the $2p^{-1}_{1/2}$ hole can decay via Coster-Kronig Auger process into the $2p^{-1}_{3/2}$ state. The probability of the non-radiative decay strongly depends on the degree of the covalency of the bond. The energy splitting of the L_η and L_l peaks is governed by the 3s hole interaction with the d states. The more covalent the bond the less d states interact with the 3s state as they are shielded by the 4s states. The energy splitting of spin-orbit components, in contrast, increases going from the oxide to the metal. The width of the emission lines decreases in the metal compared to the oxide. The difference in linewidths can be due to the decrease of the lifetime of the 3s hole or due to the optical phonon broadening of the 3s line or due to the contaction of the atomic orbitals in the oxide compared to the metal. Which process is dominating is the quation of further investigations. The effects of 2p-3d exchange interaction are observed in the resonant excited spectra also as changing of the relative intensity of the resonant and non-resonant part. The resonant behavior of the intensity of VB→2p transitions was monitored for the same Sc compounds. Due to the complex character of the spectra no quantitative conclusion can be made. However, the Raman shift of the lowest loss energy component relative to the elastic peak is a feature, showing a tend characterizing the Sc - ligand bond.

The general conclusion about the high degree of the covalent character in the bonding of the Sc atom in the fullerene compare to Sc oxide or $Sc(acac)_3$ can be made based on the analysis of SXA and RIXS spectra.

Chapter 7

Summary.

We showed that soft X-ray absorption and emission spectroscopy are excellent tools to study the electronic structure of nanostructured materials. The bulk sensitivity of the method allows to study the electronic structure of embedded materials and tubes in bundles. The local and chemical sensitivity allows to investigate atoms with different local surrounding and trace changes in the structure. The photon-in-photon-our mode is applied to all materials including isolators. The understanding of how the electronic properties of materials change with the size is an important task from both industrial and academical points of view. Even when nanomaterials have the stoichiometry similar to the bulk material they often exhibit new properties. The surrounding can be used to stabilize the nanostucture or modify its properties. In the case of Si clusters, a glass matrix protects them from oxidation. In turn, an influence of the glass matrix on the optoelectronic properties of the clusters was observed. In the case of nanowires based on Mo and S, the instability of the individual tube is compensated by the formation of bundles or introduction of iodine atoms into the structure.

In the case of Si nanoparticles embedded into the glass matrix the formation of a core-shell structure was confirmed. The size and the chemical composition of the transition layer was studied. An increase of the band gap size with a decrease of the particle size is observed. The energy shifts of the top of the valence band and of the bottom of the conduction band were measured separately. The observed opening of the band gap with the decrease of the particle size is mostly due to the shift of the top of the occupied states to higher binding energies. The quantity of the increase, however, is smaller than the theory based on the free electron approximation predicts. This can be explained by the modification of the energy of the unoccupied states due to the Coulomb interaction with the core hole. It was concluded that the formation of excitonic states counterbalances the quantum confinement effects. The corrected value of the band gap can be obtained by assuming the creation of core excitons and taking into account presence of the oxide layer around the particle. The binding energy of the exciton drastically increases due to the size confinement. These experimental data can contribute to an improved theoretical description of the electronic properties of matrix embedded nanocrystals which takes details of the confining potential well - as given by the suboxide transition region and the matrix oxide- into account.

The electronic structure of the diameter nanotubes (NTs) based on structures con-

taining Mo, S and I was studied. The density of occupied and unoccupied states of MoS_2 NTs are significantly different from the bulk MoS_2. The changes in the electronic structure are explained based on electronic structure calculation of a simple model structure including the core hole effect. Absorption and emission spectra simulated based on the model structure reproduced the experimentally observed decrease of the density of sulfur states at the bottom of empty band and the increase of the states at the top of the occupied band. These changes are mostly due to the modification of the bond angle between sulphur and molybdenum atoms. The presence of iodine atoms can additionally influence the electronic structure of the tubes but cannot be included in the simple model.

Earlier theoretical calculations of MoS_2 NTs predicted that small diameter tubes are unstable due to the strong repulsion of sulphur atoms. When the core of the tube consist of the molybdenum, the tubes may stabilize and demonstrate metallic or semimetallic properties. The electronic structure of valence and conduction bands was studied for $Mo_6S_{9-x}I_x$ nanowires for x=6 and 4.5. Similar to the MoS_2 NTs, the decrease of the density at the bottom of empty band and the increase of the states at the top of the occupied band was observed. For $Mo_6S_3I_6$ NTs complete DFT calculation in the ground state for two possible structures were carried out. The results of these calculations including the hybridization between sulphur and molybdenum states were compared to the experimental data. These theoretical calculation resemble the experimental SXE data, but some disagreement can be clearly seen in SXA and RIXS data. For instance, the shape of the S 2p resonance excited fluorescence spectra resembles in high degree the Mo d density of states. This gives a hint to a possible presence of alternative excitation channels in the nanomaterial containing transition metal atoms, where the electronic properties are dominated by the atomic nature of the d electrons.

A systematic study of the correlation between the chemical state of the Sc atom and the characteristics of the X-ray emission and absorption lines for different compounds was made. The delicate nature of the interaction of the d electrons with strongly bonded and valence electrons is reflected in spectra of Sc compounds. On one hand, well defined intermediate states are created in compounds with strong ionic character of the bond. The reason for this is the strong exchange interaction between the core states and the atomic like d states. In the compound with a bond of mixed ionic-covalent character, core states are screened from the d states and the interaction decreases. In the 2p absorption spectra the increase of the effective screening of the core hole is observed as the decrease of the energy splitting and the increase of the width of the absorption peaks. The excitation energy dependence of two channels of the fluorescence decay of the Sc 2p core hole were observed. The high energy excited core-to-core spectra of different compounds differ from each other by the increase of the relative intensity of the spin-orbit contributions, by the increase of the width of the peaks and by the decrease of the L_η – L_l splitting with increasing ionic character of the Sc-ligand bond. The effects of 2p-3d exchange interaction are observed in the resonantly excited core-to-core spectra as a change of the relative intensity of the resonant and non-resonant part of the observed signal. A correlation between the chemical state of the Sc atom and the spectral characteristics of the valence band fluorescence was observed for the compounds. It was found out that the Raman shift of the lowest loss energy component relative to the elastic peak is a "finger print" of the Sc - ligand bond. However, due to the complex character of the spectra no

quantitative conclusion regarding the numerical relation between the bond parameter and spectral characteristics could be made. The general conclusion about the high degree of the covalent character in the bonding of the Sc atom in the fullerene compare to Sc oxide or $Sc(acac)_3$ can be made based on the analysis of SXA and RIXS spectra. However, this general consideration doesn't explain all effects observed in the present work. Even in metallic Sc atomic character of the d states influences the shape of absorption and fluorescence spectra. The analysis is a complicated task as all electron interactions must be considered together with the core hole effects. A theory including all those affects is required for a detailed understanding of the experimental results.

The behavior of electrons in materials investigated in this work can be described in different approximations. The SXS spectra of Si nanoparticles are well understood in the one-electron approach. The atomic-like structure and the primary photon energy dependence of fluorescence spectra of Sc compounds must be considered as transitions between multi-electron states. It the case of nanostructures on the base of Mo, S and I the observed spectra can be only partially reproduced by theoretical calculations of the electronic system in the ground state. The exciton formation, the exchange interaction between the core hole and d electrons and multiplet interactions are processes which influence the interaction of the soft X-rays with matter. These processes are dependent on the size of material. The basic study of such effects can help to improve the design of new materials of nanometer size with desirable physical and chemical properties.

Appendix A

List of publications.

1. Eisebitt, S.; Karl, A.; Zimina, A.; Scherer, R.; Freiwald, M.; Eberhardt, W.; Hauke, F.; Hirsch, A.; Achiba, Y. Year of Conference: 2000 *Electronic Structure of Doped Fullerenes and Single Wall Carbon Nanotubes.* in Electronic Properties of Novel Materials: molecular nanostructures AIP Conference Proceedings, **544**, Melville (2000).

2. Zimina, A. V.; Shulakov, A. S.; Eisebitt, S.; Eberhardt, W. *Depth-resolved soft X-ray emission spectroscopy of Si-based materials.* Surface Review and Letters **9(1)**, p. 461-467 (2002).

3. Burgler, D. E.; Buchmeier, M.; Cramm, S.; Eisebitt, S.; Gareev, R. R.; Grunberg, P.; Jia, C. L.; Pohlmann, L. L.; Schreiber, R.; Siegel, M.; Qin, Y. L.; Zimina, A. *Exchange coupling of ferromagnetic films across metallic and semiconducting interlayers.* Journal of Physics-Condensed Matter **15(5)**, p. S443-S450 (2003).

4. Ruck, B. J.; Koo, A.; Lanke, U. D.; Budde, F.; Trodahl, H. J.; Williams, G. V. M.; Bittar, A.; Metson, J. B.; Nodwell, E.; Tiedje, T.; Zimina, A.; Eisebitt, S. *Filled and empty states of disordered GaN studied by x-ray absorption and emission.* Journal of Applied Physics **96(6)**, p. 3571-3573 (2004).

5. Zimina, A.; Eisebitt, S.; Freiwald, M.; Cramm, S.; Eberhardt, W.; Mrzel, A.; Mihailovic, D. *Electronic structure of subnanometer diameter MOS2-I-x nanotubes.*, in Nano Letters **4** p. 1749-1753 (2004).

6. Aziz, E. F.; Zimina, A.; Eisebitt, S.; Eberhardt, W. *Molecular and electronic structure in NaCl electrolytes of varying concentration: Identification of spectral fingerprints.* The Journal of Chemical Physics **124** p. 114502 (2006).

7. Zimina, A.; Eisebitt, S.; Eberhardt, W.; Heitmann, J.; Zacharias, M. *Electronic Structure and Chemical Environment of Silicon Nanoclusters Embedded in a Silicon Dioxide Matrix.* Applied Physics Letters, **77**, 163103 (2006).

Bibliography

[1] T. van Buuren, T. Tiedje, J. R. Dahn, and Way B. M. Photoelectron-Spectroscopy Measurements of the Band-Gap in Porous Silicon. *Appl. Phys. Letters*, 63:2911, 1993.

[2] Brongersma M. L., Polman A., Min K. S., and Atwater H. A. Depth distribution of luminescent Si nanocrystals in Si implanted SiO_2 films on Si. *Journal of Applied Physics*, 86:759, 1999.

[3] Hayashi S. and Yamamoto K. Optical properties of Si-rich SiO_2 films in relation with embedded Si mesoscopic particles. *Journal of Luminescence*, 70:352, 1996.

[4] Kahler U. and Hofmeister H. Visible light emission from Si nanocrystalline composites via reactive evaporation of SiO. *Optical Materials*, 17:83, 2001.

[5] Zacharias M., Heitmann J., Scholz R., and et al. Size-controlled highly luminescent silicon nanocrystals: A SiO/SiO_2 superlattice approach. *Applied Physics Letters*, 80:661, 2002.

[6] Iijima S. Helical microtubules of graphitic carbon. *Nature(London)*, 354(6348):56–58, 1991.

[7] Niyogi S., Hamon M. A., Hu H., Zhao B., Bhowmik P., Sen R., Itkis M. E., and Haddon R. C. Chemistry of Single-Walled Carbon Nanotubes. *Accounts of Chemical Research*, 35(12):1105–1113, 2002.

[8] Ajayan P. M. and Zhou O. Z. Springer, Berlin.

[9] Avouris P. Carbon nanotube electronics. *Chemical Physics*, 281(2-3):429–445, 2002.

[10] Dresselhaus M. S., Dresselhaus G., and Avouris Ph. *Carbon Nanotubes*. Springer, Berlin, 2000.

[11] Tenne R. M. L., Genut M., and Hodes G. Polyhedral and cylindrical structures of tungsten disulfide. *Nature(London)*, 360:444, 1992.

[12] Chopra N. G. L., Chopra R. J., Cherrey K., Crespi V. H., Cohen M. L., Louie S. G., and Zettl A. Boron nitride nanotubes. *Science*, 269:966, 1995.

[13] Seifert G., Terrones H., and et al. Structure and electronic properties of MoS_2 nanotubes. *PRL*, 85(1):146–149, 2000.

[14] Jäger-Waldau A., M. Ch. Lux-Steiner, and E. Bucher. Polycrystalline Semicond. III, Phys. and Technol., Solid State Phenom. *Scitec Publications (Switzerland)*, 37-38:214, 1994.

[15] Eisebitt S., Karl A., Eberhardt W., Fisher J.E., Sathe C., Agui A., and Nordgren J. Electronic structure of single-wall carbon nanotubes studied by resonant inelastic X-ray scattering. *Appl. Phys. A*, 67:89, 1998.

[16] Remskar M., Mrzel A., Skraba Z., Jesih A., Ceh M., Demsar J., Stadelmann P., Levy F., and Mihailovic D. Self-assembly of subnanometer-diameter single-wall MoS2 nanotubes. *Science*, 292(5516):479–481, 2001.

[17] Vrbanic D., M. R., Jesih A., Mrzel A., Umek P., Ponikvar M., Jancar B., Meden A., Novosel B., Pejovnik S., Venturini P., Coleman J.N., and Mihailovic D. Air-stable monodispersed Mo6S3I6 nanowires. *Nanotechnology*, 15(5):635–638, 2004.

[18] Nicolosi V., Vrbanic D., Mrzel A., McCauley J., O'Flaherty, Mihailovic D., Blau W.J., and Coleman J.N. Solubility of $Mo_6S_{4.5}I_{4.5}$ nanowires. *Chem. Phys. Lett.*, 401:13, 2005.

[19] Kroto H. W. and Heath J. R.and O'Brien S. C.and Curl R. F.and Smalley R. E. C_{60}: Buckminsterfullerene. *Nature*, 318:162.

[20] Krtschmer W. and Schuster H. *Von Fuller bis zu Fullerenen. Beispiele einer interdisziplinren Forschung.* Vieweg, Wiesbaden, 1996.

[21] Friedman S.H.

[22] Cuberes M. T., Schlittler R. R., and Gimzewsk J. K. Room-temperature repositioning of individual C60 molecules at Cu steps: Operation of a molecular counting device. *Appl. Phys. Lett.*, 69:3016–3018, 1996.

[23] Ginzburg B.M. and Tochil'nikov D.G. Effect of fullerene-containing additives on the bearing capacity of fluoroplastics under friction. *Technical Physics*, 46(2):249.

[24] Braun Th., Wohlers M., Belz T., and Schlägl R. Fullerene-based ruthenium catalysts: a novel approach for anchoring metal to carbonaceous supports. II. Hydrogenation activity. *Catalysis Letters*, 43(3-4):175 – 180, 1997.

[25] Breda N., Broglia R. A.and Colo G., Onida G., Provasi D., and Vigezzi E. C_{28}: A possible room temperature organic superconductor. *PRB*, 62:130–133, 2000.

[26] Shiflett M. B. and Foley H. C. Ultrasonic Deposition of High-Selectivity Nanoporous Carbon Membranes. *Science*, 285:1902–1905, 1999.

[27] Schlebusch C., Morenzin J., Kessler B., and Eberhardt W. Organic photoconductors with C60 for xerography. *Carbon*, 37:717–720, 1999.

[28] Nakao K., Kurita N., and Fujita M. Ab initio molecular-orbital calculation for C_{70} and seven isomers of C_{80}. *PRB*, 49:11415, 1994.

[29] Larade B., Taylor J., Zheng Q. R., Mehrez H., Pomorski P., and Guo H. Renormalized molecular levels in a $Sc_3N@C_{80}$ molecular electronic device. *PRB*, 64:195402, 2001.

[30] Alvarez L., Pichler T., Georgi P., Schwieger T., Peisert H., Dunscha L., Hu Z., Knupfer M., Fink J., Bressler P., Mast M., and Golden M. S. Electronic structure of pristine and intercalated $Sc_3N@C_{80}$ metallofullerene. *PRB*, 66:035107, 2002.

[31] Krause M., Kuzmany H., Georgi P., Dunsch L., Vietze K., and Seifert G. Structure and stability of endohedral fullerene $Sc_3N@C_{80}$: A Raman, infrared, and theoretical analysis. *J. Chem. Phys.*, 115:6596, 2001.

[32] Campanera J.M., Bo C., Olmstead M. M., Balch A. L., and Poblet J. M. Bonding within the Endohedral Fullerenes $Sc_3N@C_{78}$ and $Sc_3N@C_{80}$ as Determined by Density Functional Calculations and Reexamination of the Crystal Structure of $Sc_3N@C_{78}\cdot Co(OEP)\cdot 1.5(c_6h_6)\cdot 0.3(chcl_3)$.

[33] Pettifor D. *Bonding and structure of moleculesand solids.* Clarendon Press, Oxsford, 1995.

[34] Nordgren J., Glans P., Gunnelin K., Guo J., Skytt P., Sathe C., and Wassdahl N. Resonant soft X-ray fluorescence spectra of molecules. *Applied Physics A: Materials Science Processing*, 65(2):97, 1997.

[35] Eisebitt S., Luening J., Rubenson J.-E., and Eberhardt W. Resonant inelastic soft x-ray scattering as a bandstructure probe: a primer. *Phys. State Solids (b)*, 215:803, 1999.

[36] Ma Y. X-ray absorption, emission, and resonant inelastic scattering in solids. *Phys. Rev. B*, 49:5799, 1994.

[37] Carliste J. A., Shirley E. L., Hudson E. A., Terminello L. J., Callcott T. A., Jia J.J., Ederer D.L., Perera R.C.C., and Himpsel. Probing the Graphite Band Structure with Resonant Soft-X-Ray Fluorescence. *PRL*, 74:1234, 1995.

[38] Ma Y., Wassadahl N., Skytt P., Guo J., Nordgren J., Johnson P.D., Rubensson J.-E., Böske T., Eberhardt W., and Kevan S. D. Soft-x-ray resonant inelastic scattering at the C K edge of diamond. *PRL*, 69:2598, 1992.

[39] Luening J. *Soft X-ray spectroscopy of broadband, size confined and correlated materials.* PhD thesis, University of Cologne, 1998. Berichte des Forschungszentrums Juelich, Juel-3544, ISSN 0944-2952.

[40] Tiedje T., Colbow K.M., Rogers D., and Eberhardt W. Nature of core -electron excited states in the CaF_2 determined by high-resolution absorption and electron-emission studies. *PRB*, 65:1243, 1990.

[41] Sakurai J.J. *Advanced Quantum Mechanics.* Addison-Wesley, London, 1967.

[42] Goodings D.A. and Harris R. Calculation of the X-ray emission bands of copper using augmented plane wave Bloch functions. *J. Phys. C*, 2:1808, 1969.

[43] Jones H., Mott N. F., and Skinner H. W. B. A Theory of the Form of the X-Ray Emission Bands of Metals. *Physical Review*, 45:379384, 1934.

[44] Sparks C. J. and Fischer K. *Resonant Anomalous X-ray Scattering.* North-Holland, Amsterdam, 1994.

[45] *Å*berg T. and Crasemann B. *Resonant Anomalous X-ray Scattering.* In [44], 1994.

[46] Eisebitt S. and Eberhardt W. Band Structure Information and Resonant Inelastic Soft X-ray Scattering in Broad Band Solids. *J. El. Spec. Rel. Phen.*, 110:335, 2000.

[47] von Barth U. and Grossmann G. The effect of the core hole on x-ray emission spectra in simple metals. *Solid State Communications*, 32(8):645–649, 1979.

[48] Zaanen J., Sawatzky G. A., and Allen J. W. Band gaps and electronic structure of transition-metal compounds. *PRL*, 55:418, 1985.

[49] de Groot F.M.F., Fuggle J.C., Thole B.T., and Sawatzky G.A. $L_{2,3}$ x-ray-absorption edges of d^0 compounds: K^+, Ca^{2+}, Sc^{3+}, and Ti^{4+} in O_h (octahedral) symmetry. *PRB*, 41:928, 1990.

[50] de Groot F.M.F., Fuggle J.C., Thole B.T., and Sawatzky G.A. 2p x-ray absorption of 3d transition-metal compounds: An atomic multiplet description including the crystal field. *PRB*, 42:5459, 1990.

[51] van der Laan G. and Kirkman L.W. The 2p absorption spectra of 3d transition metal compounds in tetrahedral and octahedral symmetry. *J. Phys.: Condens. Matter*, 4:4189, 1992.

[52] Cowan R. D. *The theory of atomic structure and spectra.* University of California Press, Berkeley, 1981.

[53] EisebittS., Karl A., Zimina A., Scherer R., Freiwald M., Eberhardt W., Hauke F., Hirsch A., and Achiba Y. Electronic Structure of Doped Fullerenes and Single Wall Carbon Nanotubes. In M. Mehring S. Roth H. Kuzmany, J. Fink, editor, *Electronic Properties of Novel Materials: molecular nanostructures. AIP Conference Proceedings 544.*

[54] Attwood D. *Soft X-Rays and Extreme Ultraviolet Radiation: Principles and Applications.* Cambridge University Press, 1999.

[55] Eisebitt S., Rubensson J.-E., Bske T., and Eberhardt W. Determination of absorption coefficients for concentrated samples by fluorescence detection. *PRB*, 47:14103, 1993.

[56] Krause M. O. Atomic radiative and radiativeless yield for K and L shells. *J. Phys. Chem. Rev. Data*, 8:307, 1979.

[57] Woodruff D. P. and Delchar T. A. *Modern techniques of surface science.* Cambridge University Press, 1994.

[58] Samson J. A. R. *Techniques of vacuum ultraviolet spectroscopy.* John Wiley and Sons Inc., 1967.

[59] Rubensson J. E. Electronic structure determined by soft X-ray emission spectroscopy. *23. IFF Ferienkurs, Forschungszentrum Juelich*, 1992.

[60] Zacharias M., Heitmann J., Yi L. X., Wildanger E., and Scholz R. Towards the First Silicon Laser: Silicon technology used for size-controlled silicon nanocrystals. In Gaponenko S. Pavesi L. and Negro L. D., editors, *NATO Advanced Research Workshop*, volume 93, page 131. Kluwer Academic Publishers, Trento, Italy, 2003.

[61] Bell F.G. and Ley L. Photoemission-Study of SiO_x ($0 \leq x \leq 2$) Alloys. *Phys. Rev. B*, 37:8383, 1988.

[62] Baumvol J.R. and Stedile F.S. Nanostructure of the surface and interface and mechanisms of thermal growth of ultrathin films of Si_3N_4 on Si(001). *Phys. State Sol.*, 192:253, 1995.

[63] Eisebitt S., Luning J., Rubensson J. E., Settels A., Dederichs P. H., Eberhardt W., Patitsas S. N., and Tiedje T. Resonant inelastic soft x-ray scattering at the Si L3 edge: experiment and theory. *Journal of Electron Spectroscopy and Related Phenomena*, 93:245, 1998.

[64] S. Eisebitt, S. N. Patitsas, J. Luning, Rubensson J. E., Tiedje T., van Buuren T., and Eberhardt W. Soft-X-ray fluorescence of porous silicon: Electronic structure of Si nanostructures. *Europhysics Letters*, 37:133, 1997.

[65] Heitmann J., Scholz R., Schmidt M., and Zacharias M. Size controlled nc-Si synthesis by SiO/SiO_2 superlattices. *Journal of Non-Crystalline Solids*, 299:1075, 2002.

[66] J. Heitmann, F. Muller, L. X. Yi, Zacharias M., Kovalev D., and Eichhorn F. Excitons in Si nanocrystals: Confinement and migration effects. *PRB*, 69:195309, 2004.

[67] Daldosso N., Luppi M., Ossicini S., Degoli E., Magri R., Dalba G., Fornasini P., Grisenti R., Rocca F., Pavesi L., Boninelli S., Priolo F., Spinella C., and Iacona F. Role of the interface region on the optoelectronic properties of silicon nanocrystals embedded in SiO_2. *PRB*, 68:085327, 2003.

[68] T. van Buuren, L. N. Dinh, L. L. Chase, Siekhaus W. J., and Terminello L. J. Changes in the electronic properties of Si nanocrystals as a function of particle size. *PRL*, 80:3803, 1998.

[69] Van Buuren T., Dinh L.N., Chase L.L., Siekhaus W.J., Jumenez I., Terminello L.J., Grush M., Callcott T.A., and Carlisle J.A. Soft x-ray emission studies of the electronic structure in silicon nanoclusters. In *1996 Fall meeting of the Materials Research Society (MRS), Boston, MA (United States), 2-6 Dec 1996*, 1997.

[70] K. Rim, J. L. Hoyt, and J. F. Gibbons. Fabrication and Analysis of Deep Submicron Strained-Si N-MOSFETs. *IEEE Transactions on Electronic Devices*, 47:1406, 2000.

[71] Brus L. Zero-Dimensional Excitons in Semiconductor Clusters. *Journal of Physical Chemistry*, 90:2555, 1986.

[72] Wang L. W. and Zunger A. Dielectric-Constants of Silicon Quantum Dots. *PRL*, 73:1039, 1994.

[73] Zunger A. and Wang L. W. Theory of silicon nanostructures. *Applied Surface Science*, 102:350, 1996.

[74] Lannoo M., Delerue C., and Allan G. Screening in Semiconductor Nanocrystallites and Its Consequences for Porous Silicon. *PRL*, 74:3415, 1995.

[75] Wang L. W. and Zunger A. Electronic-Structure Pseudopotential Calculations of Large (Approximate-to-1000 Atoms) Si Quantum Dots. *Journal of Physical Chemistry*, 98:2158, 1994.

[76] Delerue C., Lannoo M., and Allan G. Concept of dielectric constant for nanosized systems. *PRB*, 68:115411, 2003.

[77] Delerue C., Lannoo M., and Allan G. Excitonic and quasiparticle gaps in Si nanocrystals. *PRL*, 84:2457, 2000.

[78] Delerue C., Lannoo M., and Allan G. Size dependence of excitons in silicon nanocrystals - Comment. *PRL*, 76:3038, 1996.

[79] Yang L., Abeles B., Eberhardt W., Stasiewski H., and Sondericker D. Photoemission spectroscopy of heterojunctions of hydrogenated amorphous-silicon with silicon-oxide and nitride. *PRB*, 39:3801, 1989.

[80] Meden A., Korde A., Padeznik Gomilsek J., Arcon I., Vilfan I., Vrbanic D., Mrzel A., and Mihailovic D. Atomic and electronic structure of $Mo_6S_{9-x}I_x$ nanowires. *Nanotechnology*, 16:1578–1583, 2005.

[81] Hermann K., Pettersson L.G.M., Casida M.E., Daul C., Goursot A., Koester A., Proynov E., St-Amant A., Salahub D.R., Carravetta V., Duarte H., Godbout N., Guan J., Jamorski C., Leboeuf M., Malkin V., Malkina O., Nyberg M., Pedocchi L., Sim F., Triguero L., and Vela A. *StoBe-deMon version 1.0*. StoBe Software, 2002.

[82] Raybaud P., Kresse G., Hafner J., and Toulhoat H. Ab initio density functional studies of transition-metal sulfides. I,II. *J. Phys: Condens. Matter*, 9(50):11085, 1997.

[83] Kim K. K. and Parkinson B. A. Detailed Photocurrent Spectroscopy of the Semiconducting Group-Vi Transition-Metal Dichalcogenides. *J. Phys. Chem.*, 86:463, 1982.

[84] Kobayashi K. and Yamauchi J. Electronic structure and scanning-tunneling-microscopy image of molybdenum dichalcogenide surfaces. *PRB*, 51:17085, 1995.

[85] Verstraete M. and Charlier J.-C. Ab initio study of MoS_2 nanotube bundles. *PRB*, 68:045423, 2003.

[86] Kovac J., Zalar A., Remskar M., Mrzel A., Mihailovic D., Gregoratti L., and Kiskinova M. An XPS spectromicroscopic study of Mo-S based nanotubes. *ELETTRA Highlights 2002-2003*, pages 62–63, 2003.

[87] Yeh J. J. *Atomic Calculation of Photoionisation Cross-Sections and Asymmetry Parameters.* Gordon and Breach Science Publishers, Langhorne, PE (USA), 1993.

[88] Vbranic D. unpublished. *privat communication*, 2006.

[89] Svensson S., Ausmees A., Osborne S. J., and et al. Observation of an anomalous decay ratio between the molecular field split levels in the S 2p core photoelectron and LVV Auger spectrum of H_2S. *PRL*, 72:3021, 1994.

[90] Schmitt T., Duda L. C., Matsubara M., Mattesini M., Klemm M.and Augustsson A., Guo J. H., Uozumi T., Horn S., Ahuja R., Kotani A., and J. Nordgren. Electronic structure studies of V_6O_{13} by soft x-ray emission spectroscopy: Band-like and excitonic vanadium states. *PRB*, 69, 2004.

[91] Bokij G. B. *Kristallochimija .(in Russian).* Izdat. Hauka, 1971.

[92] Gerloch M. and Constable E.C. *Transition metal chemistry: the valence shell in d-block chemistry.* VCH, Germany, 1994.

[93] Aronsson B., Lundström T., and Rundqvist S. *Borides, Silicides and Phosphides.* Spottiswoode, Ballantyne and Co. Ltd, 1965.

[94] Sugano S., Tanabe Y., and Kamimura H. *Multiplets of Transition-Metal Ions in Crystals.* Academic, New York, 1970.

[95] Sodhi R.N.S. and Brion C.E. Reference Energies for Inner Shell Electron Energy-Loss Spectroscopy. *J. Electron Spectr. Relat. Phenom.*, 34:363, 1984.

[96] Vinogradov A. S., Dukhnyakov A. Y., Ipatov V. M., Onopko D. E., Pavlychev A. A., and Titov S. A. Fine-Structure of $(TiF_6)^{2-}$ X-Ray Absorption-Spectra. *Fiz. Tverd. Tela (Leningrad), Sov. Phys. Solid State*, 24:1417, 1982.

[97] Wyckoff R.W.G. *Crystal Structures.* John Wiley Sons, New York, London, 1963.

[98] Nowadcki W. The crystal structure of ScF_3. *Naturw.; Z. Krist.*, 26; 101A:801; 273, 1938.

[99] Harned H. S. and Paxton T. R. The Thermodynamics of Ionized Water in Strontium Chloride Solutions from Electromotive Force Measurements. *J. Phys. Chem.*, 57(5):531 – 535, 1953.

[100] Klemm W. and Klose E. The crystal structure of $ScCl_3$, $TiCl_3$ and VCl_3. *Z. anorg. Chem.*, 253:218, 1947.

[101] Cotton F. A. *Advanced inorganic chemistry.* John Wiley Sons, New York, London, 1999.

[102] Stevenson S., Rice G., Glass T., Harich K., Cromer F., Jordan M.R., Craft J., Hadju E., Bible R., Olmstead M.M., Maitra K., Fisher A.J., Balch A.L., and Dorn H.C. Small-bandgap endohedral metallofullerenes in high yield and purity. *NATURE*, 401:55, 1999.

[103] Preobrajenski A. B., Vinogradov A. S., Molodtsov S. L., Krasnikov S. K., Chasse T., Szargan R., and Laubschat C. Molecular effects in solid $NaNO_3$ observed by x-ray absorption and resonant Auger spectroscopy. *PRB*, 65:205116, 2002.

[104] Gurtubay I. G., Pitarke J. M., Ku W., Eguiluz A. G., Larson B. C., Tischler J., Zschack P., and Finkelstein K. D. Electron-hole and plasmon excitations in 3d transition metals: Ab initio calculations and inelastic x-ray scattering measurements. *PRB*, 72(12):125117, 2005.

[105] Fink J., Mullerheinzerling T., Scheerer B., Speier W., Hillebrecht F. U., Fuggle J. C., Zaanen J., and Sawatzky G. A. 2p Absorption-Spectra of the 3d Elements. *PRB*, 32:4899, 1985.

[106] Zaanen J., Sawatzky G. A., Fink J., Speier W., and Fuggle J. C. $L_{2,3}$ Absorption-Spectra of the Lighter 3d Transition-Metals. *PRB*, 32:4905, 1985.

[107] W. Speier, Fuggle J. C., Zeller R., Ackermann B., Szot K., Hillebrecht F. U., and Campagna M. Bremsstrahlung Isochromat Spectra and Density-of-States Calculations for the 3d and 4d Transition-Metals. *PRB*, 30(12):6921–6930, 1984.

[108] Takahashi T., Ito A., Inakuma M., and Shinohara H. Divalent scandium atoms in the cage of C_{84}. *PRB*, 52:1381213814, 1995.

[109] Ley L., Dabbousi O. B., Kowalczyk S. P., Mcfeely F. R., and Shirley D. A. X-Ray Photoemission Spectra of Valence Bands of 3d Transition-Metals Sc to Fe. *PRB*, 16:5372–5380, 1977.

[110] Eastman D.E. and Grobman W.D. Photoemission Energy-Distributions for Au from 10 to 40 Ev Using Synchrotron Radiation. *PRL*, 28:1327, 1972.

[111] Kawai J. Intensity ration of transition-metal L_α AND L_β lines. *The Rigaku Journal*, 18(1):31, 2001.

[112] Pease D. $L_{3,2}$ core-hole lifetime widths of 3d transition metals. *PRB*, 44:67086714, 1991.

[113] Pease D. L_3- to L_2-intensity ratiosin soft-x-ray valence-band emission spectra of 3d transition metals. *PRB*, 46:8790, 1992.

[114] Dupin J.-C., Gonbeau D., Vinatier P., and Levasseur A. Systematic XPS studies of metal oxides, hydroxides and peroxides. *Phys. Chem. Chem. Phys.*, 2:1319–1324, 2000.

[115] Tippins H. H. Absorption edge spectrum of scandium oxide. *Journal of Physics and Chemistry of Solids*, 27:1069–1071, 1966.

[116] Veal B. W. and Paulikas A. P. Final-State Screening and Chemical-Shifts in Photoelectron-Spectroscopy. *PRB*, 31:5399–5416, 1985.

[117] Kawai J., Maeda K., Nakajima K., and Gohshi Y. Relation between Copper L X-Ray-Fluorescence and 2p X-Ray Photoelectron Spectroscopies. *PRB*, 48:8560–8566, 1993.

[118] Shin S., Fujisawa M., Ishii H., Harada Y., Watanabe M., Grush M. M., Callcott T. A., Perera R. C. C., Kurmaev E. Z., Moewes A., Winarski R., Stadler S., and Ederer D. L. Soft X-ray emission spectroscopy of early transition metal compounds. *J. Electron Spectr. Relat. Phenom.*, 92:197, 1998.

[119] Citrin P. H. and Hamann D. R. Phonon broadening of x-ray photoemission line shapes in solids and its independence of hole state lifetimes. *PRB*, 15:2923–2928, 1977.

[120] Citrin P. H., Eisenberger P. M., Marra W. C., Åberg T., Utriainen J., and Kaellne E. Linewidths in x-ray photoemission and x-ray emission spectroscopies: What do they measure? *PRB*, 10(4):1762–1765, Aug 1974.

[121] Rubensson J., Eisebitt S., Nicodemus M., Boske T., and Eberhardt W. Electron Correlation in CaF_2 Studied in Threshold-Excited Soft-X-Ray Fluorescence. *PRB*, 49:1507, 1994.

[122] Matsubara M., Uozumi T., Kotani A., Harada Y., and Shin S. Polarization dependence of resonant X-ray emission spectra in early transition metal compounds. *Journal of the Physical Society of Japan*, 69:1558–1565, 2000.

[123] Matsubara M., Uozumi T., and Kotani A. Polarization dependence of resonance X-ray emission spectra in early transition metal compounds. *Journal of Synchrotron Radiation*, 8:393–395, 2001.

[124] Matsubara M., Uozumi T., Kotani A., Harada Y., and Shin S. Polarization dependence of resonant X-ray emission spectra in 3d(n) transition metal compounds with n=0, 1, 2, 3. *Journal of the Physical Society of Japan*, 71:347–356, 2002.

[125] Matsubara M., Harada Y., Shin S., Uozumi T., and Kotani A. Resonant X-ray emission spectroscopy in scandium halides. *Journal of the Physical Society of Japan*, 73:711–718, 2004.

[126] Kurmaev E. Z., Moewes A., Butorin S. M., Katsnelson M. I., Finkelstein L. D., Nordgren J., and Tedrow P. M. Half-metallic electronic structure of CrO_2 in resonant scattering. *PRB*, 67:155105, 2003.

[127] Kobayashi K., Sano Y., and Nagase S. J. Small-bandgap endohedral metallofullerenes in high yield and purity. *Comput. Chem.*, 22:1353, 2001.